I. R. IRAN

ISSN: 2423-7167
e-ISSN: 1735-9244

International Journal of Engineering

Journal Homepage: www.ije.ir

MERC

TRANSACTIONS C: Aspects

Volume 33, Number 12, December 2020

Materials and Energy Research Center

In the Name of God

INTERNATIONAL JOURNAL OF ENGINEERING
Transactions C: Aspects

DISCLAIMER
The publication of papers in International Journal of Engineering does not imply that the editorial board, reviewers or publisher accept, approve or endorse the data and conclusions of authors.

International **J**ournal of **E**ngineering *Transactions A: Basics* (ISSN 1728-1431) (EISSN 1735-9244)
International **J**ournal of **E**ngineering *Transactions B: Applications* (ISSN 1728-144X) (EISSN 1735-9244)
International **J**ournal of **E**ngineering *Transactions C: Aspects* (ISSN 2423-7167) (EISSN 1735-9244)
Web Sites: www.ije.ir & www.ijeir.info E-mails: ije.editor8@gmail.com, Tel: (+9821) 88771578, Fax: (+9821) 88773352
Materials and Energy Research Center (MERC)

ISSN: 2423-7167, e-ISSN: 1735-9244

International Journal of Engineering, Volume 33, Number 12, December 2020

CONTENTS:

ISSN: 2423-7167, e-ISSN: 1735-9244

International Journal of Engineering, Volume 33, Number 12, December 2020

International Journal of Engineering

Journal Homepage: www.ije.ir

Thermodynamic Modeling the Solubility of CO_2 in Aqua System of Methyldiethanolamine and 2-(2-Aminoethylamino)ethanol Using the Nonelectrolyte Wilson Nonrandom Factor

M. Abdolmajidi*[a], A. H. Joshaghani[a], A. Cheraghi[b], A. Haghtalab[c]

[a] *Chemical Engineering Department, Arak Branch, Islamic Azad University, Arak, Iran*
[b] *Department of Basic Sciences, Shahid Sattari Aeronautical University of Science and Technology, Tehran, Iran*
[c] *Department of Chemical Engineering, Tarbiat Modares University, Tehran, Iran*

PAPER INFO

Paper history:
Received 21 March 2020
Received in revised form 05 September 2020
Accepted 06 September 2020

Keywords:
Gas Sweetening
Alkanolamines
Nonelectrolyte Wilson Nonrandom Factor
Thermodynamic Modeling
Solubility

ABSTRACT

Alkanolamines are used to remove acidic gases such as CO_2 and H_2S from natural gas. In this study, thermodynamic modeling of the binary component CO_2+MDEA, three component MDEA+H_2O+CO_2 and the quaternary MDEA+AEEA+H_2O+CO_2 systems were developed using an additional Gibbs argillic model for the first time in the modeling of CO_2 solubility in different solutions. The appropriate model was considered using the assumption of an entirely molecular system without any occurrence of chemical reactions and saturated gas phase from the CO_2 gas. The nonelectrolyte Wilson nonrandom factor (N-Wilson-NRF) model and the activity coefficient method (γ_φ Aproach) were used to calculate solubility of CO_2. The two-component water- CO_2 model was modeled and the results were obtained by the accuracy of 1.38 of experimental results. In a three-component, water-CO_2-MDEA system with the amount of 6.913, the optimization was developed. The quaternary water-CO_2-MDEA-AEEA system was optimized with an overall approximation of 19.537 for all experiment data.

***doi**: 10.5829/ije.2020.33.12c.01*

1. INTRODUCTION

The removal of CO_2 and H_2S from the flue gas is essential in the process of natural gas purification. In addition, for the design and construction of gas transport equipment, experimental data on the solubility of CO_2 and H_2S in aquatic alkanolamines are required [1]. Due to the weakness or power of various alkanolamines in absorption of various acid gases, the choice of a suitable combination of these materials in the process of natural gas purification has been studied [2-4]. Also, at wide range of temperatures and pressures, various experiments are carried out to obtain a suitable thermodynamic model for desired estimation of experimental data [5-7]. It became clear that, because of the ionization of these mixtures, the models that utilize the activity coefficient have been used extensively in research projects [8-10]. Typically, in these models, various equations have been used to predict wide-range of interactions using the Pitzer-Debye-Huckel method and narrow-range of interactions using other types of methods [11-13].

Separation factor is an important feature in the choice of alkanolamine solution to eliminate acidic gas or to interpret the kinetic mechanism of acidic absorption in alkanolamine solution. Recently, Barzagli et al. [14] have studied CO_2 absorption and desorption experiments with alkanolamine mixtures in non-aqueous solvents (ethylene glycol mixtures and 2,1 propanediol with methanol or ethanol) [13]. They reported relatively low separation temperature (about 80°C) and less

*Corresponding author Email address: *m.r.a.majidi@gmail.com* (M. Abdolmajidi)

Please cite this article as: M. Abdolmajidi, A. H. Joshaghani, A. Cheraghi, A. Haghtalab, Thermodynamic Modeling the Solubility of CO_2 in Aqua System of Methyldiethanolamine and 2-(2-Aminoethylamino)ethanol Using the Nonelectrolyte Wilson Nonrandom Factor, International Journal of Engineering, Transactions C: Aspects Vol. 33, No. 12, (2020) 2436-2442

evaporation. They have shown that amine recovery in non-aqueous solvents can be easily done [6]. The results of their study are given with the average and maximum relative deviation between experimental data and linear matching values. These numbers provide information about the linear extrapolation. Also, the decrease in the strength of the protonated alkanolamines was observed with an increase in fractions of organic composition and temperature. The greatest effect is observed for butanol-water mixtures as solvent. This result was expected since the butanol-water solvents had the lowest dielectric values compared to sulfolane-water and methanol-water solvents.

In the case of acid gases, thermodynamic modeling of the equilibrium solubility is also an important topic for the design of gas purification and CO_2 capture processes. Zoghi and Feizi [15] calculated the solubility of CO_2 in aqueous solutions of 2, 2-aminoethyl amino ethanol (AEEA) and compare the results with the Deshmuch-Mather model. Finally, for the quaternary system water-CO_2-N-methyldiethanolamine (MDEA)-AEEA, the modified Peng-Robinson cube parameters which were modified by the electrolyte are correlated with the emPR-CPA equation of state (EoS) and finally, the solubility of CO_2 is calculated. They studied equilibrium solubility of CO_2 in the mentioned solution in the range of 308.2 to 368.2 K and the 101 to 4448 kPa [9].

2. THERMODYNAMIC MODELING

In this work, we have used gamma-phi (γ-φ) method for modeling the behavior of under investigation systems. Specifically, to calculate the activity coefficients of the components in the gas phase, the N-Wilson-NRF state equation and to calculate the fugacity coefficients in the liquid phase, the Peng Robinson equation has been used [16]. Using the qualitative properties (PVT), we can calculate all thermodynamic properties and thermodynamic potential energies. Here, we will investigate the behavior of PVT of a pure substance in gas and liquid states.

Parameters (a and b) which are called gravity and repulsion parameters, respectively. Here, k_1 and k_2 are numerical constants that obtained by the critical properties for each pure substance.

Peng-Robinson presented his equation as follows Equation (2) where k_1= 2 and k_2=-1 [17]:

$$P=\frac{RT}{v-b}-\frac{a(T,\omega)}{v(v+b)+b(v-b)} \quad (1)$$

In this equation, a, b are:

$$a=0.457235\frac{R^2T_c^2}{P_c},\ b=0.077796\frac{RT_c}{P_c}$$

The k equation is obtained by fitting steam pressure data from boiling point to critical point in Equation (2):

$$k=0.37464+1.54226\omega-0.26993\omega^2 \quad (2)$$

The cubic equations of state for the blends are written as follows in Equation (3):

$$P=\frac{RT}{v-b}-\frac{a(T,\omega)}{v^2+k_1bv+k_2b^2} \quad (3)$$

Also, $\boldsymbol{v}$ is the molar volume of the mixture. In this case, using the mixing rule, the values of a and b can be set according to the a_i and b_i parameters for the pure substance.

2. 1. Mixture Fugacity Coefficient Using Peng-Robinson Equation The Peng- Robinson equation of state can be divided as follows in Equation (4) [8-9]:

$$P=\frac{RT}{v-b}-\frac{a\alpha(T,\omega)}{(v+(1+\sqrt{2})b)(v+(1-\sqrt{2})b)} \quad (4)$$

By proper derivation from Equation (2), the fugacity coefficient of component i is obtained as follows in Equation (5):

$$\ln\varphi_i=\frac{b_i}{b}(Z-1)-\ln(Z-B)-\frac{A}{2\sqrt{2}B}\left[\frac{2\sum_{j=1}^{c}y_ia_{ij}}{a\alpha}-\frac{b_i}{b}\right]\ln\frac{Z+B(1+\sqrt{2})}{Z+B(1-\sqrt{2})} \quad (5)$$

2. 2. An Integral Method for the Calculations of Vapor-liquid Equilibrium In the integral method, the equation of fugacity is used directly for equilibrium calculations. Therefore, for the equilibrium of two phases of vapor and liquid, the equation of fugacity is used based on the following Equation (6) [18, 19]:

$$f_i^v=f_i^l \quad (6)$$

In this case, the following two methods are proposed for the calculations of vapor-liquid equilibrium, each method depending on the nature of the components:

I. The equation of state approach (φ_φ Approach)
II. The activity coefficient approach (γ_φ Approach)

In the equation of state approach, the fugacity of each component in the vapor and liquid phases is written as follows:

$f_i^v=y_i\varphi_i^vP$ for vapor and $f_i^l=x_i\varphi_i^lP$ for liquid and x_i, y_i are the molar fractions of component I in liquid and vapor phases, respectively. Hence Equation (7):

$$K_i=\frac{y_i}{x_i}=\frac{\varphi_i^l}{\varphi_i^v} \quad (7)$$

where K_i is the ratio of components (K-value) for component i. Therefore, with the proper equation of state, the coefficients of fugacity can be calculated.

The activity coefficient is the quantity that represents the deviation of the non-ideal behavior of liquid mixtures from the ideal behavior of Lewis-Randal. When we have an ideal solution, the activity coefficient is 1 and the fugacity of component i is ideally written as follows in Equation (8):

$$f_i^{id} = x_i f_{i,pure} \tag{8}$$

In other words, liquid solutions can be divided into (ideal dilution solution) and (non-ideal solution). Therefore, in order to calculate the activity coefficients, it is necessary to calculate the first fugacity from the pure material. Therefore, fugacity can be achieved by using a dense phase fugacity in Equation (9):

$$f_{i,pure} = P_i^{sat}\varphi_i^{sat} \exp[\frac{v_i^0(P-P_i^{sat})}{RT}] \tag{9}$$

The saturation fugacity coefficient (φ_i^{sat}) is obtained at a saturation point at temperature T, which can be calculated using the ratio of the fugacity coefficient for the pure component.

2. 3. Activity Coefficient in Liquid Solutions For liquid solutions, the activity coefficient is used as the standard deviation from the ideal state, so for the component in liquid solution and constant temperature it can be written as Equation (10) [20-22]:

$$\gamma_{i,0} = \frac{f_i(T,P,x_i)}{f_i^{LR}} = \frac{f_i(T,P,x_i)}{x_i f_i^{\,0}(T,P)} \tag{10}$$

The Lewis-Randal activity coefficient is used for the solutions in which the components are either dissolved or convergent, in any ratio from dilute to concentrated. On the other hand, some solutions have a positive deviation $(\gamma_i \succ 1)$ from the Lewis-Randal law, and others have negative deviations $(\gamma_i \prec 1)$. For some solutions, you cannot use the Lewis-Randal activity factor. In this kind of systems, components are not resolved in each other with any ratio. In this case, it is not possible to use the Lewis-Randal activity factor for vapor in the solution. In this case, pure vapor may not be available as a standard solution at system temperature and pressure. Another example is the solubility of electrolytes and polymers in solvents. In this case, the activity coefficient for component i is defined as Equation (11):

$$\gamma_i^* = \frac{f_i(T,P,x_i)}{x_i H_{ij}(T,P)} \tag{11}$$

Thus, for equilibrium calculations in liquid and solid phases, using the gamma-phi method, we need to have a proper function for calculating the activity coefficient of the components in the solution. On the other hand, we know that in order to obtain an appropriate model of the activity coefficient, the Gibbs energy function (G^E) is necessary for the solution which is shown in Equation (12).

$$\ln\gamma_i = (\frac{\partial(G^E/RT)}{\partial N_i})_{T,P,N_{j\neq i}} = (\frac{\partial(Ng^E/RT)}{\partial N_i})_{T,P,N_{j\neq i}} \tag{12}$$

2. 4. Local Composition Models The local composition model is a semi-experimental method that derives from the concept of the local composition of molecules in a network. The local composition concept was first introduced by Wilson in 1964 [23].

In 2009, the Haghtalab and Mazloumi present new N-Wilson-NRF model which provided a random mode for each cell based on the literature stated [24]. Local molecular fractions are defined using non-random Γ_{ij} coefficients Equation (13):

$$\begin{aligned} &x_{ij} = x_i\Gamma_{ij},\ \Gamma_{ij} = \frac{\beta_{ij}}{\sum_{k=1}^{N} x_k\beta_{kj}},\\ &\Gamma_{ii} = \Gamma_{ij}/\beta_{ji},\\ &\beta_{ij} = \exp(-\frac{h_{ij}-h_{jj}}{ZRT}) = \exp(-\frac{\lambda_{ij}}{Z}) \end{aligned} \tag{13}$$

While $\beta_{ij} \neq \beta_{ji}, \beta_{ii} = \beta_{jj} = 1$ and N is the number of components in the system and Z is the coordination number. Using Equation (13), we can obtain the hypertension enthalpy formula for a two-component mixture. Assuming that the temperature is independent of enthalpy Equation (14):

$$\frac{g^E}{RT} = Z[x_1\ln\Gamma_{11} + x_2\ln\Gamma_{22} + x_1x_2\ln(\beta_{12}\beta_{21})] \tag{14}$$

by deriving the Equation (14), the activity coefficient for a component in a two-component mixture is obtained as Equation (15):

$$\ln\gamma_1 = Z[\ln\Gamma_{11} + x_2(\Gamma_{21}-\Gamma_{12}) + x_2^2\ln(\beta_{12}\beta_{21})] \tag{15}$$

The general format of the equations for a multi-component mixture is obtained as Equations (16) and (17):

$$\frac{g^E}{RT} = Z[\sum_i x_i(\ln\Gamma_{ii} + \sum_j x_j\ln\beta_{ij})] \tag{16}$$

$$\begin{aligned} &\ln\gamma_i = Z[1+\ln\Gamma_{ii} - \sum_j x_j(\Gamma_{ij} - \ln\beta_{ij}\beta_{ji} + \sum_k x_k\ln\beta_{kj})]\\ &\lambda_{ij} = (h_{ij}-h_{jj})/RT,\ \lambda_{ii} = \lambda_{jj} = 0, \beta_{ii} = \beta_{jj} = 1.0 \end{aligned} \tag{17}$$

2. 5. The Process Flowchart of Calculating co_2 Gas Solubility The general method for calculating the

vapor pressure of each of the various system components using the bubble-pressure calculations flowchart is shown in Figure 1. For higher order systems, these equations for the mixtures can be used [17]. As shown in Figure 1 by the help of laboratory pressure, temperature and composition of the components percentage in the liquid phase, by the initial guess for the system pressure, the simulations can be done, and also the composition of the components in the gas phase and the calculated pressure can be gained using this system. It should be noted that for the two-component and multi-component systems the overall process is the same and for the higher order systems, the classic rules of the hybrid can be used.

3. RESULT AND DISCUSSION

3. 1. Quaternary Water-CO_2-MDEA-2, 2-aminoethyl (amino) ethanol System One of the most important factors in the design of absorption unit is the solvent material. The most important features of a solvent for absorption are higher absorption speed, better function in absorption process, high net recycling capacity and better chemical stability. In the previous studies [25], researchers measured the rate of CO_2 absorption among various amines, which showed that 2-2-Aminoethyl(Amino)Ethanol (AEEA) and (2-Aminoethyl) 1,3-Propandiamine solvents can absorb CO_2 more quickly. Ma'mum et al. [26] used a screening test and found that the aqueous solution of AEEA could be used as an absorbent in the process of absorbing CO_2 from combustion gases. AEEA has a high absorption rate and net recycling capacity, which is clearly higher than monoethanolamine indexes. Also, this material has also shown its high absorption capacity at higher CO_2 loads. Recently, Zoghi et al. [27] investigated the effect of various activators in methyl diethanolamine on the CO_2 capture process. They showed that AEEA can greatly increase the rate of CO_2 absorption compared with other activators such as Piperazine. The amount of waste lost in the recovery process is another important factor that should be considered in choosing the appropriate solvent. Wilson [28] measured the vapor pressure of AEEA under the temperature of the recovery process (395 K) and showed that AEEA had much lower vapor pressure (959 Pa) than monoethanolamine (15900 Pa). Also, thermodynamic modeling of the equilibrium solubility of acid gases in the process of sweetening and absorbing CO_2 gas is another vital point. When acid gases are absorbed in an aqueous solution of alkanolamine, different ionic species are produced by chemical reactions. It makes it difficult to calculate the liquid-vapor balance for aqueous solutions of alkanolamine. In this section, we used the gamma-phi(γ-φ) method and the experimental data of Zoghi experiment [15], to develop a thermodynamically model of the quaternary water-CO_2-MDEA-AEEA system. It is important to assume the system physically, in order to reduce the volume of the calculations and to simplify the process of chemical reactions. Based on the results of the above four-component system, the target function was equal to 19.537.

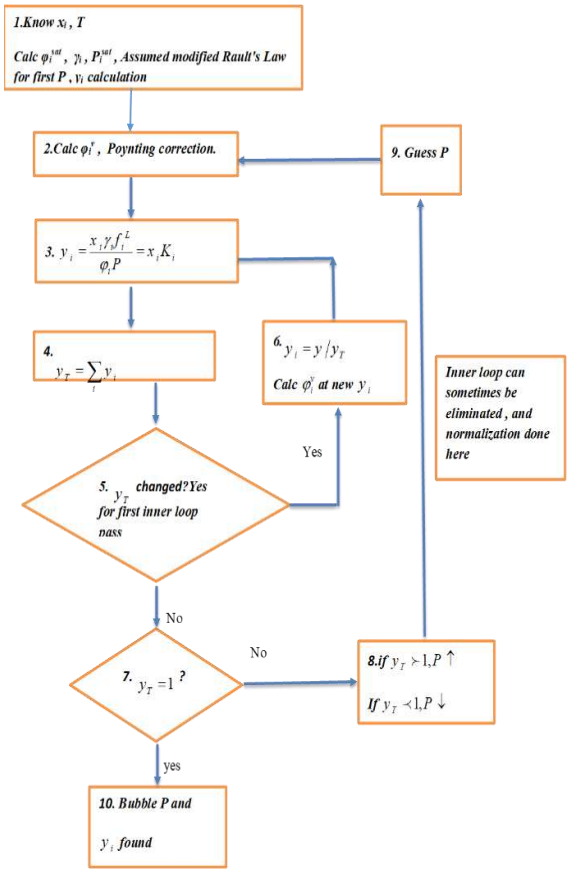

Figure 1. The Process Flowchart of Calculating CO_2 Gas Solubility in Amine Solutions

TABLE 1. Optimized Values of the N-Wilson-NRF Equation for the Quaternary Water-CO_2-MDEA-AEEA System

i-j	λ_{ij} *	a_{ij}	b_{ij}
CO_2-AEEA	λ_{14}	-27/8734	-48669/667
AEEA-CO_2	λ_{41}	-8/3472	-7713/6611
H_2O-AEEA	λ_{24}	278/2278	-941/2250
AEEA-H_2O	λ_{42}	8/4826	1323/4516
MDEA_AEEA	λ_{34}	5/8430	-62/8829
AEEA_MDEA	λ_{43}	2/3283	-221/7266

$\lambda_{ij} = a_{ij} + \frac{b_{ij}}{T}$

3. 2. Interaction Parameter In the previous sections and in the equation of activity coefficients, we used equation 17 to calculate the interaction parameters, where two parameters a and b were obtained and optimized simultaneously. In this section, by developing the interaction parameter equation, we examined the effect of this change on the accuracy of the calculations. The equation of interaction parameter with the three sub-parameters a, b and c is defined in Equation (18):

$$\lambda_{ij} = a_{ij} + \frac{b_{ij}}{T} + c_{ij}[\frac{T - T^0}{T} + \ln\frac{T}{T^0}] \quad (18)$$

For the quaternary water-CO_2-MDEA-AEEA system, the target function was equal to 19.084 and the values of interaction parameters are shown in Table 3.

TABLE 2. Experimental and Calculated Pressure in the Quaternary Water-CO_2-MDEA-AEEA System

Loading	Pexp (kPa)	P cal(kPa)	Loading	Pexp(kPa)	P cal(kPa)
	308.2(K)			328.2(K)	
0.735	103.3	130.66	0.516	100.7	90.96
0.753	111.6	140.02	0.544	114.5	114.5
0.807	146.7	171.0261	0.56	128.3	129.3136
0.832	187.4	187.4	0.62	133.5	197.655
0.862	232.9	207.4161	0.652	163.9	242.6039
0.89	350.6	227.9479	0.704	249.7	329.7518
0.906	483.8	240.3064	0.765	373.8	456.6946
0.934	746.8	263.113	0.805	531.8	556.0085
0.944	908.8	271.57	0.846	793.2	672.2862
0.954	1082	280.1942	0.868	963.6	741.1162
0.966	1254.7	290.766	0.885	1165.9	797.5861
0.974	1438.8	298.3437	0.895	1335.3	832.1222
0.988	1652.1	311.3575	0.917	1574.4	911.7242
1.002	1952.7	324.6064	0.934	1798.8	976.6611
	343.2(K)			368.2(K)	
0.489	170.9	158.3485	0.406	281	177.09
0.514	189.4	194.8241	0.429	322	224.31
0.556	230.9	267.88.907	0.47	405.5	327.27
0.626	349.6	426.1947	0.527	585.6	514.45
0.688	468.8	609.5557	0.543	649.5	577
0.73	593.3	759.5985	0.589	821	783.34
0.759	724.3	876.4672	0.626	1010	979.8
0.81	968.3	1110.433	0.67	1241.7	1251.96
0.822	1172.2	1172.2	0.708	1490.3	1523.53
0.835	1316.5	1239.3	0.742	1656.7	1796.68
0.896	2128.4	1596.662	0.852	2758.1	2917.502
0.913	2373.6	1707.78	0.867	3002.9	3101.764
0.916	2898.6	1728.127	0.883	3266.8	3305.867
0.929	3082.6	1817.519	0.899	3502.9	3524.257
0.942	3253.2	1910.189	0.916	3869.6	3766.08

TABLE 3. Optimized Values of the N-Wilson-NRF Equation in the Quaternary Water-CO_2-MDEA-AEEA System

i-j	λ_{ij}	a_{ij}	b_{ij}	c_{ij}
CO_2-AEEA	λ_{14}	-27/8734	-48669/667	-0/01153
AEEA-CO_2	λ_{41}	-8/3472	-7713/6611	-0/01552
H_2O-AEEA	λ_{24}	287/2285	-941/2250	-0/07370
AEEA-H_2O	λ_{42}	8/4826	1323/4516	-0/01154
MDEA_AEEA	λ_{34}	5/8430	-62/8829	0/01758
AEEA_MDEA	λ_{43}	2/3283	-221/7266	0/01680

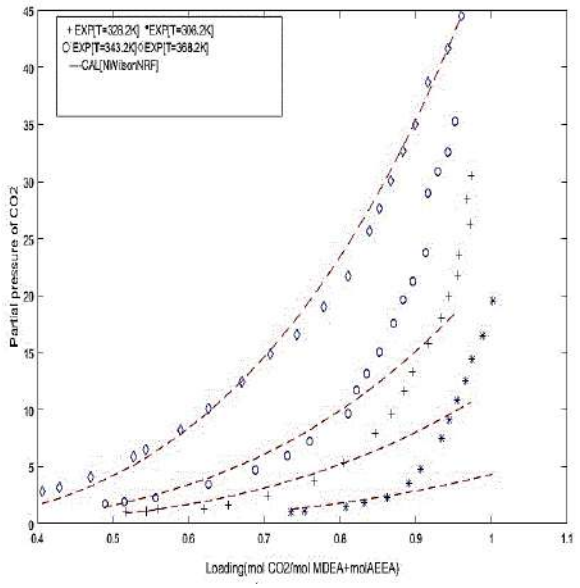

Figure 2. Molecular Concentration of CO_2 in Aqueous Solution of MDEA+AEEA

4. CONCLUSION AND FUTURE PERSPECTIVE

In this project, the solubility of CO_2 gas was investigated in alkanolamine solutions. The N-Wilson-NRF model and the activity coefficient method (γ_φ Approach) were used to calculate solubility of CO_2. The two-component water- CO_2 model was modeled and the results were obtained by the accuracy of 1.38 of experimental results. In a three-component, water-CO_2-MDEA system with the amount of 6.913, the optimization was developed.

The quaternary water-CO_2-MDEA-AEEA system was optimized with an overall approximation of 19.537 for all experiment data. By changing the interaction parameter equation of λ_{ij} to the three-parametric equation in the two-component system, the approximation of 6.581 and in the three-component system, 19.084 were obtained. The systems used in this study have made a completely reasonable approximation considering that the solubility modeling of gas in solutions is based on the physical interaction. To make the calculation and mentioned systems more accurate, some suggestions are presented which are:

1. considering chemical reactions in the liquid phase to improve the accuracy of the model,
2. performing more experiments at higher temperatures and pressures to obtain more operational data,
3. using mixing rules in multi-component system computing procedure,
4. using the equations of electrolyte activation to improve the accuracy of the model.

5. REFERENCES

1. Barzagli, F., Mani, F. and Peruzzini, M., "A comparative study of the CO_2 absorption in some solvent-free alkanolamines and in aqueous monoethanolamine (MEA)", ***Environmental Science & Technology***, Vol. 50, No. 13, (2016), 7239-7246. DOI: 10.1021/acs.est.6b00150
2. Akhmetshina, A.I., Petukhov, A.N., Vorotyntsev, A.V., Nyuchev, A.V. and Vorotyntsev, I.V., "Absorption behavior of acid gases in protic ionic liquid/alkanolamine binary mixtures", ***ACS Sustainable Chemistry & Engineering***, Vol. 5, No. 4, (2017), 3429-3437. DOI: 10.1021/acssuschemeng.7b00092
3. Akbartabar, I., Yazdanshenas, M.E., Tayebi, H.-A. and Nasirizadeh, N., "Physical chemistry studies of acid dye removal from aqueous media by mesoporous nano composite: Adsorption isotherm, kinetic and thermodynamic studies", ***Physical Chemistry Research***, Vol. 5, No. 4, (2017), 659-679. DOI: 10.22036/PCR.2017.83378.1371
4. Patel, H.A., Karadas, F., Canlier, A., Park, J., Deniz, E., Jung, Y., Atilhan, M. and Yavuz, C.T., "High capacity carbon dioxide adsorption by inexpensive covalent organic polymers", ***Journal of Materials Chemistry***, Vol. 22, No. 17, (2012), 8431-8437. https://doi.org/10.1039/C2JM30761H
5. He, X., Fu, C. and Hägg, M.-B., "Membrane system design and process feasibility analysis for CO_2 capture from flue gas with a fixed-site-carrier membrane", ***Chemical Engineering Journal***, Vol. 268, (2015), 1-9. DOI: 10.1016/j.ijggc.2013.03.026
6. Yan, H., Fu, Q., Zhou, Y., Li, D. and Zhang, D., " CO_2 capture from dry flue gas by pressure vacuum swing adsorption: A systematic simulation and optimization", ***International Journal of Greenhouse Gas Control***, Vol. 51, (2016), 1-10. https://doi.org/10.1016/j.ijggc.2016.04.005
7. Shi, W., Siefert, N.S. and Morreale, B.D., "Molecular simulations of CO_2, H_2, H_2O, and H_2S gas absorption into hydrophobic poly (dimethylsiloxane)(PDMS) solvent: Solubility and surface tension", ***The Journal of Physical Chemistry C***, Vol. 119, No. 33, (2015), 19253-19265. DOI: 10.1021/acs.jpcc.5b05806
8. Sadegh, N., Stenby, E.H. and Thomsen, K., "Thermodynamic modeling of hydrogen sulfide absorption by aqueous n-methyldiethanolamine using the extended uniquac model", ***Fluid Phase Equilibria***, Vol. 392, (2015), 24-32. https://doi.org/10.1016/j.fluid.2015.01.024
9. Barati-Harooni, A., Najafi-Marghmaleki, A. and Mohammadi, A.H., "Efficient estimation of acid gases (CO_2 and H_2S) absorption in ionic liquids", ***International Journal of***

Greenhouse Gas Control, Vol. 63, (2017), 338-349. https://doi.org/10.1016/j.ijggc.2017.05.014

10. Koronaki, I., Prentza, L. and Papaefthimiou, V., "Modeling of CO_2 capture via chemical absorption processes−an extensive literature review", ***Renewable and Sustainable Energy Reviews***, Vol. 50, (2015), 547-566. https://doi.org/10.1016/j.rser.2015.04.124
11. Suleman, H., Nasir, Q., Maulud, A.S. and Man, Z., "Comparative study of electrolyte thermodynamic models for carbon dioxide solubility in water at high pressure", ***Chemical Engineering Transactions***, Vol. 45, (2015). DOI: 10.3303/CET1545099
12. Shekaari, H., Zafarani-Moattar, M.T., Mokhtarpour, M. and Faraji, S., "Effect of 1-ethyl-3-methylimidazolium ethyl sulfate ionic liquid on the solubility of indomethacin in aqueous solutions at various temperatures", ***Journal of Molecular Liquids***, Vol. 260, (2018), 166-172. https://doi.org/10.1016/j.molliq.2018.03.061
13. Castañeda, C.A., Wolfson, N.A., Leng, K.R., Kuo, Y.-M., Andrews, A.J. and Fierke, C.A., "Hdac8 substrate selectivity is determined by long-and short-range interactions leading to enhanced reactivity for full-length histone substrates compared with peptides", ***Journal of Biological Chemistry***, Vol. 292, No. 52, (2017), 21568-21577.
14. Barzagli, F., Mani, F. and Peruzzini, M., "Efficient CO_2 absorption and low temperature desorption with non-aqueous solvents based on 2-amino-2-methyl-1-propanol (AMP)", ***International Journal of Greenhouse Gas Control***, Vol. 16, (2013), 217-223. https://doi.org/10.1016/j.ijggc.2013.03.026
15. Zoghi, A.T. and Feyzi, F., "Equilibrium solubility of carbon dioxide in aqueous 2-((2-aminoethyl) amino) ethanol and n-methyldiethanolamine solution and modeling by electrolyte mpr-cpa eos", ***The Journal of Chemical Thermodynamics***, Vol. 67, (2013), 153-162.
16. Haghtalab, A. and Shojaeian, A., "High pressure measurement and thermodynamic modelling of the solubility of carbon dioxide in n-methyldiethanolamine and 1-butyl-3-methylimidazolium acetate mixture", ***The Journal of Chemical Thermodynamics***, Vol. 81, (2015), 237-244. https://doi.org/10.1016/j.jct.2014.10.011
17. Smith, J., Van Ness, H. and Abbott, M., "Chemical engineering thermodynamics", ***Sat***, Vol. 18, (1996), 1-3.
18. He, P. and Chu, J., "Low pressure vapor-liquid equilibrium validation with special pseudo-components", in Control Conference (CCC), 2017 36th Chinese, IEEE. 10381-10386.
19. Løvseth, S.W., Austegard, A., Westman, S.F., Stang, H.G.J., Herrig, S., Neumann, T. and Span, R., "Thermodynamics of the carbon dioxide plus argon (CO_2+ ar) system: An improved reference mixture model and measurements of vapor-liquid, vapor-solid, liquid-solid and vapor-liquid-solid phase equilibrium data at the temperatures 213–299 k and pressures up to 16 mpa", ***Fluid Phase Equilibria***, Vol. 466, (2018), 48-78. https://doi.org/10.1016/j.fluid.2018.02.009
20. Chen, M., Xie, Y., Wu, H., Shi, S. and Yu, J., "Modeling solubility of nitrogen in clean fire extinguishing agent by peng-robinson equation of state and a correlation of henry's law constants", ***Applied Thermal Engineering***, Vol. 110, (2017), 457-468. https://doi.org/10.1016/j.applthermaleng.2016.08.179
21. Ashassi-Sorkhabi, H. and Kazempour, A., "Application of pitzer and six local composition models to correlate the mean ionic activity coefficients of aqueous 1-butyl-3-methylimidazolium bromide ionic liquid solutions obtained by emf measurements", ***The Journal of Chemical Thermodynamics***, Vol. 110, (2017), 71-78. https://doi.org/10.1016/j.jct.2017.02.015
22. Mester, Z. and Panagiotopoulos, A.Z., "Mean ionic activity coefficients in aqueous nacl solutions from molecular dynamics simulations", ***The Journal of Chemical Physics***, Vol. 142, No. 4, (2015), 044507.
23. Renon, H. and Prausnitz, J.M., "Local compositions in thermodynamic excess functions for liquid mixtures", ***AIChE Journal***, Vol. 14, No. 1, (1968), 135-144. https://doi.org/10.1002/aic.690140124
24. Haghtalab, A. and Mazloumi, S.H., "Electrolyte cubic square-well equation of state for computation of the solubility CO_2 and H_2S in aqueous mdea solutions", ***Industrial & Engineering Chemistry Research***, Vol. 49, No. 13, (2010), 6221-6230.
25. Bonenfant, D., Mimeault, M. and Hausler, R., "Determination of the structural features of distinct amines important for the absorption of CO_2 and regeneration in aqueous solution", ***Industrial & Engineering Chemistry Research***, Vol. 42, No. 14, (2003), 3179-3184.
26. Ma'mun, S., Jakobsen, J.P., Svendsen, H.F. and Juliussen, O., "Experimental and modeling study of the solubility of carbon dioxide in aqueous 30 mass% 2-(2-aminoethylamino)ethanol solution", ***Industrial & Engineering Chemistry Research***, Vol. 45, No. 8, (2006), 2505-2512.
27. Zoghi, A.T., Feyzi, F. and Dehghani, M.R., "Modeling CO_2solubility in aqueous n-methyldiethanolamine solution by electrolyte modified peng–robinson plus association equation of state", ***Industrial & Engineering Chemistry Research***, Vol. 51, No. 29, (2012), 9875-9885. doi: 10.1021/ie2026053
28. Dumée, L., Scholes, C., Stevens, G. and Kentish, S., "Purification of aqueous amine solvents used in post combustion CO_2capture: A review", ***International Journal of Greenhouse Gas Control***, Vol. 10, (2012), 443-455. https://doi.org/10.1016/j.ijggc.2012.07.005

Persian Abstract

چکیده

زدودن هیدروژن سولفید و دی اکسید کربن از گاز دودکش در فرایند تصفیه گاز طبیعی و گیرانداختن گازهای اسیدی اهمیت دارد به علاوه، برای طراحی و ساخت تجهیزات اتصال گاز، داده های تجربی انحلال پذیری H_2S و CO_2 در آلکانول آمین های آبی مورد نیاز هستند. به دلیل ضعف یا قدرت آلکانول آمین های مختلف در جذب گازهای اسیدی گوناگون انتخاب یک ترکیب مناسب از این مواد در فرایند تصفیه گاز طبیعی مورد مطالعه قرار گرفته و در دما و فشارهای مختلف آزمایش های گوناگونی برای بدست آوردن مدل ترمودینامیکی مناسب جهت تخمین بهتر دادهای آزمایشگاهی انجام شده است که به خاطر تجزیه یونی این مخلوط ها مدل هایی که از روش ضریب اکتیویته استفاده کرده اند جواب دقیق تری را پیش بینی کرده اند. به طور معمول در این مدل ها برای پیش بینی برهمکنش های برد بلند از روش پیتزر_دبای_هوکل و برای نیروهای برد کوتاه از معادلات مختلفی استفاده شده است. در این مقاله با مطالعه دادهای آزمایشگاهی و محاسباتی مقایسه ای بین حلال های مختلف و مدل های ترمودینامیکی متناظر بر آنها در جهت انتخاب حلال و مدل مناسب انجام شده است.

International Journal of Engineering

Journal Homepage: www.ije.ir

Neuro-fuzzy Modelling and Experimental Study of the Physiological Comfort of Green Cotton Fabric Based on Yarn Properties

M. S. Hesarian*[a], J. Tavoosi[b], S. H. Hosseini[c]

[a] *Department of Textile Engineering, Urmia University of Technology, Urmia, Iran*
[b] *Department of Electrical Engineering, Ilam University, Ilam, Iran*
[c] *Department of Chemical Engineering, Ilam University, Ilam, Iran*

PAPER INFO

Paper history:
Received 01 July 2020
Received in revised form 10 September 2020
Accepted 29 October 2020

Keywords:
Garment
Finishing
Comfort Properties
Adaptive Neuro Fuzzy Inference System

ABSTRACT

In textile and garment industry, the physiological comfort of fabric as one of the important parameters, can be improved by the fabric finishing treatment. Nevertheless, the toxic chemicals produced in this process leads to the pollution of the environment. Therefore, this study aims to improve the physiological comfort of the cotton fabric without applying the finishing process as green technology. Accordingly, air permeability and moisture transfer as two important parameters of the fabric physiological comfort are evaluated with the structural parameters of the cotton yarn using experimental and theoretical procedures. For theoretical evaluations, a novel neuro-fuzzy network (ANFIS) is proposed and used for modelling and estimation. The structural parameters of yarn are the yarn linear density, yarn twist and fineness of fibers, which are defined as inputs and air permeability and moisture transfer of the cotton samples are considered as the outputs of developed ANFIS model. According to the experimental and modeling results, the fiber fineness, yarn linear density (Ne) and yarn twist have the same effect on the output parameters. It is also found that both parameters of the physiological comfort sensory can be improved effectively without finishing process. Simulation results show the novel proposed ANFIS that has high learning capability, fast convergence and accuracy greater than 99% and negligible error value smaller than of 1% can be reasonably used in textile industry. In addition, for the winter garments, the optimum points of turns per meter (T.P.M) coefficient, English count of yarn, and fibers fineness are 4.5, 25 and 3, respectively.

***doi**: 10.5829/ije.2020.33.12c.02*

1. INTRODUCTION

Nowadays, the environmental pollution concerns are important topics for academic studies and there are many researches in the open literature, accordingly [1-3]. In textile industry, the toxic materials have been used in different processes such as bleaching, sizing, de-sizing, scouring, dying, printing, finishing, anti-static, and anti-wrinkling. Recently, the famous brands of clothing industry have attempted to develop their products based on "Green Technology Methods". In the textile and clothing industry, the green technologies can be applied with the fiber preparation, yarn production, fabric production, dyeing and printing and finishing processes [4]. In garment industry, the clothing comfort as an important parameter is improved by finishing process. The effect of weaving pattern and number of the picking sequences on the wetting, wicking and air permeability (AP) properties of the samples were analyzed.

The effect of moisture finisher on the comfort sensory of woven fabrics was also studied by the researchers [5]. The moisture finishing parameters were analyzed to optimize the sportswear' comfort. The results revealed that when the ethylated alcohol was synthesized as wetting agent with the recipe containing amino silicone polyether copolymer and hydrophilic polymer in the ratio of 1:2 with pH of 5.5 at 600-700 ℃ temperature, better comfort properties for sportswear is obtained. Hermophysiological comfort and mechanical properties of cotton fabrics for lady's summer apparel were

*Corresponding Author Institutional Email: *S.hesarian@uut.ac.ir* (M. S. Hesarian)

Please cite this article as: M. S. Hesarian, J. Tavoosi, S. H. Hosseini, Neuro-fuzzy Modelling and Experimental Study of the Physiological Comfort of Green Cotton Fabric Based on Yarn Properties, International Journal of Engineering, Transactions C: Aspects Vol. 33, No. 12, (2020) 2443-2449

evaluated by fabric weight characteristic (number of the warp / weft yarns per inch and yarn count) [6]. The weight of the cotton samples studied in that research was 50 to 80 g/m^2. The main target of that work was to make a balance between two parameters of the yarn count and number of ends and picks per inch in fabric to achieve the appreciate fabric comfort and strength. The results showed that the fabric samples with 60 Ne warp count, 50 Ne weft count, 90 ends/in as warp density and 50 pick/in as weft density have suitable air permeability and mechanical properties [6]. Water vapor resistance and thermal resistance of commercial apparel as comfort parameters were studied based on the fabric structural parameters and fiber type by regression analysis [7-8].

Adaptive neuro-fuzzy inference system (ANFIS) and image processing method as the well-known soft computing techniques have been used in various applications of the function approximation and control in different scopes for the last two decades. [9-11]. There are many published works in the literature about applying ANFIS in the different areas of on-line approximation applications in the textile industry [12-13]. For example, ANFIS was used to predict the bending rigidity of woven fabrics [14]. For this purpose, a set of cotton fabrics used in the clothing industry was de-sized, scoured and relaxed. The weight and thickness and cover factor of fabric were selected as input parameters and the bending rigidity of fabric was considered as the model output.

In the present study physiological comfort is developed based on the new yarn parameters without environmental pollution as a result of finishing treatment elimination. In addition, the improvement of physiological comfort by the yarn parameters is studied here for the first time. the linear density, twist yarn and fineness of fiber are the parameters used in this study as structural parameters of cotton yarn for experimental evaluation of the air permeability and moisture transfer as physiological comfort properties.

Finally, the theoretically analysis was done by an improved ANFIS technique. In this model the linear density, twist yarn and fineness of fibre are input parameters and moisture transfer and air permeability are model outputs .A brief review on the novelties of methodology and ANFIS modeling performed in the present research can be listed as follows:

- A novel ANFIS with fuzzy coefficient in consequent part
- A new parameter learning method with fast convergence
- The new parameters concerning the yarn structure used to evaluate the physiological comfort of fabric.

2. METHODOLOGY

In this research we developed the cotton fabrics with the plain weave structures and different thicknesses by using the cotton yarns with the characteristics presented in Table 1. The characteristics of yarn are measured by an experimental instrument that its name is electronic twist tester (Figure 1). Twist in yarn is essential to hold the fibers together and is added to the spinning and plying processes. In this study, the yarn twist is determined by T.P.M coefficient. In the textile industry the English count of yarn is an indirect method of expressing the size of a cotton yarn. In this system by increasing the yarn number or count, the weight of yarn length decreases. Another parameter is thickness of fabric (mm). This parameter is measured by the thickness gauge presented in Figure 2.

TABLE 1. Characteristics of the cotton yarns used in fabrics

Moisture transfer rate (g/cm^2.h)	Air permeability (ml/cm^2)	Linear density (Ne)	T.P.M coefficient	Fineness (micron)	sample
2.00	26.0	20	4.5	3.2	1
2.10	27.0	20	4.7	3.2	2
2.15	27.0	20	4.8	3.2	3
2.01	26.5	20	4.5	4.2	4
2.20	26.0	20	4.7	4.2	5
2.25	27.7	20	4.8	4.2	6
2.30	27.0	20	4.5	5.3	7
2.20	27.1	20	4.7	5.3	8
2.25	26.9	20	4.8	5.3	9
2.15	27.0	30	4.5	3.2	10
2.17	30.0	30	4.7	3.2	11
2.20	32.0	30	4.8	3.2	12
2.22	31.0	30	4.5	4.2	13
2.19	31.5	30	4.7	4.2	14
2.20	35.0	30	4.8	4.2	15
2.25	35.5	30	4.5	5.3	16
2.22	36.0	30	4.7	5.3	17
2.28	37.0	30	4.8	5.3	18
2.29	37.0	40	4.5	3.2	19
2.30	38.0	40	4.7	3.2	20
2.20	45.0	40	4.8	3.2	21
2.31	33.0	40	4.5	4.2	22
2.30	35.0	40	4.7	4.2	23
2.33	38.0	40	4.8	4.2	24
2.30	37.0	40	4.5	5.3	25
2.37	38.0	40	4.7	5.3	26
2.39	45.0	40	4.8	5.3	27
2.40	37.0	50	4.5	3.2	28
2.39	40.0	50	4.7	3.2	29
2.45	43.0	50	4.8	3.2	30

2.42	43.0	50	4.5	4.2	31
2.41	45.0	50	4.7	4.2	32
2.42	44.0	50	4.8	4.2	33
2.44	46.0	50	4.5	5.3	34
2.46	48.0	50	4.7	5.3	35
2.49	50.0	50	4.8	5.3	36
2.50	65.0	70	4.5	3.2	37
2.49	70.0	70	4.7	3.2	38
2.51	69.0	70	4.8	3.2	39
2.60	70.0	70	4.5	4.2	40
2.58	71.0	70	4.7	4.2	41
2.55	69.0	70	4.8	4.2	42
2.61	73.0	70	4.5	5.3	43
2.62	75.0	70	4.7	5.3	44
2.62	74.0	70	4.8	5.3	45

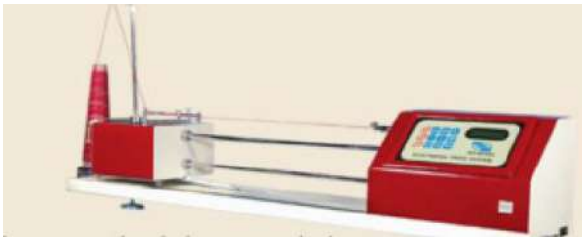

Figure1. Electronic twist tester

Figure 2. Thickness gauge

The final parameter is Fiber fineness which this parameter is determined by measuring the diameter of a single fiber of yarn using microscope in micron. The two main parameters are used for expressing the physiology comfort of garment. First parameter is "air permeability".

This parameter expresses air transferring through the fabric. Second parameter is "moisture transition" that indicates the transfer of moisture through the fabric. It should be noted that the air permeability and moisture transition parameters have a great importance for the summer clothes. Figure 3 shows the method applied for measuring the moisture transfer of fabric. In this method the sample of fabrics were cut as the specific dimensions of the circular metal containers, then put the fabric firmly on the dish containing 50 ml distilled water, and tighten the container thoroughly with adhesive to allow water vapor to pass through the surface of the fabric, and reweight the set. Then weight the set for every two hours during 6 hours for measuring the amount of discharged steam. The measuring results are presented in Table1.

During the movement due to the rise in metabolic heat, the body begins to sweat; therefore, the quick transferring the steam of the water through the fabric. This property greatly affects the ability of fabric breath and exhausts the excess heat by the fabric. It should be noted that the environment and water temperature is hold at 23ºC and the relative humidity is about 35%. The instrument for measuring the air permeability is presented in Figure 4.

This device is based on the air vacuuming through the sample of the fabric by a vacuum pump. The flow rate of the air passed through the sample is in 20 cm^2 of the surface area of sample, in which the volume of air passed through the sample is determined at a certain pressure. The result of air permeability measuring of samples are showed in Table 1.

In summer, the high metabolic heat is produced in the body and the considerable air permeability in the fabric

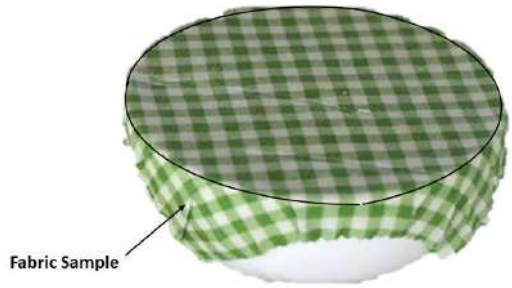

Figure 3. Test method for the moisture transfer measuring of fabric

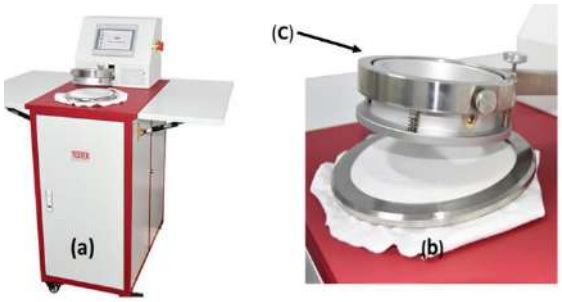

Figure 4. Air permeability tester: (a) Main body of tester, (b) fabric specimen, (c) interchangeable test head

is required in order to allow air flow in clothing for providing the respiratory function in the fabric and keep the person cool. However, in the winter clothes this parameter should be restricted. Due to the high diffusion of the air into the cloth causes a drop of air temperature inside the garment that results the person feels cold in the cloths, which it is a negative factor in the winter for the body comfort.

2. 1. Adaptive Neuro-Fuzzy Inference System

In this section, we introduce our new Adaptive Neuro-Fuzzy Inference System (ANFIS). The fuzzy rules of the proposed ANFIS are as follows:

R^1: *if* u_1 *is* $\tilde{A}_1$ *and* u_2 *is* $\tilde{B}_1$ *then* $\tilde{y}_1 = \tilde{r}_1 + \tilde{p}_1 u_1 + \tilde{q}_1 u_2$

R^2: *if* u_1 *is* $\tilde{A}_2$ *and* u_2 *is* $\tilde{B}_2$ *then* $\tilde{y}_2 = \tilde{r}_2 + \tilde{p}_2 u_1 + \tilde{q}_2 u_2$

where $\boldsymbol{u_1}$ and $\boldsymbol{u_2}$ are network inputs, $\widetilde{\boldsymbol{A}}_1$, $\widetilde{\boldsymbol{A}}_2$, $\widetilde{\boldsymbol{B}}_1$ and $\widetilde{\boldsymbol{B}}_2$ are type-1 fuzzy sets. $\widetilde{\boldsymbol{y}}_1$ and $\widetilde{\boldsymbol{y}}_2$ are the network output. $\tilde{\boldsymbol{r}}_1$, $\widetilde{\boldsymbol{p}}_1$ and $\widetilde{\boldsymbol{q}}_1$ are the coefficient of the consequent part, that all of them are type-1 fuzzy sets. Figure 5 shows the proposed ANFIS.

All parameters and layers of the proposed ANFIS are the same as traditional ANFIS except the consequent layer. The calculation of the consequent layer in this paper is as follows (General form):

$$\hat{y}_1 = \frac{\sum_{k=1}^{n} \overline{W}^k \left(m_{r_k} \sigma_{r_k} + m_{p_k} \sigma_{p_k} u_1 + m_{q_k} \sigma_{q_k} u_2 \right)}{\sum_{k=1}^{n} \overline{W}^k \left(\sigma_{r_k} + \sigma_{p_k} + \sigma_{q_k} \right)} \quad (1)$$

where $\boldsymbol{m_{r_k}}$, $\boldsymbol{m_{p_k}}$ and $\boldsymbol{m_{q_k}}$ are the means of Gaussian type-1 fuzzy sets $\tilde{\boldsymbol{r}}_1$, $\widetilde{\boldsymbol{p}}_1$ and $\widetilde{\boldsymbol{q}}_1$, respectively. Also, $\boldsymbol{\sigma_{r_k}}$, $\boldsymbol{\sigma_{p_k}}$ and $\boldsymbol{\sigma_{q_k}}$ are the variances of Gaussian type-1 fuzzy sets $\tilde{\boldsymbol{r}}_1$, $\widetilde{\boldsymbol{p}}_1$ and $\widetilde{\boldsymbol{q}}_1$, respectively. The output of one layer before consequent layer from k-th fuzzy rule is shown by $\overline{\boldsymbol{W}}^{\boldsymbol{k}}$. More details of feedforward and learning phase of the proposed ANFIS can be found elsewhere [15].

2. 2. Applying ANFIS for Fabric Physiological and Comfort Sensory Modelling

A mathematical relationship between two (or more) variables or parameters can be obtained by neuro fuzzy networks. For example, if the parameter x affects the y parameter, the mathematical relationship between x and y by applying x as input to the neural network and also y as the desired output can be found. In addition, if the system is dynamic from x to y, we can use the past moments y as input and next to x. In this study, the experimental data extracted from the test results have been used for the proposed ANFIS training and testing. For ANFIS training, there are some steps that have been fully followed, such as data pre-processing, deletion of discarded data, deletion of unimportant fuzzy membership functions, unimportant fuzzy rules and so on.

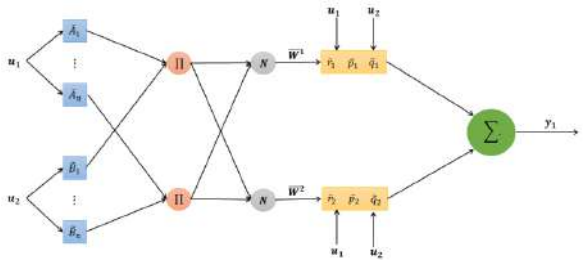

Figure 5. The proposed ANFIS

3. RESULTS AND DISCUSSION

Fabrics woven by fine fibers are softer than those with coarseness fibers and have a relatively smooth surface. In fabrics where the fineness of the fiber is lower in the yarn, the stiffness of the fabric is higher. Therefore, handmade of fabric is not appropriate. Figures 6 and 7 show that there is a relationship between the fineness of fibers produced the fabric and the parameter of air permeability and humidity transfer of the sample. Based on the results, with increasing the fiber diameter, the air permeability and humidity transfer of the fabric are increased. In other words, there are reverse relation between fineness of the fiber and air permeability and humidity transfer of the fabric woven by these fibers.

Fabrics woven from the yarn with linear density of 40 and 50 Ne mainly are used in women's garments. This type of fabric has a high softness. This fabric gets better

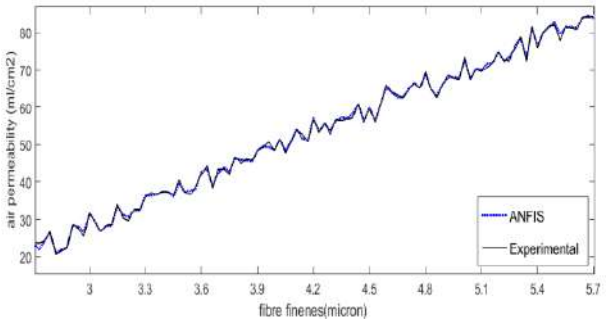

Figure 6. The relation between fiber fineness and air permeability of fabric

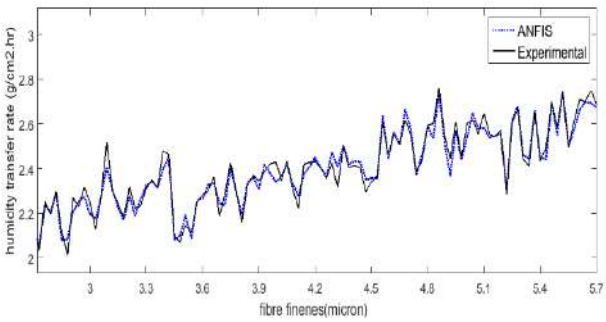

Figure 7. The relation between fiber fineness and humidity transfer rate of fabric

hand value when it is used from finer fibres to reach a higher English count yarn (Ne) and use a number of twist in a suitable way for the yarn. By increasing the English count of yarn, the empty space within the yarn structure are increased and the empty spaces between yarns in fabric structure are increased. As a result, air diffusion is low in the case of fabrics woven from coarse yarn (Figure 8).

According to Figure 9, by increase of the yarn linear density (Ne) or yarn English count, the rate of humidity transfer increases. by increasing the linear yarn density (yarn english count) the rate of humidity transfer increases. Yarn count expresses the coarseness or fineness of a yarn.There are two systems of expressing yarn number or yarn count: 1) Direct yarn numbering system that is defined by weight per unit length of yarn and 2) Indirect yarn numbering system which is defined by length per unit weight. English yarn count refers to the indirect system. In this system by increasing the yarn number or count, the weight of yarn in length decreases. By decreasing of the linear weight of the yarn, the empty spaces between yarns in fabric structure increase Therefore, based on the mentioned increasing behavior, the humidity transfers through the fabric increases.

The stiffness of the fabric increases when the yarn with high twist in fabric has been used. As a result, in this type of fabric the hand value is not suitable. In the yarn with high value of twist the empty space in yarn structure is decreased. According to this fact, the empty space in the fabric structure is increased. Figures 10 and 11 show that by increasing the empty space in the fabric structure, both the air permeability and transfer humidity rate increase. Figures 6 to 11 show that the proposed neuro fuzzy network (ANFIS) is capable of estimating textile' parameters, reasonably. The simulation results show that the system theory analysis is completely correct and can be inferred in the future.

3. 1. Evaluation of Optimum Point or Pointing Stability of Parameters

Physiological comfort of fabric depends on the end using. For the summer garments, the high values of air permeability and humidity transfer are appreciated, while, for the winter garments both mentioned parameters should be decreased to achieve the physiological comfort. Therefore, the pointing stability or the optimum points of yarn structural parameters (yarn twist, yarn English count and fiber fineness) depend on the end use of the fabric. From Figures 6-12, for the winter garment the optimum values of T.P.M coefficient and English count of yarn and fineness of fibers are 4.5, 25 and 3, respectively. Because in these points the air permeability and moisture transfer of fabric have their minimum values.

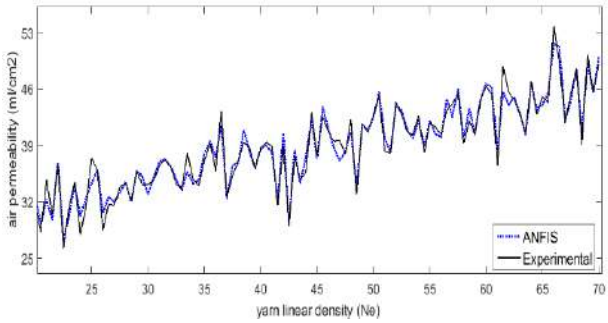

Figure 8. The relation between the yarn English count and the air permeability of fabric

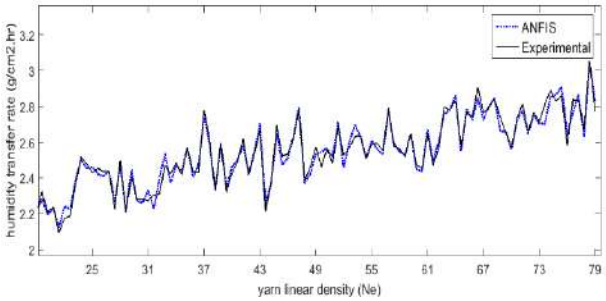

Figure 9. The relation between the yarn English count and the humidity transfer rate of fabric

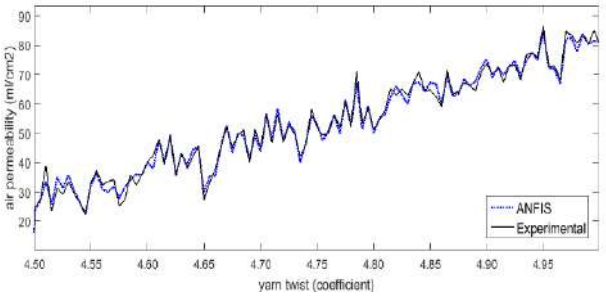

Figure 10. The relation between the yarn twist and the air permeability of fabric

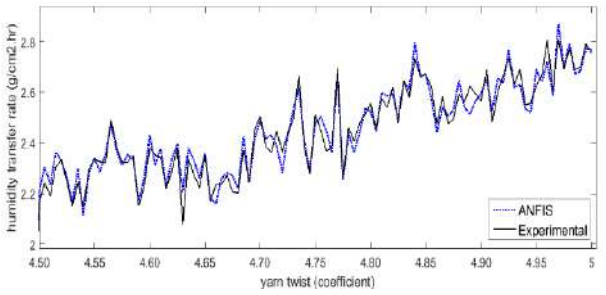

Figure 11. The relation between the yarn twist and the humidity transfer rate of fabric

4. CONCLUSION

In this article the effects of structural parameters of the cotton yarn on the physiological comfort of fabric were

studied by experiments and intelligent method of neuro-fuzzy network (ANFIS). The fabric comfort was improved according to the structural parameters of yarn instead of using finishing treatment. The result of this study is useful for green textile industries.

The physiological comfort parameters such as air permeability and moisture transfer of the garment were strongly affected by the characteristics of the yarn and fibers such as fiber fineness, yarn twist and English count of yarn. The modeling and experimental results showed that by increasing the diameter of fibers and English count of the yarn and yarn twist both comfort parameters increase. The theoretical analysis was performed by the new smart model, i.e. improved ANFIS, developed in this work. In the model the linear density, twist yarn and fineness of fibre were input parameters and moisture transfer and air permeability were outputs. Simulation results show the novel proposed ANFIS has high learning capability, fast convergence and accuracy greater than 99% and negligible error value smaller than of 1%. It was also found that both parameters of the physiological comfort sensory, namely, the air permeability and humidity transfer can be improved effectively without finishing process. Finally, the physiological comfort for the winter garment can be achieved at optimum values of 4.5, 25 and 3 for T.P.M coefficient, English count, and fineness of yarn, respectively.

5. REFERENCES

1. Vancza, J., Noh S. D., Yoon, H. S., "Preface for the Special Issue of Green Smart Manufacturing", ***International Journal of Precision Engineering and Manufacturing-Green Technology***, Vol. 7, (2020), 545-546. DOI: 10.1007/s40684-020-00218-2
2. Sun, Y., Bi, K., Yin, S., "Measuring and Integrating Risk Management into Green Innovation Practices for Green Manufacturing under the Global Value Chain", ***Sustainability***, Vol.12, (2020), 545-578. DOI: https://doi.org/10.3390/su12020545
3. Ghaly, A., Ananthashankar, R., Alhattab, M., Ramakrishnan, V., "Production, characterization and treatment of textile effluents: a critical review", ***Journal of Chemical Engineering Process Technology***, vol.5, (2014), 1-18. DOI: 10.4172/2157-7048.1000182
4. Hesarian, M. S., Tavoosi. J., "Green technology used in finishing process study of wrinkled cotton fabric by radial basis function (Experimental and modeling analysis)", ***Advances in Environmental Technology***. Vol. 5, No. 1, (2019), 35-45. DOI: 10.22104/aet.2019.3730.1183
5. Udaya Krithika, S. M., Sampath, M. B., Prakash, C., Senthil Kumar, M., "Moisture management finish on woven fabrics", ***Indian Journal of Textile & Fibre Research***, Vol. 44, (2019), 486-491. DOI: http://nopr.niscair.res.in/handle/123456789/52717
6. Iftikhar. F., Hussain, T., Ali, Z., Nazir Dominique, A., Adolphe, C., Schacher, L., (2019). "investigation of thermo-physiological comfort and mechanical properties of fine cotton fabrics for ladies' summer apparel", ***Journal of Nature Fibers***. In press (2019). DOI: https://doi.org/10.1080/15440478.2019.1588185
7. Stoffberg, M. E., Hunter, L., Botha, A., "The effect of fabric structural parameters and fiber type on the comfort-related properties of commercial apparel fabrics", ***Journal of Natural Fibers***, Vol. 12, No. 6, (2015), 505-517. DOI:10.1080/15440478.2014.967370
8. Hesarian, M. S., "Evaluation of fabric wrinkle by projected profile light line method", ***Journal of The Textile Institute***, Vol. 101, No. 5, (2010), 463-470. DOI: https://doi.org/10.1080/13598130802528238
9. Hesarian, M.S., Eshkevari, M., Jahangoshaei, M., "Angle analysis of fabric wrinkle by projected profile ligt line method, image processing and neuro-fuuzy system", ***International Journal of Computer Integrated Manufacturing***, in press, (2020), DOI:10.1080/0951192X.2020.1829060
10. Tavoosi, J., "Stable Backstepping Sliding Mode Control Based on ANFIS2 for a Class of Nonlinear Systems", ***Jordan Journal of Electrical Engineering (JJEE)***, Vol.6, No.1, (2020), 49-62. DOI: 10.5455/jjee.204-1580573666
11. Vajdiana, M., Zahrai, S. M., Mirhosseinia, S. M., Zeighamia, E. "Predicting Shear Capacity of Panel Zone Using Neural Network and Genetic Algorithm". ***International Journal of Engineering, Transactions B: Applications***. Vol.33, No.8, (2020), 1512-1521. DOI: 10.5829/ije.2020.33.08b.09
12. Hassanpour, M., Malek, H. "Learning Document Image Features with SqueezeNet Convolutional Neural Network". ***International Journal of Engineering, Transactions A: Basics***, Vol.33, No.7, (2020), 1201-1207. DOI: 10.5829/ije.2020.33.07a.05
13. Aslipour, Z., Yazdizadeh, A. "Identification of Wind Turbine using Fractional Order Dynamic Neural Network and Optimization Algorithm" ***International Journal of Engineering, Transactions B: Applications,*** Vol. 33, No. 2, (2020), 277-284. DOI:10.5829/ije.2020.33.02b.12
14. Behera, B. K., Guruprasad R., "Predicting bending rigidity of woven fabrics using adaptive neuro-fuzzy inference system (ANFIS)", ***Journal of The Textile Institute***, Vol. 103, No. 11, (2012), 1205-1212. DOI: https://doi.org/10.1080/00405000.2012.673296
15. Tavoosi, J, "A New Type-2 Fuzzy Sliding Mode Control for Longitudinal Aerodynamic Parameters of a Commercial Aircraft", ***Journal Européen des Systèmes Automatisés,*** Vol.53, No. 4, (2020), 479-485 DOI: https://doi.org/10.18280/jesa.530405

Persian Abstract

چکیده

اخیراً با افزایش آلودگی های زیست محیطی ، استفاده از فناوری های سبز در زمینه های مختلف صنایع نساجی و پوشاک همانند فرآیند تکمیل به طور جدی توسعه یافته است. در این خصوص یکی از مهمترین پارامترهای موجود در صنعت پوشاک که می¬تواند تحت عملیات تکمیل پارچه بهبود یابد راحتی فیزیولوژیکی پارچه می¬باشد. اما متاسفانه مواد شیمیایی سمی تولید شده در این فرآیند منجر به آلودگی زیست محیطی می¬شود. بنابراین در این تحقیق ، بهبود راحتی فیزیولوژیکی پارچه پنبه¬ای بدون استفاده از عملیات تکمیل به عنوان هدف اصلی این مقاله محسوب می¬گردد. برای این منظور ، خواص نفوذپذیری هوا و انتقال رطوبت که به عنوان دو پارامتر مهم راحتی فیزیولوژیکی پارچه می¬باشد به صورت تجربی و نظری و بر اساس پارامترهای ساختاری نخ پنبه¬ای مورد ارزیابی قرار می¬گیرد. علاوه بر این، بمنظور بررسی تئوری، یک شبکه عصبی- فازی جدید (ANFIS) جهت مدل سازی پیشنهاد شده است. در مقاله حال حاضر ، پارامترهای ساختاری نخ که عبارتند از چگالی خطی نخ، تاب نخ و ظرافت الیاف نخ به عنوان پارامترهای ورودی مدل و عوامل نفوذپذیری هوا و انتقال رطوبت پارچه بعنوان خروجی مدل مورد استفاده قرار می¬گیرند. با توجه به نتایج تجربی و مدل سازی دو عامل ظرافت الیاف و چگالی خطی نخ تأثیر یکسانی بر روی دو پارامتر خروجی مدل داشته و از طرفی تاب نخ اثر معکوس بر روی آنها دارد. نتایج بررسیهای انجام شده در این مقاله نشان می¬دهد که راحتی فیزیولوژیکی پارچه می¬تواند بطور مطلوبی بر اساس پارامترهای ساختاری نخ و بدون انجام عملیات تکمیل بهبود یابد. نتایج شبیه سازی نشان می دهد که مدل پیشنهادی از توانایی یادگیری بالا ، همگرایی سریع، دقت بالای ۹۹٪ و خطای قابل اغماض کوچکتر از ۱٪ برخوردار است. نقاط ٤.٥، ۲۵ و۳ بعنوان مقادیر پارامترهای ضریب تاب و نمره انگلیسی نخ و ظرافت الیاف نخ بعنوان نقاط اپتیمم پارامترهای نخ برای لباسهای زمستانی می باشند.

International Journal of Engineering

Journal Homepage: www.ije.ir

Simulation of Deposition Detection inside Wellbore by Photon Backscatter Radiography

V. Jamshidi, R. Davarnejad*

Department of Chemical Engineering, Faculty of Engineering, Arak University, Arak, Iran

PAPER INFO

Paper history:
Received 03 July 2020
Received in revised form 03 October 2020
Accepted 30 October 2020

Keywords:
Deposition
Backscatter Radiography
Simulation
In-situ
Nondestructive Testing

ABSTRACT

In the process of extracting oil and gas from hydrocarbon reservoirs, the formation of depositions inside pipes, fittings, and storage tanks, not only accelerates corrosion but also reduces a significant volume of operating capacities. The most critical step in solving the problem of deposition formation is their early and timely detection. In industries, internal surfaces of the pipeline are usually inspected by nondestructive testing (NDT) methods. The detection of depositions should operationally be difficult if there were special conditions for accessing the back of pipelines. Therefore, a suitable method is encouraged to detect deposition in the pipes and tubes when one side or a small part of them is accessible. In this paper, the Monte Carlo simulation tool was applied to use backscatter radiography (as an NDT inspection technique) for in-situ detection of depositions inside the metallic pipelines. In fact, the simulation process shows the correctness and efficiency of the backscatter radiography technique. It would determine some significant factors such as photon energy, angle of irradiation, or location of detectors which affect the design before experiment. The results showed that backscatter radiography as a viable technique could properly detect the location of depositions inside the pipes.

***doi**: 10.5829/ije.2020.33.12c.03*

1. INTRODUCTION

In the field of oil and gas industries, monitoring of depositions is a significant subject for preventing harmful consequences and costly damages due to flow restriction through transmission pipelines [1]. Some changes in pressure and temperature cause some physical and chemical phenomena for deposition formation when the fluids approach the earth's surface from underground in the extraction process of hydrocarbon reservoirs [2]. Organic and inorganic (such as asphaltene, wax, hydrate, and mineral compounds) depositions commonly formed in the pipelines and equipment [3]. Asphaltene has a complex molecular structure and is the most polar composition in oil [4]. Waxes are high molecular weight and complex compounds which generally are in the solid phase at ambient temperature. Wax depositions (with normal chains of alkanes) stick on the internal pipes at low temperatures and make longer chains [5, 6]. Hydrate depositions are typically formed in gas transmission pipelines, as well. In the cold seasons, gas molecules in pipes are imprisoned and frozen in cages made from water. Plugs will block the flow path and stop gas processing during hydrate crystals formation [7].

Petroleum industries often suffer from inorganic depositions, including carbonates and sulfates [8]. These deposits are generally associated with water formed in calcium carbonate, calcium sulfate, and barium sulfate. Some deposits, such as iron sulfide and iron carbonate, may also be produced as corrosion agents [9].

Caliper Pipeline Inspection Gauge (Caliper PIG) with mechanical arms is a device that is used in fluids (such as water, oil, and gas) transfer pipes for measuring holes geometry [10].

Some methods for monitoring deposition formation or narrowing in the pipelines and equipment are radiography, ultrasonic, determination of fluid pressure in various points, thermal imaging, and the other inspection techniques [11-14]. However, there is some information about the strengths and weaknesses of

*Corresponding Author Institutional Email: *R-Davarnejad@araku.ac.ir* (R. Davarnejad)

Please cite this article as: V. Jamshidi, R. Davarnejad, Simulation of Deposition Detection inside Wellbore by Photon Backscatter Radiography, International Journal of Engineering, Transactions C: Aspects Vol. 33, No. 12, (2020) 2450-2454

various inspection methods [15, 16] but, a predictable technique based on the Monte Carlo simulation tool is widely encouraged for the depositions formation location detection and their contents determination. In this research, the mentioned technique was carefully studied in detail and validated.

2. METHODOLOGY

According to the radiography applications, X and γ-rays penetrate through materials structure to find their quality [17]. The radiography tool advantage compared with the other methods (such as Caliper PIG) is the observation of the visual image of pipe cross-section without demanding mechanical arms and sticking on the internal surface of the tube [10]. The conventional radiography is feasible for pipes and tubes, which both sides of them are available. The positions of radiation source on one side and detector or film on the other side are important. Compton scattering shows good potential for use in the field of NDT monitoring. The backscatter radiography based on Compton scattering has been proposed for single-sided radiography under inspection. This type of radiography can be applied for in-situ detection of faults inside pipelines without demanding the back of them [15, 18]. Figure 1 illustrates the principle of the backscatter radiography method for the detection of depositions inside a pipeline [19].

Figure 2 shows the simulated geometry used in the Monte Carlo N-Particle (MCNP) code. Specifications of materials used in the simulation were extracted from literature [5, 8, 20-25]. A mono-energetic source of photon produced a ring-shaped sharp beam and irradiated the inner side of the pipeline. Deposition in one area of the pipe was defined as the thickness of wax, asphaltene, salt, or hydrate over the internal surface of it. Simulations were carried out several times by different photon energies and depositions with various thicknesses, lengths, and materials. The best results were obtained in the counter cell with about 11 cm far from the radiation source for the design investigated in this research.

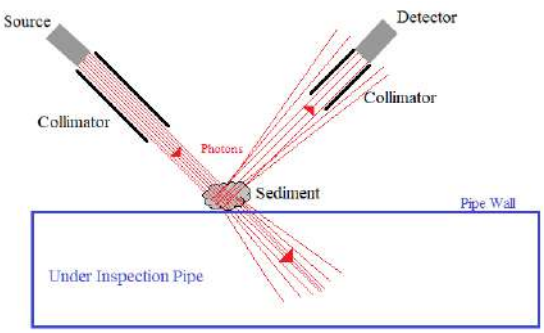

Figure 1. Principle of photon backscatter radiography for detection of deposition on a pipe wall

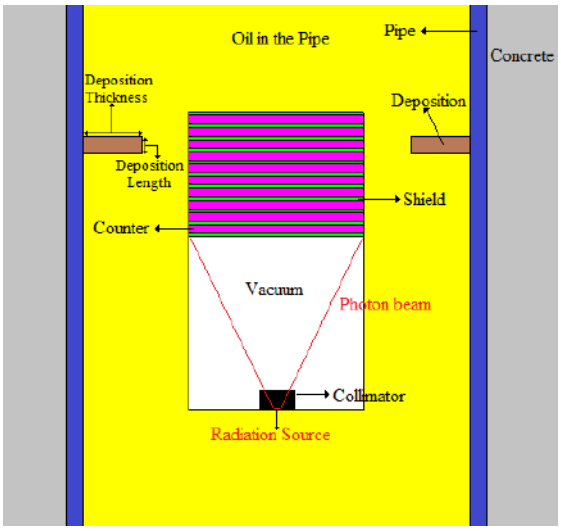

Figure 2. The geometry used for input of MCNP code

As shown in Figure 3, the depositions can be monitored by moving the inspection device through the pipeline. Some scattered photons entered the detector were counted after photons emission from source and their interactions consideration with fluid, pipe, deposition, and concrete behind the tube. Then, the results were drawn as a graph versus the traveled distance. A change in the number of photons in the log can indicate the deposition occurrence along the pipeline.

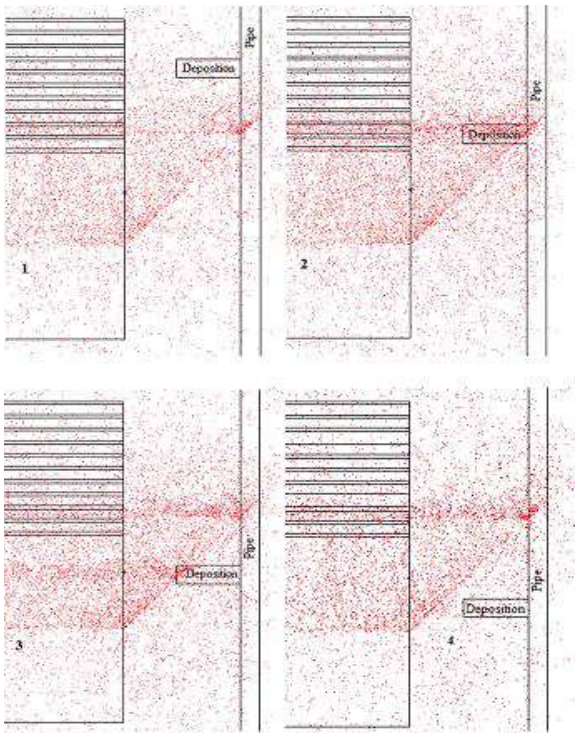

Figure 3. Moving the inspection device in front of the deposition through the pipe (dots show traced photons)

The speed of inspection by backscatter radiography in the experiment depends on several factors. The most important parameter is the source strength or exposure rate of photon sources. The efficiency of the detectors and electronics used in the setup can have an essential role in the inspection speed, as well.

3. RESULTS AND DISCUSSION

Since there only are theoretical data on this type of research and still, no practical setup is tested, the necessary data (such as the energy of photons, angle of irradiation, and kind of photon beam) were obtained from the literature considering ALARA principle [15, 26]. The deposition should be significant when it occupies at least 20% of the pipe diameter. Figure 4 shows the results of this method for detection of $CaCO_3$ deposition inside a pipe with 1 cm length and 2.2 cm thickness of internal pipe diameter using 75, 200, and 660 keV photon sources. The results showed that low-energy photons could not produce good results due to passing photons through the fluid, penetration into the deposition, re-entry through the fluid, and finally, into the detector. Figures 5 and 6 show detecting asphaltene, $CaCl_2$, $CaCO_3$, $CaSO_4$, and wax depositions inside a pipe using 200 and 660 keV photons. All depositions had 1 cm length and 20% of internal pipeline diameter in thickness. The peaks shown in Figuers 5 and 6 indicate the presence of deposition on the pipe surface. Furthermore, these figures clearly show that scattering will be increased, and more scattered photons may be detected (by a detector) when a high energy photon source is applied. The location of the deposition on the internal surface of the pipe can be found by counting backscattered photons in the detector versus distance. The difference in the number of backscattered photons in the area of deposition in comparison with the other parts of the pipeline led to some peaks. The material of the deposition area, density, and photon scattering property in the location of deposition may be different from the other internal areas of a pipeline. Figure 7 shows the results of backscatter radiography by 200 keV photons for detecting $CaCO_3$ depositions with various thicknesses. The deposition thickness range is 10 to 50% of the internal diameter of the pipe. The results showed that this method can detect thin depositions to prevent further problems. Figure 7 indicates the better results for thicker depositions (which are closer to the source and detector), as well.

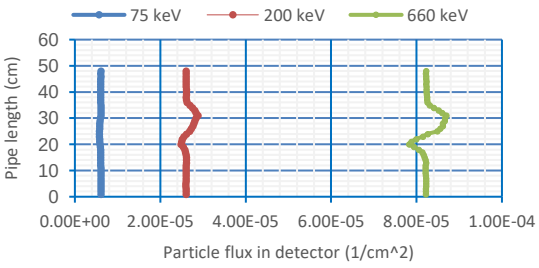

Figure 4. Photon log for various photon energies along the pipe with CaCO3 deposition (deposition thickness is equal to 20% of internal pipe diameter and deposition length is equal to 1 cm)

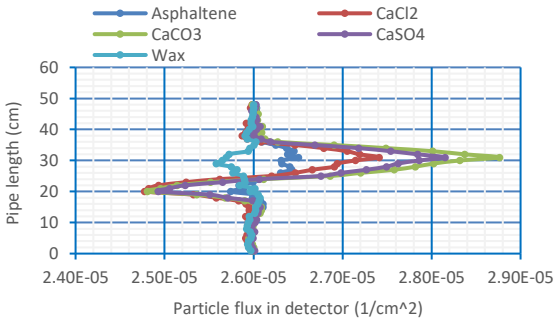

Figure 5. Photon log for various deposition materials (deposition thickness is equal to 20% of internal pipe diameter, deposition length is equal to 1 cm, and photon energy is equal to 200 keV)

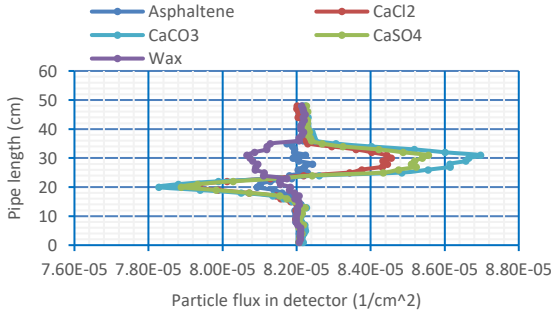

Figure 6. Photon log for various deposition materials (deposition thickness is equal to 20% of internal pipe diameter, deposition length is equal to 1 cm, and photon energy is equal to 660 keV)

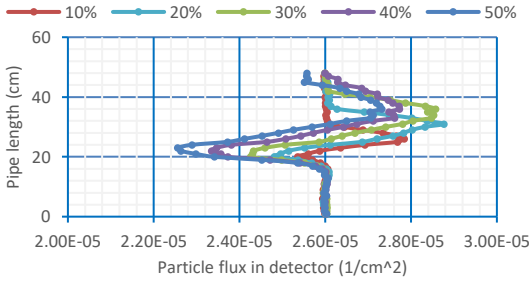

Figure 7. Photon log for various deposition thicknesses of $CaCO_3$ (deposition thickness=10, 20, 30, 40, and 50% of internal pipe diameter, deposition length=1 cm, photon energy=200 keV)

Since hydrate depositions may be formed in gas pipelines, their depositions can also be studied. For hydrate deposition detection, the fluid inside the pipeline was assumed as natural gas. Figure 8 shows the results of hydrate deposition detection simulation inside the pipe with 1 cm length and thickness of 2.2 cm (20% of the internal diameter of the pipe) of internal pipe diameter using 200 keV and 660 keV photon sources. Figure 9 shows the results of deposition detection with a thickness range of 10 to 40% of the internal diameter of the pipe. Simulations were repeated for depositions with the same thicknesses but with different lengths. Figure 10 shows the hydrate deposition detection with a length range of 1-2.5 cm. The results showed that dimensions of peaks in photon logs were in good compatibility with depositions inside pipelines.

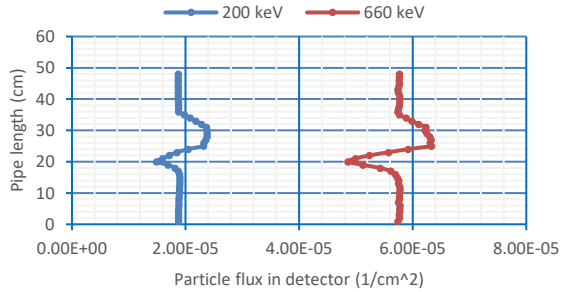

Figure 8. Photon log for various photon energies along the pipe with hydrate deposition (deposition thickness=20% of internal pipe diameter and deposition length=1 cm)

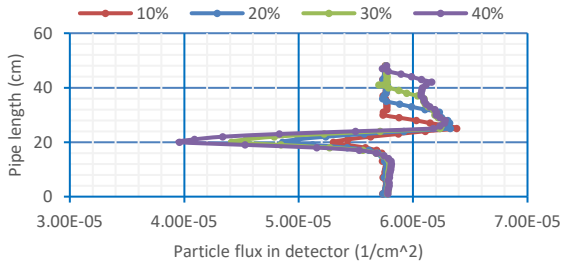

Figure 9. Photon log for various deposition thicknesses of hydrate deposition (deposition thickness=10, 20, 30, and 40% of internal pipe diameter, deposition length=1 cm, and photon energy=660 keV)

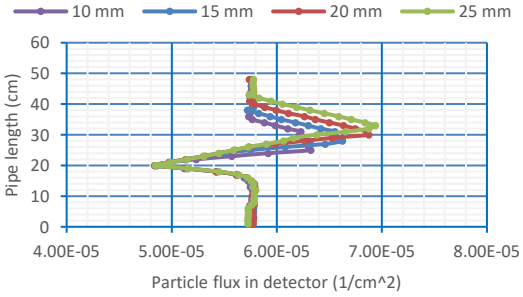

Figure 10. Photon log for various deposition lengths of hydrate (deposition thickness=20% of internal pipe diameter and photon energy=660 keV)

4. CONCLUSIONS

In the field of oil and gas production, various factors can prevent from the maximum operational volumes. One of these factors which has a remarkable effect on these industries is the formation of depositions inside the pipelines. Backscattered photon radiography can be applied as a practical and viable method for the detection of depositions inside the pipes where located in the wellbores without enough access to them or in the other positions where both sides of pipes cannot be accessible. In the current research, the Monte-Carlo tool was properly applied to simulate various depositions such as organic, inorganic, and hydrates detection (with various thicknesses, lengths, materials, and photon energies) inside the pipelines by backscattered photon radiography. Since counting scattered photons in detectors is easy, this technique can detect depositions in the early stages of their formation with reasonable accuracy. Furthermore, no mechanical movable part is requested in the structure of backscattered photon radiography, which is used for detecting depositions where are not accessible.

5. REFERENCES

1. Ragunathan, T., Husin, H., Wood, C.D., "Wax Formation Mechanism, Wax Chemical Inhibitators and Factors Affecting Chemical Inhibition", ***Applied Sciences***, Vol. 10, No. 2, (2020), 1-18. DOI: 10.3390/app10020479
2. Civan, F., "Reservoir Formation Damage, Gulf Professional Publishing", (2015), 23rd September. eBook ISBN: 9780128019108
3. Mousavi-Dehghani, S., Riazi, M., Vafaie-Sefti, M., Mansoori, G., "An analysis of methods for determination of onsets of asphaltene phase separations", ***Journal of Petroleum Science and Engineering***, Vol. 42, No. 2-4, (2004), 145-156. DOI: 10.1016/j.petrol.2003.12.007
4. Fakher, S., Ahdaya, M., Eltukl, M., Imqam, A., Critical review of asphaltene properties and factors impacting its stability in crude oil. ***Journal of Petroleum Exploration and Production Technology***, Vol. 10, (2019), 1183-1200. DOI: 10.1007/s13202-019-00811-5
5. Ganeeva, Y.M., Yusupova, T.N., Romanov, G.V., "Waxes in asphaltenes of crude oils and wax deposits", ***Journal of Petroleum Science***, Vol. 13, No. 4, (2016) 737-745. DOI: 10.1007/s12182-016-0111-8
6. Martyushev, D., Modeling and Forecasting of Paraffin Settings on an Existing Extractive Fund of Oil Deposits, ***International Journal of Engineering, Transactions C: Aspects***, Vol. 32, No. 12, (2019), 1704-1709. DOI: 10.5829/IJE.2019.32.12C.02
7. Makwashi, N., Zhao, D., Ismaila T.A., Paiko, I., "Pipeline Gas Hydrate Formation and Treatment: A Review", 3rd National Engineering Conference on Building the Gap between Academia and Industry, Faculty of Engineering, Bayero University, Kano. (2018), https://www.researchgate.net/publication/330262173

8. Vazirian, M. M., Charpentier, T. V. J., de Oliveira Penna, M., & Neville, A. "Surface inorganic scale formation in oil and gas industry: As adhesion and deposition processes", ***Journal of Petroleum Science and Engineering***, Vol. 137, (2016), 22-32. DOI: 10.1016/j.petrol.2015.11.005
9. Al Rawahi, Y.M., Shaik, F., Rao, L.N., Studies on scale deposition in oil industries & their control, ***International Journal for Innovative Research in Science & Technology***, Vol. 3, (2017), 152-167. http://www.ijirst.org/articles/IJIRSTV3I12056.pdf
10. Darling. T. "Well Logging and Formation Evaluation", Elsevier Inc. (2005). https://www.sciencedirect.com/book/9780750678834/well-logging-and-formation-evaluation
11. Ellinger, M., "A history of in-line inspection tools", ***Inspectioneering Journal***, (2017). https://inspectioneering.com/journal/2017-04-27/6416/a-history-of-in-line-inspection-tools
12. Serra, O., Fundamentals of Well-logging Interpretation: The Interpretation of Logging Data, ***Developments in Petroleum Science,*** Vol. 15, (1986) https://www.academia.edu/10053890/Fundamentals_of_Well_Log_Interpretation_OSerra
13. Liu, E., Peng, S., Zhang, H., Huang, L., "Blockages detection technology for oil pipeline", ***Journal of the Balkan Tribological Association***, Vol. 22, (2016), 1045–1057. https://www.researchgate.net/publication/330845379
14. Díaz-Sánchez, H., Rojas-Trigos, J.B., Leyva, C., Trejo-Zárraga, F., "An approach for determination of asphaltene crystallite by X-ray diffraction analysis: A case of study", ***Petroleum Science and Technology***, Vol. 35, No. 13, (2017), 1415-1420. DOI: 10.1080/10916466.2017.1336771
15. Jamshidi.V., Davarnejad, R., "Simulation of corrosion detection inside wellbore by X-ray backscatter radiography", ***Applied Radiation and Isotopes***, Vol. 145, (2019), 116-119. DOI: 10.1016/j.apradiso.2018.12.026
16. Saxena, H., Majhi, A., Behera, B., "Prediction of wax content in crude oil and petroleum fraction by proton NMR", ***Petroleum Science and Technology***, Vol. 37, No. 2, (2019), 226-233. DOI: 10.1080/10916466.2018.1536713
17. Gawdzinska, K., Grabian, J., Przetakiewicz, W., "Use of X-ray radiography in finding defects in metal-matrix composite casts", ***Metalurgija***, Vol. 47, (2008), 199-201. https://hrcak.srce.hr/file/35671
18. Xiong, X., Yantao, L., Daquan, C., Wei, Z., Xiaoming, W., Yingjie, W., Zhiming, Z., "A compact, high signal-to-noise ratio line-detector array Compton scatter imaging system based on silicon photomultipliers", ***Applied Radiation and Isotopes***, Vol. 154, (2019), 108845. DOI: 10.1016/j.apradiso.2019.108845
19. Tsoulfanidis, N., Landsberger, S., Measurement and Detection of Radiation. Taylor & Francis: USA. (2015), DOI: 10.1201/b18203
20. Jowett, F., Petroleum waxes. In: Hobson G.D., editor. ***Petroleum Technology***. New York: Wiley. (1984)
21. Diallo, M.S., Cagin, T., Faulon, J.L., Goddard III. W.A. "Thermodynamic properties of asphaltenes through computer assisted structure elucidation and atomistic simulations", ***Development in Petroleum Science***, Vol. 40, (2007), 103-127. DOI: 10.1081/LFT-120040254
22. Max, M.D. "Natural Gas Hydrate in Oceanic and Permafrost Environments". Springer Netehrlands Publishers. (2003) https://www.springer.com/gp/book/9781402013621
23. Chong, Z. R., Yang, S.H.B., Babu, P., Linga, P., Li, X.-S., 2016. Review of natural gas hydrates as an energy resource: Prospects and challenges, ***Applied Energy***, Vol. 162, 1633-1652. DOI: 10.1016/j.apenergy.2014.12.061
24. Hosseinipour, A., Japper-Jaafar, A., Yusup, S., Ismail, L., "Application of the Avrami Theory for Wax Crystallization of Synthetic Crude Oil", ***International Journal of Engineering, Transactions A: Basics***, Vol. 32, No. 1, (2019), 18-27. DOI: 10.5829/IJE.2019.32.01A.03
25. Speight, J.G. "Handbook of petroleum analysis", John Wiley & Sons, US. ISBN: 0-471-36167-4. (2001)
26. "NRC's Regulations, Title 10, Code of Federal Regulations", Standards for protection against radiation, Section 20.1003. (2016), https://www.nrc.gov/reading-rm/doc-collections/cfr/part020/

Persian Abstract

چکیده

در استخراج نفت و گاز از مخازن هیدروکربوری، تشکیل رسوبات مختلف داخل لوله‌های انتقال، اتصالات و در نهایت مخازن ذخیره، نه تنها باعث تشدید فرآیند خوردگی این تجهیزات می‌گردد بلکه حجم قابل توجهی از ظرفیت‌های عملیاتی را نیز کاهش می‌دهد. مهمترین گام در حل معضل تشکیل رسوبات داخل تجهیزات، تشخیص زود هنگام و به موقع آنهاست. در صنایع، سطوح داخلی خطوط لوله معمولاً با روش‌هایآزمون غیر مخرب (NDT) بررسی می‌شود. در شرایط عملیاتی چنانچهدسترسی به پشت خطوط لوله امکان‌پذیر نباشد، تشخیص رسوبات با استفاده از آزمون‌های غیر مخربمرسوم دشوار می‌گردد. به همین دلیلامروزه روش‌های مناسب تشخیص رسوب داخل لوله‌ها، بدون لزوم دسترسی به هر دو سمت آنها در حال توسعه می‌باشد. در این مقاله،به کمک شبیه سازی مونت کارلو، رادیوگرافیبا فوتون‌های پس‌پراکنده شده (در قالبیک روش بازرسیغیر مخرب) به عنوان روشی برای تشخیص درجای رسوبات داخل خطوط لوله فلزیمعرفیشده و صحت و کارآیی آن مورد ارزیابی قرار گرفته است.به کمک شبیه‌سازی می‌توان برخی عوامل تاثیرگذار مانند انرژی فوتون، زاویه تابش، یا محل قرارگیریشمارنده‌ها را قبل از آزمایشتجربی تعیین نمود. نتایجبه دست آمده از این مطالعه نشان داد که رادیوگرافیبا فوتون‌های پس‌پراکنده شدهمی‌تواند بدون نیاز به دسترسی به هر دو سمت لوله، به طور صحیح محل تشکیل رسوبات درون آنها را تشخیص دهد.

International Journal of Engineering

Journal Homepage: www.ije.ir

Evaluating Applicability of ASTM C 928 Approach in Assessing Adequacy of Patch Repair of Bridge Piers

S. Rahmanzadeh, S. Tariverdilo*

Department of Civil Engineering, Faculty of Engineering, Urmia University, Urmia, Iran

P A P E R I N F O

Paper history:
Received 13 July 2020
Received in revised form 06 August 2020
Accepted 26 August 2020

Keywords:
Patch Repair
ASTM C 928
Slant Shear Test
Self-compacting Concrete
Polymer Modified
Fiber Reinforced

A B S T R A C T

Severe environmental conditions in many parts of Iran could adversely affect infrastructures, especially bridge piers. This research evaluates the efficiency of fiber-reinforced polymer-modified self-compacting concrete in patch repair of bridge piers. The efficiency of this material for repair has been verified using ASTM C 928 and a novel testing method (patch test) that uses a cylindrical compression test simulating indirect force transfer from old (existing) concrete to new (patch repaired) concrete. To investigate the efficiency of self-compacting concrete in patch repair and derive the correlation between bond strength and patch strength, two sets of specimens have been included in the experimental program. These include 24 and 27 specimens which are prepared for patch and slant shear tests, respectively. Test results show significant improvement in strength due to use of polymer modified and fiber reinforced self-compacting concrete in slant shear tests, where strength enhancement as much as 50% (compared to undamaged specimens) was observed. Meanwhile, in the patch tests, repaired specimens are only able to barely exceed the original strength of undamaged specimens. In the slant shear tests, the use of polymer is very effective in increasing bond strength and using fibers reduces observed variation in the strength of repaired specimens. Considering force path in the patch repair and regardless of materials used for repair, the results show that judging the efficiency of the repair method based on the slant shear test, as proposed by ASTM C 928, in the case of patch repaired elements could be misleading.

***doi**: 10.5829/ije.2020.33.12c.04*

1. INTRODUCTION

Due to increasing infrastructure life in recent years, repair and reconstruction of the existing structures have become a major part of construction activities. Some estimates indicate that in 2010 repair and maintenance costs accounted for about 85% of total construction costs in the world [1]. Hence, it is important to select simple, applicable, efficient, and low-cost methods for repairing damaged structures.

Bridge piers are subjected to severe environmental conditions, and commonly are in need of localized patch repairs. There are different options for these repair attempts, including [2]

- steel jacket
- FRP jacket
- concrete jacketing using normal strength concrete
- self-compacting concrete jacket.

Steel jackets are relatively easy to install, and have less thickness in comparison with the RC jackets [3-5], where cement or epoxy mortar are used to fill the gaps between the jacket and column. However, in contrast to concrete jackets, steel jackets are difficult to apply especially in the case of round bridge piers. Steel jackets provide a useful solution for element-wise repair/retrofit as opposed to patch repair and are not suitable for aggressive environments.

FRP jackets provide a corrosion resistant, lightweight and durable solution for repair of damaged reinforced concrete elements [6-8]. This method is also used extensively in retrofitting historic buildings [9-10] and different structural elements [11]. But on the other hand, it is expensive and weak when exposed to fire and ultraviolet radiation.

*Corresponding Author Institutional Email: *s.tariverdilo@urmia.ac.ir* (S. Tariverdilo)

Please cite this article as: S. Rahmanzadeh, S. Tariverdilo, Evaluating Applicability of ASTM C 928 Approach in Assessing Adequacy of Patch Repair of Bridge Piers, International Journal of Engineering, Transactions C: Aspects Vol. 33, No. 12, (2020) 2455-2463

Normal strength concrete (NSC) jackets, due to the need for compaction, are difficult to apply in small thickness [12-13]. In contrast, self-compacting concrete (SCC) jackets are easy to apply in narrow thicknesses with no need for compaction. These have led to a wide range of SCC applications for improving and repairing concrete bridges and tunnels [14-15] and they are applicable at thicknesses less than 50 mm even with reinforcement layers. This allows the possibility of repairing structures with slight changes in their rigidity and dynamic properties, which are very important in controlling structural performance.

Different researchers have investigated improvement in bond strength between old and new concrete making use of polymer-modified cement mortar. In polymer modified concrete, part of the resistance is due to the hydration in the cement matrix and the other part is due to the formation of a polymer film around the aggregates. This leads to improved adhesion and bonding between the cement matrix and the concrete grains. Compared to NSC, the compressive strength of polymer-modified concrete increases at a higher rate, even after 28 days. Park et al., [16] with the aim of investigating the flexural behavior of beams repaired with cementitious mortar, tested 8 beams repaired in the tension region with ordinary Portland and polymer-modified cement mortar. They concluded that polymer-modified mortar, due to its high adhesion to base concrete, performs better in repairing beam tensile zones than ordinary Portland cement mortar. To investigate the effect of polymer used on the adhesion of base and repair concrete, Pellegrino et al. [17] experimentally investigated the enhancement in the strength of samples with polymer-modified mortar. The results indicated that deep repair including longitudinal reinforcement will behave well but the surface repair did not perform well due to early separation of repaired concrete from the old one.

Addition of fiber improves different durability characteristics of reinforced concrete element including fire endurance, freezing and thawing resistance, weathering, scaling and corrosion resistance [18-19]. At the same time, application of steel fibers in repair concrete leads to increased ductility and energy absorption of the concrete samples [20]. Polymer and fibers, both improve the durability of the structure against aggressive environmental factors and reduce the likelihood of damage to the structure.

Repair measures could be classified as local (patch) versus element-wise. Different tests have been devised and widely used for measuring the efficiency of the repair. These include, but is not limited to the following tests

- Slant shear test
- Indirect tensile test that is also called splitting tensile test
- Pull-off test
- Compression test
- Flexural test

Table 1 presents a description of different versions of these tests reported or used by different researchers or standards.

As can be seen in Table 1, ASTM C928 [22] that covers rapid repair of concrete pavements and structures using cementitious mortar or concrete materials, makes use of slant shear test of ASTM C882 to measure bond strength between repair material and old concrete. It should be noted that ASTM C928 is also considered as the standard covering requirements for patch repairs. Slant shear test was originally used in ASTM C882 on cylindrical samples to evaluate epoxy bond strength. The test uses a cylindrical mold, where repair material is poured on dummy section with slant interface that is skewed 30° from the cylinder axis. Different researchers used different variants of this test to evaluate bond strength between old and new concrete, making use of cylindrical and rectangular prism samples with different slant angles ranging from 30 to 70°. An important observation made in this test was that its strength strongly depends on the surface preparation of the interface. Austin et al. [25] using Mohr-Coulomb failure envelope concluded that the critical slant angle (associated with minimum compressive strength) for different types of surface preparation varies between 19~27°.

Dave [32] concluded that slant shear test has a large deviation, requiring careful sample preparation. They do not include slant shear test in the set of their recommended tests required for checking adequacy of repair material for partial depth repair attempts as an alternative for ASTM C928. They also found that considering the stress field in concrete slabs for partial depth repairs, there is no correlation between bond strength (evaluated adopting ASTM C900 anchor pullout test) and flexural strength of the partial depth repairs. It should be noted that stress fields for patch repair of bridge piers is similar to that of partial depth repairs in the bridge deck.

In Table 1, there are also other types of bond strength evaluation tests including indirect tensile and pull-off tests. Indirect tensile test also known as splitting tensile test similarly is used to measure bond strength between old and new concrete. Again, cylindrical and rectangular prism samples are used as an alternative. Contrary to those seen in the slant shear test, observations show less dependence of this test to surface preparation. Pull-off test is also proposed by some researchers to evaluate bond strength. In fact, the appropriateness of different tests for given conditions of the bonding interface depends on the stress state at the interface.

All of the above-mentioned tests assume a continuous path of load in old to new concrete accompanied mainly by some form of shear transfer in between. This is not the case for localized repair attempts, where there is indirect force transfer from old concrete to the repair concrete. This is accompanied by some form of stress concentration in the repair location in the old concrete. In the patch repair, the main contribution of the repair

TABLE 1. Testing methods employed by different researchers for evaluating repair efficiency

Test	Researcher	Used for evaluating	Variants
Slant shear test	ASTM C882 [21]	Epoxy bond strength	Cylindrical, Angle 30°
	ASTM C928 [22]	Repaired concrete	Uses ASTM C882 to measure bond strength
	BS EN 12615 [23]		Rectangular prism, Angle 30°
	Knab and Spring [24]		Cylindrical, Angle 30°
	Austin et al. [25]		Cylindrical sample Different preparation of interface
	Ehsani et al. [26] Momayez et al. [27]		Rectangular prism, Angle 30° Different preparation of interface
	Muñoz [28]		Rectangular prism, Angle 20, 30, 35° Different preparation of interface
	Pan [29]		Rectangular prism, Angle 70° Different preparation of interface
	Nayak et al. [30]	Evaluating bond strength	Cylindrical, Angle 30°
Indirect tensile test	Ehsani et al. Momayez et al.		Prism
	Nayak et al.		Cylindrical sample
	Pan		
Pull-off test	Ehsani et al. Momayez et al. Pan		Cylindrical sample
Modified pull-out test	Cleland and Long [31] Dave [32]		Uses ASTM C900 developed for anchor pull-out test
Compression test	Pan		Rectangular prism
	Dave	Repaired concrete	Cylindrical sample
Flexural test	Dave		Rectangular prism / three points flexural test

concrete is to provide a protective shield and some degree of confinement. This discontinuous stress field could not be simulated by the above-mentioned tests and consequently the results could not be trusted as the actual behavior of the repaired section/element.

This study investigates application of SCC with polymer and fiber in patch repair of bridge piers. Two testing methods are used in this study, including slant shear test as required by ASTM C928 and a novel compression test accounting for indirect load transfer from old to new concrete (hereafter called patch test). The latter is developed in this study to simulate stress fields in the elements with patch repair. In the following, first materials used in the study are introduced and then the testing methods are described in detail. Finally results of tests are reviewed and the correlation between the two testing methods considered in this study is assessed.

2. MATERIALS

The materials used in this study include:

- Cement: the used cement is type 2 cement of Urmia cement plant.
- Water: The used water is drinking water with a pH between 5 and 8.5
- Aggregates: River aggregates are obtained from Ghar e Ghom mine in Khoy with a maximum grain size of 6.35 mm.
- Micro-silica: Micro-silica used in self-compacting concrete is manufactured by Lorestan Ferro-silica plant.
- Limestone powder: Limestone powder is obtained from Azarshahr Lime Plant.
- Polymer: The polymer used was Latex Styrene-Butadiene Rubber (SBR) latex for modifying self-compacting concrete, it was a milky white liquid polymer with a pH of about 8.
- Steel fibers: Steel fibers used are per ASTM 510M standard with a tensile strength of 1500 MPa, and a hook at its ends for better development in concrete. The fiber length is 30 mm, its diameter is 0.6 mm and its apparent ratio is 50.

- Superplasticizer: The used superplasticizer is polycarboxylate ether (PCE) type in accordance with ASTM C 1017.

Table 2 shows the mixing proportion for normal strength concrete (NSC), self-compacting concrete (SCC), polymer modified SCC (PM-SCC), and fiber reinforced PM-SCC (FR-PM-SCC). Strength of the hardened concrete samples are given in Tables 3 and 4.

3. TESTING METHODS AND SPECIMENS

The experimental program includes two sets of specimens, including:

- New test, called patch test that is designed to simulate indirect force transfer from old concrete to repaired one and discussed in section 3.1.
- Slant shear test in conformance with ASTM C 928, which is mainly designed to verify adequacy of bond strength between the two concretes. The specimens used in this test are introduced in section 3.2.

3. 1. Patch Test The test called patch test is designed to simulate indirect force transfer from old to new concrete. While in bond strength evaluation tests such as slant shear test, old and new (repair) concrete experience the same stress field, in the patch test, load is mainly introduced through old concrete. This is the loading situation that patched piers experience during their life time.

TABLE 2. Mixing proportion for different types of concrete used in this study.

Concrete	Cement content (kg)	Water (kg)	w/c	Plasticizer (kg)	Micro-silica (kg)	Limestone Powder (kg)	Sand (kg)	Aggregate (kg)	Polymer (kg)	Steel fiber (kg)
NSC	300	201	0.67	-	-	-	1150	800	-	-
SCC	420	152	0.36	17	80	175	1500	-	-	-
PM-SCC	420	153	0.36	26	80	175	1500	-	32	-
FR-PM-SCC	445	147	0.33	28	85	185	1403	-	33	60

TABLE 3. Specimen description in the patch tests.

Designation	Damage/Repair	No. of specimens	Old concrete type/ Strength (MPa)	Repair concrete type/ Strength (MPa)	Interface
PD	**Damaged Specimen**: Damage induced/No repair	6	NSC/24	-	-
PC	**Control Specimen**: No damage/No repair	6	NSC/24	-	No interface
PR1	**Repaired Specimen**: Damage induced/Repaired	6	NSC/24	PM-SCC/50	Roughened with long. grooves
PR2	**Repaired Specimen**: Damage induced/Repaired	6	NSC/24	FR-PM-SCC/60	Roughened with long. grooves

TABLE 4. Specimens description in the slant shear tests

Designation	No. of specimens	Old concrete type/ Strength (MPa)	New concrete type/ Strength (MPa)	Interface
S1A	3	NSC/20	PM-SCC/50	Smooth interface
S1B	3			Brushed interface
S1C	3			Crossover grooved interface
S2A	3			Smooth interface
S2B	3			Brushed interface
S2C	3			Crossover grooved interface
S3A	3		FR-PM-SCC/44	Smooth interface
S3B	3			Brushed interface
S3C	3			Crossover grooved interface

The patch test specimens consist of a core cylinder of height and diameter of 310 and 120 mm from old concrete, and a surrounding cylinder from repair concrete of 300 mm in height with interior and exterior diameter of 120 and 150 mm (Figure 1a). Compression load is applied through old concrete, and there is no direction load application on the top and bottom surfaces of repair concrete .

Table 3 gives a description of the specimens considered in the tests simulating patch repair. These include six control samples (undamaged specimens PC) and eighteen cylindrical samples with induced damage. After opening the mold for a period of up to 28 days, the samples were cured in water of 20°C. In samples simulating damage a circumferential layer of 15 mm thickness is removed (specimens PD, PR1 and PR2), reducing the diameter of the damaged sample to 120 mm. Specimens PR1 and PR2 are repaired using different methods as described in Table 3.

The lateral surface of damaged samples (interface) is roughened by longitudinal grooves of width and depth of 4 mm and with spacing of 20 mm (Figure 1b). A specimen ready for test is shown in Figure 1c. Table 3 also gives strength of different concretes (old and repair concrete) used in the tests. The repaired samples were cured by 1 day dry, 3 days water curing, and then 24 days with nylon coating in the laboratory condition (20 ± 2°C). The repaired samples were loaded under compressive axial load 28 days after repair and their load-bearing capacity and axial deformations were read .

The loading rate of the samples in the axial loading test was set at 1 MPa / sec. The load-displacement values were read up to load reduction of about 70% of the failure load.

(a) (b) (c)

Figure 1. Patch test specimen, a) dimensions, b) damaged concrete (old concrete) of diameter 120 mm, c) tested specimen

3. 2. Slant Shear Test To evaluate bond strength between old and repaired concrete interface, 27 samples of cylindrical slant tests are molded as depicted in Figure 2. The skewed interface has a slope of 45°. Table 4 gives a description of specimens tested in the slant shear tests. As described in Table 4, three types of surface are considered in the slant shear tests, which include: a) smooth surface, b) brushed surface, c) surface with crossover grooves of width and depth of 4 mm at intervals of about 20 mm (Figure 3). After 28 days, the second part the specimen is constructed and after curing they are subjected to compressive axial loading.

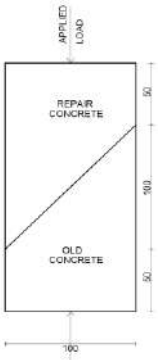

Figure 2. Dimensions of slant shear test

(a) (b) (c)

Figure 3. Surface preparations in slant shear tests, a) smooth surface, b) brushed surface, c) grooved surface

4. TEST RESULTS

4. 1. Patch Tests Figure 4 depicts cracking pattern of two specimens in the patch test. The first crack in the repaired samples are longitudinal cracks in the surface of repair concrete. Due to the application of the load on the core concrete, the formation of longitudinal cracks in repair concrete have been due to different modulus of elasticity and consequently different transverse deformation of the core and repair concrete. In the repaired specimens, four longitudinal cracks occur at approximately equal radial angles.

The load-displacement curve for different specimens is shown in Figure 5. The maximum load carrying capacity of repaired specimens (PR1 and PR2) barely exceed that of control specimen (PC). Figure 6 gives minimum, maximum and mean of different specimens evaluated using the patch test. The results of the compression test on the patch specimens could be summarized as follows:

- The mean load carrying capacity of the control and damaged samples (PC versus PD) are 389 and 226 kN respectively. This shows a reduction of about 42% for damaged samples. It should be noted that the cross-sectional area of core concrete in damaged samples is reduced by 36% compared to the control samples.
- Introduction of damage resulted in about 60% reduction in axial stiffness. Repair attempts introduces no improvement in increasing stiffness of the repaired samples.

Figure 4. Cracking pattern of repaired specimens in patch tests

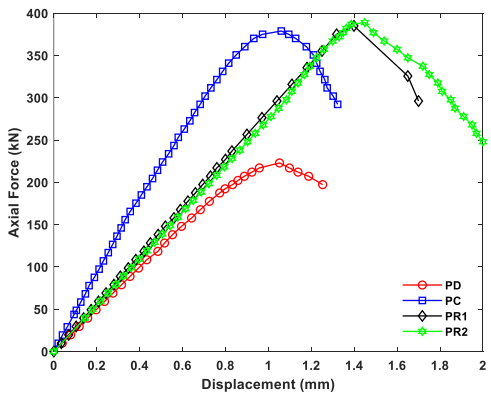

Figure 5. Typical load-displacement of specimens in patch test

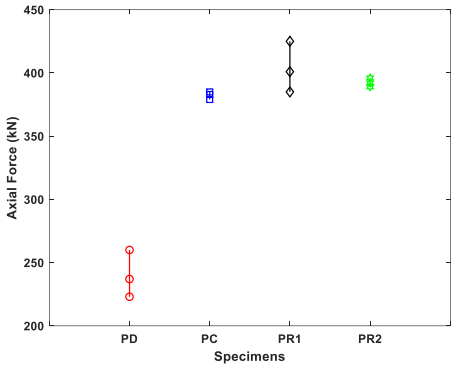

Figure 6. Results of patch tests including minimum, mean and maximum axial strengths

- Samples repaired by PM-SCC has a mean load carrying capacity of 387 kN, which shows an increase of about 71% compared to the damaged samples and slightly lower than the control specimen.
- Samples repaired using FR-PM-SCC has a mean load carrying capacity of 392 kN, an increase of about 73% compared to the damaged samples and slightly larger than the control specimen.
- Introduction of damage increases anticipated variation in the specimen's strength. On the other hand, the use of fiber reinforced repair concrete significantly reduces the variation in the strength.
- Referring to Table 3, although strength of old concrete is about 24 MPa and repair materials have much higher strength between 50~60 MPa, there is only slight increase in the strength of the repaired specimens compared to the old concrete. This shows that due to existing load path in the repaired specimens, even with high quality repair materials, strength of old concrete limits the efficiency of the repair method.

Compared to the control samples, it can be seen that by repairing the damaged samples, the load carrying capacity of the control samples could be recovered.

4. 2. Slant Shear Tests Figure 7 depicts failure pattern of two specimens tested using the slant shear test method. Interface between the two concretes is also visible in one of the figures. Figure 8 depicts results of the tests. By reviewing results for different specimens, the following conclusions could be drawn:

- In specimens repaired by PM-SCC or FR-PM-SCC, there is about 50% increase in strength compared to the specimens repaired by NSC. It can be inferred that the use of SBR latex polymer has significant effect on the adhesion between old and repair concrete.
- Different surface treatment methods have substantial impact on the strength of the repaired specimen. Increased effort in preparing interface from smooth to brushed and grooved surfaces, increases the strength of the specimens. No interface failure is observed for specimens with minimal surface

Figure 7. Failure pattern of typical specimens in slant shear tests

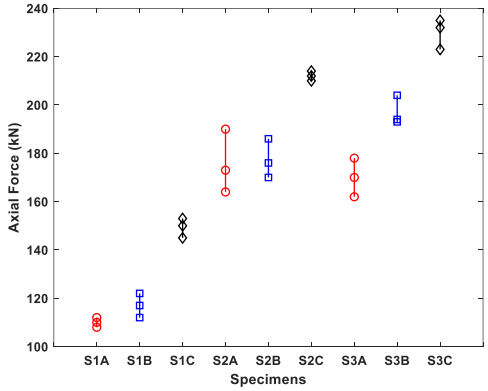

Figure 8. Results of slant shear tests including minimum, mean and maximum strengths

preparation attempt, i.e. specimens with brushed or grooved interface.

- There is reduced sensitivity to the interface preparation method in the specimens repaired by PM-SCC or FR-PM-SCC concrete. This is another indication of superior performance of latex in improving bond strength between old and repair concrete.
- Making use of fiber reduces anticipated variation in the results of slant shear strength. The same pattern is also observed in patch tests.
- Referring to Tables 3 and 4, strength of repair martials is smaller than those used in the patch test, however the results of the slant shear test shows more efficient repair.

4. 3. Correlation between Patch and Slant Shear Tests ASTM C 928 uses slant shear test to evaluate the adequacy of concrete repair. The main question is that by using the results of slant shear test, is it possible to evaluate the adequacy and efficiency of repair in increasing load carrying capacity of the repaired element. To answer this question, in the present study, the correlation between the results of the patch tests

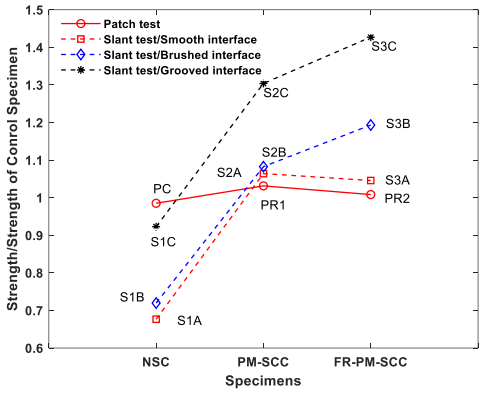

Figure 9. Evaluating correlation between slant shear and patch tests

(section 4.1) and slant shear tests (section 4.2) is evaluated. Figure 9 shows the efficiency of different repair methods compared with the compressive strength of the old concrete as assessed using two different testing methods. It is anticipated that as the patch test accounts for indirect load transfer to the repaired concrete, it provides a better estimate of the repaired element. As could be seen, while use of latex significantly improves strength evaluated by the slant shear test results, there is only a slight increase in the strength as assessed by the patch test.

In patch repair, due to the short length of the repair, the repaired concrete could not be considered fully effective. Indirect load transfer from old concrete to repair concrete in patch repair could not be simulated by the slant shear test. Accounting for load path in patch repair, strength of the old concrete introduces a limit on the maximum efficiency of the repair material and method. The slant shear test is more appropriate for testing continuous shear transfer in elementwise repairs rather than local patch repairs.

5. CONCLUSION

This study was conducted to investigate the efficiency of using polymer modified self-compacting concrete with or without steel fiber for patch repair of damaged laboratory samples. Two testing methods are considered in the study for evaluating the effectiveness of the repair procedure, including ASTM C 928 proposed slant shear test and a novel testing method devised to simulate indirect force transfer path in patch repairs. The following results were obtained.

- Results of slant shear tests show the effectiveness of latex polymer in enhancing bond strength between old and repair concrete.
- Results of the patch tests and slant shear tests, both show that use of fibers reduces variation in the strength of the specimens, and results in more predictable repair material.

- Observed variation in the strength of the specimens tested by the patch test and slant shear test is approximately on the same order.
- Strength of old concrete as a weak link in the load path should impose an upper limit on the strength of the repaired specimens. This is not the case for the slant shear test and using repair materials of higher strength leads to higher strength for the repaired specimens in the slant shear test. Although slant shear test shows about an 50% increase in strength compared to undamaged specimens, new proposed test methods evaluating patch repair effectiveness show little if any increase in the strength of the repaired specimens compared to the undamaged specimens.
- Considering force path in the patch repair and regardless of the materials used for repair, the efficiency and adequacy of patch repair could not be evaluated using slant shear test as suggested by ASTM C 928 and the use of this test in evaluating adequacy of patch repair could be misleading.

6. REFERENCES

1. Mourad, S.M., Shannag, M.J., Repair and strengthening of reinforced concrete square samples using ferro-cement jackets**,** ***Cement and Concrete Composites***, Vol. 34, No. 2, (2012), 288–294, https://doi.org/10.1016/j.cemconcomp.2011.09.010.
2. Delatte, N., Failure, Distress and Repair of Concrete Structures, Elsevier, (2009).
3. Giménez, E., Adam, J. M., Ivorra, S., Moragues, J. J., & Calderón, P. A. (2009). Full-Scale Testing of Axially Loaded RC Columns Strengthened by Steel Angles and Strips. ***Advances in Structural Engineering***, Vol. 12, No. 2, (2009), 169–181. https://doi.org/10.1260/136943309788251704.
4. Choi, E., Chung, Y-S., Park, J., Cho, B-S., Behavior of Reinforced Concrete Samples Confined by New Steel-Jacketing Method, **ACI Structural Journal**, Vol. 107, No. 6, (2010), 654-662.
5. Islam, N., Hoque, M., Strengthening of reinforced concrete columns by steel jacketing: a state of review, ***Asian Transaction on Engineering***, Vol. 5, No. 3, (2015), 6-14.
6. He, R., Grelle, S., Sneed, L.H., Belarbi, A., Rapid repair of a severely damaged RC column having fractured bars using externally bonded CFRP**,** ***Composite Structures***, Vol. 101, (2013), 225-242, https://doi.org/10.1016/j.compstruct.2013.02.012.
7. Chellapandian, M., Prakash, S.S., Sharma, A., Axial compression–bending interaction behavior of severely damaged RC columns rapid repaired and strengthened using hybrid FRP composites. ***Construction and Building Materials***, Vol. 195, (2019), 390-404, https://doi.org/10.1016/j.conbuildmat.2018.11.090
8. Mohammed, A.A., Manalo, A.C., Ferdous, W., Zhuge, Y., Vijay, P.V., Alkinani, A.Q., Fam, A., State-of-the-art of prefabricated FRP composite jackets for structural repair, Engineering ***Science and Technology***, (2020), https://doi.org/10.1016/j.jestch.2020.02.006.
9. Ozturk, B., Senturk, T., Yilmaz, C., Analytical investigation of effect of retrofit application using CFRP on seismic behavior of a monumental building at historical Cappadocia region of Turkey, 9th U.S. National and 10th Canadian Conference on Earthquake Engineering, Toronto, Canada (2010).
10. Ozturk, B., Yilmaz, C., Senturk, T., Effect of FRP retrofitting application on seismic behavior of a historical building at Nigde, Turkey, 14th European Conference on Earthquake Engineering, Ohrid (2010).
11. Dehghani, H., Fadaee, M.J., Reliabilty-based torsional design of reinforced concrete beams strengthened with CFRP laminate, ***International Journal of Engineering***, ***Transactions A: Basics***, Vol. 26, No. 10, (2013), 1103-1110.
12. Júlio E.N.B.S., Branco F.A., Reinforced concrete jacketing-interface influence on cyclic loading response, ***ACI Structural Journal***, V. 105, No. 4, (2008), 471-477.
13. Rodrigues, H., Pradhan, P.M., Furtado, A.F., Rocha, P., Vila-Pouca, N., Structural repair and strengthening of RC elements with concrete jacketing, ***Strengthening and Retrofitting of Existing Structures, Springer***, Vol. 9, (2018), 181–198.
14. Omar, M.Y.M., Gomes, R.B., Reis, A.P.A., Experimental analysis of reinforced concrete samples strengthened with self-compacting concrete, ***Revista IBRACON de Estruturas e Materiais***, Vol. 3, No. 3, (2010), 271–283.
15. Dubey, R., Kumar, P., Experimental study of the effectiveness of repairing RC cylindrical samples using self-compacting concrete jackets, ***Construction and Building Materials***, Vol. 124, (2016), 104–117.
16. Park S.K., Yang D.S., Flexural behavior of reinforced concrete beams with cementitious repair materials, ***Materials and Structures***, Vol. 38, (2005), 329–341.
17. Pellegrino, C., Porto, F., Modena, C., Rehabilitation of reinforced concrete axially loaded elements with polymer-modified cementicious mortar, ***Construction and Building Materials***, Vol. 23, (2009), 3129–3137.
18. Lampropoulos, A.P., Paschalis, S.A., Tsioulou, O.T., Dritsos, S.E., Strengthening of reinforced concrete beams using ultra high performance fibre reinforced concrete (UHPFRC), ***Engineering Structures***, Volume 106, (2016), 370-384, https://doi.org/10.1016/j.engstruct.2015.10.042
19. Meda, A., Mostosi, S., Rinaldi, Z., Corroded RC columns repair and strengthening with high performance fiber reinforced concrete jacket. ***Materials and Structures***. Vol. 49, (2016), 1967–1978, https://doi.org/10.1617/s11527-015-0627-1.
20. Beddar, M., Ayadat, T., Belgara, L., Optimizing of steel fiber reinforced concrete mix design ***International Journal of Engineering***, ***Transactions B: Applications***, Vol. 17(1), (2004) 41-50.
21. ASTM C 882, Test method for bond strength of epoxy-resin systems used with concrete by slant shear, American Society for Testing and Materials, (2005).
22. ASTM C 928, Standard specification for packaged, dry, rapid-hardening cementitious materials for concrete repairs, American Society for Testing and Materials, (2008).
23. BS EN 12615, Products and systems for the protection and repair of concrete structures: Test methods- Determination of slant shear strength, (1999).
24. Knab, L.I., Spring, C.B., Evaluation of test methods for measuring the bond strength of Portland cement-based repair materials to concrete, National Bureau of Standards, (1988).
25. Austin, S., Robins, P., Pan, Y., Shear bond testing of concrete repairs, ***Cement and Concrete Research*** Vol. 29, (1999), 1067–1076.
26. Ehsani, M.R., Rajaie, H., Raezanianpour, A., Momayez, A., Experimental investigation of the methods of evaluating the bond strength between concrete substrate and repair materials, ***International Journal of Engineering***, ***Transactions A: Basics***, Vol. 15, No. 4, (2002), 319-332.
27. Momayez, A., Ehsani, M.R., Ramezanianpour, A.A., Rajaie, H., Comparison of methods for evaluating bond strength between concrete substrate and repair materials, ***Cement and Concrete Research***, Vol. 35, (2005), 748–757.

28. Muñoz, M.A.C., 2012, Compatibility of ultra high-performance concrete as repair material: Bond characterization with concrete under different loading scenarios, M.S. Thesis, Michigan Technology University.
29. Pan, Y., Bond Strength of Concrete Patch Repairs: An Evaluation of Test Methods and the influence of workmanship and environment, PhD Thesis, Loughborough University of Technology, (1995).
30. Nayak, D., Pattnaik, R.R., Bhoi, K.C., Panda, B., (2019). Investigation into material strength and direction of applied forces to assess bonding behavior of micro-concrete. ***Journal of The Institution of Engineers (India): Series A***, 100, 75–82 (2019). https://doi.org/10.1007/s40030-018-0338-z.
31. Cleland, D.J., Long, A.E., The pull-off test for concrete patch repairs, Proceeding of Institute for Civil Engineering Structures and Buildings, Vol. 122, (1997), 451-460.
32. Dave, E.V., Evaluation of concrete and mortars for partial depth repairs, Research Report 2014-41, University of Minnesota Duluth, (2014).

Persian Abstract

چکیده

شرایط محیطی شدید در بسیاری از مناطق ایران می‌تواند منجر به آسیب به زیرساخت‌ها به خصوص پایه پل‌ها شود. این تحقیق به بررسی کارایی بتن خودتراکم اصلاح شده با پلیمر و فیبر به عنوان یک ماده ترمیم و کاربرد آنها در تعمیر لکه‌گیری پایه پل می‌پردازد. راندمان این مواد برای تعمیر لکه‌گیری با استفاده از روند ارائه شده در ASTM C 928 و یک آزمایش جدید (آزمایش لکه‌گیری) کنترل می‌شود. آزمایش لکه‌گیری برای ارزیابی مقاومت المان لکه‌گیری شده با در نظر گرفتن انتقال نیروی غیرمستقیم از بتن قدیمی (موجود) به بتن جدید (بتن لکه‌گیری) تدوین شده است. به منظور بررسی کارآیی بتن خودتراکم در ترمیم لکه‌گیری دو مجموعه از آزمایشات مرکب از آزمایشات لکه‌گیری و برش اریب انجام شدند. نتایج آزمایشات برش اریب بهبود قابل توجهی در استحکام به دلیل استفاده از خودتراکم اصلاح شده با و تقویت شده با الیاف حتی تا میزان ۵۰٪ افزایش مقاومت در مقایسه با نمونه های بدون آسیب نشان دادند. در حالی که در آزمایشات لکه‌گیری روی نمونه‌های آسیب‌دیده، نمونه‌های تعمیر شده به سختی قادر به تامین مقاومت نمونه‌های آسیب‌ندیده بودند. در آزمایشات برش اریب استفاده از پلیمر در افزایش استحکام پیوستگی بتن جدید و قدیم بسیار مؤثر ارزیابی شد و در عین حال استفاده از الیاف منجر به کاهش در پراکندگی مقاومت مصالح شد. بدون توجه به مصالح مورد استفاده برای تعمیر، نتایج این مطالعه نشان می‌دهد که قضاوت در مورد کارآیی روش ترمیم بر اساس آزمایش برش اریب آن چنان که در ASTM C 928 پیشنهاد شده است در مورد مقاومت المان‌های تعمیرشده با لکه‌گیری می‌تواند گمراه‌کننده باشد.

International Journal of Engineering

Journal Homepage: www.ije.ir

Image Edge Detection with Fuzzy Ant Colony Optimization Algorithm

Z. Dorrani, H. Farsi*, S. Mohamadzadeh

Department of Electrical and Computer Engineering, University of Birjand, Birjand, Iran

P A P E R I N F O

Paper history:
Received 05 July 2020
Received in revised from 20 August 2020
Accepted 03 September 2020

Keywords:
Ant Colony Optimization Algorithm
Edge Detection
Fuzzy System

A B S T R A C T

Searching and optimizing by using collective intelligence are known as highly efficient methods that can be used to solve complex engineering problems. Ant colony optimization algorithm (ACO) is based on collective intelligence inspired by ants' behavior in finding the best path in search of food. In this paper, the ACO algorithm is used for image edge detection. A fuzzy-based system is proposed to increase the dynamics and speed of the proposed method. This system controls the amount of pheromone and distance. Thus, instead of considering constant values for the parameters of the algorithm, variable values are used to make the search space more accurate and reasonable. The fuzzy ant colony optimization algorithm is applied on several images to illustrate the performance of the proposed algorithm. The obtained results show better quality in extracting edge pixels by the proposed method compared to several image edge detection methods. The improvement of the proposed method is shown quantitatively by the investigation of the time and entropy of conventional methods and previous works. Also, the robustness of the proposed method is demonstrated against additive noise.

***doi**: 10.5829/ije.2020.33.12c.05*

1. INTRODUCTION

Image edges are one of the simplest but most important elements in image processing. Therefore, the appropriate implementation of some image processing algorithms depends on the accuracy of edge extraction [1, 2]. The location of an object in an image can be measured by identifying its edges [3, 4]. Also, edge detection is one of the basic techniques in segmentation, separation, and understanding the position of targets in image and scene variation detection [5]. Edge detection is known as a critical tool in machine vision [6], separating the background in image compression in order to reduce computation time and storage.

There are many methods for extracting and detecting edges that differ in finding accurate edges [7]. A powerful operator such as the Canny operator [8] which is one of the most important tools in edge detection, may have problems with detecting disrupting edges.

The ACO algorithm is used to discover image edges. In the proposed method, the ACO algorithm with a fuzzy system is applied for image detection. In addition, the following steps are applied in the multi-dimensional approach to obtain accurate edges: A) the connection provides a good quality in terms of connectivity and interconnection of the edges. B) Connecting to neighboring points can be considered quadruple or octahedral, resulting in two outcomes, C) the other parameters of the proposed algorithm are selected to provide better results.

In this article, the first steps of implementing an ACO algorithm are described based on how to find the edges. A fuzzy system is used in the proposed method and then the obtained results are presented. Finally, a summary of the results is presented and discussed.

2. RELATED WORKS

Several edge detection methods have been proposed to discover edges with first- and second-order derivative so far. The Canny edge detection algorithm is known as an optimal edge detector [8]. The globalized probability of boundary (gPb) algorithm combines contour detection and spectral clustering technique [9].

*Corresponding Author Institutional Email: *hfarsi@birjand.ac.ir* (H. Farsi)

Please cite this article as: Z. Dorrani, H. Farsi, S. Mohamadzadeh, Image Edge Detection with Fuzzy Ant Colony Optimization Algorithm, International Journal of Engineering, Transactions C: Aspects, Vol. 33, No. 12, (2020), 2464-2470.

There are many methods for edge detection with ACO [10]. An algorithm based on the ACO is proposed for edge detection in the construction step and a repair operator in the improvement step. The hybrid ACO algorithm for edge detection is proposed by using heuristic and knowledge data in the manufacturing phase and a repair operator in the improvement phase [11]. In another method, the adaptive threshold value is defined based on particle swarm optimization to overcome the restraint of existing ACO-based edge detection techniques [12]. The feature selection is permitted by the ACO algorithm to determine the most protuberant and final features [13]. In [14], the reported method involved pre-processing, achieving the edges in an independent style, and emerging an algorithm to discover the best applicants of initial locations for the ant colonies.

The threshold-based techniques for edge detection with ACO are combined to use in an optical character recognition system [15]. This method is used to sharpen the edge shape of skin lesion images [16]. The reported method in [17] identified the complex area of the cover image and detected complex areas' pixels by using employed data in the ACO based information hiding method. The fuzzy logic is another method that simply answers the problems where static values cannot be obtained. Anwar and Raj proposed the adaptive-neuro fuzzy inference system for edge detection [18]. A bio-inspired edge detection method was suggested using a mixture of bird swarm algorithm (BSA) and fuzzy reasoning [19, 20].

To further develop edge detection methods, we have proposed an optimization algorithm for edge detection. In this approach, an ant's behavior of exploring optimal paths by using fuzzy rules is investigated. Ant colony optimization is used to identify edges of a ship in ocean water. To reduce time and complexity, the fuzzy function is used. The results of the proposed method confirm the clear edges of small and partial objects. The proposed method provides better results compared to other methods for edge detection.

3. PROPOSED METHOD

3. 1. Introducing ACO Algorithm The aim of optimizing the ant colony is to find the best solution for a problem. In the natural world, ants are randomly searching for food. When they return to the nest, they leave a trail of pheromones if they find food. Other ants follow paths where pheromone levels are higher, return to the nest if food is found, leave another trace of pheromone behind, and the pheromone of that path is strengthened. As the ant travels shorter paths at a specific time, each path is better reinforced. The chemical structure of pheromone causes it to evaporate over time, thus reducing the amount of pheromone on less traveled paths over time.

In the algorithm inspired by the natural behavior of ants, the pheromone value of all points in the sample space of the problem is represented by a pheromone matrix. The path leading to the target consists of a set of points that have the highest values in the pheromone matrix. The algorithm starts by considering the initial pheromone values for each pixel and then updates the pheromone matrix based on the problem's information. When the pheromone value changes in successive steps of the algorithm are negligible, the algorithm is stopped and the path with the highest pheromone residue is considered as the best way to solve the problem.

3. 2. ACO Method for Edge Detection In this approach, a number of ants move on a two-dimensional image, hypothetically. An image edge is equivalent to the food which ants seek. First, the algorithm assigns a pheromone matrix to all pixels of the image so that the initial value of each component in the matrix represents the probability of each pixel being edged. This value is the same for all pixels. Then by applying the algorithm and using the equations of probability, the pheromone matrix value is changed and points where brightness level changes occur become more probable. When the ant lies on one pixel, the pheromone level of the pixel increases. At this time no other ants can be placed on this pixel. In other words, two or more ants cannot sit on one pixel at the same time. The next track of ant movement is chosen from 4 or 8 neighboring pixels. If it is assumed that an octagonal connection is used, the ant will choose from the 8 pixels in its vicinity the most probable pixel, and if two or more pixels have the same probability value, a pixel is randomly selected. In quadruple connection, the same previous steps are repeated, except that the next path has to be selected from four neighboring pixels.

Figure 1 shows the direction of the ant's movement at the octagonal and quadratic junctions. Therefore, the points with the highest probability in the pheromone matrix are separated as image edges. The steps for implementing the algorithm are described as follows:

-Initialization step: In the first pheromone matrix, the initial value of each component is $\rho_{init} = 0.0001$.

-Construction step: One of the ants is randomly selected from the X stage and is moved over the image to the Y stage. This ant moves with the probability obtained by the following relation [1] from a pixel to the neighboring pixel.

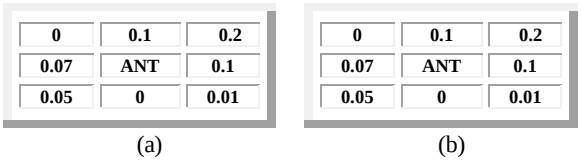

(a) (b)

Figure 1. (a) Ant's movement path at the octagonal junctions (b) Ant's movement path at the quadratic junctions

$$P_{i.j}^{(n)} = \frac{(\rho_{i.j}^{(n-1)})^{\alpha}(\mu_{i.j})^{\beta}}{\sum_{l\in\delta_k}\rho_{i.j}^{(n-1)})^{\alpha}(\mu_{i.j})^{\beta}} \quad (1)$$

where, $P^{(n)}$, $\rho^{(n-1)}$ and μ are the probability of transfer, the pheromone value and the distance of motion from pixel i to pixel j. The values of α and β are the pheromone impact and heuristic information, respectively. The pheromone matrix is updated twice during the execution of the algorithm, once after each ant moves using the following equation [1], and again when the search and completion of all ants is completed.

$$\rho^{(n)} = (1-\lambda)\rho_{i.j}^{(n-1)} + \lambda\rho_{init} \quad (2)$$

where λ is the evaporation ratio, $\rho_{i.j}^{(n-1)}$ is the Pheromone amount before the update step.

Update step: Once every ant has completed it's search, the pheromone matrix is updated using Equation (3) [1].

$$\rho^{(n)} = (1-\omega)\rho^{(n-1)} + \omega\sum_{k=1}^{k}\Delta\rho^{(k)} \quad (3)$$

where ω is the pheromone reduction coefficient and $\Delta\rho^{(k)}$ is determined according to the following [1,20]:

$$\begin{cases}\frac{1}{L_k} & if\ the\ kth\ ant\ goes\ from\ i\ to\ j \\ 0 & otherwise\end{cases} \quad (4)$$

The edges of the image can be detected using the ant-optimization algorithm. All optimization algorithms contain hyperparameters. The values of these parameters are determined by either using the same values used by the algorithm's publishers, or investigated by researchers themselves through trial and error. Depending on the static parameters, the algorithm may be disorganized on some iterations. Therefore, standard ACO may in some iterations interfere with finding optimal edge points. In these cases, a fuzzy controller can solve this problem. Therefore, we use a fuzzy method to control the effect of pheromone and heuristic information.

3. 3. Design of a Fuzzy System for Controlling ACO Parameters The amount of pheromone impact and heuristic information are influential parameters in the implementation of the algorithm so that increasing the pheromone effect strengthens the exploration ability and, if considered smaller, enhances the browsing ability. The heuristic information parameter is the opposite of the pheromone effect parameter, which means that it increases the pheromone linkage between the ants and reduces its browsing.

The first step in the design of a fuzzy system is to select the appropriate inputs and outputs according to the problem's conditions. Due to the problem's conditions and the requirement of uniform convergence for this algorithm, the fuzzy structure consists of two inputs and two outputs for parametric control of the convergence of this algorithm. The inputs to this system include the value of the objective function's fit and the number of iterations. The two outputs are controlled by this fuzzy system, which is the effect of pheromone and exploratory information. The general approach of the proposed fuzzy system for controlling the parameters of the ACO algorithm is shown in Figure 2.

3. 4. Membership Functions The fuzzy membership functions are defined according to the problem's conditions and their correct definition is required to provide an appropriate answer to the problem.

There is a great variety of membership functions. Choosing effective and rational rules for controlling parameters results in better performance. In this case, the trapezoid type is selected. The overlap conditions of the fuzzy system rules and decision levels shown in Figure 3 illustrate the effective and appropriate selection of membership functions.

The rules for controlling input and output can affect global and local search, speed of response, and result in fewer steps being repeated, causing a reduce in response time, especially for immediate applications. So searches in the early stages of the nation (?) and as we approach the final stages of repetition, local search is saturated and more exploration is done.

4. EXPERIMENTAL RESULTS

4. 1. Standard Images Initially, the standard image is called with any size that is a factor of 8, and the ACO algorithm is executed on it. To run the algorithm, we need the basic parameters:

α =0.0001, β=1, λ =10, ω=0.6.

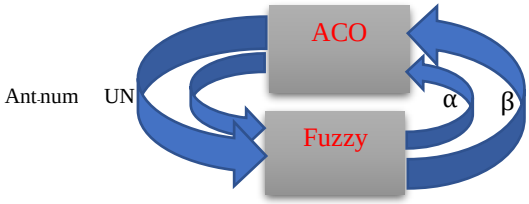

Figure 2. Fuzzy system for controlling the parameters of the ACO algorithm

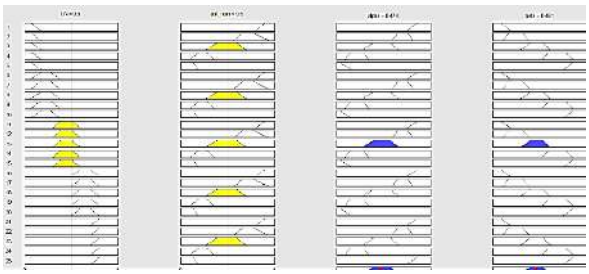

Figure 3. Schematic of the fuzzy rules for fuzzy systems

The number of ants is 4 and each ant moves about 20 times during the construction phase. To run the algorithm, we selected some images and implemented the fuzzy ACO algorithm on them. To compare the proposed algorithm's performance at edge detection with robust edge detection methods such as Canny, Sobel, ACO edge detection, and Laplacian of Gaussian (LOG) method [1], the simulation results are also shown in Figure 4. The proposed algorithm has demonstrated its ability to correctly identify the edges of the image. In any form it can be observed that the pixels of the edge are correctly recognized and compared to other edge detection methods, the sublimation and priority of the edge quality (?) are higher.

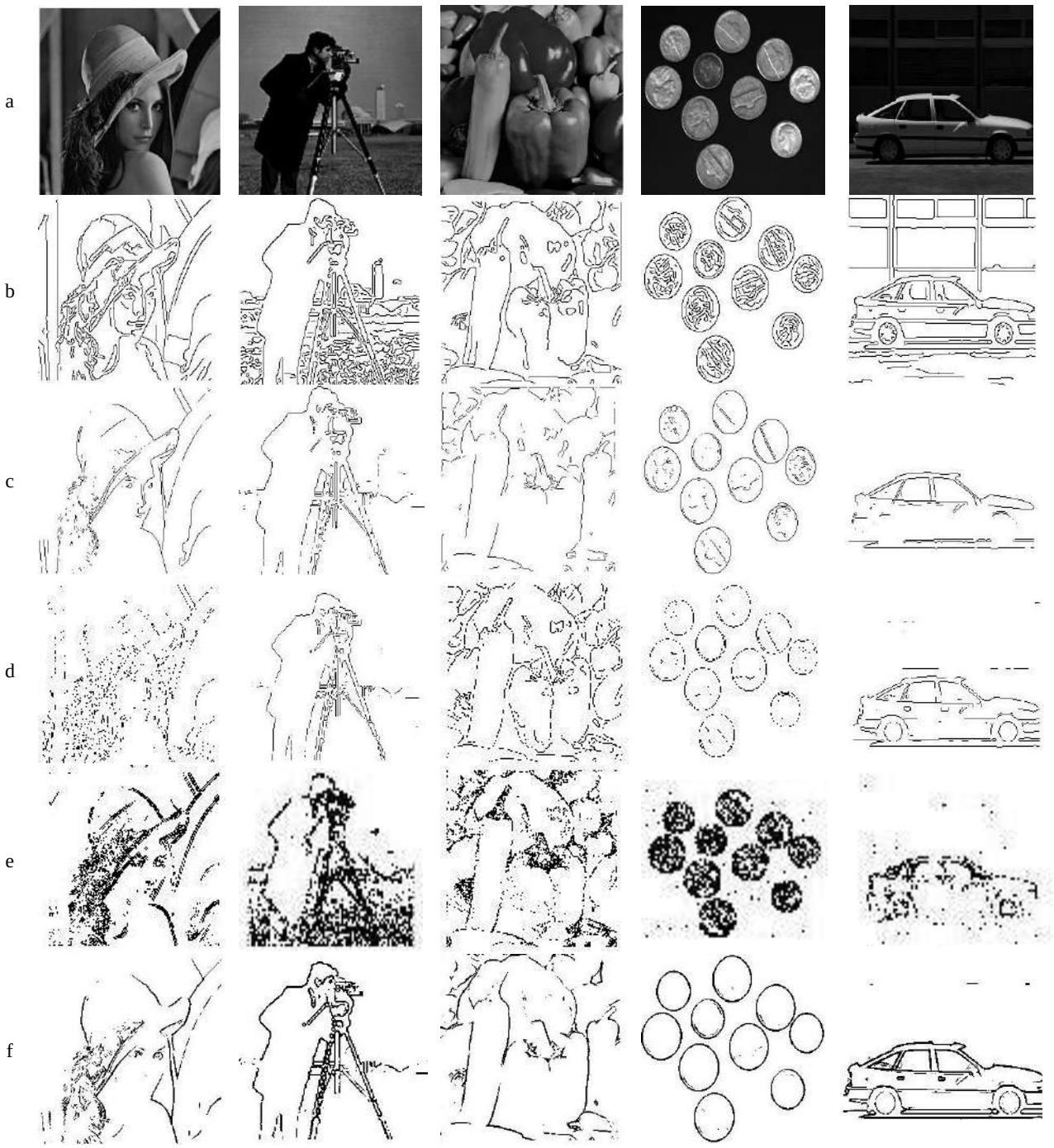

Figure 4. (a) Original image; (b) Detected edges using Canny method; (c) Detected edges using Sobel method;(d) Detected edges using ACO method; (e) Detected edges using LOG method; (f) Detected edges using the proposed method

To compare system and output performance, Shannon's entropy function is used [21]. The information that the output image holds can be measured by this function. The information in the image decreases as the value of entropy increases. This is calculated by:

$$H(I) = -\sum_{i=0}^{L} q_i \, log q_i \quad (5)$$

where I and q_i are the image and the pixels' frequency having intensity i, respectively.

Table 1 shows the entropy values for the outputs of different edge detectors on various images. A higher value of entropy corresponds to more randomness and less information. The proposed algorithm achieves the least entropy value and is capable of discovering important edges.

Table 2 shows time values obtained by hybrid ACO, gPb and the proposed method over four standard images (Lena, Cameraman, Pepper and, Mandril). As observed, the proposed method's performance is better compared to hybrid ACO, and gPb.

4. 2. Berkley Segmentation Dataset To evaluate the effectiveness of the proposed method, images from Berkeley Segmentation Dataset have been used. Table 3 presents the entropy values for outputs of some of the edge detectors [19]. As observed, the proposed algorithm provides the minimum value.

4. 3. The Medical Images At this stage, the medical images are considered. Three skin lesion images [16, 22] are used (Figure 5).

The efficiency of the proposed method is tested by comparing the entropy of Canny and Prewitt operator in Table 4.

4. 4. Noisy Images To study the stability of the proposed method, Gaussian Noise is added to the images. As an example Figure 6 shows the results obtained by the proposed method.

TABLE 1. Entropy values for the outputs of different edge detectors on standard images

Image	Fuzzy BFO	Neuro-Fuzzy	BSA-Fuzzy	Proposed Method
Lena	0.5773	0.6997	0.5002	**0.3750**
Cameraman	0.6556	0.6135	0.6112	**0.4072**
Monarch	0.6929	0.7822	0.6772	**0.5452**
Barbara	0.6001	0.5667	0.5474	**0.3101**
Pepper	0.5662	0.5998	0.5453	**0.3837**

TABLE 2. Time values(s) for the outputs of different edge detectors on standard images with 256 *256

Image	Hybrid ACO	gPb	Proposed Method
Lena	4.4	219.5	**3.33**
Cameraman	4.7	196.7	**4.366**
Pepper	4.1	227.1	**3.79**
Mandril	5.2	215.7	**4.9**

TABLE 3. The entropy values for the outputs of some of the edge detectors on Berkley segmentation dataset

Image	GA	PSO	ACO	Deep Learnig	BFA	Fuzzy+BFO	Neuro-Fuzzy	PSO for Noisy	BSA-Fuzzy	Proposed Method
35010	0.8211	0.7213	0.7715	0.6882	1.6124	0.6331	0.6110	0.6995	0.6002	**0.5960**
42049	0.8322	0.6811	0.7722	0.6243	1.5216	0.5999	0.6561	0.6778	0.5991	**0.3911**
118035	0.8836	0.6992	0.7765	0.6836	1.4245	0.5876	0.5788	0.6476	0.5521	**0.3980**
135069	0.9214	0.8112	0.8833	0.7210	1.2124	0.6675	0.6689	0.7889	0.6433	**0.4217**
119082	0.9914	0.8365	0.8987	0.7991	1.4642	0.7999	0.7989	0.8999	0.7782	**0.5711**

A B C

Figure 5. The medical images (skin lesion)

TABLE 4. Entropy values for the medical images

Image	Canny	Prewitt	Proposed Method
A	0.4791	0.1283	**0.1106**
B	0.7677	0.2174	**0.1293**
C	0.6238	0.1502	**0.0876**

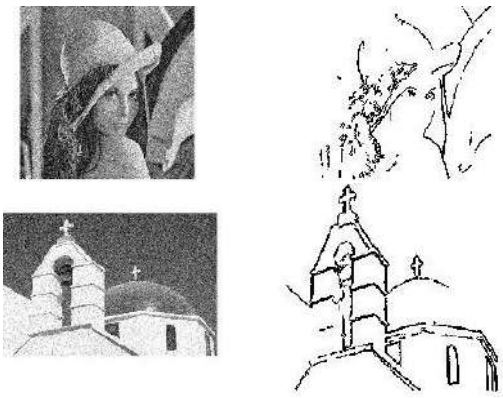

Figure 6. The proposed edge detection on noisy images

5. CONCLUSIONS

In this paper, an ACO algorithm was developed for edge detection. The fuzzy controller was used to control the algorithm's hyperparameters. The obtained results demonstrate the success of this algorithm in finding the edges of an image. The efficient and appropriate selection of fuzzy controllers as well as the membership functions can improve the convergence speed of the algorithm by preventing pheromone control as well as preventing the inertia and immobility of the ant during the algorithm implementation. This process results in a dynamic search corresponding to a finer edge. Using fuzzy abilities, we were able to improve the capabilities of the ACO algorithm. On the other hand, by fuzzing, we are able to improve the behavior of the algorithm against the anomalous position of some ants. Therefore, a smarter and more accurate algorithm resulted in increased edge search quality. The effectiveness of the fuzzy ACO based approach has been examined on images and the obtained results showed that the detected edges are more connected and smooth compared to other latest edge detectors while reducing time and entropy.

6. REFERENCES

1. Tian, J., Yu, W., and Xie, S. "An ant colony optimization algorithm for image edge detection." In 2008 IEEE Congress on Evolutionary Computation, CEC, (2008), 751–756. https://doi.org/10.1109/CEC.2008.4630880
2. Dorrani, Z., and Mahmoodi, M. S. "Noisy images edge detection: Ant colony optimization algorithm." ***Journal of Artificial Intelligence and Data Mining***, Vol. 4, No. 1, (2016), 77–83. https://doi.org/10.5829/idosi.jaidm.2016.04.01.09
3. Sezavar, A., Farsi, H., and Mohamadzadeh, S. "Content-based image retrieval by combining convolutional neural networks and sparse representation." ***Multimedia Tools and Applications***, Vol. 78, No. 15, (2019), 20895–20912. https://doi.org/10.1007/s11042-019-7321-1
4. Romani, L., Rossini, M., and Schenone, D. "Edge detection methods based on RBF interpolation." ***Journal of Computational and Applied Mathematics***, Vol. 349, (2019), 532–547. https://doi.org/10.1016/j.cam.2018.08.006
5. Nasiripour, R., Farsi, H., and Mohamadzadeh, S. "Visual saliency object detection using sparse learning." ***IET Image Processing***, Vol. 13, No. 13, (2019), 2436–2447. https://doi.org/10.1049/iet-ipr.2018.6613
6. Sun, J., Gu, D., Chen, Y., and Zhang, S. "A multiscale edge detection algorithm based on wavelet domain vector hidden Markov tree model." ***Pattern Recognition***, Vol. 37, No. 7, (2004), 1315–1324. https://doi.org/10.1016/j.patcog.2003.11.006
7. Vinod Kumar, R. S., and Arivazhagan, S. "Region Completion in a Texture using Multiresolution Transforms." ***International Journal of Engineering, Transactions B: Applications***, Vol. 27, No. 5, (2014), 747–756. https://doi.org/10.5829/idosi.ije.2014.27.05b.10
8. Salih, Y. A., and George, L. E. "Dynamic scene change detection in video coding." ***International Journal of Engineering, Transactions B: Applications***, Vol. 33, No. 5, (2020), 966–974. https://doi.org/10.5829/IJE.2020.33.05B.30
9. Maire, M., Arbeláez, P., Fowlkes, C., and Malik, J. "Using contours to detect and localize junctions in natural images." In 26th IEEE Conference on Computer Vision and Pattern Recognition, CVPR, (2008), 1–8. https://doi.org/10.1109/CVPR.2008.4587420
10. Rafsanjani, M. K., and Varzaneh, Z. A. "Edge detection in digital images using Ant Colony Optimization." ***Computer Science Journal of Moldova***, Vol. 23, No. 3(69), (2015), 343–359. Retrieved from https://ibn.idsi.md/ro/vizualizare_articol/40697#
11. Martínez, C. A., and Buemi, M. E. "Hybrid ACO algorithm for edge detection." ***Evolving Systems***, (2019), 1–12. https://doi.org/10.1007/s12530-019-09321-5
12. Gautam, A., and Biswas, M. "Edge Detection Technique Using ACO with PSO for Noisy Image." In Advances in Intelligent Systems and Computing (Vol. 740, pp. 383–396). Springer Verlag. https://doi.org/10.1007/978-981-13-1280-9_36
13. Jayaprakash, A., and KeziSelvaVijila, C. "Feature selection using Ant Colony Optimization (ACO) and Road Sign Detection and Recognition (RSDR) system." ***Cognitive Systems Research***, Vol. 58, (2019), 123–133. https://doi.org/10.1016/j.cogsys.2019.04.002
14. Andersson, T., Kihlberg, A., Sundström, A., and Xiong, N. "Road Boundary Detection Using Ant Colony Optimization Algorithm." In Advances in Intelligent Systems and Computing (Vol. 1074, pp. 409–416). Springer. https://doi.org/10.1007/978-3-030-32456-8_44
15. Asgari, M., Pirahansiah, F., Shahverdy, M., Fartash, M., Prabhu, A. S., Ravichandran, D., Rokhhman, N., Subanar, E. W., Marlisah, E., Yaakob, R., and Sulaiman, M. N. "Using an ant colony optimization algorithm for image edge detection as a threshold segmentation for OCR system." ***Journal of Theoretical and Applied Information Technology***, Vol. 95, No. 21, (2017), 5654–5664. Retrieved from https://jatit.org/volumes/ninetyfive21.php
16. Sengupta, S., Mittal, N., and Modi, M. "Improved skin lesion edge detection method using Ant Colony Optimization." ***Skin Research and Technology***, Vol. 25, No. 6, (2019), srt.12744. https://doi.org/10.1111/srt.12744
17. Khan, S., and Bianchi, T. "Ant Colony Optimization (ACO) based Data Hiding in Image Complex Region." ***International Journal of Electrical and Computer Engineering (IJECE)***, Vol. 8, No. 1, (2018), 379–389. https://doi.org/10.11591/ijece.v8i1.pp379-389
18. Anwar, S., and Raj, S. "A Neural Network approach to edge detection using Adaptive Neuro-Fuzzy Inference System." In Proceedings of the 2014 International Conference on Advances in Computing, Communications and Informatics, ICACCI, (2014), 2432–2435. Institute of Electrical and Electronics Engineers Inc.

https://doi.org/10.1109/ICACCI.2014.6968406

19. Pruthi, J., Arora, S., and Khanna, K. "Modified Bird swarm algorithm for edge detection in noisy images using fuzzy reasoning." ***Computer Methods in Biomechanics and Biomedical Engineering: Imaging and Visualization***, Vol. 7, No. 4, (2019), 450–463. https://doi.org/10.1080/21681163.2018.1523751
20. Sezavar, A., Farsi, H., and Mohamadzadeh, S. "A modified grasshopper optimization algorithm combined with CNn for content based image retrieval." ***International Journal of Engineering, Transactions A: Basics***, Vol. 32, No. 7, (2019), 924–930. https://doi.org/10.5829/ije.2019.32.07a.04
21. Shannon, C. E. "A mathematical theory of communication." ***ACM SIGMOBILE Mobile Computing and Communications Review***, Vol. 5, No. 1, (2001), 3–55. https://doi.org/10.1145/584091.584093
22. Skin Lesion image. https://www.dermn etnz.org/topics/. Accessed 11 August 2020.

Persian Abstract

چکیده

جستجو و بهینه‌سازی با استفاده از هوش جمعی روش‌هایی بسیار کارآمدی هستند که می‌تواند برای حل مشکلات پیچیده مهندسی مورد استفاده قرار گیرند. الگوریتم بهینه‌سازی کلونی مورچه مبتنی بر هوش جمعی است که از رفتار مورچه‌ها در یافتن بهترین مسیر در هنگام جستجوی غذا الهام گرفته شده است. در این مقاله از الگوریتم ACO برای تصویر تشخیص لبه استفاده شد. الگوریتم سیستم فازی برای افزایش پویایی و سرعت این الگوریتم پیشنهاد شد. این سیستم میزان فرومون و فاصله را کنترل می‌کند. بنابراین به جای یک مقدار ثابت برای پارامترهای الگوریتم، از مقادیر متغیر استفاده می‌شود تا فضای جستجو دقیق‌تر و منطقی‌تر شود. الگوریتم بهینه‌سازی کلونی مورچه فازی شده روی چندین تصویر پیاده‌سازی و عملکرد الگوریتم پیشنهادی نشان داده شد. نتایج نشان داد که این الگوریتم در استخراج پیکسل‌های لبه، کیفیت بهتری نسبت به روش‌های دیگر تشخیص لبه دارد که منجر به کاهش زمان و آنتروپی می‌شود. بهبود این روش از نظر کمی با بررسی زمان و آنتروپی در مقایسه با روش‌های متداول و کارهای قبلی نشان داده شده است. همچنین نشان دادیم که این روش در برابر نویز از پایداری خوبی برخوردار است.

International Journal of Engineering

Journal Homepage: www.ije.ir

Determining the Composition Functions of Persian Non-standard Sentences in Terminology using a Deep Learning Fuzzy Neural Network Model

H. Motameni*

Department of Computer Engineering, Sari Branch, Islamic Azad University, Sari, Iran

P A P E R I N F O

Paper history:
Received 01 August 2020
Received in revised form 02 September 2020
Accepted 03 September 2020

Keywords:
Nonstandard Sentences
Recurrent Neural Network
Standard Sentences

A B S T R A C T

Organizations can enhance the speed of well-informed decision-making by correctly understanding and using data. Since there is a tremendous gap between the speed of data processing and data generation in the world, exploring data mining in the digital world becomes inevitable. In the Persian language, similar to other languages, with the expansion of communications through social networks, the spelling of words has become abridged and the engagement of foreign loan words and emoticons has been increasing on a daily basis. Given the richness of Persian and its typographical-grammatical similarities to Arabic, research in Persian can be applied to other akin languages as well. In this regard, the current study deals with data mining of Persian non-standard sentences in order to find the function of each word in the sentence. The volume of computation might be limited in traditional methods of natural language processing for each factor contributing to functions. That is because the minimum number of computations is (5 × number of words 9) + (5 × number of words 15). Therefore, this study adopted the Gated Recurrent Unit (GRU) method to process such computations. The newly proposed method reinforces the results of word function identification by using two categories of "independent" and "dependent" Persian language functions as well as five factors contributing to the functions of words in sentences as five output gates. Meanwhile, the values of the training tables in this method are fuzzy, where the center-of-gravity fuzzy method is adopted to decide on the fuzzy values as well as to reduce the complexity and ambiguity of such computations on the probability of each event occurring. Therefore, the new method is briefly called "fuzzy GRU". The results show that the proposed algorithm achieves 80 % reduction in the amount of calculations per gate of updates and reinforcement is approximately 2 % up from 67 % in standard sentences to 69 % of the non-standard sentences.

***doi**: 10.5829/ije.2020.33.12c.06*

1. INTRODUCTION

Also known as Farsi, Persian is spoken officially in several countries including Iran, Afghanistan and Tajikistan. In addition, it is used in a few countries as a second language. Moreover, Persian was remarkably predominant in other Asian and European languages. This language is very much akin to Arabic in terms of alphabet and grammar. These issues have compelled scholars to more than ever explore the Persian language [1]. In the modern age, the expansion of social networks among the public has led to divergence of writing and speech styles in every language, turning phrases into a rather abridged, colloquial form. Therefore, the current study has covered nonstandard sentences of Persian language. One of the most important reasons behind doing such research is that the results are exclusively applicable to a number of linguistic areas such as smart filtering [2], machine translation [3], speech recognition [4, 5], text recognition [6], text summarization [7], etc. The majority of Persian linguistic research projects adopt traditional methods of neural networks. In this regard, our study has used this system to resolve the defects in the previous methods [8, 9] and to benefit from the disambiguation property of fuzzy neural networks. In the newly proposed fuzzy system, center of gravity defuzzification has been employed owing to its versatility and practical advantages [10, 11]. This system

*Corresponding Author Institutional Email: *motameni@iausari.ac.ir* (H. Motameni)

Please cite this article as: H. Motameni, Determining the Composition Functions of Persian Non-standard Sentences in Terminology using a Deep Learning Fuzzy Neural Network Model, International Journal of Engineering, Transactions C: Aspects, Vol. 33, No. 12, (2020), 2471-2481.

relies on Gated recurrent units (GRU) architecture [11] with fuzzy values, because it simply uses 0 and 1, while there are fuzzy training matrix values for deep learning recurrent neural network so that accurate decisions can be made in values [0, 1]. In the recovery gateway section, after sorting in ascending order the values obtained in each section, 80% of the bottom values are discarded and the top 20% are transferred to the next class.

To solve the above problems, this paper makes four contributions:

- The output of this research can be used in all data mining projects mentioned above.
- The method of this research can be used in all Persian-speaking countries and in Arabic-speaking countries.
- The calculation accuracy in the proposed method is 2% higher in standard sentences than in non-standard sentences.
- The proposed method in terms of computational complexity at each stage of the transition from each of the five factors affecting the acceptance of the role is reduced by 80%.

2. LITERATURE REVIEW

This section first delves into linguistics as the original discipline, and then discusses computational linguistics and morphology as two major sub disciplines. The next section describes the new fuzzy system adopted in this paper, while reviewing the relevant literature on fuzzy techniques for Persian. Since the system proposed in this paper is a classified fuzzy system, we will next explain why it has been named so, and generally elaborate on the independent and dependent roles. Finally, nonstandard sentences and words are defined.

2. 1. Linguistics Language is a complex phenomenon, where any precise and comprehensive investigation on a language require knowledge from numerous fields, including sociolinguistics, psycholinguistics, neurolinguistics, forensic linguistics, clinical linguistics, analytical linguistics, educational linguistics, logic, and even computer sciences over the last few decades. Linguistics include the fields of grammar, syntax, phonetics, phonology, semantics, pragmatics, discourse analysis, comparative historical linguistics and typology, reflecting its various dimensions [12, 13]. The definition of linguistics states: "a science that systematically studies language". Thus, a linguist is the one who "conducts linguistic studies" [14].

Studies in the field of linguistics date back several centuries, but the linguistics research in its modern sense is totally recent, barely stretching back to a hundred years [14]. In fact, early studies on language were written in Sanskrit grammar by Indian Pāṇini during the fifth century BC. Later on, William Jones, a British lawyer, conducted significant research into linguistics. Ferdinand de Saussure, a Swedish linguist, established structuralism in linguistics over the first half of the twentieth century [15]. Noam Chomsky (1957) considered transformational grammar as a technique to examine language syntax, where "sentence" is a unit of study for linguistics. Chomsky's linguistic ideas are still popular in North America today. In the 1960s, a rival method to that of Chomsky was introduced with a discourse approach, where sentence is not studied as an independent unit, but as a dependent element within a context. Every text contains three semantic levels: "What is content about?", "How does interaction take place in the Equation of this content?", and the third level examines to what extent sentence (as a textual element) is helpful in formulation of content. This method even views word as text. Hence, text is not restricted to a pre-specified length [15]. Regarding the Persian language, the early research was carried out at the Department of General Linguistics and Ancient Languages, Faculty of Literature and Humanities, Tehran University [15]. The first Persian grammar was developed by the Iranian Linguistics Foundation. In the final years of the 20th century, Bateni conducted a series of studies obtaining a variety of sentence structures through the Persian grammar. He then investigated how each sentence could be converted into other types.

2. 1. 1. Computational Linguistics One of the most fascinating branches of linguistics is known as computational linguistics, which dates back no longer than fifty years. In a definition provided by Dr. Meghdari, computational linguistics refers to an interdisciplinary field consisting of linguistics and computer science, serving to model natural language through statistical and rule-based techniques for machine use [16, 17]. Computational linguistics initially covered only machine translation. In fact, many researchers sought after machine translation from the earliest days of the advent of computers.

This avenue of research was initiated in the 1950s. The first specialized journal on computational linguistics was known as Mechanical Translation published in 1954. Later on, the Association for Computational Linguistics was founded in 1962. Within a few years, the journal's title was revised into Computational Linguistics [18]. Nowadays, computational linguistics is applied in numerous fields and is not limited to machine translation [19, 20].

With respect to computational linguistics in Persian, several scholars such as Dr. Bijankhan and Dr. Shamsfard [21, 22] conducted exclusive research into word formation and construction of machine translators mentioned in [8, 23]. In addition, Iranian universities have taken a giant step in the Persian computational linguistics by admitting new students for this field in

recent years, while establishing several major computational linguistic labs. These labs include Web Technology Laboratory at Ferdowsi University of Mashhad [24], Institute of Humanities and Cultural Studies, Linguistic Research Institute, and the Center for Languages and Linguistics at Sharif University of Technology [16, 19]. Table 1 compares the most important studies in the field of Persian morphology.

In Table 1, the first two rows indicate the earliest and most important researches in the field of Persian corpora construction. In Oxford Dictionary, fuzzy has been defined as "having a frizzy texture or appearance, difficult to perceive; indistinct or vague". In another definition, "Fuzzy systems describe vague, inaccurate, and uncertain phenomena [25]," but this does not mean that the theory is inaccurate; on the contrary, fuzzy theory itself is a precise one. Introduced by Lotfizadeh, the fuzzy system then found its way into Persian linguistics research. It has been used in a limited way and often as a combination with Arabic language. In another study [8, 26], the fuzzy method was adopted to identify composition roles in Persian sentences.

2. 1. 2. Morphology Morphology has been given different definitions. One of the ordinary definitions is "the hybrid study of morphemes and their functions in words". Morphology involves specific steps, because grammar, alphabet, phonemes and speech vary in each language. For instance, morphology in English is different from those in Persian and Arabic [27–29].

2. 2. Recurrent Neural Networks Since, a basis of natural language processing is modeling the language; Recursive neural networks are a method to obtain a model of natural languages [30]. Recursive neural networks are a type of neural network. This type of neural network was presented in 1970, in studies LSTM recurrent neural network method peaked again and today is widely used in the processing of data series. Including these series there are writing, speech, text, meteorological data, etc. that have time series. The reason this neural network is recursive is that an operation is repeated on each series unit. In language processing, these units can be sentence, word, letters, etc. Figure 1 illustrates the recurrent neural network. There exists two traditional return networks namely, LSTM and GRU.

The reason for choosing LSTM method instead of GRU in this research is that the LSTM method in long sentences may be forgotten therefore, the GRU method was used to employ its long-term memory.

In the processing of any language, all input units from the first to the last one affect the results. In methods like LSTM, however, if the sequence is long enough, they will be "forgotten" and can only store the last few inputs in their memory. This problem is rooted in the inability of many traditional conditional methods. In 2014, Chou et al. proposed the GRU Recurrent Neural Network Method, which solved the problem of traditional methods with its long-term memory [11].

2. 3. Independent and Dependent Roles The Persian sentence roles include two independent and dependent categories. The independent roles include subject, predicate, object, complement and verb. The dependent roles include noun, adjective, genitive, governing genitive, dependent adverb, apposition, governing transducer, bending, retroactive exclamation and annunciator [14, 31]. Independent roles in Persian deal with the position of words in every sentence. As the name suggests, each independent role is applied without any dependence on another role. For this reason, we call these roles independent in Persian language sentences. Independent roles are also known as *primary* because they adopt the main position of words in Persian sentences [31]. Dependent roles are called so because they are applied in pairs. In this category of roles, the dependent pairs in a Persian sentence include noun-adjective, genitive-governing genitive, dependent adverb-verb/other role/sentence, apposition-governing transducer, bending-retroactive, and exclamation-annunciator. This structure, however, is not always true, since a sentence may show only one pair of dependent

TABLE 1. Comparison of morphological research

Researcher	Methodology	Advantages	Disadvantages
Bijankhan el al. [21]	Eagles standard	One of the basic Persian morphological corpora	Tagging words and constructing corpora merely based on word types, nonstandard corpora textual documents, eagles-based methodology
Assi and Abdolhosseini [23]	Manual	One of the basic Persian colloquial morphological corpora	Tagging words and constructing corpora merely based on word types, nonstandard corpora textual documents, manual methodology
Motameni and Peykar [8]	Fuzzy HMM	Using fuzzy system to determine word roles	Tagging standard sentences, high computational complexity
Motameni et al. [25]	Classified fuzzy	Low computational complexity, determining word roles, using fuzzy system	Only tagging standard sentences

roles. A few of paired roles are more frequently seen than others. Therefore, this paper divided the dependent roles into two subcategories: 1) dominant (noun, adjective, genitive, governing genitive and dependent adverb), and 2) rare (apposition, governing transducer, focused, exclamation, and annunciator) [31].

2. 4. Nonstandard Sentences and Words Given the increasing popularity of media and social networks, textual materials have been truncated or mistyped, sometimes transforming the formally established version of writing styles. It has therefore become critical to process such sentences in morphological applications. Generally speaking, there are several types of nonstandard sentences in every language.

1- Sentences with truncated words
2- Sentences with incorrect grammar
3- Sentences with loan words
4- Sentences with slang terms and emoticons,

which are senseless in the standard form.

This paper intended to investigate nonstandard sentences in 72 differently formulated sentences, while achieving the proper combination with the input sentence through classified fuzzy method [26].

3. PROPOSED METHOD

This study examines five different effective linguistic units adopting the role of words in the sequence of words and sentences. In each unit, specific fuzzy computations are frequently implemented on the sequences. In order to implement research in that procedure (i.e. a sequence of input units with variable lengths), the best possible method involves deep learning recurrent neural network. Each deep learning neural network has three gates (forget gate, update gate/input gate and output gate). One advantage of this method is that processing load is lower than that of in the method proposed in [8]. The new method proposed in this paper curtails the extent of computations in each class while enhancing the detection rate. By complying with the order of importance for each word adoption factor, it also improves the detection quality of word roles. Therefore, the novelty of the newly proposed method is that the fuzzy method is classified and the success rate has increased. In this paper, we first extract the two-dimensional arrays or matrices required for processing. Then, considering the success rate in finding the roles, the best combination of fuzzy classification is extracted in each array. In each of these classes, the results of possible role adoptions are arranged in ascending order. Then, 20% of the cases with the largest values are transferred to the next step, while the bottoms 80% are removed.

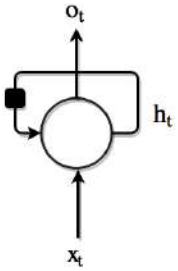

Figure 1. Recurrent neural network loop

Initially, we examined five major matrices processed in different fuzzy classes separately in 72 types of sentence structures. Then, we obtained the best possible composition. Section 2.3 provides 72 types of Persian sentences with different grammatical compositions of nonstandard sentences. In addition to the input sentences, their decompositions were imported into the system. Hence, the sentence decomposition was conducted through NLP Tools v 1.3.3 [24] or other similar software programs. In matrices dealing with alphabetical letters, a total of 44 Persian characters were covered In matrix dimensions, 21 represents the number of roles, i.e. 18 independent and dependent roles and 3 spacing characters. In addition, 10 in the matrix dimension indicates seven Persian word types plus three spacing characters.

3. 1. Sentence Formulation Scenarios In independent roles, there are $9^{\text{count of words in the input sentence}}$ number of possible composition scenarios. In this regard, the 9 represents the number of independent roles and spacing characters in Persian sentences (verb, letter, subject, predicate, object, complement and spacing character).

In dependent roles, there are $15^{count\ of\ words\ in\ the\ input\ sentence}$ number of possible composition scenarios. In this regard, the 15 indicates the number of dependent roles and spacing characters in Persian sentences (adjective, noun, adverb, unknown, apposition, governing transducer, bending, retroactive exclamation and annunciator).

3. 2. Training Matrices This section introduces the five main training matrices used to make decisions in the newly proposed method. Each of these arrays is obtained from 194 training sentences containing 76,274 words.

These five matrices have been summarized below:

A) Additional roles appearing after each role in sentences. Bi_gram_Combine: This is a two-dimensional matrix with 21x21 elements. This matrix determines the probability of each role occurring after another role (Bi-gram) in 194 Persian sentences.

$$1 \le Bi\_gram\_combine_{l.l+1}(k.j) \ge 0.1 \le k \le 21.1 \le j \le 21 \quad (1)$$

$$Bi\_gram\_Combine(k.j) = \prod_{i=1}^{count\ of\ (j)} Bi\_gram\_Combine_{i.i+1}(k.j)$$

In Equation (1), *i* indicates the word counter, *K* is the row counter, while *j* is the column counter. The value of Bi_gram for each word is a number between zero and one.

B) Composition role following each type of decomposition Transfer_Bi_gram: This matrix also functions as a transition from decomposition into composition. For the purpose of decomposition and composition, a total of 194 types of training sentences were tagged manually by experts. At the next step, data was inserted into a 10×21 table.

$$\text{Multiplication of jth roles placed after the ith type} \geq 0.1 \leq i \leq 10\ .1 \leq j \leq 21 \quad (2)$$

$$Transfer\_Bi\_gram(i,j) = \prod_{i=1}^{\text{count of (j)}} \text{Multiplication of jth roles placed after the ith type}$$

In Equation (2), *i* indicates the word type counter, while *j* indicates the word role counter.

C) Composition role in each type of decomposition (Transfer_Uni_gram): This can be considered as transition matrix, because it delivers the moment of transition (instead of word role in composition applied in each word type in decomposition). This is a 21×10 matrix. This 21×10 matrix can be obtained in 194 training sentences by tagging the decomposition and the composition values. Then, the production of multiplication indicates the mean of values as in Equation (3).

$$\text{Average value of jth roles replacing the jth type} \geq 0.1 \leq i \leq 10\ .1 \leq j \leq 21 \quad (3)$$

$$Transfer\_Uni\_gram(i.j) = \prod_{l=1}^{\text{count of (j)}} \text{Average value of jth roles replacing the jth type}$$

where, *i* is a word position counter, while *j* is the word role counter in the two-dimensional matrix.

D) Word-forming letters (Len_Word): The words weight matrix was obtained according to the letters in input sentences. These matrices contain 21×number_of_words elements, which is why we applied bi_gram tagging. Firstly, 76274 words are checked to see what character has followed another character in what percentage of words for each role. Divided by the total number, a numerical value from zero to one is obtained. Hence, Len_Bi_gram is extracted for each role, where the 44x44 array is a cell as large as the characters under examination. After obtaining the Len_Bi_gram matrix for each role with regard to the input sentence, the Len_Word matrix is extracted using Equation (4).

$$\text{Len\_Bi\_gram}_j(k) \geq 0 \text{ and } 1 \leq j \leq N \text{ and } 1 \leq k \leq M \quad (4)$$

$$\text{Len\_Bi\_gram}(k.j) = \prod_{i=1}^{\text{count of (j)}} \text{Len\_Bi\_gram}_{i.i+1}(k.j)$$

As can be seen, i indicates the letters counter, the weight of *j*th word, including *K*th, was computed through bi-gram tagging. In each M-sentence input, there are *N*-word items. In Equation (4), the product of multiplying the occurrence value for each letter with the next letter continues as long as the total number of letters in a word.

E) Position of each word according to the number of sentence words. Member_Word: This matrix indicates the probability of occurrence for each word in a particular position according to its length. First, a matrix trainer is extracted in 194 sentences. In each N-word sentence, each role is observed in a small percentage of cases. Then, the Member_Word matrix of that sentence is obtained according to the length of the input sentence and Equation (5).

$$Member(k.j) \geq 0\ and\ 1 \leq k \leq M \quad (5)$$

$$Member\_Word(k) = \prod_{i=1}^{count\ of\ (j)} Member_{i.i+1}(k)$$

Equation (5) delivers the membership rate of the *k*th sentence from the M-sentence, i indicates the words counter in sentence, including the length of each *N*-length sentence. This matrix is a Bi-gram tagging type.

3. 3. Order of Steps Each training matrix is implemented individually on the input data tested. Once the computations are completed, the success percentage values from each learning matrix, i.e. degree of importance for each training matrix, is obtained. Then, this arrangement is used in the fuzzy GRU steps.

Table 2 provides the success rate for each matrix through a classified fuzzy method from 72 random nonstandard sentences sorted in descending order. In the fuzzy computational section, the sequence of steps for the new fuzzy method can be found in Table 2. Figure 2 compares the success rates of matrices in two standard and nonstandard sentences. In Table 2, the highest success rate with the Bi_gram_combine matrix and with less than 2 % difference, the Transfer _ Bi _ gram matrix is in the second place.

TABLE 2. Order of fuzzy computation classes

No.	Matrix	Success percentage with nonstandard input sentences
1	Bi_gram_combine	66.77%
2	Transfer_Bi_gram	65.14%
3	Transfer_Uni_gram	63.84%
4	Len_Bi_gram_Word	58.95%
5	Member_Word	57.65%

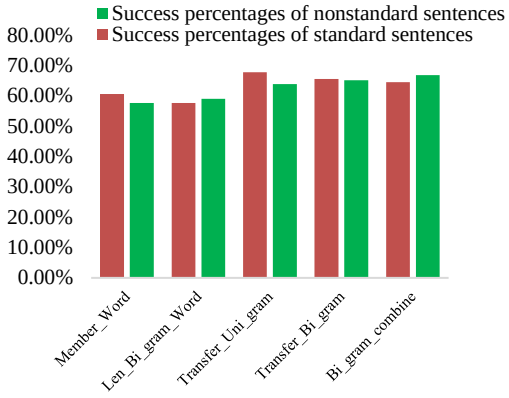

Figure 2. Comparison of success rate in standard and nonstandard input sentences [31]

According to the results in Table 2, the order of 5 steps for the newly proposed computational method is obtained as shown in Figure 2. This arrangement of standard sentences is different from that of nonstandard sentences.

3. 4. Fuzzy GRU Computations The proposed method has been implemented using Visual Studio 2012. Furthermore, the statistics are calculated using Excel 2013 and the results are converted to SQL server 2008. The steps of the proposed method come with a simple format of fuzzy GRU computations illustrated in Figure 3.

The components of Figure 3 are as follows:

C(t-1): The main input in these computations is the output values of the previous steps, where the current step is actually the remaining states of the previous step. In the first step, the value of this input is a matrix to the number of all possible states as well as the array of corresponding values.

C(t): The output of each array step is as long as 20% of the remaining state of the fuzzy computations, which obtained the highest values from the current step computations, as well as the array of possible states values with the same length.

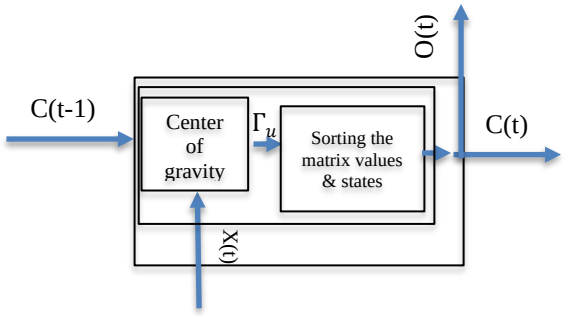

Figure 3. Overall steps of the proposed fuzzy GRU method

X(t): is the values of matrices training in each class, the user's input sentences, and the decomposition of the input sentences.

O(t): indicates removing bottom 80% of possible sentence formulation scenarios as well as reducing 80% of the array length of possible values and array of possible states.

Γ_u: updates gate varies in each class. It updates the array table for sentence states through the center of gravity method after receiving 20% of the highest values of the previous step, the matrix values of the current class and the input sentence states, user's input sentences, as well as the decomposition of input sentences.

According to Table 2, the fuzzy GRU algorithm will be similar to the proposed algorithm. The remarkable point in the new algorithm is that the values are arranged from largest to smallest at each step after computing the roles of possible scenarios. In this procedure, 20% of cases with the highest values are passed to the next step, while discarding the rest.

Proposed algorithm-Classified fuzzy proposed method

1. Obtain the Transfer_Uni_gra, Transfer_Bi_gram,
2. Obtain Bi_gram_Combine, Member_Word, and Len_Word matrices according to the input sentence and the word input composition.
3. Obtain the number of possible states for the input sentence and screening it according to the pair of roles and the composition inserted into the system.
4. Start the first step by entering all possible states as C(t-1) of the first step.
5. The first step is to enter Bi_gram_Combine matrices and user input sentences and decompose input sentences as X(t).
6. The first step of operation Γ_u as the first step of obtaining the center of gravity for all the remaining states with the Bi_gram_Combine matrix.

$$\text{center of gravity } Bi\_gram\_Combine = \frac{\sum_{i=1}^{1-\text{word number}} \text{Bi\_gram\_combine}(the\ role\ of\ \text{i}-1\ th\ word, role\ of\ ith\ word) \times \text{placeof i th word})}{\sum_{i=1}^{1-\text{word number}} \text{place of i th word}} \quad (6)$$

In Equation (6), i indicates the words counter in sentence and indicates how the center of gravity for each input sentence is computed using the membership matrix in the fuzzy decision-making process.

7. The second step of operation Γ_u in the first step: Descending order of possible states and values of possible states.
8. Separate 20% of the largest possible sentence formulation states with maximum values, send those states to the output as C(t) and remove other possible states as O(t) of the current step.
9. Start the second step by inserting C(t-1) as the output of the first step.
10. The second step is to enter the Transfer_Bi_gram matrix and user input sentences and decompose input sentences as X(t).

11. The second step of operation Γ_u in the second step: Obtain the center of gravity for all input states with the Transfer_Bi_gram matrix.

The center of gravity for the matrix values is employed according to the input sentence, the sentence input type and the position of words in each sentence in each of the remaining cases through Equation (7).

$$\text{center of gravity } transfer\_Bi\_gram = \frac{\sum_{i=1}^{1-\text{word number}} (Bi\_gram\_combine(\text{role of i+1th word, type of i th word}) \times \text{placeof i th word})}{\sum_{i=1}^{1-\text{word number}} \text{place of i th word}} \quad (7)$$

Note: Since Bi_gram tagging has been used in Equation (7), the counter changes from the first word to the last remaining word.

12. The second step of operation Γ_u in the second step: Descending order of possible states and values of possible states.

13. Separate 20% of the largest possible sentence formulation states with maximum values, send those states to the output as C(t) and remove other possible states as O(t) of the second step.

14. Start the third step by inserting C(t-1) as the output of the second step.

15. The second step is to enter the Transfer_Uni_gram matrix and user input sentences and decompose input sentences as X(t).

16. The second step of operation Γ_u in the third step: Obtain the center of gravity for all remaining states with the Transfer_Uni_gram matrix according to Equation 8.

$$\text{Center of gravity } Transfer\_\text{uni\_gram} = \frac{\sum_{i=1}^{\text{word number}} \left(Uni\_\text{gram\_combine}(\text{role i th word and type of i th word}) \times \text{place of i th word}\right)}{\sum_{i=1}^{\text{number of words}} \text{place of i th word}} \quad (8)$$

In Equation (8), i indicates the words counter in sentence and indicates how the center of gravity is computed for each input sentence using the Uni_gram_Combine matrix in the fuzzy decision-making process.

17. The second step of operation Γ_u in the third step: Descending order of possible states and values of possible states.

18. Separate 20% of the largest possible sentence formulation states with maximum values, send those states to the output as C(t) and remove other possible states as O(t) of the third step.

19. Start the fourth step by inserting C(t-1) as the output of the second step.

20. The fourth step is to enter the Len_Word matrix and user input sentences and decompose input sentences as X(t).

21. The second step of operation Γ_u in the fourth step: Obtain the center of gravity for all remaining states with the Len_Word matrix.

$$\text{center of gravity } Len\_Word = \frac{\sum_{i=1}^{\text{word number}} (\text{Length of i th word} \times \text{place of ith word})}{\sum_{i=1}^{\text{word number}} \text{place of ith word}} \quad (9)$$

In Equation (9), i indicates the words counter in sentence and displays how to calculate the center of gravity for the word weights according to the resulting Len_Bi_gram and the center of gravity defuzzifier. Descending order of possible states and values of possible states.

22. The second step of operation Γ_u in the fourth step: Descending order of possible states and values of possible states.

23. Separate 20% of the largest possible sentence formulation states with maximum values, send those states to the output as C(t) and remove other possible states as O(t) of the fourth step.

24. Start the fifth (last) step by inserting C(t-1) as the output of the fourth step.

25. The fifth step is to enter Member _Word matrix and user input sentences and decompose input sentences as X(t).

26. The second step of operation Γ_u in the fifth step: Obtain the center of gravity for all remaining states with the Member_Word matrix.

$$\text{center of gravity } member = \frac{\sum_{i=1}^{\text{word number}} (\text{membership of i th word} \times \text{place of i th word})}{\sum_{i=1}^{\text{word number}} \text{place of i th word}} \quad (10)$$

In Equation (10), i indicates the words counter in sentence and indicates how the center of gravity for each remaining sentence is computed using the membership matrix in the fuzzy decision-making process.

27. The second step of operation Γ_u in the fifth step: Descending order of possible states and values of possible states.

28. Obtain the largest value of the remaining values and the corresponding state. Send that state to the output as the roles of that input sentence.

As can be seen in the newly proposed algorithm, the computational load in the new method in each step was curtailed by 80% compared to its previous class. These matrices contain fuzzy values requiring no fuzzification tools. In contract, matrices in fuzzy morphological techniques (e.g. [17]) are first fuzzified with complex sequences. In this respect, the newly proposed method offers an optimal computational load.

Therefore, the quasi-code of the newly proposed algorithm can be considered as follows: Algorithm 1- Recurrent Neural Networks with Gated Recurrent Unit

```
1.  Function Sort_As(Matrix_Method by val
    ,MatrixASe_InDe by ref, MatrixSe_InDe by ref,
    MatrixASe_De by ref, MatrixSe_De by ref)
2.  {
3.  MatrixASe_InDe =Make Matrix_Method
    with Pos_word && MatrixSe_InDe;
4.  MatrixASe_De =Make Matrix_Method with
    Pos_word && MatrixSe_De;
5.  Sort Ascending MatrixASe_InDe &&
    MatrixSe_InDe , MatrixASe_De &&
    MatrixSe_De ;
6.  Get Twenty percent of the largest numbers:
```

```
    MatrixASe_InDe && MatrixSe_InDe,
    MatrixASe_De && MatrixSe_De;
7.  Return MatrixASe_InDe && MatrixSe_InDe,
    MatrixASe_De && MatrixSe_De;
8.  }
9.  Const Matrixes:
    Transfer_Uni_gram،Transfer_Bi_gram ،
    Bi_gram_Combine ،Member_Word و Len_Word;
10. Input Se: Get sentences from the user;
11. Input ASe: Get analyses for Sentences from the user;
12. Begin
13. For  i=1 to Len(Sentences)
14. Set  MatrixSe_InDe (15^Len(SE[i]))
    &&MatrixSe_De (9^Len(SE[i])) as string;
    //Matrix for status of Independent and
    dependent Roles
15. Set MatrixASe_InDe(15^Len(SE[i])) &&
    MatrixASe_De(9^Len(SE[i])) as single;
    //Matrix for Value_status of Independent
    and dependent Roles
17. Get All Value in Matrix: MatrixSe_InDe,
    MatrixASe_InDe, MatrixSe_De,
    MatrixASe_De;
18. Call Sort_As (COG_Bigram_combine,
    MatrixASe_InDe , MatrixSe_InDe,
    MatrixASe_De , MatrixSe_De) //eq6-Step1
19  Call Sort_As (COG_Transfer_Bigram,
    MatrixASe_InDe , MatrixSe_InDe,
    MatrixASe_De , MatrixSe_De) //eq7-step2
20  Call Sort_As (COG_Transfer_Uni_gram,
    MatrixASe_InDe , MatrixSe_InDe,
    MatrixASe_De ,
    MatrixSe_De) //eq8-step3
21. Call Sort_As (COG_Len_Word ,
    MatrixASe_InDe , MatrixSe_InDe,
    MatrixASe_De , MatrixSe_De) //eq9-step4
22. Call Sort_As (COG_Member_Word,
    MatrixASe_InDe , MatrixSe_InDe,
    MatrixASe_De , MatrixSe_De) //eq10-step5
23. Next i
24. Output : MatrixSe_InDe(1) , MatrixSe_De(1);
25. End
```

4. RESULTS

In addition to the roles provided in Section 3, there are "verb-letter" roles, which were discarded because of their shared decomposition and composition.

$$\text{Success percentages} = \frac{\text{Success} \times 100}{Total} \quad (11)$$

Relying on Equation (11), we obtained the success rate in each section. The *total number* in Equation (11) changes in each section. In addition, the *success rate* in this regard varies according to each section.

4. 1. Overall Success Rate in Persian Sentences Composition The test results in this method indicates that the fuzzy classified overall success rate in nonstandard sentences is 68.73% in all roles. In standard sentences, however, the success rate is 67% in identification of all roles. In this case, the new fuzzy method outperformed by roughly 2%.

Therefore, in 72 nonstandard sentences inserted into the system to test the newly proposed method, 211 out of 307 roles are correctly detected. In Equation (11), 307 is inserted for Total Number, while 211 is inserted for Success Rate, which together deliver Figure 4.

4. 2. Success Percentage in Independent Roles Among 307 roles in 72 sentences, 152 of them were related to independent roles. Of the 152 independent roles in nonstandard sentences, the tests suggested that 110 were correctly detected, with a success rate of 72.37% based on Equation (11) (Figure 4). In the standard sentences, however, the success rate was approximately 70% in 106 cases. Figure 5 illustrates the values.

If we want to examine the roles separately and calculate the success rates (according to Equation (11)), Table 3 is obtained.

As can be seen, the highest success rate in nonstandard input sentences is *predicate*, whereas this role assumes the lowest value in standard sentences.

Figure 6 compares the success rates of two sentence structures in the independent role category. As for *subject*, the success values for the two role categories

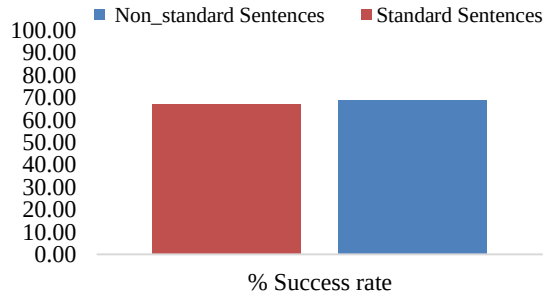

Figure 4. The success rates of standard and nonstandard sentences in general [26]

Figure 5. The success rates of independent and dependent roles in two types of standard input [26] and nonstandard sentences

TABLE 3. Success rates for independent roles of standard and nonstandard input sentences [26]

Independent roles	Success percentages of independent roles in nonstandard sentences	Success percentages of independent roles in standards sentences
Predicate	75.76	60.61
Subject	72.53	73.63
Object	66.67	61.11
Complement	70	80.00

were roughly equal. Only in *complement*, the success rates of standard sentences are higher than those of nonstandard sentences.

4. 3. Success Percentage in Dependent Roles

Among 307 roles in 72 sentences, 155 of them were related to dependent roles. Of 155 dependent roles in nonstandard sentences, 101 cases were correctly obtained. According to Equation (11), success rate was 65.16% for nonstandard sentences. This value is 64.52% for standard sentences, which has been compared in Figure 5.

If we want to examine the roles separately, Table 4 is obtained based on Equation (11).

Some words in Persian sentences may not take any dependent roles. Alternatively, the new method may not identify any roles for certain words, thus sending *unknown* to output.

Table (4) displays the success rate for each of the 12 dependent roles in both standard and nonstandard Persian sentence inputs. Rows 1 to 6 indicate frequently used dependent roles in Persian sentences, while rows 7 to 12 cover roles less commonly found in Persian sentences. As shown in Table (4), the highest success values in most frequently used roles were achieved in nonstandard sentences. In less commonly used roles except for *bending*, however, the success values were equal.

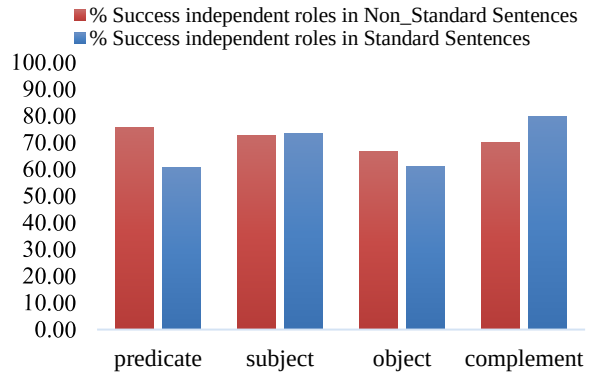

Figure 6. The success rate of each independent role in two types of standard [26] and nonstandard sentences

TABLE 4. The success rates of dependent roles in both standard [26] and nonstandard sentences

No.	Independent and dependent roles	Success percentages of independent roles in nonstandard sentences	Success percentages of independent roles in standards sentences
1	Adjective	33.33	55.56
2	Noun	54.55	72.73
3	Adverb	96.55	89.66
4	N.A.	57.14	61.22
5	Governing genitive	76.92	46.15
6	Genitive	76.92	46.15
7	Apposition	100	100
8	Governing transducer	100	100
9	Bending	25	75
10	Retroactive	100	75
11	Exclamation	50	50
12	Annunciator	50	50

Figure 7 compares the success rates of dependent roles in standard and nonstandard Persian sentences. The noteworthy point in this figure is that the success rate decreases because of low presence of the rare roles in Persian sentences (marked in blue/proposed method). For that reason, success rates were 100% and 50% in apposition-governing transducer and exclamation-annunciator, respectively. Another point is that most dependent roles appear in pairs in Persian sentences [31].

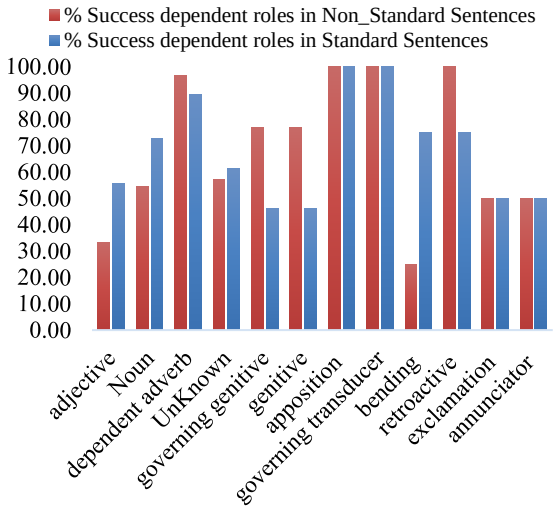

Figure 7. The success rate of each dependent role in two types of standard [26] and nonstandard sentences

5. CONCLUSION AND FUTURE WORK

Considering that the current study covers nonstandard sentences of Persian language, the results obtained by the newly proposed method demonstrate how it provides better results in sentences that barely follow Persian language grammar. Hence, the greater success rate in obtaining sentence roles was achieved by standard [26] and nonstandard sentences separately for two categories of independent and dependent roles. Independent roles are better when comparing the success rates of two categories of nonstandard sentence roles. In all independent roles except complement, the success of the proposed method is achieved with nonstandard sentences. Similarly, in all dependent roles except noun, adjective, noun and bending, the proposed method has performed better on nonstandard sentences than standard sentences.

In this paper, the memory of the new fuzzy GRU method allows the researcher to select irregular values relative to the input states. This is because 20% of the highest values in the current step may include the first, middle, last, or *N*th values of the input states (output of the previous step). On the other hand, the fuzzy nature of the newly proposed method allows us to use the fuzzy values of the matrices obtained using statistical methods to train the possible states desirably.

Reducing the computation of steps in different steps of this algorithm is one of the most important advantages compared to [8]. When employing the fuzzy method [8], if the amount of computations for each class is 100,000, the total will be 500,000, while it is exactly 124960 in the fuzzy GRU. In fact, there is nearly as much as $\frac{4}{5}$ reduction in computations compared to [8]. Therefore, further investigation and research in the field of neural network computing, deep fuzzy recurrent learning can provide Persian-Arabic language linguists with clear results for this topic from the data mining progress. In this regard, one of the areas to be covered in future research is that, the sequence of steps 2-3 in each of the independent and dependent roles can be obtained separately and the results can be discussed.

Moreover, the research will adopt the second fuzzy type in order to take advantage of the uncertainty of this method and ultimately enhance the results.

6. REFERENCES

1. "Persian language, Encyclopædia Britannica.", Written by The Editors of Encyclopaedia Britannica, Retrieved from https://www.britannica.com/topic/Persian-language
2. Alshammari, M., Nasraoui, O., and Sanders, S. "Mining Semantic Knowledge Graphs to Add Explainability to Black Box Recommender Systems." ***IEEE Access***, Vol. 7, (2019), 110563–110579. https://doi.org/10.1109/access.2019.2934633
3. Heo, Y., Kang, S., and Yoo, D. "Multimodal Neural Machine Translation with Weakly Labeled Images." ***IEEE Access***, Vol. 7, (2019), 54042–54053. https://doi.org/10.1109/ACCESS.2019.2911656
4. Wu, B., Li, K., Ge, F., Huang, Z., Yang, M., Siniscalchi, S. M., and Lee, C. H. L. "An end-to-end deep learning approach to simultaneous speech dereverberation and acoustic modeling for robust speech recognition." ***IEEE Journal on Selected Topics in Signal Processing***, Vol. 11, No. 8, (2017), 1289–1300. https://doi.org/10.1109/JSTSP.2017.2756439
5. Vani, H., and Anusuya, M. "Fuzzy Speech Recognition: A Review." ***International Journal of Computer Applications***, Vol. 177, No. 47, (2020), 39–54. https://doi.org/10.5120/ijca2020919989
6. Keysers, D., Deselaers, T., Rowley, H. A., Wang, L. L., and Carbune, V. "Multi-Language Online Handwriting Recognition." ***IEEE Transactions on Pattern Analysis and Machine Intelligence***, Vol. 39, No. 6, (2017), 1180–1194. https://doi.org/10.1109/TPAMI.2016.2572693
7. Jayashree, R., Murthy, S. K., and Sunny, K. "Keyword extraction based summarization of categorized Kannada text documents." ***International Journal on Soft Computing***, Vol. 2, No. 4, (2011), 81–93. https://doi.org/10.5121/ijsc.2011.2408
8. Motameni, H., and Peykar, A. "Morphology of compounds as standard words in Persian through hidden Markov model and fuzzy method." ***Journal of Intelligent and Fuzzy Systems***, Vol. 30, No. 3, (2016), 1567–1580. https://doi.org/10.3233/IFS-151865
9. Graves, A. "Generating Sequences With Recurrent Neural Networks." arXiv:1308.0850, Vol. 5, (2014), 1–43. Retrieved from http://arxiv.org/abs/1308.0850
10. Dim Lam, C., and Khin Mar, S. Joint Word Segmentation and Part-of-Speech Tagging for Myanmar Language, PhD Dissertation, University of Computer Studies, Yangon. Retrieved from http://onlineresource.ucsy.edu.mm/handle/123456789/2530
11. Chung, J., Gulcehre, C., Cho, K., and Bengio, Y. "Empirical Evaluation of Gated Recurrent Neural Networks on Sequence Modeling." arXiv:1412.3555, (2014). Retrieved from http://arxiv.org/abs/1412.3555
12. Obin, N., and Lanchantin, P. "Symbolic modeling of prosody: From linguistics to statistics." ***IEEE Transactions on Audio, Speech and Language Processing***, Vol. 23, No. 3, (2015), 588–599. https://doi.org/10.1109/TASLP.2014.2387389
13. Shin, Y., and Xu, C. Intelligent systems: modeling, optimization, and control. CRC press, 2017.
14. Natel Khanlari, P. "Linguistics and Persian Language." Tehran: Toos Publication, 1987.
15. Li, F. K. "A Short History of Linguistics, R. H. Robins." ***American Anthropologist***, Vol. 70, No. 6, (1968), 1186–1186. https://doi.org/10.1525/aa.1968.70.6.02a00210
16. Moniri, M. "Fuzzy and intuitionistic fuzzy turing machines." ***Fundamenta Informaticae***, Vol. 123, No. 3, (2013), 305–315. https://doi.org/10.3233/FI-2013-812
17. Taheri, A., Meghdari, A., Alemi, M., and Pouretemad, H. R. "Teaching music to children with autism: A social robotics challenge." ***Scientia Iranica***, Vol. 26, No. 1, (2019), 40–58. https://doi.org/10.24200/sci.2017.4608
18. Mitkov, R. The Oxford handbook of computational linguistics, Oxford University Press, 2004.
19. Tatar, D. "Word Sense Disambiguation by Machine Learning Approach: A Short Survey." ***Fundamenta Informaticae***, Vol. 64, No. 1–4, (2005), 433–442.
20. Hinrichs, E. W., Meurers, W. D., and Wintner, S. "Linguistic Theory and Grammar Implementation: Introduction to this Special Issue." ***Research on Language and Computation***, Vol. 2,

No. 2, (2004), 155–163. https://doi.org/10.1023/b:rolc.0000016748.09606.a9

21. Bijankhan, M., Sheykhzadegan, J., Bahrani, M., and Ghayoomi, M. "Lessons from building a Persian written corpus: Peykare." ***Language Resources and Evaluation***, Vol. 45, No. 2, (2011), 143–164. https://doi.org/10.1007/s10579-010-9132-x
22. Shamsfard, M., Ilbeygi, M., and Sadat Jafari, H. "STeP-1: A Set of Fundamental Tools for Persian Text Processing." In Proceedings of the Seventh International Conference on Language Resources and Evaluation (LREC'10), (2010), 859–865. Retrieved from https://www.researchgate.net/publication/220746093
23. Assi, S. M. "Grammatical Tagging of a Persian Corpus." ***International Journal of Corpus Linguistics***, Vol. 5, No. 1, (2000), 69–81. https://doi.org/10.1075/ijcl.5.1.05ass
24. Natural Language Processing Software of Ferdowsi University of Mashhad Version 1.3.(persian)," Web Technology Lab of Ferdowsi University of Mashhad, Mashhad, 2012.
25. Safari, A., Hosseini, R., and Mazinani, M. "A Novel Type-2 Adaptive Neuro Fuzzy Inference System Classifier for Modelling Uncertainty in Prediction of Air Pollution Disaster." ***International Journal of Engineering, Transactions B: Applications***, Vol. 30, No. 11, (2017), 1746–1751. https://doi.org/10.5829/ije.2017.30.11b.16
26. Sadeghi, H., Motameni, H., Ebrahimnejad, A., and Vahidi, J. "Morphology of composition functions in Persian sentences through a newly proposed classified fuzzy method and center of gravity defuzzification method." ***Journal of Intelligent and Fuzzy Systems***, Vol. 36, No. 6, (2019), 5463–5473. https://doi.org/10.3233/JIFS-181330
27. Haspelmath, M., and Sims, A. Understanding morphology, London: Hodder Education and Hachette UK Company, 2010.
28. Geeraerts, D., and Cuyckens, H. The Oxford Handbook of Cognitive Linguistics. Oxford University Press, 2007. https://doi.org/10.1093/oxfordhb/9780199738632.001.0001
29. Perry, J. R. "Persian Morphology." In Morphologies of Asia and Africa, Winona, EIS - Eisenbrauns, (pp. 975–1019), 2007.
30. Amidi, A., Amidi, S., 'Super VIP Cheatsheet: Machine Learning,' https://stanford.edu/~shervine/, stanford, 2018.
31. Peykar, A. Pars Process Persian sentence analyzer software, Gorgan: Golestan University, Faculty of Basic Sciences, 2011.

Persian Abstract

چکیده

سرعت روبه‌رشد ورود املای کلمات مختصر و حضور کلمات خارجی و شکلک‌ها در زبان فارسی اهمیت پژوهش‌های داده‌کاوی در این زبان را دوچندان می‌سازد، از طرفی تشابه املایی–دستوری زبان فارسی به عربی نشان دهنده‌ی آن است که می‌توان در سایر زبان‌های مشابه نیز از این پژوهش استفاد کرد. در این راستا این پژوهش به داده‌کاوی جملات غیر استاندارد زبان فارسی در جهت یافتن نقش هر کلمه در جمله می‌پردازد. میزان محاسبات با روش‌های سنتی در هر کدام از پنج عامل پذیرش نقش حداقل تعداد محاسبات ((۵×تعدادکلمات ۹)+ (۵×تعدادکلمات ۱۵)) است که ممکن است خارج از توان روش‌های سنتی پردازش زبان‌های طبیعی می‌باشد، بنابراین در این پژوهش از روش GRU برای پردازش این محاسبات استفاده شده است. روش پیشنهادی حاضر با استفاده از دو دسته نقش‌های "مستقل- وابسته" و پنج عامل پذیرش نقش کلمات در جملات به عنوان پنج دروازه ساخت خروجی، نتایج شناسایی نقش کلمات را تقویت می‌بخشد. مقادیر جداول آموزش دهنده‌ی این روش، فازی هستند؛ بنابراین برای تصمیم‌گیری درباره مقادیر فازی و نیز کاهش پیچیدگی و ابهام این محاسبات، از روش فازی مرکزثقل استفاده شده است. به طور خلاصه می‌توان این روش پیشنهادی را "GRU فازی" نامید. نتایج نشان می دهد که روش پیشنهادی، کاهش ۸۰٪ میزان محاسبات در هر دروازه به روزسانی و تقویت تقریبا ۲٪ از ٦٧٪ در جملات استاندارد به ٦٩٪ جملات غیر استاندارد را دارا است.

IJE TRANSACTIONS C: Aspects Vol. 33, No. 12, (December 2020) 2482-2488

International Journal of Engineering

Journal Homepage: www.ije.ir

Improved Distributed Particle Filter Architecture with Novel Resampling Algorithm for Signal Tracking

Z. Talebi[a], S. Timarchi*[b]

[a] *Faculty of Electrical Engineering, Shahid Beheshti University, Tehran, Iran*

[b] *Faculty of Electrical Engineering, Shahid Beheshti University, Tehran, Iran; and School of Computer Science, Institute for Research in Fundamental Sciences (IPM), Tehran, Iran*

PAPER INFO

Paper history:
Received 27 July 2019
Received in revised form 01 September 2020
Accepted 03 September 2020

Keywords:
Particle Filter
Independent Metropolis Hasting Resampling
FPGA
Signal Tracking

ABSTRACT

Resampling is a critical step in Particle Filter (PF) because of particle degeneracy and impoverishment problems. Independent Metropolis Hasting (IMH) resampling algorithm is a robust and high-speed method that can be used as the resampling step in PF. In this paper, a new algorithm based on IMH resampling is first proposed. The proposed algorithm classifies the particles before entering to the resampling module. The classification causes those essential particles are only routed to the IMH resampler. Then we propose a distributed architecture to reduce the execution time and high-speed processing for resampling. Simulation results for tracking a signal indicate that the PF with the proposed resampling architecture has acceptable tracking performance in comparison to other resampling methods. The PF architecture with the novel Improved IMH (IIMH) resampling algorithm has 33% more speed than the best-reported method in PF. Also, the proposed distributed PF architecture achieve 79% more speed compared with the best-reported method in PF. FPGA-based implementation results indicate that the utilization of the proposed IIMH resampling algorithm in PF and also distributed architecture lead to hardware resource and area usage reduction.

***doi**: 10.5829/ije.2020.33.12c.07*

1. INTRODUCTION

Object tracking through multiple cameras is a popular research topic in security and surveillance systems especially when human objects are the target [1]. Utilizing adaptive filters is a dominant solution for visual tracking problems [2]. The signal tracking in Particle Filter (PF) is performed by searching the space of the states with randomly generated samples called particles. PF consists of three steps, 1) particle sampling, 2) weight calculation, and 3) resampling. Without resampling, PF suffered from a degeneracy problem, which means that a few particles with higher weights participate in the resampling and those particles with lower weights will be discarded [3-7]. Resampling, however, may introduce undesired effects. One of them is sample impoverishment.

Two main types of resampling methods used in PF are sequential resampling and compound resampling. Sequential resamplings are standard methods that have high complex computation load. Systematic Resampling (SR) [8-10], Residual Resampling (RR) [11-14], Residual-Systematic Resampling (RSR) [3] are the three most common examples for sequential resampling. Compound resampling operates based on grouping the particles. The grouping can be done by one or more threshold values or based on the ratio between particle weights. The thresholds can be fixed, variable, or adaptive [7].

Independent Metropolis Hasting (IMH) algorithm in one of the robust and high-speed compound resampling methods that works based on the ratio between the particle weights. This method works as soon as the first particle and its corresponding weights are produced and it doesn't wait until whole particles to be generated.

*Corresponding Author Institutional Email: *s_timarchi@sbu.ac.ir* (S. Timarchi)

Please cite this article as: Z. Talebi, S. Timarchi, Improved Distributed Particle Filter Architecture with Novel Resampling Algorithm for Signal Tracking, International Journal of Engineering, Transactions C: Aspects Vol. 33, No. 12, (2020), 2482-2488.

By using multiple Processing Elements (*PEs*) and a Central Unit (*CU*) we can process the particles simultaneously. This is known as Distributed resampling methods. The methods include Centralized resampling, resampling with proportional allocation, resampling with non-proportional allocation and they use two types of resampling, one resampling inside each *PE* called *intra-resampling* and another between two *PEs* called *inter-resampling*.

In this paper, a new IMH algorithm and architecture, called Improved IMH (IIMH) to increase the processing speed in IMH resampler is proposed that is derived from both threshold-based resampling methods and the ratio between the weights. Moreover, Distributed IIMH (DIIMH) architecture with 4 *PEs* to process the particles in parallel is explored in this paper. Results of tracking a random signal show that the proposed IIMH algorithm can have the same accuracy of standard SR. Comparison results of hardware resource utilization and processing speed show that proposed architectures have acceptable performance in comparison to existing efficient methods reported in the literature.

The rest of the paper is organized as follows: In Section 2, a literature review and a brief theory of PF and resampling are presented, and then, we review the IMH and Modified IMH (MIMH) resamplers. In Section 3, the proposed IIMH algorithm and architectures, as well as DIIMH architecture are presented. In Section 4, the comparison and results of the proposed methods are discussed. Section 5 concludes the paper.

2. LITERATURE REVIEW ON PF AND RESAMPLING METHODS

PFs are used for tracking states of dynamic state-space models described by the following equation [8]:

$$x_n = f(x_{n-1}) + u_n; \qquad y_n = g(x_n) + v_n \tag{1}$$

where x_n is the state vector of target position, y_n is a vector of observations, u_n and v_n are independent noise vectors with known distributions. PFs accomplish tracking of x_n by updating a random measure $\{x_{1:n}^{(m)}, w_n^{(m)}\}_{m=1}^{M}$ which is composed of M particles $x_n^{(m)}$ and their weights $w_n^{(m)}$ defined at time instant n, recursively [3]. The random measure a page no. proximates the posterior density of the unknown trajectory $x_{1:n}$, $p(x_{1:n}|y_{1:n})$, where $y_{1:n}$ is the set of observations. After resampling, the next particles are more concentrated in domains of the higher posterior probability. The PF operations are performed according to the following steps:

1. Generation of particles (samples) $x_n^{(m)} \sim \pi(x_n|x_{n-1}^{(t_{(n-1)}^m)}, y_{1:n})$, where $\pi(x_n|x_{n-1}^{(t_{(n-1)}^m)}, y_{1:n})$ is an importance density and $i_n^{(m)}$ is an array of indexes, which shows that the particle m should be reallocated to the position $i_n^{(m)}$;

2. computation of weights by:

$$w_n^{*(m)} = \frac{w_{n-1}^{(t_{(n-1)}^m)}}{a_{n-1}^{(t_{(n-1)}^m)}} \frac{p(y_n|x_n^{(m)})p(x_n^{(m)}|x_{n-1}^{(t_{(n-1)}^m)})}{\pi(x_n^{(m)}|x_{n-1}^{(t_{(n-1)}^m)}, y_{1:n})} \tag{2}$$

3. Resampling $i_n^{(m)} \sim a_n^{(m)}$, where $a_n^{(m)}$ is a suitable resampling function for the particle $x_n^{(m)}$.

Different classifications of resampling methods exist [3, 8, 11]. Recently, Li et al. [7] propose a complete classification for resampling methods. For reducing hardware complexity, the *RR* algorithm offers interesting features for fixed-point implementation presented in literature [5]. The CR architecture consists of two loops. The first loop selects the substantial particles, and the second one multiplies the selected particles sequentially [12].

Recently, most of the researches are tended to distributed architecture for PF. The main reason is to minimize the execution time through paralleling and pipelining of operations.

Most of the resampling algorithms can start only after all particles are generated and then cumulative sum and normalized weights start to be calculated. This fact is a bottleneck in the pipelined implementation. To remove this weakness, some resampling algorithms operate based on the ratio between the weights, like Metropolis Hastings (MH) [13] and IMH algorithm [14]. These methods do not need to normalize weights and therefore they are suitable for parallel processing. The details of the IMH algorithm is described in literature [14]. A Modified IMH (MIMH) algorithm is proposed in literature [15]. In the IMH algorithm, the new particle will be retained when $u < \alpha(\hat{x}_t^{j-1}, x_t^j)$, which can be simplified as follows:

$$u \le \alpha(\hat{x}_t^{(j-1)}, x_t^{(j)}) = min\{\frac{w(x_t^{(j)})}{\hat{x}_t^{(j-1)}}, 1 \le \frac{w(x_t^{(j)})}{\hat{x}_t^{(j-1)}} \tag{3}$$

and this equation in the MIMH algorithm is equal as follows:

$$u \times w(\hat{x}_t^{(j-1)}) \le w(x_t{}^{(j)}) \tag{4}$$

If the weight of the new particle is larger than the product of the uniform random-number u and the weight of the last accepted particle in the chain, the new particle is selected, otherwise, the last accepted particle is repeated once more.

3. PROPOSED IIMH ALGORITHM

3. 1. Proposed IIMH Resampling Algorithm

The proposed IIMH algorithm can be defined as Algorithm 1. In the first step, two threshold values T1 and

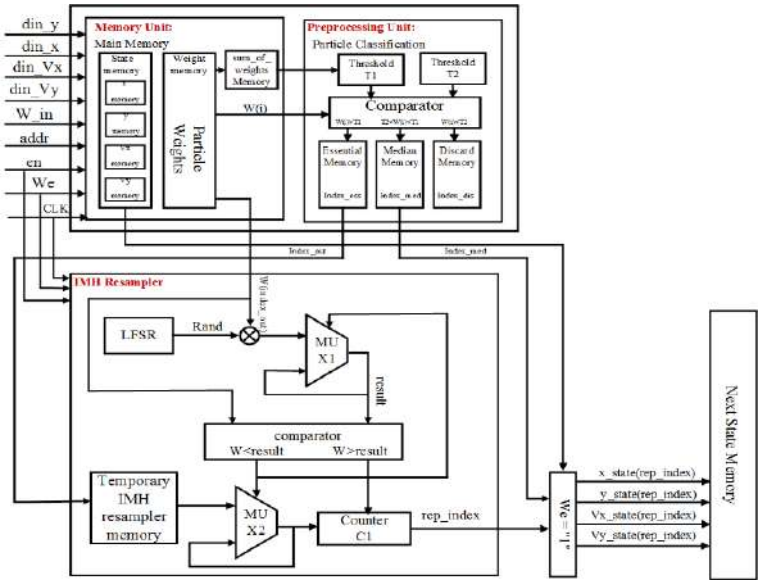

Figure 1. Proposed architecture for IIMH resampling in PF

T2 are calculated. These values are based on particle weights. Then the weight of the particles is compared with the two threshold values in the second step. According to comparison results, the particles are grouped into three different categories as below:

1. Essential particles (N_{ess}): Particles whose weights are greater than $T1$, are assumed as essential particles. These high weight particles are used as inputs of the resampler module.
2. Median particles (N_m): The particles whose weights are less than $T1$ and greater than $T2$ are assumed in this group. These particles are not replicated, but they apage no. ear in outputs of the resampler module. These particles included essential information about the target trajectory.
3. Discarded particles (N_d): These particles whose weights are less than $T2$ are considered as discarded particles. It means that they are low weight particles and don't have any useful information about the trajectory.

After classifying the particles, the indexes of essential particles are used for resampling. In the third step, the first essential particle will be used as an initialized value in the chain. In step 4, a Linear Feedback Shift Register (LFSR) will be used to generate a uniform random number u as a resampling function [16].

Algorithm 1. Proposed IIMH algorithm

$\{\tilde{x}_k^{(j)}\}_{j=1}^{N}$ =IMH-Sampler $\{x_k^{(j)}, w_k^{(j)}\}_{j=1}^{N-N_m-N_d+N_b}$

1. Threshold T1 and T2 calculation:

$$T1 = \frac{\sum_{i=1}^{M} w_i}{M}, \quad T2 = \frac{T1}{2}$$

2. Classify the particles into 3 groups:

$N_{ess}: T1 \le w(i) \quad for \quad i = 1,2,\dots,N$

$N_m: T2 \le w(i) \le T1 \quad for \quad i = 1,2,\dots,N$

$N_d: w(i) \le T2 \quad for \quad i = 1,2,\dots,N$

3. Initialize the chain with $\hat{x}_k^{(1)} = x_k^{(1)}$. The first particle is accepted as seed.

4. For $j = 2,3,\dots,N - N_m - N_d + N_b$

- Calculate the acceptance probability:

$\alpha(\hat{x}_k^{(j-1)}, x_k{}^{(j)}) = \min\{\frac{w(x_k^{(j)})}{w(\hat{x}_k^{(j-1)})}, 1\}$ where $x_k^{(j)}$ represents the new particles, $\hat{x}_k^{(j-1)}$ is the last accepted particle and $w(x_k^{(j)})$ is the associated weight of the particle $x_k^{(j)}$.

- Generate a uniform random-number as a resampling function:

$u \sim u[0,1]$

- Determining the accepted and removed particles:

$$\hat{x}_k^{(j)} = \begin{cases} x_k^{(j)}, & if \quad u \times w(\hat{x}_t^{(j-1)}) \le w(x_t^{(j)}) \\ \hat{x}_k^{(j-1)}, & otherwise \end{cases}.$$

5. Discard the first N_b samples for burn-in particles and keep $N - N_m - N_d$ samples:

$\{\tilde{x}_k^{(j)}\}_{j=1}^{N-N_m-N_d} = \{\hat{x}_k^{(j)}\}_{j=N_b+1}^{N-N_m-N_d+N_b}$

3. 2. Proposed IIMH Resampling Architecture

Proposed IIMH resampling architecture is shown in Figure 1.

The proposed architecture contains a memory unit and a preprocessing unit. Before resampling, the four-element vectors (x, y, V_x, V_y) are loaded into state memory separately and their associated weights are loaded into the weight memory as parts of the memory unit. The weight memory consists of a register file with a size of $M \times w$ for storing the weights of each particle, where w represents the length of weight value.

The preprocessing unit contains the particle classification module, where the two threshold values are calculated as described in the first step of Algorithm 1. As the weights of particles are loaded into weight memory, the cumulative sum of weights is calculated in *sum_of_weights* memory, simultaneously with calculating T1 and T2. As T1 and T2 are calculated, the

weight of the particles is compared with these two threshold values according to the results of the comparison, the particles are loaded in three different memory are named as *Essential memory*, *Median memory*, and *Discard memory*. After classifying the particles, the index of essential particles is routed into the IMH resampler module. Instead of storing four-element vectors of particles in this scheme, their indexes are only stored in the memory and routed in this scheme, because they have a similar addressing index. So memory size $M \times 4$ is substituted by memory with size $M \times 1$.

3. 3. Proposed Distributed Architecture For IIMH

By employing distributed architecture and several *PEs*, the particles are divided and assigned to *PEs* to be processed in parallel. The execution time in distributed architecture for IIMH (DIIMH) would be reduced to the number of *PEs*. By choosing a large number of *PEs*, hardware resource utilization would be increased. So to achieve a trade-off between hardware resource usage and execution time, choosing a page no. proximates number of *PEs* is essential. Figure 2 shows DIIMH architecture with 4 *PEs* and 1 *CU*.

Each *PE* in our architecture is similar to the IMH resampler shown in Figure 1. The function of *CU* is to collect the partial sums of the weights from *PEs* to calculate the output weights and finally perform the *inter-resampling*. If the number of particles produced by each *PE* produces is not equal to the number of the particles that *CU* reports, median particles would be routed to the output of *CU* from $(N_{ess}+1)^{th}$ address of *next_state_memory*.

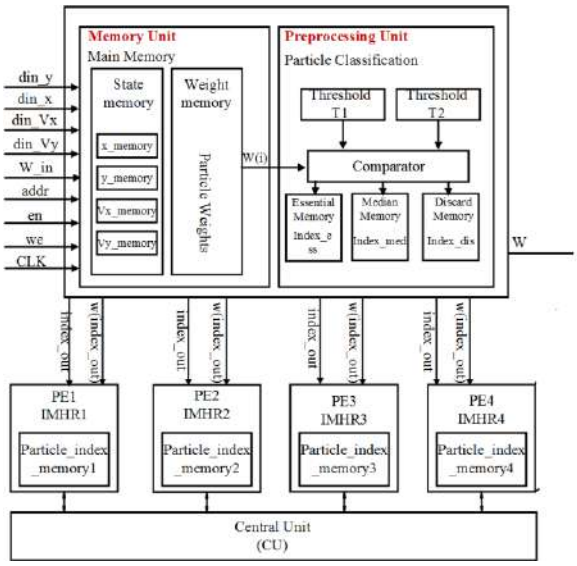

Figure 2. Proposed DIIMH resampler architecture

4. RESULTS AND COMPARISON

4. 1. Signal Tracking Performance The tracking performance of the proposed IIMH resampling algorithm in PF has been studied for random signals. Figure 3 and Figure 4 show the tracking result of the PF with the proposed IIMH algorithm for $\boldsymbol{M = 32}$ and $\boldsymbol{M = 1024}$ particles, respectively.

As we know, tracking a random signal with PF depends on several parameters. One of the most important factors is the number of particles. It can be observed that in the above figures, increasing the number of particles leads to more accuracy in random signal tracking. As the number of particles entering to the PF with the proposed IIMH algorithm increases, the amount of tracking error decreases.

The tracking result of the PF with the proposed IIMH algorithm in comparison to PF with the Systematic Resampling (SR) algorithm is shown in Figure 5.

To determine the quality of signal tracking depicted in Figure 5, Root Mean Squared Error (RMSE) is measured for two algorithms. *RMSE* is a mixture measure that reflects the bias and variance of PF estimation [4]. In our design, the output state vector consists of coordinate components *x* and *y* and the weight component *w*. From Figure 6 it is obvious that the *RMSE* value of the proposed architecture is lower than the SR algorithm.

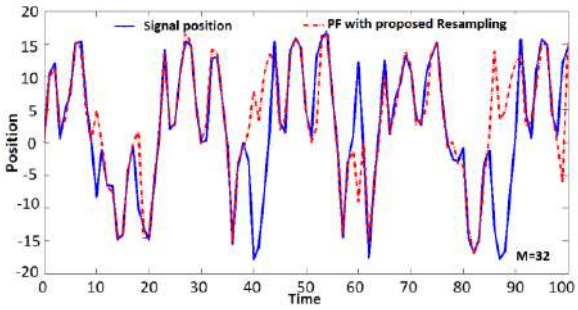

Figure 3. Tracking a random signal with a proposed IIMH algorithm in PF with M=32 particles

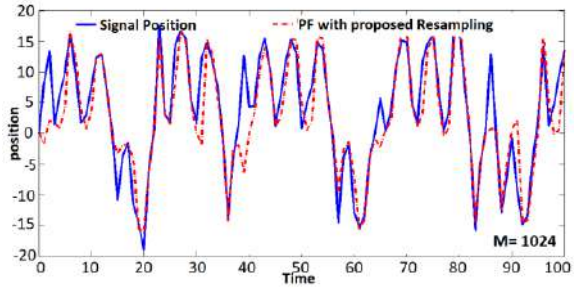

Figure 4. Tracking a random signal with a proposed IIMH algorithm in PF with M=1024 particles

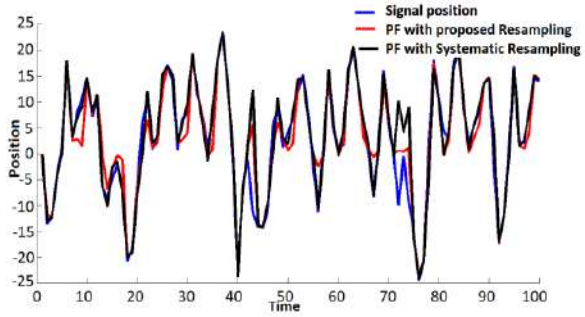

Figure 5. Tracking a random signal with a proposed IIMH algorithm and SR algorithm in PF with M=1024 particles

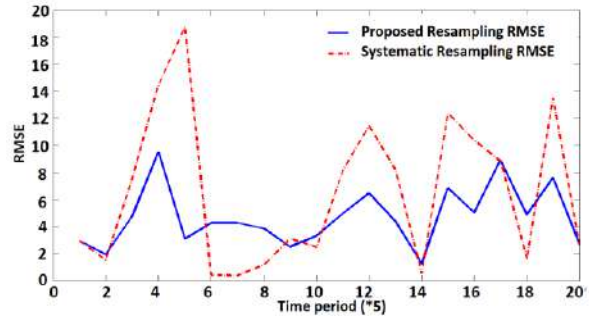

Figure 6. RMSE values of the proposed IIMH algorithm and SR algorithm in PF

Tha average *RMSE* value of the proposed IIMH method is about 25% lower than the SR algorithm that demonstrates the high quality of the proposed method.

4. 2. Execution Time Figure 7 shows the execution timing diagram of PF with the proposed IIMH resampling architecture. The overall execution time for PF can be achieved as below:

$$T_{proposed} = (L_c + L_w + L_s + L_{IMH} + M - N_d - N_m)\, T_{clk} \quad (5)$$

where L_c, L_w, L_s, L_{IMH} represent the startup latencies of the particle classification, weight calculation, sampling, IMH resampler, respectively. N_d and N_m are the numbers of discarded particles and median particles, respectively. T_{clk} is the system clock period. M is the total number of particles.

The overall execution time for PF with proposed DIIMH architecture can be achieved as below:

$$T_{DIIMH} = (L_c + K + L_I + L_{IMH} + (\frac{M-N_d-N_m}{K}) + L_w + L_s)\, T_{clk} \quad (6)$$

Tables 1 and 2 show the resampling frequency comparison for proposed IIMH and DIIMH resampling architectures and other hardware-based resampling methods at a clock frequency of 60 MHz. From the tables, it is concluded that the proposed IIMH and DIIMH methods suggest an acceptable speed in comparison to other resampling methods in PF. The comparison result shows that the proposed IIMH and DIIMH architecture have 33% and 79% more speed than the best reported methods in single *PE* and 4 *PEs*, respectively.

4. 3. Resource Utilization Table 3 shows the resource utilization of proposed IIMH and DIIMH and the existing resampling methods on a Xilinx Virtex5 FPGA (XC5VSX50T) platform as an example.

It is observed that the proposed IIMH and DIIMH reduce the number of DSP units, Block RAM, LUTs, slice FFs and Registers in comparison to other methods. Distributed resampling architectures with more *PEs* consume more device utilization. However, the performance of distributed architectures is better than

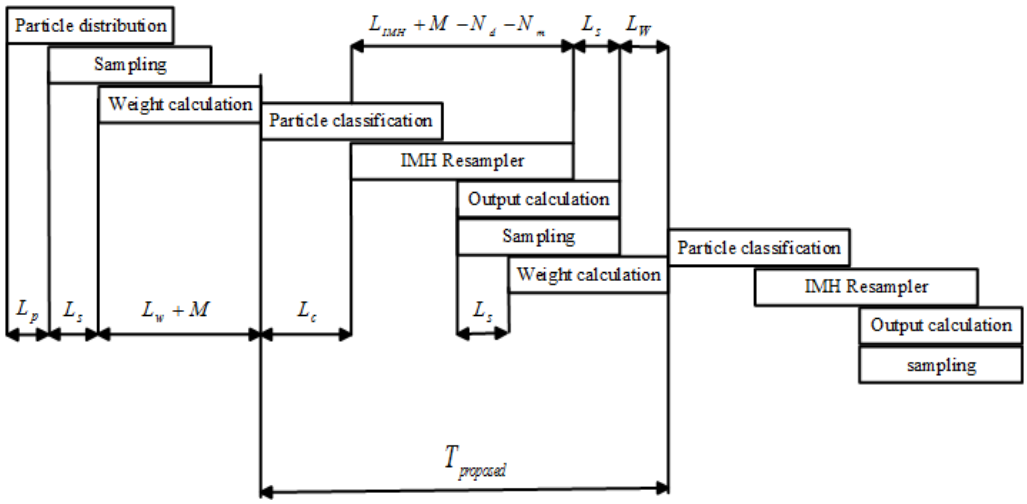

Figure 7. Execution time of PF with proposed IIMH architecture

TABLE 1. Resampling frequency of PF at $f_{clk} = 60$MHz with single *PE* for different resampling methods

Resampling method	Resampling frequency
Proposed IIMH	60 KHz
HR [9]	27 KHz
RSR [6]	45 KHz
RR [5]	19.5 KHz
SR [12]	9.6 KHz
CR [12]	14.4 KHz

TABLE 2. Resampling frequency of PF at $f_{clk} = 60$MHz with 4 *PEs* for distributed resampling methods

Resampling Method	Resampling Frequency
Proposed DIIMH	174 KHz
Distributed IMH [15]	50 KHz
Distributed HR [9]	97 KHz
Distributed RSR [6]	64 KHz
Distributed RR [12]	40 KHz

TABLE 3. Resource utilization of resampling methods implemented on Xilinx Virtex5 (XC5VSX50T)

Resampling methods	Slice register	Slice LUTs	Slice FFs	Block RAM	DSP48Es
Proposed IIMH	2728	4398	3662	12	7
Proposed DIIMH	10712	18395	15641	17	27
IMH [15]	19350	28065	26474	48	101
Distributed HR [9]	11883	20607	16320	28	30

resampling methods with single *PE*. Resource usage reduction of the proposed architectures is due to two main reasons; The first reason is because of using the index of particles instead of using four-element input vectors. The second reason is that a simple routing of *CU* is employed in the proposed DIIMH scheme. Therefore this scheme doesn't need large temporary memories with high capacity in *PEs* and *CU*.

5. CONCLUSION

In this paper, an improved algorithm and an efficient architecture for IMH resampling, namely IIMH were first proposed. The algorithm is based on classifying the particles before assigning them to the resampling module. The technique would speed up the resampling step by considering only the essential particles in PF. Afterward we proposed a distributed architecture for IIMH, namely DIIMH to increase the processing speed through parallel processing. The results show that resampling frequencies of IIMH and DIIMH methods are 60 KHz and 174 KHz that they are about 33% and 79% more than the best reported methods. Also, we can achieve about 39% reduction in RAM usage due to the simple designing of *CU* in comparison to the most efficient hardware-based method.

6. ACKNOWLEDGMENT

The authors would like to thank the Institute for Research in Fundamental Sciences (IPM) which supported this research in the context of research project number CS1396-4-670.

7. REFERENCES

1. Feizi, A., "Convolutional gating network for object tracking", ***International Journal of Engineering*, *Transactions A: Basics*,** Vol. 32, No. 7, (2019), 931-939. DOI: 0.5829/IJE.2019.32.07A.05
2. Sadegh Moghadasi, S. and Faraji, N., "An efficient target tracking algorithm based on particle filter and genetic algorithm", ***International Journal of Engineering*, *Transactions A: Basics*,** Vol. 32, No. 7, (2019), 915-923. DOI: 10.5829/IJE.2019.32.07A.03
3. Liu, J.S., Chen, R. and Logvinenko, T., A theoretical framework for sequential importance sampling with resampling, in Sequential monte carlo methods in practice. 2001, Springer.225-246. DOI: 10.1007/978-1-4757-3437-9_11
4. Zhao, Z., Wang, T., Liu, F., Choe, G., Yuan, C. and Cui, Z., "Remarkable local resampling based on particle filter for visual tracking", ***Multimedia Tools and Applications***, Vol. 76, No. 1, (2017), 835-860. DOI: 10.1007/s11042-015-3075-6
5. Hong, S., Chin, S.-S., Djurić, P.M. and Bolić, M., "Design and implementation of flexible resampling mechanism for high-speed parallel particle filters", ***Journal of VLSI Signal Processing Systems for Signal, Image and Video Technology***, Vol. 44, No. 1-2, (2006), 47-62. DOI: : 10.1007/s11265-006-5919-9
6. Abd El-Halym, H.A., Mahmoud, I.I. and Habib, S., "Proposed hardware architectures of particle filter for object tracking", ***EURASIP Journal on Advances in Signal Processing***, Vol. 2012, No. 1, (2012), 17. DOI: 10.1186/1687-6180-2012-17
7. Li, T., Bolic, M. and Djuric, P.M., "Resampling methods for particle filtering: Classification, implementation, and strategies", ***IEEE Signal Processing Magazine***, Vol. 32, No. 3, (2015), 70-86. DOI: 10.1109/MSP.2014.2330626
8. Bolić, M., Djurić, P.M. and Hong, S., "Resampling algorithms for particle filters: A computational complexity perspective", ***EURASIP Journal on Advances in Signal Processing***, Vol. 2004, No. 15, (2004), 403686. DOI: 10.1155/S1110865704405149
9. Pan, Y., Zheng, N., Tian, Q., Yan, X. and Huan, R., "Hierarchical resampling algorithm and architecture for distributed particle filters", ***Journal of Signal Processing Systems***, Vol. 71, No. 3, (2013), 237-246. DOI: 10.1007/s11265-012-0712-4
10. Gan, Q., Langlois, J.P. and Savaria, Y., "A parallel systematic resampling algorithm for high-speed particle filters in embedded

systems", ***Circuits, Systems, and Signal Processing***, Vol. 33, No. 11, (2014), 3591-3602. DOI: 10.1007/s00034-014-9820-7

11. Douc, R. and Cappé, O., "Comparison of resampling schemes for particle filtering", in ISPA 2005. Proceedings of the 4th International Symposium on Image and Signal Processing and Analysis, IEEE. (2005), 64-69. DOI: 10.1109/ISPA.2005.195385
12. Hong, S.-H., Shi, Z.-G., Chen, J.-M. and Chen, K.-S., "A low-power memory-efficient resampling architecture for particle filters", ***Circuits, Systems and Signal Processing***, Vol. 29, No. 1, (2010), 155-167. DOI: 10.1007/s00034-009-9117-4
13. Murray, L., "Gpu acceleration of the particle filter: The metropolis resampler", arXiv Preprint arXiv:1202.6163, (2012).
14. Sankaranarayanan, A.C., Srivastava, A. and Chellappa, R., "Algorithmic and architectural optimizations for computationally efficient particle filtering", ***IEEE Transactions on Image Processing***, Vol. 17, No. 5, (2008), 737-748. DOI: 10.1109/TIP.2008.920760
15. Hong, S., Shi, Z. and Chen, K., "Easy-hardware-implementation mmpf for maneuvering target tracking: Algorithm and architecture", ***Journal of Signal Processing Systems***, Vol. 61, No. 3, (2010), 259-269. DOI: 10.1007/s11265-010-0450-4
16. Medina, A.R., "Hardware-based particle filter with evolutionary resampling stage", Master thesis, 3-2014, Universidad Politécnica de Madrid, (2014).

Persian Abstract

چکیده

نمونه‌برداری مجدد به دلیل انحطاط و ضعف ذرات یک مرحله ضروری در فیلتر ذره است. الگوریتم نمونه برداری مجدد Independent Metropolis Hasting (IMH) یک روش قوی و پر سرعت است که می‌تواند در مرحله نمونه‌برداری مجدد در فیلتر ذره مورد استفاده قرار گیرد. در این مقاله ابتدا یک الگوریتم جدید بر اساس نمونه‌برداری مجدد IMH پیشنهاد شده است. الگوریتم پیشنهادی ذرات را قبل از ورود به ماژول نمونه‌برداری مجدد طبقه‌بندی می‌کند. این طبقه‌بندی باعث می‌شود که تنها ذرات ضروری به واحد نمونه‌بردار مجدد IMH وارد شود. سپس معماری توزیع شده ای به منظور کاهش زمان اجرا و پردازش سرعت بالا برای نمونه‌برداری مجدد ارائه شده است. نتایج شبیه‌سازی برای ردیابی یک سیگنال نشان می‌دهد که فیلتر ذره با معماری نمونه‌برداری مجدد پیشنهادی دارای عملکرد ردیابی قابل قبول در مقایسه با سایر روش‌های نمونه‌برداری مجدد است. معماری فیلتر ذره با الگوریتم نمونه‌برداری مجدد پیشنهادی IIMH دارای ۳۳ ٪ سرعت بیشتر در مقایسه با بهترین روش گزارش داده شده در فیلتر دره است. همچنین معماری فیلتر ذره توزیع شده‌ی پیشنهادی دارای ۷۹ ٪ سرعت بیشتر در مقایسه با بهترین روش گزارش داده شده است. نتایج پیاده‌سازی بر اساس FPGA نشان می‌دهد که استفاده از الگوریتم نمونه‌برداری مجدد پیشنهادی در فیلتر ذره و همچنین معماری توزیع شده منجر به کاهش منابع سخت افزاری و مساحت مورد استفاده می شود.

International Journal of Engineering

Journal Homepage: www.ije.ir

A New Optimal Distributed Strategy to Mitigate the Phase Imbalance in Smart Grids

H. R. Mansouri, B. Mozafari*, S. Soleymani, H. Mohammadnezhad

Department of Electrical Engineering, Science and Research Branch, Islamic Azad University, Tehran, Iran

P A P E R I N F O

Paper history:
Received 03 June 2019
Received in revised form 22 August 2020
Accepted 03 September 2020

Keywords:
Smart Distribution Grid
Smart Meter
Phase Imbalance
Phase Rearrangement

A B S T R A C T

In a three-phase distribution system, due to unequal distribution of single-phase loads, load diversities, the different consumption patterns, and growing penetration of renewable energy resources in smart grids, the problem of unbalanced power flow becomes more challenging. In this paper, we propose a new innovative phase imbalance mitigation (PIM) scheme performed by smart meters. With aid of the proposed optimal phase assignment for 3-phase power distribution input feeders known as phase rearrangement (PR), Electrical storages (ES), and the Renewable energy sources (RES), smart meter owners are inspired to assist the distribution system operator (DSO) in diminishing the phase imbalance. This is achieved by employing a proposed connection point assignment system which has the flexibility of selecting the power input among the three phases and management of ESs and RESs. We model this problem into a mixed integer linear program, where smart meter owners minimize their electricity bill. Simulation results confirm the proposed approach and show smart meter owners will save on their electricity bill and the DSO will get benefit by improving the power quality of the grid and significant decrements of the power flow imbalance.

***doi**: 10.5829/ije.2020.33.12c.08*

1. INTRODUCTION

Due to the unequal distribution of single-phase loads, load diversities, and the different consumption patterns, the three-phase distribution system is innately unbalanced [1]. Unequal power distribution among the three phases leads to unfavorable impacts on the power distribution system and its electrical devices. Under these conditions, currents in two of the phases as well as in the neutral line will rise which provoking more energy losses and heating effects as a consequence [2], even causing tripping of the overload-protection circuits of the feeders [3]. The imbalance also lessens the available capacity of transformers and feeders, leading to additional investment costs [4]. Besides, power imbalance will depreciate the power quality, efficiency, and lifetime of the electrical devices. Furthermore, the increasing penetration of distributed renewable energy sources and the intermittency and uncertainty power generation inherent characteristics as well as the arbitrary installation of them among the three phases, the power imbalance problem is becoming more challenging [5], [6]. Consequently, the DSO has to take action to resolve the power imbalance in the distribution grid. A lot of works have been made to answer the PR problem. Conventionally, rephasing procedures in which re-assign loads to phases are generally employed [7]. In [7], optimal rephasing is done by suggesting a mixed-integer optimization of decisions. Besides, in [8], a rephasing method is proposed wherein a particle swarm optimization problem has been solved to diminish the imbalance. The above-mentioned research all have manual operations for rephasing because the required customer service interruption and manual labor will entail significant costs, strategies, and methods that executing them need offline procedures which depend on the previous plans so are not effective for dynamic and hourly load changes. Most of the traditional methods are put in this category [9-11]. One of the well-known and effective strategies for balancing the loads is rearranging

*Corresponding Author Institutional Email: *mansouri@tbtb.ir* (H. R. Mansouri)

Please cite this article as: H. R. Mansouri, B. Mozafari, S. Soleymani, H. Mohammadnezhad, A New Optimal Distributed Strategy to Mitigate the Phase Imbalance in Smart Grids, International Journal of Engineering, Transactions C: Aspects Vol. 33, No. 12, (2020), 2489-2495.

the connection point of single-phase customers. The feeders' phase of customers is changed somehow that the unequal loading of the grid's phases gets minimized with regards to the balancing requirements [12]. It is commonly done based on the customers' contractual power or the method of counting them additionally the strategy of their average power consumption based on bills' data information. Versus, the online strategies are existed such as converters. They are commonly used for compensating the active and reactive powers. Convertors are online and in the form of hot-line and act based on the component of sequences of the positive, negative, and/or zero for voltage or current parameters. The devices which support these methods are located in the field where a pre-determined node should be getting balanced. They are based on the current injection to nullify the existing neutral current in a way that the sum of these two current vectors will be equal to zero or near-zero [13-15]. These online strategies are optimal or close to optimal but expensive and have high installation and maintenance costs that causes their utilization lesser. From this category, we can suggest the designed device in [16] especially for reducing the imbalance. It introduces a special type of transformer with an innovating winding arrangement and special core structure so that the current of neutral wire would be zero in every side of the transformer.

These mentioned works are lacking to address the dynamic PR challenges. For it, in [17], static transfer switches (STS) have been presented to relocate residential loads from one phase to a different dynamically. Also, none of those has pondered the smart meters' interaction with each other to make the phase re-arranging autonomously.

In future smart grids, the smart meters will be different from existing ones, they will have cloud computing applications and can exchange data and information between the DSO and each other throw the cloud computing environment. In this paper, we present the smart meters which are ready to be online on the internet and can be accessible and programmable by the DSO, and communicable with other smart meters or authorized entities. We explain the PIM problem from the perspective of smart meter owners, where encouragements such as financial incentives are arranged to increase their participation in the DR programs such as the novel idea of this paper. The PIM problem is modeled as a linear program wherein the decision values are the connection points to the three-phase input feeders. Finally, the main contributions of this paper are summarized as follows:

• To avoid the significant challenge of employing the in practice, an extended connection point assignment system is proposed for handling the original PR strategy.
• An efficient algorithm is established to attain the optimal connection point and management of ESs and RESs.
• Benefits to both the DSO and smart meter owners are proven through all-encompassing simulations.
• Preparation of the method does not need any change in electrical structure, devices, or consumers' part except equipping the smart meters with the proposed module.

The remainder of this literature is prepared as follows. Section II presents the system model and formulates the PIM problem as a linear program. In Section III, Developing a distributed algorithm and explaining the procedure of phase assigning are put in it. Numerical results are obtainable in Section IV and Section V includes the conclusions of this paper.

2. SYSTEM MODEL

The distribution grid is the last step in transferring energy to the consumers. Reconfiguring the grid means the change or keep the normal state of open/close keys to increase the parameters of power quality, reliability, and loss reduction. Assume the optimal reconfiguration is done based on the grid loss reduction, the proposed phase assignment of customers is online and leads to reducing the aggregate load imbalance in 3 phase feeders in addition to its important result which is mitigating the neutral current. These mentioned results are the advantages of the proposed method in this paper. Since the consumption pattern of customers is unpredictable, so we cannot achieve the optimal assignment offline even in the condition of relying on the results of clustering. In the following, the proposed strategy, initial implementing requirements, algorithm, and mathematical formulations will be explained. It is worth mentioning that the three-phase customers can be assumed as three single-phase subscribers; but as the three-phase consumers mostly possess three-phase inductive motors, related protective and control circuits, the phase altering without special technical considerations cannot be possible. So, we assume the three-phase customers will not participate in the proposed program, however, the consumption pattern should be considered in the calculation of baseload.

In this paper, the load balancing is carried out in such a way that the exchanged power with the grid on each node is the same value for all three phases. Since customers who possess DGs and storage systems should also be considered in the problem-solving procedure. It is clear that by increasing the rearranging number of customers, the grid would be closer to the balance condition but this operation should be practically and economically limited due to the lifespan of switching devices.

A sample feeder with three phases and one neutral supply the buildings with photovoltaic and energy storage units is shown in Figure 1.

Assume there are a set of smart meter owners who participate in the PR scheme. These smart meters are fed with 3phases. Power flows inside the customers of the same node compared with the grid's main feeders have negligible effects on their voltages. Additionally, electrical lines originating from the same node usually, in normal conditions, have enough capacity to support all the customers. Consequently, for simplicity, the power flow constraints within a node are not considered. However, this proposed PR strategy can be employed when power flow constraints should not be disregarded. Each smart meter is connected to a 3 phase electricity line but gets power from one phase at the same time. The key idea of the proposed PR scheme is to exploit the input phase flexibility among the three phases. To be precise, the DSO offers the customers encouragement to reassign the connected phase, such that power consumptions on each phase are moved to another phase when compared with the other two, which is relatively light-loaded. We assume that each customer equipped with the smart meter also has electrical storage (ES) which needs to hold a predetermined state-of-charge (SOC) between the minimum and maximum boundaries over a time horizon e.g. a day. It has a charger with a specific charging rate and characteristics. Thus, the following constraint must be satisfied:

$$SOC_i[t+1]=SOC_i[t]+\left(1-\zeta_i^{ch}\right).E_{t,i}^{ch} -\left(1+\zeta_i^{dch}\right).E_{t,i}^{dch} \quad (1)$$

$$P_{t,i}^{ch}\times P_{t,i}^{dch}=0 \quad (2)$$

where $P_{t,i}^{ch}$ *and* $P_{t,i}^{dch}$ indicate the storage charge power and discharge power of ES i at time instant t, respectively. The charging rates are constrained. Consequently, the feasible values are the solution set of linear inequalities that are finite in number. Also, $E_{t,i}^{ch}$ *and* $E_{t,i}^{dch}$ are the energies of these power in the time horizon [t,t+1]. (1) reflecting the state of charge (SOC) for the ESs and (2) sets the limit that they should not be charged and discharged simultaneously. It is obvious that a portion ζ_{ch} *or* ζ_{dch} of the stored energy due to inefficiency is typically loss; thus the energy effectively stored is $\left(1-\zeta_i^{ch}\right).E_{t,i}^{ch}$, while the released one needed to guarantee a power supply $P_{t,i}^{ch}$ is $\left(1+\zeta_i^{dch}\right).E_{t,i}^{dch}$. The stored energy in ESs should be between the minimum (DOD) and maximum SOC_{max} (3); allowable limits in accordance with the technical specifications that bring about lifetime increase and avoids deep discharging or over-charging events.

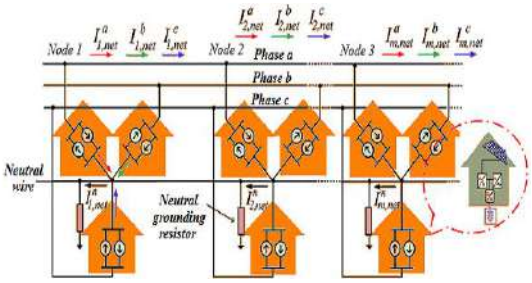

Figure 1. A sample feeder with three-phase and neutral that supply the buildings with photovoltaic DGs and energy storage units

$$\forall t:\ DOD_i \le SOC_i(t) \le SOC_{i,max} \quad (3)$$

(4) notes the amount of the $SOC\,(end)$, stored energy in batteries at the end of the time horizon should be greater than a minimum desirable value $SOC_{desired}$.

$$SOC_{i,desired} \le SOC_i(end) \quad (4)$$

The generation amount of RESs are considered as negative loads, and vice versa, selling the electricity to the grid as a positive load consumption. However, note that the power balance equation should be met as follow:

$$P_{t,i}^{buy}-P_{t,i}^{sell}+P_{t,i}^{RESs}-P_{t,i}^{ch}+P_{t,i}^{dch}-P_{t,i}^{load}=0 \quad (5)$$

where $P_{t,i}^{buy}$ *and* $P_{t,i}^{sell}$ are the amount of buying/selling electricity of customer i at time instant t. Also, $P_{t,i}^{load}$ is the amount of power consumption and $P_{t,i}^{RESs}$ is the amount of power generation of RESs of customer i.

We express the phase imbalance with the optimization function based on the proposed strategy which at each grid node at time instant t is obtained according to the following constraints and equations.

$$I_{avg}^{m,t}=1/3.\sum\left|I_{m,net}^{ph,t}\right|, ph\in\{a,b,c\} \quad (6)$$

$I_{avg}^{m,t}$ is the average total load of three-phases at node m at a time instant. Consequently, the indices of the original three phases which have imbalance are formulated as below:

$$ph_{ideal}^{m,t}=\min_{ph,ph\in\{a,b,c\}}\left|I_{m,net}^{ph,t}-I_{avg}^{m,t}\right| \quad (7)$$

$$ph_{incr}^{m,t}=\min_{ph,ph\in\{a,b,c\}}\left|I_{m,net}^{ph,t}\right| \quad (8)$$

$$ph_{shed}^{m,t}=\max_{ph,ph\in\{a,b,c\}}\left|I_{m,net}^{p,t}\right| \quad (9)$$

$ph_{ideal}^{m,t}$ is the phase at node m at time instant t which its loads remain untouched. Also, loads of phase $ph_{incr}^{m,t}$ will be increased by assigning smart meter loads on phase $ph_{shed}^{m,t}$ to it at node m at time instant t.

$$I_{ideal}^{m,t\circ} = I_{m,net}^{ph=ph_{ideal}^{m,t}} \;\&\; I_{shed}^{m,t\circ} = I_{m,net}^{ph=ph_{shed}^{m,t}} \tag{10-11}$$

where $I_{ideal}^{m,t\circ}$ is the current of phase $ph_{ideal}^{m,t}$ and $I_{shed}^{m,t\circ}$ is the current of phase $ph_{shed}^{m,t}$ both of them at node m at a time instant t which are measured as initial values at the beginning of the optimization time horizon.

To summarize, smart meter i solves the following optimization problem:

$$\min_{x_k\in\psi_k} (I_{shed}^{m,t\circ} - I_{ideal}^{m,t\circ} - \sum_{k=1}^{Ksw} I_{k,m}^{ph_{shed}^{m,t}} \times sw_{k,m}^{incr,t} + \sum_{k'=1}^{Kch} I_{k',m}^{ph_{shed}^{m,t},ch} - \sum_{k''=1}^{Kdch} I_{k'',m}^{ph_{shed}^{m,t},dch} - \sum_{k'''=1}^{KRESs} I_{k''',m}^{ph_{shed}^{m,t},RES}) \tag{12}$$

where $\psi_k = \left\{ sw_{k,m}^{incr,t}, I_{k',m}^{ph_{shed}^{m,t},ch}, I_{k'',m}^{ph_{shed}^{m,t},dch}, I_{k''',m}^{ph_{shed}^{m,t},RES} \right\}$ is the decision value set of the optimization function.

While regarding to the (1-5) for ESs, the below constraints (13) should also be considered for each smart meter:

$$sw_{k,m}^{incr} \;\&\; sw_{k,m}^{shed} \in \{0,1\}; \sum sw_{k,m}^{incr,t} + sw_{k,m}^{shed,t} = 1 \tag{13}$$

In the above equations, $I_{k',m}^{ph_{shed}^{m,t},ch}$ is the smart meter k' ES charge current at node m connected to the phase $ph_{shed}^{m,t}$. Also, $I_{k'',m}^{ph_{shed}^{m,t},dch}$ is the smart meter k'' ES discharge current at node m connected to the phase $ph_{shed}^{m,t}$. For taking into account the RESs , the $I_{k''',m}^{ph_{shed}^{m,t},RES}$ is used to indicates the smart meter k''' RES generation current at node m connected to the phase $ph_{shed}^{m,t}$. Furthermore, $sw_{k,m}^{incr,t}$ and $sw_{k,m}^{shed,t}$ are respectively the switch position for smart meter k at phases $ph_{incr}^{m,t}$ and $ph_{shed}^{m,t}$.

The optimization (12), and its constraints are linear equations. Since decision variables are binary and real, for optimization, the mixed linear programming methods or innovative methods such as genetic or PSO can be used. In addition, the number of switching times can be restricted to extend their lifespan. This constraint can be applied to the decision variables itself or by utilization of the penalty factor in the optimization function. The relevant switching indicators, according to the initial and next states of the connected phase with details of the proposed switching system are listed in Table 1. Also, Figure 2 represents the Connection point assignment system for applying the PR strategy in the smart meters.

3. DISTRIBUTED ALGORITHM

An algorithm is presented in this section to decide the best customers' side strategies that are the load connection points, ESs charging/discharging control, and RESs generation profile management. The procedure of the algorithm shows the interaction between the customers when the suggested way is used in practice. It is explained briefly in Algorithm 1; the smart meters update their consumption current vector via the determined procedure. The recommended procedure is founded on the smart meter abilities such as cloud-enabled features. Actually, the algorithm converges to a number at that the power imbalance will getting as less as predetermined. The innovation of this strategy is its distributed best response structure and optimal performance. Its algorithm in a sample repeat is as follows.

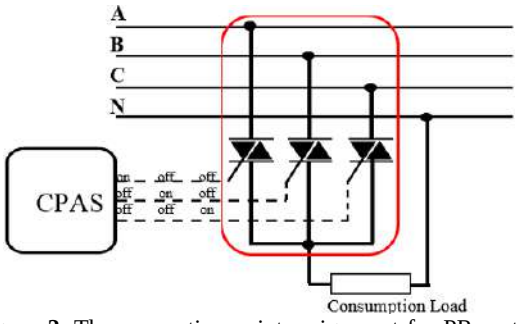

Figure 2. The connection point assignment for PR system integrated into the smart meters

TABLE 1. The Switching Strategies

First State	Next State	(u_j^a, u_j^b, u_j^c)
	A	(1,0,0)
A	B	(-1,1,0)
	C	(-1,0,1)
	A	(1,-1,0)
B	B	(0,1,0)
	C	(0,-1,1)
	A	(1,0,-1)
C	B	(0,1,-1)
	C	(0,0,1)

Algorithm 1. Distributed best response algorithm

1-Start

2-Three-phase and neutral voltage vector parameters, load current, amount of RES power generation, charged and discharged power in the ESs monitored and recorded by the smart meter.
3-Smart meter calculates three phases grid current vector.
4-Smart meters send/receive the current vectors with the connected phase number to/from other smart meters in a node.
5-If $\left\| I_{shed}^{m} - I_{ideal}^{m} \right\| < \varepsilon$, go to Step 2; otherwise, go to the next step.
6-Every smart meter executes the optimization (12) based on the data gathered from Steps 3 and 4 and sends the keep or change control commands to the controller module of Connection point assignment System(CPAS), ES controllers, and RESs management system.
7-CPAS, ES charger/discharger, and RESs Controllers based on the received command perform the operation and smart meters informs the other ones; then go to Step 2.

4. NUMERICAL RESULTS

In this section, the performance of the proposed PIM scheme is numerically evaluated. A period of 24 hours is considered. The proposed strategy is implemented in the modified 13-node IEEE sample distribution grid which loaded unbalanced; a four-wire three-phase feeder with isolated neutral, shown in Figure 3. Changes such as adding RESs and an ES unit. RESs are added to nodes 611 and 675, and an ES unit is added to node 652, where the others are kept untouched as the original test feeder. In the simulation, following Gaussian distributions, 1000 sets of inflexible load data are generated randomly to validate our proposed scheme. The ES capacity is set as 100 kWh and finally, in this simulation, a linear pricing function is selected. Unbalanced power flow calculation in this sample is carried out in form of a forward/backward sweep that has been programmed, executed, and implemented. The optimization has been performed using a linear method. Since the reassignment operation, generation of RESs, and ESs charge managements per node was done individually and is distributed, the execution time for the proposed strategy remains constant as the number of smart meters increases. The neutral current values and the line current values are presented in Table 2 before and after implementing the optimization. As can be seen, the optimal assignment of single-phase loads reduces the peak current in the highly loaded phase. This will increase grid stability plus the possibility of distributing more energy in the grid. Table 2 confirms the considerable dynamically and real-time reduction of unbalanced loading. For example, the mean index value of neutral conductors' current, was reduced above 48%. Figure 4 shows the voltage of the grid's nodes with or without optimization. As it is known, the optimal allocation of single-phase loads causes the balancing of the feeders' current that mitigates the voltage drop at the nodes. In this case, the minimum voltage value increases from 0.98 (PU) to 0.97 (PU). This will reduce the need for reactive power compensation. By optimal managing of the energy storage and allocating some of their capacity to the demand response programs, the grid functioning will be enhanced. In Figure 5, it has been shown that the storages lead to imbalance reductions at node 652 during the day. By implementing this method,

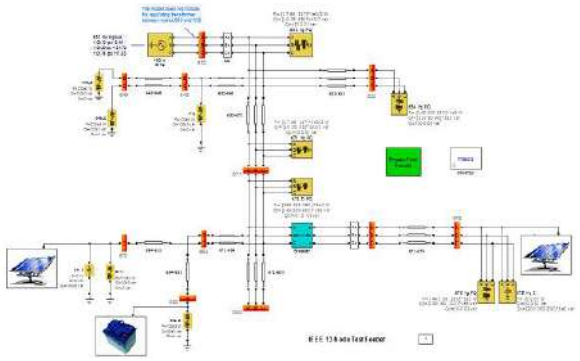

Figure 3. The diagram of the sample grid, a modified version of IEEE 13 Node Test Feeder

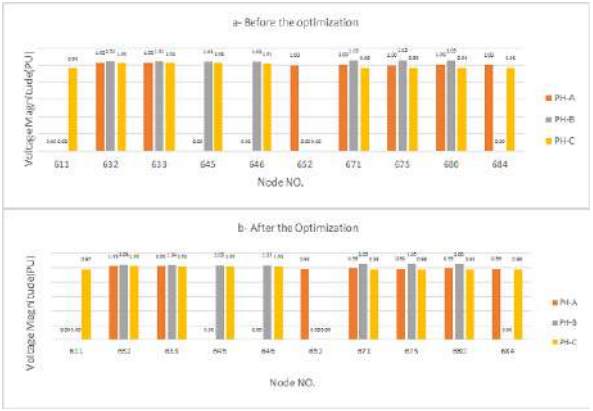

Figure 4. The node's voltage magnitude before and after the optimization

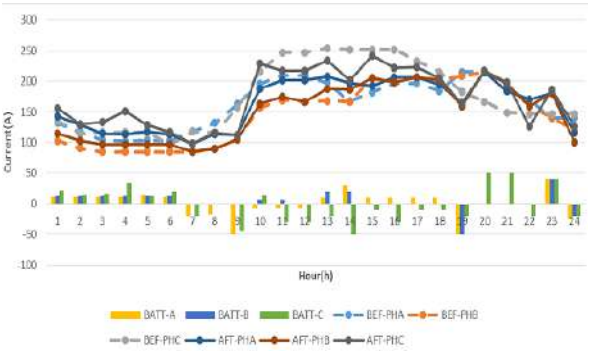

Figure 5. The three-phases feeder current at node 652 with the amount of power charged or discharged in the storages before and after the optimization

TABLE 2. The line current and neutral current values before and after the optimization

		Before Optimization				After Optimization			
		N.	**A**	**B**	**C**	**N.**	**A**	**B**	**C**
611	684	71	0	0	71	50	14	0.0	57
632	633	226	79	60	61	94	569	450	538
632	645	19	0.0	143	65	3	71	67	61
632	671	85	0	65	65	60	20	133	52
645	646	64	63	0.0	0.0	45	13	59	52
652	684	299	441	211	522	149	56	6	0.0
671	675	191	202	61	125.9	117	479	254	435
671	680	0	0	0	0	0	164	86	124
671	684	23	63	0	71	15	0	0	0

the current of three-phase feeders is distributed more equally; therefore, the peak current of each distribution feeder significantly reduces due to current reduction in the relatively heavy-loaded phase of it and leads to neutral current mitigation which is apparent in Figure 5. The reduction of the grid's power imbalance also reduce power losses in it, by assuming 20% of all grid's electricity meters were smart and equipped with the proposed strategy, it would reduce from 52KW to 43KW which is about 18% lower.

5. CONCLUSIONS

Load diversities, the different consumption patterns, and increasing penetration of renewable energy resources cause the problem of unbalanced power flow to become more challenging. Moreover, asymmetric three-phase loads or asymmetrical impedances of lines cause an unbalanced grid and excessive and undesirable flow of current in the neutral. In this paper, a novel strategy of rearranging the phases is introduced with a distributed structure, carried out with aid of the facilities in smart grids. The proposed method is based on the optimal assigning of the single-phase customers' grid connection point to one of the phases and also, by controlling the ESs, and managing the RESs generation profiles. Simulation results validated the proposed strategy and demonstrated a considerable reduction in the phase unbalancing and reduction in power losses.

6. REFERENCES

1. Kersting, W.H., "Distribution system modeling and analysis, CRC Press, (2012).
2. Martinenas, S., Knezović, K. and Marinelli, M., "Management of power quality issues in low voltage networks using electric vehicles: Experimental validation", ***IEEE Transactions on Power Delivery***, Vol. 32, No. 2, (2016), 971-979, doi:10.1109/TPWRD.2016.2614582.
3. Mostafa, H.A., El-Shatshat, R. and Salama, M.M., "Multi-objective optimization for the operation of an electric distribution system with a large number of single-phase solar generators", ***IEEE Transactions on Smart grid***, Vol. 4, No. 2, (2013), 1038-1047, doi:10.1109/TSG.2013.2239669.
4. Ma, K., Li, R., and Li, F., "Quantification of additional asset reinforcement cost from 3-phase imbalance", ***IEEE Transactions on Power Systems***, Vol. 31, No. 4, (2015), 2885-2891, doi:10.1109/TPWRS.2015.2481078.
5. Shahnia, F., Majumder, R., Ghosh, A., Ledwich, G. and Zare, F., "Voltage imbalance analysis in residential low voltage distribution networks with rooftop pvs", ***Electric Power Systems Research***, Vol. 81, No. 9, (2011), 1805-1814, doi:10.1016/j.epsr.2011.05.001.
6. Karimi, M., Mokhlis, H., Naidu, K., Uddin, S. and Bakar, A., "Photovoltaic penetration issues and impacts in distribution network–a review", ***Renewable and Sustainable Energy Reviews***, Vol. 53, (2016), 594-605, doi:10.1016/j.rser.2015.08.042.
7. Gray, M.K. and Morsi, W.G., "Economic assessment of phase reconfiguration to mitigate the unbalance due to plug-in electric vehicles charging", ***Electric Power Systems Research***, Vol. 140, (2016), 329-336, doi:10.1016/j.epsr.2016.06.008.
8. Soltani, S., Rashidinejad, M. and Abdollahi, A., "Stochastic multiobjective distribution systems phase balancing considering distributed energy resources", ***IEEE Systems Journal***, Vol. 12, No. 3, (2017), 2866-2877, doi:10.1109/JSYST.2017.2715199.
9. Sedighi, A.R., "A novel method for implementing of time-of-use to improve the performance of electric distribution systems: A case study", ***International Journal of Engineering, Transactions C: Aspects***, Vol. 30, No. 3, (2017), 357-365, doi:10.5829/idosi.ije.2017.30.03c.05.
10. Sattarpour, T., "Assessing the impact of size and site of dgs and sms in active distribution networks for energy losses cost", ***International Journal of Engineering, Transactions A: Basics***, Vol. 28, No. 7, (2015), 1002-1010, doi:10.5829/idosi.ije.2015.28.07a.06.

11. Farzinfar, M., Shafiee, M. and Kia, A., "Determination of optimal allocation and penetration level of distributed energy resources considering short circuit currents", ***International Journal of Engineering, Transactions C: Aspects***, Vol. 33, No. 3, (2020), 427-438, doi:10.5829/ije.2020.33.03c.07.
12. Siti, M.W., Nicolae, D.V., Jimoh, A.A. and Ukil, A., "Reconfiguration and load balancing in the lv and mv distribution networks for optimal performance", ***IEEE Transactions on Power Delivery***, Vol. 22, No. 4, (2007), 2534-2540, doi:10.1109/TPWRD.2007.905581.
13. Hong, T. and De León, F., "Controlling non-synchronous microgrids for load balancing of radial distribution systems", ***IEEE Transactions on Smart Grid***, Vol. 8, No. 6, (2016), 2608-2616, doi:10.1109/TSG.2016.2531983.
14. Czarnecki, L.S. and Haley, P.M., "Unbalanced power in four-wire systems and its reactive compensation", ***IEEE Transactions on Power Delivery***, Vol. 30, No. 1, (2014), 53-63, doi:10.1109/TPWRD.2014.2314599.
15. Hooshmand, R.A. and Soltani, S., "Fuzzy optimal phase balancing of radial and meshed distribution networks using bf-pso algorithm", ***IEEE Transactions on Power Systems***, Vol. 27, No. 1, (2011), 47-57, doi:10.1109/TPWRS.2011.2167991.
16. Gupta, N., Swarnkar, A. and Niazi, K., "A novel method for simultaneous phase balancing and mitigation of neutral current harmonics in secondary distribution systems", ***International Journal of Electrical Power & Energy Systems***, Vol. 55, (2014), 645-656, doi:10.1016/j.ijepes.2013.10.014.
17. Shahnia, F., Wolfs, P.J. and Ghosh, A., "Voltage unbalance reduction in low voltage feeders by dynamic switching of residential customers among three phases", ***IEEE Transactions on Smart Grid***, Vol. 5, No. 3, (2014), 1318-1327, doi:TSG.2014.2305752.

Persian Abstract

چکیده

در یک سیستم توزیع نیروی برق سه فاز، به علت توزیع ناهمگون بارهای تک فاز، پراکندگی بارها، الگوهای مختلف مصرف و نفوذ فزاینده منابع انرژی تجدیدپذیر در شبکه‌های هوشمند، مسأله پخش بار نامتعادل چالشی تر شده است. در این مقاله، ما یک روش جدید کاهش عدم تعادل فاز ابتکاری که با کمک تخصیص بهینه فاز برای فیدر ورودی ۳ فاز سیستم توزیع نیرو با جابجایی فاز، ذخیره‌سازهای الکتریکی و منابع انرژی تجدیدپذیر، صاحبان کنتورهای هوشمند را تشویق به کمک به اپراتور سیستم توزیع جهت کاهش نامتعادلی فاز می‌نمایند، معرفی کرده‌ایم. این مهم توسط بکارگیری سیستم تخصیص بهینه نقطه اتصال که انعطاف در انتخاب ورودی توان از یکی از ۳ فاز و مدیریت ذخیره سازها و منابع انرژی را دارد، حاصل می‌گردد.نتایج شبیه‌سازی مؤید کارایی این راهکار بوده که نشان می‌دهد مشتریان توانسته اند هزینه‌های خود را کاهش داده و اپراتور سیستم توزیع به افزایش کیفیت توان و کاهش نامتعادلی در توزیع بار دست یافته است.

International Journal of Engineering

Journal Homepage: www.ije.ir

Evaluating the Reliability of PwCOV: A Loosely Coupled Software as a Service for COVID-19 Data Processing System

A. Bora*, T. Bezboruah

Department of Electronics & Communication Technology, Gauhati University, Guwahati, Assam, India

PAPER INFO

Paper history:
Received 01 July 2020
Received in revised form 13 August 2020
Accepted 03 September 2020

Keywords:
Dataset
Load Balancing Cluster-based Web Server
Load Testing
Reliability
Software as a Service
Web Service

ABSTRACT

The pandemic coronavirus diseases 2019 are generating different data sets in different regions of the world. The data sets are observed to be available in geographically separated medical entities. However, the demand for accessing and reliable delivery of such datasets through a web-based module is increasing gradually. In this work, we propose a novel cycle of reliability evaluation model for deployment of Software as a Service-based prototype for the coronavirus disease data processing system. We call it as PwCOV. The prototype generates clinical remarks through the paradigm of service-oriented computing, cluster-based load balancing web servers, and loosely coupled software principles. The applicability of PwCOV for processing isolated disease datasets is discussed against different stress of set of user entities. The validity and applicability of the proposed model are evaluated through statistical analysis. The reliability of the PwCOV is observed by evaluating the recorded status of the business logic execution, failure count and failure rate. The study reveals that the PwCOV is affective for processing disease data set for a collaborative set of tenants. A novel methodology is designed for the deployment of software as a service for the COVID-19 data processing system using a load balancing cluster base web server, where the roles of service-oriented computing are segregated among different layers. The limitation of such deployment is also discussed for multi-tenant environment.

***doi**: 10.5829/ije.2020.33.12c.09*

1. INTRODUCTION

The worldwide pandemic issues of coronavirus diseases 2019 (COVID-19) have created a typical vision of life for human beings and societies across the globe. The experiences of symptoms with different side effects in the human body have broadened the history of COVID-19 [1]. As such, the pharmaceutical and clinical entities have become the key player for managing and handling emergency issues of health management cares [2]. According to Cortegiani et al. (2020), the clinical test cases of COVID-19 are generating regional-based different data sets based on blood samples, symptoms, population, histopathology, clinical images, and affected organs [3]. The clinical test reports of drug repositioning, antibody agents, an antimalarial drug, chemical structure, and the effect of hydroxyl chloroquine are observed to be important resources for the development of vaccines and antibody injections [4–6]. Dhouha et al. [7] had elaborated on the image data set for clinical investigation over diseases. They had discussed the feasibility of deploying a multi-tenant software environment for processing such data sets. However, in the medical industry, the deployment of software as a service (SaaS) for generating clinical reports is getting popularity [8]. With the increase in users over web-based systems, the execution of a multi-tenant environment for disease data set and observing its service reliability has become an important measure. In the health care units, the integration of data set from different geographical locations and observing the reliability of the report has also become a crucial factor for medical industries. The core problem of SaaS during COVID-19 can be categorized as follows: (a) Finding the reliability of the service, (b) Evaluating the operational limit during high usage of the service, (c) Assessing the reliability beyond the capacity of the service, and (d) Observing the nature of the distribution of service failure. As such, a proper

*Corresponding Author Email: *abhijit.bora0099@gmail.com* (A.Bora)

Please cite this article as: A. Bora, T. Bezboruah, Evaluating the Reliability of PwCOV: A Loosely Coupled Software as a Service for COVID-19 Data Processing System, International Journal of Engineering, Transactions C: Aspects, Vol. 33, No. 12, (2020), 2496-2502.

methodology is required to be developed to evaluate the reliability of service, so that the medical units can obtain an assessment of SaaS before their projection in the society. In this work, a novel SaaS oriented model as a prototype web service (WS) for COVID-19 (PwCOV) is proposed for processing disease data set. A novel reliability assessment cycle for PwCOV is also discussed to observe the reliability of such deployment during high stresses of usage. The novelty of the PwCOV from the viewpoint of service-oriented computing (SOC) can also be observed in the way of deployment methodology where the roles of SOC are segregated among WSs for consumer, parent, and service layer. This work also emphasizes the reliability evaluation of the PwCOV while executing through load balancing clustered (LBC) webserver against the massive growth of users.

2. RELATED WORK

Many authors have discussed the importance of processing the COVID-19 dataset and the role of software agents for the clinical domain [3, 7]. In the year 2017, Medhi et al. [9] had discussed a novel model to evaluate the data set processing system through the paradigm of SOC. In the year 2019, Al Azab et al. [10] had emphasized the study of clinical features for muscles, eye and ear, oral cavity, upper and lower airway, gut, cardiovascular, nervous system, urinary tract, skeleton, and skin. The properties of such a dataset are elaborated through a data model. Lai et al. [11] had introduced an index parameter over the cumulative measure of COVID-19 impact in the societies. An infection control management technique was introduced that can be followed to restrict the spread of the diseases. In the year 2020, Benjamin et al. had introduced a novel software agent called 'ChatBot' for processing interactive medical data set [8]. In the same year, Jorge et al. had introduced a data model that can be followed to evaluate the probability of the spread of the COVID-19 in native communities and societies [12]. Juan et al. [13] emphasized the deployment methodology and tool while considering the importance of mechanical ventilation management, biosafety measures, patient route management, management strategies, and patient wise ventilation mode. A novel model was introduced to implement a decision-making system based on available data reports. Gilmiyarova et al. [14] had proposed a diagnostic tool that can be deployed to evaluate the clinical remarks of oral fluid. They had introduced an empirical model to study various characteristics of data set over blood groups. In the same year, Lee et al. had carried out a study over the test case results and outcomes of treatment for COVID-19 patients [15]. The study highlighted the pros and cons of the applied treatment measure for COVID-19 infected patients. Bora and Bezboruah [16] had proposed a WS oriented model for processing clinical service. They proposed the importance of reliability and performance metrics for implementing WS for medical industries. In the same year, Lai et al. [17] had evaluated a statistical model to study the daily cumulative index for COVID-19 in different regions of the world. The analysis was carried out by preparing a data set of cumulative cases, incidence per population, number of death, death per population, mortality rate, local transmission, and days since last reported. In the research community of biomedical engineering units, medical practitioners, and pharma industries, the processing and evaluating the geographically separated data model is getting popularity, as it can provide better outcomes for the collaborative fight against COVID-19 [12]. Many authors have emphasized the importance of deploying SaaS for medical services. During the outbreak of COVID-19, the clinical remarks and instruction based on different patients asymptomatic and symptomatic are generated at different locations. As such, the clinical experiments are generating medical data set for better medical service delivery to society. In the domain of COVID-19, the delivery of clinical remarks over the web even during the high usage of the service has become the primary role. As such, the deployment of SaaS with LBC based web server can enhance the reliability of the service. With the rapid growth of medical infrastructure, the deployment of SaaS and evaluating its reliability against massive users has become a critical call for processing the COVID-19 data set. Hence, deployment of a collective support system and generation of clinical remarks among health care units and service consumers of the COVID-19 management system has become a demanding concern. This work proposes a novel reliability assessment methodology for the deployment of SaaS in LBC based web server while processing clinical remarks against the asymptomatic and symptomatic nature of COVID-19.

3. MATERIALS AND METHOD

The features of SaaS are deployed through the paradigm of service-oriented architecture (SOA) [18, 19]. The programmable interface can be developed for establishing tightly and loosely coupled SaaS modules [20, 21]. The SOC provides different communication hierarchies through WSs [22, 23]. Figure 1 shows the architecture of SaaS for the deployment of PwCOV. The hardware and software configuration for deployment is discussed elsewhere [24]. The load balancing web server is clustered into two working nodes. Each working node contains the module of PwCOV architecture. The PwCOV consists of three WS. They are: (a) consumer layer, (b) parent layer and (c) service layer, respectively for functional execution of business logic (BL). It also contains the database layer for the clinical mapping of the

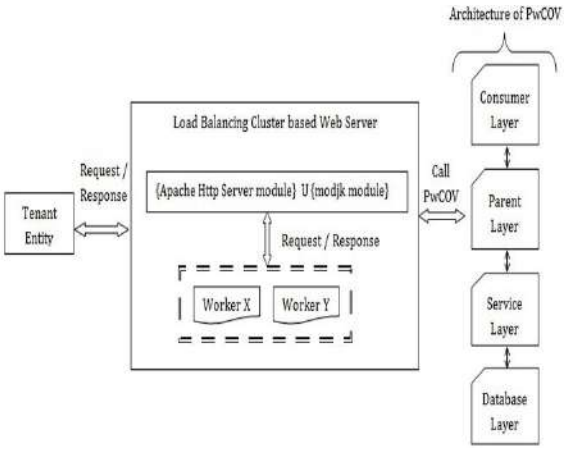

Figure 1. The architecture of SaaS deployment for PwCOV

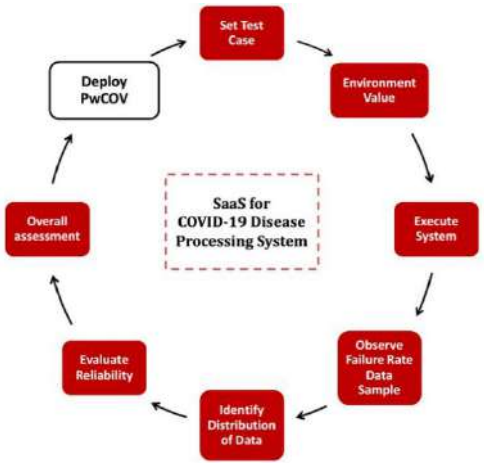

Figure 2. The cycle of the reliability evaluation model for SaaS with PwCOV

disease data set. The consumer layer contains a WS for handling the graphical user interface (GUI) of the PwCOV. The presentation code including server-side Java class files, Java Server Pages (JSP), and Javascript form controls are included in this layer. The objective of this layer is to capture end-user data and send it to the parent layer. The parent layer contains a WS for capturing, validating and forwarding the end user parameter as received from the consumer layer. The layer also responds back to the consumer layer of the query results of the service layer. The service layer contains a WS for executing functions and querying the database layer. The primary role of this layer is the establishment of the database connection, generating results set, and sending back the report to the parent layer. The database layer contains the database engine for clinical instructions of the symptoms as per COVID-19. The tenant entity is the set of system generated users that can invoke PwCOV through the cluster-based load balancing web server. The load balancing of the webserver is configured as discussed elsewhere [25]. The necessary system variables are configured to support the simultaneous execution of the working node. As such, the set of tenant will get a response of PwCOV even during the failure or high load in a particular working node. Figure 2 shows the cycle of the reliability evaluation model for evaluation of SaaS execution for PwCOV. It contains 8 steps. They are: (a) Deployment of PwCOV, (b) Set test case, (c) Environment value, (d) Execute system, (e) Observe failure rate data sample, (f) Identify the distribution of data sample, (g) Evaluating reliability, and (h) Overall assessment. In step (a), the SaaS for processing COVID-19 disease data is developed and deployed in LBC based web server after functional testing. In step (b), the test case is created. Here, the test case is set by using the Mercury LoadRunner load testing tool [26]. The test case contains the necessary path of the hosted SaaS along with instruction for fetching records through PwCOV. In step (c), the environmental value is assigned. It contains instructions for the ramp-up and ramps down of all tenants that executes the SaaS under the same testbed environment. The ramp down parameter is set to release the load gradually from the SaaS. In step (d), the system is executed. Here, the load of the tenant is generated gradually. Once, all the tenants enter the system, the SaaS is executed simultaneously by the set of enants that are active. The system is executed for a specific turnaround time. In this case, the turnaround time is set to be 15 minutes. In step (e), the failure rate data sample is observed. Here, each run of the test case against each set of tenants is observed. If failure records are observed, a data sample of 30 repetitive test is collected for further study of the data points. In step (f), the distribution of the recorded data points is identified. This step helps to identify the validation and analysis of the recorded data sample. The data sample is recorded for each turnaround system execution. The PwCOV is monitored for failure records. In step (g), the reliability metric is evaluated. The reliability metric is evaluated for the observed failure records against the stress of a set of tenants. In step (h), the overall assessment of the study is carried out. This step contains the interpretation of the data sample and concluding the overall assessment.

4. EXPERIMENTAL RESULTS

In this study, the test case is set for fetching data from the clinical data set. The test case is prepared as discussed elsewhere [27]. The PwCOV is executed for the set of tenant 50, 100, 200, 400, 600, 800, 1000, 1200, 1400, 1700 and 1800. Table 1 shows the observed records of SaaS transaction pass, fail and failure rate for the execution of PwCOV. Many studies described that "With an increase in users the connection refusal increases. This behavior is due to the garbage collected heap in the server-side" [9, 24, 27]. In this work, from Table 1, it is

TABLE 1. SaaS transaction records for PwCOV against different stress of tenant sets

Set of tenant for PwCOV	SaaS transaction pass for PwCOV	SaaS transaction fail for PwCOV	SaaS transaction failure rate for PwCOV
50	235	0	0
100	405	0	0
200	819	0	0
400	16152	0	0
600	18974	0	0
800	23547	0	0
1000	26785	0	0
1200	36251	0	0
1400	41054	0	0
1700	62982	0	0
1800	83798	40002	0.32

observed that the SaaS along with LBC based web server can manage the heap up to 1700. The role of the heap at server-side is to manage the correlation of Java class, objects, and member variables for each Hyper Text Transfer Protocol (HTTP) request. However, beyond this capacity limit, the heap error occurs, due to which the failure of HTTP processing generates. At the set of 1800 tenants, the SaaS transaction failure record of 40002 is observed out of 123800 HTTP requests. To further study the failure distribution, the data sample of 30 repeated executions is generated. However, to study the reliability metric (RM), the recorded failure record is evaluated through Equation (1) [28, 29]. The RM value is evaluated over a service time 't' and failure rate 'f' [30, 31]. In this study, 't' is set to be day one as each data sample record is collected over 30 calendar days.

$$RM=e^{-ft} \quad (1)$$

The RM is evaluated to be in the range of 0 to 1. The RM estimated value nearer to 1 reveals the strong reliability of the system. Otherwise, moderate reliable service can be observed. To study the distribution of the recorded failure rate and RM, the interpretation of histogram and normal probability plot (NPP) is followed [31]. The SaaS is stable up to 1700 tenants. That means the SaaS will process the HTTP request properly without any failure. However, the SaaS is generating a failure rate for the recorded HTTP request of 1800 tenants. To further study the failure record, the distribution of the data is evaluated through a histogram. Figure 3 and Figure 4 show the histogram of the data sample of 30 failure rate and RM against 1800 tenants. In Figure 3, it is observed that 1 data count is in the range of 0 to <=30%, 6 data count is in the range of >30% to <=32%, 11 data count is in the range of >32% to <=34%, 7 data count is in the range of

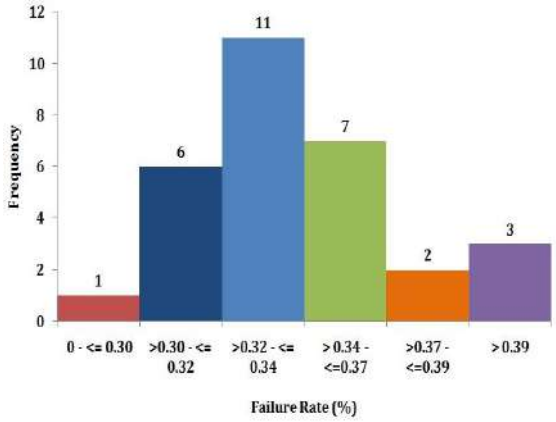

Figure 3. Histogram of observed failure rate

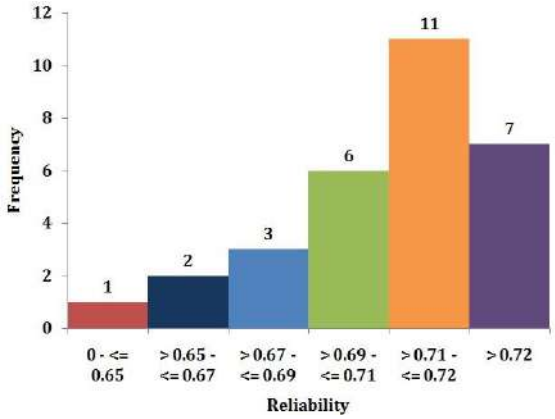

Figure 4. Histogram of observed reliability

>34% to <=37%, 2 data count is in the range of >37% to <=39% and 3 data count is in the range of >39%, respectively for failure rate. In Figure 4, it is observed that 1 data count is in the range of 0 to <=0.65, 2 data count is in the range of >0.65 to <=0.67, 3 data count is in the range of >0.67 to <=0.69, 6 data count is in the range of >0.69 to <=0.71, 11 data count is in the range of >0.71 to <=0.72% and 7 data count is in the range of >0.72%, respectively for RM. Here, for each case, a single peak value is observed. For the failure rate data sample, the highest recorded data points lie within the range of >0.32 to <= 0.34. For the RM data sample, the highest recorded data points lies within the range of >0.71 to <= 0.72. Figure 3 concludes normal distribution and Figure 4 concludes left-skewed distribution. However, based on the data range, we may evaluate different observations. As such, we evaluate further through NPP. The NPP states the normality of observed data points for each data sample of failure rate and RM. Figure 5 and Figure 6 show the NPP of the data points recorded for failure rate and RM, respectively. The data samples are linear and following the mean of the recorded parameters.

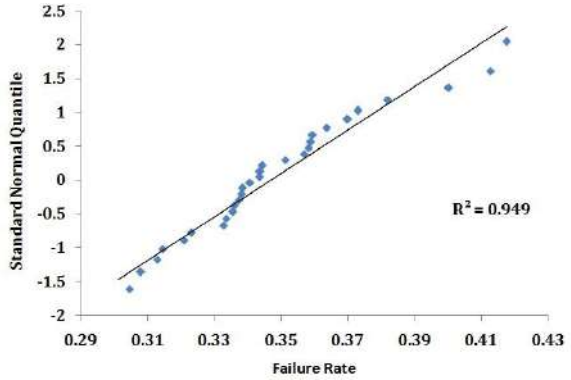

Figure 5. NPP interpretation of failure rate

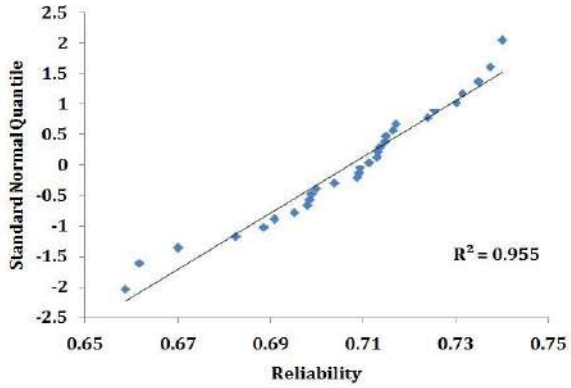

Figure 6. NPP interpretation of reliability

5. OVERALL EVALUATION

The overall evaluation of the system reveals that the RM of the PwCOV execution can be observed to be strong up to the set of 1700 tenant. However, for the set of 1800 tenant, the RM is evaluated to be within >0.71 to <= 0.72, i.e. 71% to 72% of valid service response can be obtained during that stress of 1800 tenants. The test of normality is observed for the set of data points collected for failure rate and RM. The data points are not scattering far from the mean. The applicability of the cycle of the reliability evaluation model is observed for different sets of tenants. The deployment of a cluster- based load balancing web server for executing PwCOV is observed to be valid. The stability of the consumer layer, parent layer, service layer, and database layer of PwCOV is observed for the set of tenant 1700. Beyond that set, the collaborative execution of the PwCOV layers generates a system failure response.

6. CONCLUSION

The present work proposes a novel methodology for evaluating the reliability of SaaS for the COVID-19 disease processing system. A novel architecture of PwCOV is introduced that can be executed for different stress of usages. The contribution of the work highlights the reliability evaluation of SaaS while processing clinical remarks of COVID-19 against the massive growth of multi-tenant set in LBC based web server. The work emphasizes the deployment of SaaS through the segregation of SOC roles among WSs. The reliability of SaaS is recorded to be strong while executing PwCOV up to 1700 sets of tenants. Beyond that capacity, the PwCOV is generating failure records. As such, the reliability degrades up to a range of 0.71 to 0.72. For recorded stress of 1800 tenants set, the reliability lies within 71% to 72%. The applicability of the cycle of the reliability evaluation model for SaaS with PwCOV is observed. The proposed SaaS architecture for the execution of PwCOV can deliver reliable service for processing COVID-19 disease data sets. The scalability of SaaS can be achieved for the massive growth of a set of tenants. The study can help the medical industries, software practitioners, and other clinical entities to gain an in-depth idea about reliability for the deployment of SaaS and PwCOV for processing COVID-19 data sets.

7. FUTURE PROSPECTS

The development of a model for the performance and scalability study of SaaS while processing the COVID-19 data set can mimic a scenario for any size of consumers. Undoubtedly, future work will focus on optimizing the performance aspects of SaaS for COVID-19, as it can provide effective support for the treatment delivery and reliable service to the society.

8. REFERENCES

1. Leite, H., Hodgkinson, I. R., and Gruber, T. "New development: 'Healing at a distance'—telemedicine and COVID-19." ***Public Money and Management***, Vol. 40, No. 6, (2020), 483–485. https://doi.org/10.1080/09540962.2020.1748855
2. Wang, L., Wang, Y., Ye, D., and Liu, Q. "Review of the 2019 novel coronavirus (SARS-CoV-2) based on current evidence." ***International Journal of Antimicrobial Agents***, Vol. 55, No. 6, (2020), 105948. https://doi.org/10.1016/j.ijantimicag.2020.105948
3. Cortegiani, A., Ingoglia, G., Ippolito, M., Giarratano, A., and Einav, S. "A systematic review on the efficacy and safety of chloroquine for the treatment of COVID-19." ***Journal of Critical Care***, Vol. 57, , (2020), 279–283. https://doi.org/10.1016/j.jcrc.2020.03.005
4. Mullard, A. "Drug repurposing programmes get lift off." ***Nature Reviews Drug Discovery***, Vol. 11, , (2012), 505–506. https://doi.org/https://doi.org/10.1038/nrd3776
5. Zhou, P., Yang, X. Lou, Wang, X. G., Hu, B., Zhang, L., Zhang, W., Si, H. R., Zhu, Y., Li, B., Huang, C. L., Shi, Z. L. "A pneumonia outbreak associated with a new coronavirus of probable bat origin." ***Nature***, Vol. 579, No. 7798, (2020), 270–273. https://doi.org/10.1038/s41586-020-2012-7
6. Polz-Dacewicz, M. "Novel coronavirus – SARS CoV-2." ***Polish***

Journal of Public Health, Vol. 129, No. 4, (2020), 113–117. https://doi.org/10.2478/pjph-2019-0026

7. Bacha, D., Bacha, D., Gharbi, L., Talbi, G., Ferjaoui, W., Slama, S. Ben, and Saadia, B. "Power Point in Medical Education: The Interest of Hybrid Strategies to Pass from'' Passive Power Point'' to Active Power Point''." ***International Journal of Progressive Sciences and Technologies***, Vol. 20, No. 2, (2020), 174–178. Retrieved from http://www.ijpsat.es/index.php/ijpsat/article/view/1778
8. Chaix, B., Guillemassé, A., Nectoux, P., Delamon, G., and Brouard, B. "Vik: A Chatbot to Support Patients with Chronic Diseases." ***Health***, Vol. 12, No. 07, (2020), 804–810. https://doi.org/10.4236/health.2020.127058
9. Medhi, S., Bora, A., and Bezboruah, T. "Investigations On Some Aspects of Reliability of Content Based Routing SOAP based Windows Communication Foundation Services." ***International Journal of Information Retrieval Research***, Vol. 7, No. 1, (2016), 17–31. https://doi.org/10.4018/ijirr.2017010102
10. Al Azab, M., Safi, M., and Wang, B. "ANCA-Associated Vasculitis: Advancement in Pathogenesis, Clinical Features and Management." ***Biomedical Journal of Scientific & Technical Research***, Vol. 21, No. 2, (2019), 15813–15819. https://doi.org/10.26717/bjstr.2019.21.003589
11. Lai, C. C., Wang, C. Y., Wang, Y. H., and Hsueh, P. R. "Global coronavirus disease 2019: What has daily cumulative index taught us?" ***International Journal of Antimicrobial Agents***, Vol. 55, No. 6, (2020), 106001. https://doi.org/10.1016/j.ijantimicag.2020.106001
12. Valdes, J. H., Najera, M. J., Ruiz, H. D. M., Ramirez, M. A., Lirios, C. G., and Morales, F. E. "Specification of a Social Intervention Model Against COVID-19." ***Biomedical Journal of Scientific & Technical Research***, Vol. 26, No. 3, (2020). https://doi.org/10.26717/bjstr.2020.26.004366
13. Sebastián Espinosa-Serna, J. "SARS-CoV-2, COVID 19 Useful information." ***Biomedical Journal of Scientific & Technical Research***, Vol. 27, No. 2, (2020), 20657–20668. https://doi.org/10.26717/BJSTR.2020.27.004484
14. Gilmiyarova, F., Kuzmicheva, V., Ryskina, E., Kolotyeva, N., Gusyakova, O., Baisheva, G., and Gilmiyarov, E. "Saliva as a Diagnostic Tool for AB0 Blood Group Determination." ***Biomedical Journal of Scientific & Technical Research***, Vol. 26, No. 5, (2020), 20335–20339. https://doi.org/10.26717/BJSTR.2020.26.004424
15. Lee, S. H., Son, H., and Peck, K. R. "Can post-exposure prophylaxis for COVID-19 be considered as an outbreak response strategy in long-term care hospitals?" ***International Journal of Antimicrobial Agents***, Vol. 55, No. 6, (2020), 105988. https://doi.org/10.1016/j.ijantimicag.2020.105988
16. Bora, A., and Bezboruah, T. "Some Aspects of Implementation of Web Services in Load Balancing Cluster-Based Web Server." ***International Journal of Information Retrieval Research***, Vol. 10, No. 1, (2019), 48–72. https://doi.org/10.4018/ijirr.2020010104
17. Lai, C. C., Wang, C. Y., Wang, Y. H., Hsueh, S. C., Ko, W. C., and Hsueh, P. R. "Global epidemiology of coronavirus disease 2019 (COVID-19): disease incidence, daily cumulative index, mortality, and their association with country healthcare resources and economic status." ***International Journal of Antimicrobial Agents***, Vol. 55, No. 4, (2020), 105946. https://doi.org/10.1016/j.ijantimicag.2020.105946
18. Rezaee, M. S., Haeri, A., and Noori, S. "Automotive Vendor\'s Performance Evaluation and Improvement Plan Presentation by Using a Data Envelopment Analysis." ***International Journal of Engineering, Transactions B: Applications***, Vol. 31, No. 2, (2018), 374–381. https://doi.org/10.5829/ije.2018.31.02b.23
19. Mokhtari, H., Noroozi, A., and Molla-Alizadeh-Zavardehi, S. "A Reliability based Modelling and Optimization of an Integrated Production and Preventive Maintenance Activities in Flowshop Scheduling Problem." ***International Journal of Engineering, Transactions C: Aspects***, Vol. 28, No. 12, (2015), 1774–1781. https://doi.org/10.5829/idosi.ije.2015.28.12c.10
20. Jamshidi, R. "Bi-level Model for Reliability based Maintenance and Job Scheduling." ***International Journal of Engineering, Transactions C: Aspects***, Vol. 31, No. 3, (2018), 432–439. https://doi.org/10.5829/ije.2018.31.03c.05
21. Kia, G., and Hassanzadeh, A. "HYREP: A hybrid low-power protocol for wireless sensor networks." ***International Journal of Engineering, Transactions A: Basics***, Vol. 32, No. 4, (2019), 519–527. https://doi.org/10.5829/ije.2019.32.04a.09
22. Bora, A., and Bezboruah, T. "Some Aspects of QoS for High Performance of Service-Oriented Computing in Load Balancing Cluster-Based Web Server." In Handbook of Research on Recent Developments in Intelligent Communication Application (pp. 557–592). IGI Global. Retrieved from https://pdfs.semanticscholar.org/5c1f/7fde3e2b4ed0f26b1d894a884140b67f55e4.pdf
23. Saberi Varzaneh, M., and Salajegheh, A. "Preventing Key Performance Indicators Violations Based on Proactive Runtime Adaptation in Service Oriented Environment." ***International Journal of Engineering, Transactions B: Applications***, Vol. 29, No. 11, (2016), 1539–1548. https://doi.org/10.5829/idosi.ije.2016.29.11b.07
24. Bora, A., and Bezboruah, T. "Investigation on reliability estimation of loosely coupled software as a service execution using clustered and non-clustered web server." ***International Journal of Engineering, Transactions A: Basics***, Vol. 33, No. 1, (2020), 75–81. https://doi.org/10.5829/ije.2020.33.01a.09
25. Cluster Configuration. (2020). Retrieved on April 21, 2020, from, http://tomcat.apache.org/tomcat-5.5-doc/cluster-howto.html
26. Mercury LoadRunner (2020), Retrieved online 29/03/2020, Available at: https://qageek.files.wordpress.com/2007/05/loadrunner_tutorial.pdf
27. Bora, A., and Bezboruah, T. "Testing and Evaluation of a Hierarchical SOAP based Medical Web Service." ***International Journal of Database Theory and Application***, Vol. 7, No. 5, (2014), 145–160. Retrieved from https://www.earticle.net/Article/A235208
28. Rahmani, M., Azadmanesh, A., and Siy, H. "Architectural reliability analysis of framework-intensive applications: A web service case study." ***Journal of Systems and Software***, Vol. 94, , (2014), 186–201. https://doi.org/10.1016/j.jss.2014.03.070
29. Mougiakakou, S. G., Bartsocas, C. S., Bozas, E., Chaniotakis, N., Iliopoulou, D., Kouris, I., Pavlopoulos, S., Prountzou, A., Skevofilakas, M., Tsoukalis, A., … Nikita, K. S. "SMARTDIAB: A communication and information technology approach for the intelligent monitoring, management and follow-up of type 1 diabetes patients." ***IEEE Transactions on Information Technology in Biomedicine***, Vol. 14, No. 3, (2010), 622–633. https://doi.org/10.1109/TITB.2009.2039711
30. Medhi, S., Bora, A., and Bezboruah, T. "Security Impact on e-ATM Windows Communication Foundation Services using Certificate based Authentication and Protection." ***International Journal of Information Retrieval Research***, Vol. 6, No. 3, (2016), 37–51. https://doi.org/10.4018/ijirr.2016070103
31. NIST/SEMATECH e-Handbook of Statistical Methods, (2020), Retrieved online 29/04/2020, Available at www.itl.nist.gov/div898/handbook/apr/section1/apr162.html

Persian Abstract

چکیده

بیماری همه گیر ویروس کرونا ۲۰۱۹ در مناطق مختلف جهان مجموعه داده‌های مختلفی تولید می‌کند. مجموعه داده‌ها مشاهده می‌شود که در نهادهای پزشکی استخراج شده از نظر جغرافیایی موجود است. با این حال، تقاضا برای دستیابی و تحویل مطمئن این مجموعه داده‌ها از طریق یک ماژول تحت وب به تدریج در حال افزایش است. در این پژوهش، یک چرخه جدید از مدل ارزیابی قابلیت اطمینان برای استقرار نرم‌افزار به عنوان نمونه اولیه مبتنی برخدمات برای سیستم پردازش داده‌های بیماری ویروس کرونا ارائه می‌شود که در این مقاله PwCOV نامیده می‌گردد. نمونه اولیه اظهارات بالینی را از طریق الگوی محاسبات سرویس گرا، سرورهای وب متعادل‌کننده بار خوشه‌ای و اصول نرم‌افزاری همراه ارائه می‌دهد. کاربرد PwCOV برای پردازش مجموعه داده‌های بیماری‌های جدا شده در برابر فشارهای مختلف مجموعه موجودات کاربر مورد بحث قرار گرفته است. اعتبار و کاربرد مدل پیشنهادی از طریق تجزیه و تحلیل آماری ارزیابی می‌شود. قابلیت اطمینان PwCOV با ارزیابی وضعیت ثبت شده اجرای منطق کسب و کار، شمارش خرابی و میزان خرابی مشاهده می‌گردد. این مطالعه نشان می‌دهد که PwCOV برای پردازش داده‌های بیماری برای مجموعه‌ای مشترک از Tenant تأثیرگذار است. یک روش جدید برای استقرار نرم‌افزار به عنوان سرویس برای سیستم پردازش داده COVID-19 با استفاده از یک وب سرور پایه خوشه‌ای متعادل کننده طراحی شده است، جایی که نقش محاسبات سرویس گرا در بین لایه‌های مختلف تفکیک شده است. محدودیت چنین استقرار برای محیط Multi-Tenant نیز مورد بحث قرار گرفته است.

International Journal of Engineering

Journal Homepage: www.ije.ir

A Post-disaster Assessment Routing Multi-objective Problem under Uncertain Parameters

T. S. Danesh Alagheh Band*[a,b], A. Aghsami[a,c], M. Rabbani[a]

[a] *School of Industrial Engineering, College of Engineering, University of Tehran, Tehran, Iran*
[b] *Arts et Métiers Paris Tech, Paris, France*
[c] *School of Industrial Engineering, College of Engineering, K. N. Toosi University of Technology (KNTU), Tehran, Iran*

P A P E R I N F O

Paper history:
Received 22 May 2020
Received in revised form 26 June 2020
Accepted 03 September 2020

Keywords:
Post-disaster
Assessment
Multi-objective
Grasshopper Optimization Algorithm

A B S T R A C T

Given that disasters are unavoidable, and many people are suffering from them each year, we should manage the emergencies and plan for them well to reduce mortality and financial losses. One of the measures that organizations must take after the disaster is the assessment of the conditions and needs of the people. We consider some characteristics for sites and roads and two teams for assessment as well as the uncertain assessment time to modeling. A multi-objective model is proposed in this study. The first objective function maximizes the gain from the assessment of areas and roads. The second and third objective functions maximize total coverage at damaged areas and roads. We use the LP-metric technique to solve small size problems in the GAMS software and the Grasshopper Optimization Algorithm (GOA) as a Meta-heuristic algorithm to solve a case study. Numerical results are presented to prove the credibility and efficiency of our model.

***doi**: 10.5829/ije.2020.33.12c.10*

NOMENCLATURE

Sets			
N	Set of all nodes (i,j ∈ N)	N_0	$N \cup \{0\}$, 0 is the origin node
A	Set of all arcs	RT	Set of Red Crescent Assessment Team (k ∈K)
GT	Set of Governmental Assessment Team (h∈H)	L	Set of all teams (l ∈ L)
C	Set of critical characteristics of nodes (c ∈ C)	R	Set of critical characteristics of arcs (r ∈ R)
S	Set of probability scenario (s ∈ S)		
Parameters			
$\widetilde{ta}_{il}^{s}$	The assessment time at node I under scenario s by team l	$\widetilde{ta}_{ijl}^{s}$	The assessment time at arc (i,j) under scenario s by team l
$Tmax_l^s$	The maximum time that team l is allowed to evaluate under scenario s	C_l^s	Transportation cost for team l per unit of distance under scenario s
$dmax_k^s$	The maximum distance that team k is allowed to traverse under scenario s	$dmax_h^s$	The maximum distance that team h is allowed to traverse under scenario s
d_{ij}	Distance from node $i \in N$ to node $j \in N$	d_{0i}	Distance from origin node to $i \in N$
Bud_{GT}^s	Total transportation budget of the Governmental team under scenario s	Bud_{RT}^s	Total transportation budget of the Red Crescent team under scenario s
α_{ic}^s	The probability that node i has the characteristic c under scenario s	α_{ijr}^s	The probability that arc (i,j) has the characteristic r under scenario s
p_i^s	The importance of node $i \in N$ under scenario s	q_{ij}^s	The importance of arc $(i,j) \in A$ under scenario s
E_{ij}	1 if arc $(i,j) \in A$ exists in the transportation network, and 0 otherwise		
Variables			
u_i	The sequence in which node i is visited	x_{0il}^s	1 if node i is first node in the path of the team l under scenario s, and 0 otherwise
x_{iol}^s	1 if node i is last node in the path of team l under scenario s, and 0 otherwise	x_{ijl}^s	1 if team l visits node $j \in N$ after node $i \in N$ under scenario s, and 0 otherwise
A_{il}^s	1 if team l visits node $i \in N$ under scenario s, and 0 otherwise	z_{ijl}^s	1 if team l visits arc $(i,j) \in A$ under scenario s, and 0 otherwise

*Corresponding Author Institutional Email: *mrabani@ut.ac.ir* (T. S. Danesh Alagheh Band)

Please cite this article as: T. S. Danesh Alagheh Band, A. Aghsami, M. Rabbani, A Post-disaster Assessment Routing Multi-objective Problem under Uncertain Parameters, International Journal of Engineering, Transactions C: Aspects Vol. 33, No. 12, (2020), 2503-2508.

1. INTRODUCTION

Human beings are threatened at any moment by natural and technological disasters. The number and magnitude of disasters have increased dramatically [1]. However, these catastrophes could not have been avoided, preparedness and response planning can eliminate or mitigate their casualties. Humanitarian supply chain has an important role in the efficient response to the affected people. One of the sections of this framework is Disaster Operations Management. It performs a set of operations before, during, and after a disaster [2]. As a matter of fact, effective response operations are impossible without disaster situation assessment and precise evaluation of demand for humanitarian and relief items. A comprehensive needs assessment should be started immediately after the disaster and completed within three days so assessment teams are not able to evaluate all demolished sites [3]. The rapid need assessments can gather a large amount of information about the post-disaster conditions. This information can be collected from different assessment teams (Red Crescent and governmental). They have to select a limited number of sites and roads. The rapid need assessments the sites can be sampled randomly or with purpose in order to be visited [4]. Purposive sampling comprises three stages of identifying critical characteristics, sites selection, and vehicle routing. Also, assessments can focus on sites (node) or roads (arcs) or both of them.

2. LITERATURE REVIEW

In this section, we review papers about humanitarian supply chain, and humanitarian routing papers. Çelik [5] illustrated the outcome of a general review of the literature on network reconstruction and improving humanitarian activities. Beiki et al. [6] considered a relief chain by proposing a novel location-routing model for assessing injured people under uncertainty. Oruc and Kara [7] presented a bi-objective mathematical model for collecting data from damaged areas on the transportation network. Huang et al. [8] concentrate on the assessment routing problem to evaluate demand points, and relief productivities after a disaster occurred. Kaviyani-Charati et al. [9] developed a multi-objective mathematical model to respond to disaster considering the location-transportation problem. Talarico et al. [10] illustrated an ambulance routing problem to response catastrophe. An integrated multi-objective model has been derived by Beiki et al. [11], which addressed the post-disaster challenges. Akbari et al. [12] scheduled relief teams to repair and rebuild the blocked routes. Nikoo et al. [13] studied the multi-objective model to demonstrate the optimal paths for emergency vehicles. Ostermeier and Hübner [14] studied a vehicle routing and selection problem of flexible compartment vehicles for food distribution. Nair et al. [15] presented a mathematical model for scheduling and routing. For further reading about disaster management and humanitarian logistics refer to literature [16-19]. This study presents a multi-objective model to maximize the gain from the assessment of areas and roads and the minimum cover of sites and roads. Two types of assessment teams, i.e., governmental, and Red Crescent teams are investigated. It is assumed that the governmental teams focus on the infrastructure and financial affairs, and the Red Crescent teams are more in charge of humanitarian and medical relief. The assessment times are assumed uncertain.

3. PROBLEM DESCRIPTION

For this purpose, teams and emergency agencies should be sent to affected areas. In this study, we consider two emergency teams such as Red Crescent and governmental assessment Team. We consider the following assumption for modeling:

- The division of scenarios is set up based on the intensity of the disaster and the relief items needs. We assume three scenarios: The first scenario for disaster with the least intensity and damage, the second scenario for disaster with an average level of severity and damage, the third scenario for the most severe and damage.
- The route of evaluation of each team starts from the origin node.
- Any team that leaves the origin node should return to it.
- Considering transportation budgets for teams.
- Nodes and roads have critical characteristics.
- Nodes are monitored by avoiding subtours but allowing total tours comprising the origin node.
- The assessment of each road and node is possible only by passing it.
- The limitation of the assessment time and the distance traveled have been considered.
- The assessment times are assumed to be fuzzy triangular numbers.

3. 1. Mathematical Modelling This section illustrates the mathematical model for the post-disaster assessment routing problem:

$$\text{Max Obj1} = \sum_i p_i^s \sum_l A_{il}^s + \sum_{i<j} q_{ij}^s \sum_l z_{ijl}^s \quad (1)$$

$$\text{Max Obj2} = Z_1 \quad (2)$$

$$\text{Max Obj3} = Z_2 \quad (3)$$

$$Z_1 \le \sum_{i \in N} \alpha_{ic}^s \left(\sum_l A_{il}^s\right) \quad \forall c \in C, s \quad (4)$$

$$Z_2 \le \sum_{i<j} \alpha_{ijr}^s \left(\sum_l z_{ijl}^s\right) \quad \forall r \in R, s \quad (5)$$

$$\sum_l A_{il}^s = 1 \quad \forall i \in N, s \quad (6)$$

$$\sum_{i \in N} x_{oil}^{s} = \sum_{i \in N} x_{i0l}^{s} \quad \forall l, s \tag{7}$$

$$\sum_{\substack{i \in N \\ i \neq j}} x_{jil}^{s} + x_{oil}^{s} = A_{il}^{s} \quad \forall i \in N, l, s \tag{8}$$

$$\sum_{\substack{i \in N \\ i \neq j}} x_{ijl}^{s} + x_{i0l}^{s} = A_{il}^{s} \quad \forall i \in N, l, s \tag{9}$$

$$\sum_{i \in N} x_{0il}^{s} \leq 1 \quad \forall l, s \tag{10}$$

$$\sum_{i \in N} x_{i0l}^{s} \leq 1 \quad \forall l, s \tag{11}$$

$$x_{ijl}^{s} \leq E_{ij} \quad \forall (i,j) \in A, l, s \tag{12}$$

$$z_{ijl}^{s} \leq E_{ij} \quad \forall (i,j) \in A, l, s \tag{13}$$

$$z_{ijl}^{s} \leq x_{ijl}^{s} + x_{jil}^{s} \quad \forall (i,j), (j,i) \in A, l, s \tag{14}$$

$$z_{ijl}^{s} \geq \frac{x_{ijl}^{s} + x_{jil}^{s}}{2} \quad \forall (i,j), (j,i) \in A, l, s \tag{15}$$

$$\sum_{i \in N} \widetilde{ta}_{ik}^{s} A_{il}^{s} + \sum_{(i,j) \in A} \widetilde{ta}_{ijk}^{s} z_{ijk}^{s} \leq Tmax_{k}^{s} \; \forall l \in k, k, s \tag{16}$$

$$\sum_{i \in N} \widetilde{ta}_{ih}^{s} A_{il}^{s} + \sum_{(i,j) \in A} \widetilde{ta}_{ijh}^{s} z_{ijh}^{s} \leq Tmax_{h}^{s} \; \forall l \in h, h, s \tag{17}$$

$$\sum_{(i,j) \in A} d_{ij} x_{ijl}^{s} + \sum_{i} d_{oi} x_{0il}^{s} + \sum_{i} d_{oi} x_{i0l}^{s} \leq dmax_{k}^{s} \quad \forall l \in k, k, s \tag{18}$$

$$\sum_{(i,j) \in A} d_{ij} x_{ijl}^{s} + \sum_{i} d_{oi} x_{0il}^{s} + \sum_{i} d_{oi} x_{i0l}^{s} \leq dmax_{h}^{s} \quad \forall l \in h, h, s \tag{19}$$

$$\sum_{(i,j) \in A} \sum_{l=1}^{k} C_{l}^{s} d_{ij} x_{ijl}^{s} + \sum_{l \in h} \sum_{i} C_{l}^{s} d_{oi} x_{0il}^{s} + \sum_{l \in h} \sum_{i} C_{l}^{s} d_{oi} x_{i0l}^{s} \leq Bud_{GT}^{s} \; \forall s \tag{20}$$

$$\sum_{(i,j) \in A} \sum_{l=k+1}^{k+h} C_{l}^{s} d_{ij} x_{ijl}^{s} + \sum_{l \in k} \sum_{i} C_{l}^{s} d_{oi} x_{0il}^{s} + \sum_{l \in k} \sum_{i} C_{l}^{s} d_{oi} x_{i0l}^{s} \leq Bud_{RT}^{s} \; \forall s \tag{21}$$

$$u_i - u_j + N x_{ijl}^{s} \leq N - 1 \quad \forall i, j, i \neq j, l \tag{22}$$

$$u_i, Z_1, Z_2 \geq 0 \quad \forall i \tag{23}$$

$$x_{ijl}^{s}, A_{il}^{s}, z_{ijl}^{s} \in \{0,1\} \quad \forall i, j, l, s \tag{24}$$

The first objective function (1) maximizes the total value made by evaluating the sites and roads. The objective function (2) maximizes the minimum cover of sites, which is defined by constraint (4). The objective function (3) maximizes the minimum cover of roads, which is specified by constraint (5). Equation (6) ensures that each node must be assigned to one team. Equation (7) indicates that the number of paths that each team starts is equal to the number of paths that it ends. Equations (8) and (9) ensure that each node is immediately visited after the origin node or every other node, and after that, exactly one node is visited or it returns to the origin node. In addition, these constraints make the paths between the nodes and the assigned team to be made. Constraints (10) and (11) show that each team runs a maximum of one path. Constraints (12) and (13) guarantee that each arc traversed/assessed exists in the transportation network. constraints (14) and (15) show monitoring arc (i, j) by each team. Constraints (16) and (17) guarantee that sites and roads are evaluated during the allowed time, respectively. Constraints (18) and (19) display maximum distance in order to transfer from node i to node j. Constraints (20) and (21) show transportation budget constraints for the Governmental team and Red Crescent team, respectively. Constraint (22) is for eliminating subtours. Constraint (23) defines positive variables, and constraint (24) defines the binary variables.

4. SOLUTION METHODS

Regarding this issue that model has three objective functions, the LP-metric method is used to find the optimal solution in the GAMS software. The LP-metric method is one of the multi-objective methods that minimize the deviation of each objective function from its ideal point [20]. In this method, we can define the objective function as follows:

$$\min z = \sum w_i \left(\frac{z_i^* - z_i}{z_i^*} \right) \tag{25}$$

Also, we decided to solve the case study as large size problems with GOA that was proposed by Saremi et al. [21]. It is a meta-heuristic algorithm that is inspired by the swarm's behavior of the grasshoppers. The nature-inspired algorithms rationally divide the search process into two proclivities, namely exploration, and exploitation. Immature and mature grasshoppers move slowly with small steps, and abruptly with big steps, respectively, which leads to exploration and exploitation functions. Therefore, the grasshoppers perform these two abilities naturally, and by modeling this behavior, we have a new nature-inspired algorithm. So, we applied GOA to our problem as a powerful optimization algorithm. The GAMS and the GOA ran on an Intel(R) Core (TM)2 Duo CPU with 2.26 GHz and 3 GB RAM. It should be noted that we have considered three values for each uncertain parameter, namely, optimistic, pessimistic and most likely. To solve the model, mean of uncertain parameter are calculated with following formula [22]:

$$\mu = \frac{X_o + 4X_m + X_p}{6} \tag{26}$$

5. NUMERICAL EXAMPLE

5. 1. Deterministic Method In this section, the test problems are solved under the second scenario. We solved a small size and some test problem. First, we solved the small size problem by considering an origin

node and three sites in GAMS. We also assumed four characteristics for sites and three characteristics for roads. In addition, the Red Crescent team has two assessment team members, and the Governmental team has three assessment team members. Pareto surface and Pareto front relating to this problem are depicted in Figures 1 and 2, respectively. We solved some problems with the proposed model by GAMS. The objective function values of all test problems are displayed in the Table 1.

5. 2. Meta-heuristic Method and Parameters Tuning We solved the test problems with the GOA to evaluate efficiency of it. First, we should adjust the GOA parameter such as the number of iteration (NI) and the population size of Grasshoppers (PG). For this purpose, the Taguchi method is used to adjust the parameters in the MINITAB software. We applied the L9(3**2) designing to adjust the GOA parameters. As you can see in the Figure 3, and given that the objective functions are all maximizing, the best Number of Iteration (NI) is 200 and the best Population size of Grasshoppers (PG) is 75. We solved again the test problems and obtain objective functions using the GOA to compare them with the optimal values computed by GAMS. Table 2 demonstrates the efficiency of the GOA.

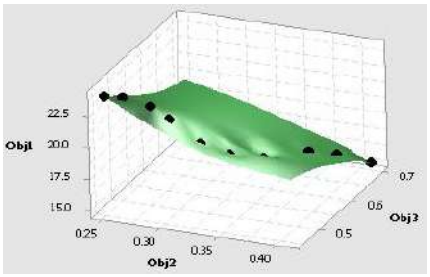

Figure 1. Pareto surface of small size problem

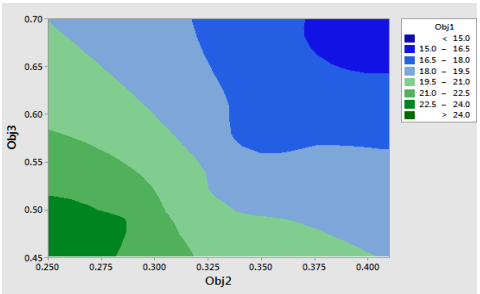

Figure 2. Pareto front of small size problem

TABLE 1. The objective values of test problems

Test problem	Node	Objective functions		
		Obj1	Obj2	Obj3
1	3	24	0.41	0.70
2	4	32	0.45	0.58
3	5	40	0.48	0.45

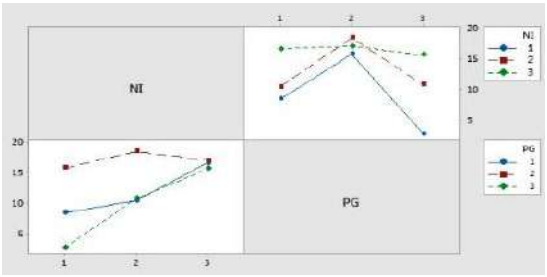

Figure 3. Mean diagrams from the Taguchi method

TABLE 2. The Comparison of exact and GOA

Test Problem	GOA			Gap %			
	Obj1	Obj2	Obj3	O1	O2	O3	Average gap
1	23.85	0.4078	0.689	0.62	0.54	1.49	0.88
2	31.79	0.4435	0.568	0.66	1.44	2.07	1.39
3	38.95	0.4699	0.444	2.62	2.10	1.24	1.99
Average				1.3	1.36	1.6	1.42

6. SENSITIVITY ANALYSIS

In this section, we changed some parameters to observe the objective functions behavior. Figure 4 displays the changes in all objective functions that are based on the changes in the total budget of the Red Crescent and the Governmental team. As shown in Figure 4, the changes on that parameter caused the first objective function to rise. When the assessment teams have more budget, they can visit and evaluate the more damaged area and roads. As a result, the second and third objective function increases too. Figure 5 shows the changes of all objective functions by changing the maximum time of the Red Crescent teams. As can be seen, the first objective function first increases with gentle gradients and then increases with a nearly steep slope. The second objective function increases with a gentle slope. The third objective function after passing a point grows slowly. We also changed the maximum evaluation time for the government team depicted in Figure 6.

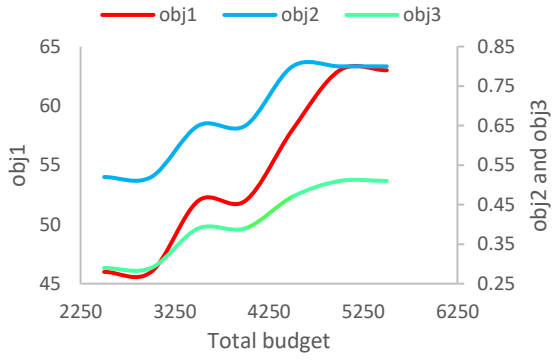

Figure 4. The impact of total budget changes of both Assessment Team on the objective functions

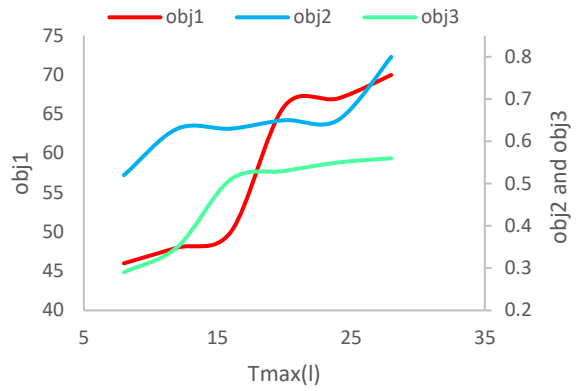

Figure 5. The impact of Tmax changes of the Red Crescent Team on the objective functions

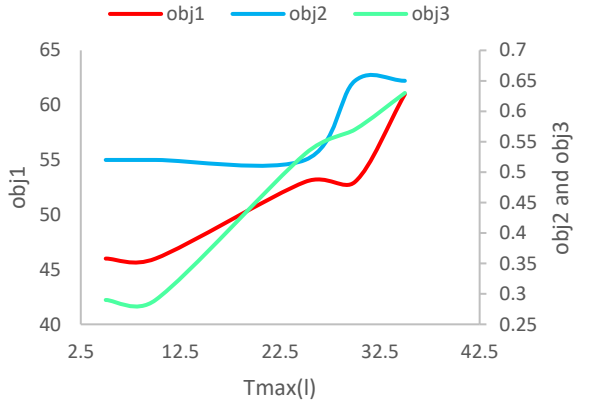

Figure 6. The impact of Tmax changes of the government Team on the objective functions

7. CASE STUDY

From mid-March to April 2019, widespread flash flooding occurred in large parts of Iran, most severely in Golestan, Khuzestan, Lorestan. In the present paper, we implement our model to Lorestan province. Heavy rains on 3 April, have entirely overwhelmed several towns in Lorestan. Figure 7 delineates Lorestan's map that damaged cities are marked with red circles, and the existing roads are marked with black lines. According to available data, we assume the flood as second scenario[1]. We consider Borujerd as the origin node, so there are sixteen roads between the damaged cities and the origin node. The cities in Lorestan may have rivers, forests, or be mountainous. Moreover, Lorestan has both smooth and mountainous roads. Therefore, we consider these characteristics for cities and roads. Figure 8 shows the Pareto front of the case study and Table 3 depicts the allocation of assessment teams.

[1] https://www.wunderground.com/cat6/Record-Floods-Iran-Kill-62-Cause-Over-1-Billion-Damage?cm_ven=cat6-widget

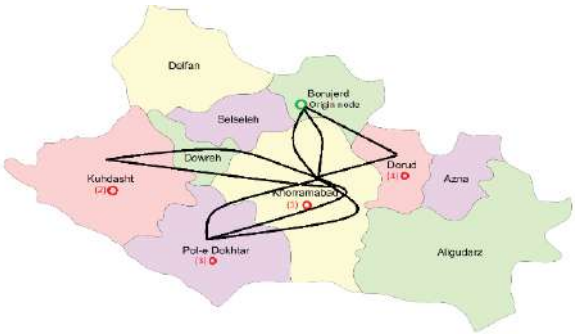

Figure 7. Lorestan's map

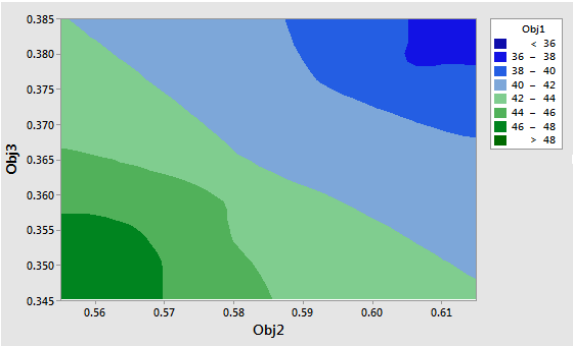

Figure 8. Pareto front of the case study

TABLE 3. The Allocation of assessment teams to nodes (RT: Red Crescent team, GT: Governmental team)

Node	Origin to i	i to j	j to origin	team
1	✓			RT3
2	✓		✓	GT2
3		✓	✓	RT3

8. CONCLUSION AND FUTURE RESEARCH

In this study, our focus was on the assessment of the conditions and requirements after the disaster. To this end, a multi-objective model is presented that can be useful for managing and planning assessment operation. The intended goals include maximizing the useful information gained from the assessment of cities and roads and the coverage of cities and roads, separately. We categorized disasters in different scenarios according to conditions and after-disaster damage and injuries. We solved the proposed model with the Lp-metric method and the GOA for several test problem. It was found that this algorithm has been efficiently applied and has useful application in real large-scale issues. Also, a case study in Lorestan, Iran is investigated. For future research, we can study a two-stage or three-stage problem. In addition to the different assessment teams that were considered in this research.

9. REFERENCES

1. Özdamar, L. and M.A. Ertem, *Models, "*solutions and enabling technologies in humanitarian logistics*",* ***European Journal of Operational Research***, Vol. 244, No. 1, (2015), 55-65. DOI: 10.1016/j.ejor.2014.11.030.
2. Altay, N. and W.G. Green III, "OR/MS research in disaster operations management", ***European Journal of Operational Research***, Vol. 175, No. 1, (2006), 475-493. DOI: 10.1016/j.ejor.2005.05.016.
3. Parmar, P., M. Arii, and S. Kayden, "Learning from Japan: Strengthening US emergency care and disaster response*"*, ***Health Affairs***, Vol. 32, No. 12, (2013), 2172-2178. DOI: 10.1377/hlthaff.2013.0704.
4. Balcik, B., "Site selection and vehicle routing for post-disaster rapid needs assessment", ***Transportation Research Part E: Logistics and Transportation Review***, Vol. 101, (2017), 30-58. DOI: 10.1016/j.tre.2017.01.002
5. Çelik, M., "Network restoration and recovery in humanitarian operations: Framework, literature review, and research directions", ***Surveys in Operations Research and Management Science***, Vol. 21, No. 2, (2016), 47-61. DOI: 10.1016/j.sorms.2016.12.001.
6. Beiki, H., Seyedhosseini, S.M., Ghezavati, V.R. and Seyedaliakbar, S.M., "A Location-Routing Model for Assessment of the Injured People and Relief Distribution under Uncertainty*",* ***International Journal of Engineering, Transactions A: Basics***, Vol. 33, No. 7, (2020), 1274-1284. DOI: *10.5829/ije.2020.33.07a.14*.
7. Oruc, B.E. and B.Y. Kara, "Post-disaster assessment routing problem*".* ***Transportation Research Part B: Methodological***, Vol. 116, (2018),76-102. DOI: 10.1016/j.trb.2018.08.002.
8. Huang, M., K.R. Smilowitz, and B. Balcik, "A continuous approximation approach for assessment routing in disaster relief*"*. ***Transportation Research Part B: Methodological***, Vol. 50, (2013), 20-41. DOI: 10.1016/j.trb.2013.01.005.
9. Kaviyani-Charati, M., F. Heidarzadeh Souraki, and M. Hajiaghaei-Keshteli, "A Robust Optimization Methodology for Multi-objective Location-transportation Problem in Disaster Response Phase under Uncertainty", ***International Journal of Engineering, Transactions B: Applications***, Vol. 31, No. 11, (2018). 1953-1961. doi: 10.5829/ije.2018.31.11b.20
10. Talarico, L., F. Meisel, and K. Sörensen, "Ambulance routing for disaster response with patient groups*",* ***Computers & Operations Research***, Vol. 56, (2015), 120-133. DOI: 10.1016/j.cor.2014.11.006.
11. Beiki, H., Seyedhosseini, S.M., Ghezavati, V.R. and Seyedaliakbar, S.M., "Multi-objective Optimization of Multi-vehicle Relief Logistics Considering Satisfaction Levels under Uncertainty", ***International Journal of Engineering, Transactions B: Applications***, Vol. 33, No. 5, (2020). 814-824. DOI: 10.5829/ije.2020.33.05b.13.
12. Akbari, V. and F.S. Salman, "Multi-vehicle synchronized arc routing problem to restore post-disaster network connectivity*",* ***European Journal of Operational Research***, Vol. 257, No. 2, (2017), 625-640. DOI: 10.1016/j.ejor.2016.07.043.
13. Nikoo, N., M. Babaei, and A.S. Mohaymany, "Emergency transportation network design problem: Identification and evaluation of disaster response routes*",* ***International Journal of Disaster Risk Reduction***, Vol. 27, (2018), 7-20. DOI: 10.1016/j.ijdrr.2017.07.003.
14. Ostermeier, M. and A. Hübner, "Vehicle selection for a multi-compartment vehicle routing problem". ***European Journal of Operational Research***, Vol. 269, No. 2, (2018), 682-694.DOI: 10.1016/j.ejor.2018.01.059.
15. Nair, D.J., Grzybowska, H., Fu, Y. and Dixit, V.V., "Scheduling and routing models for food rescue and delivery operations", ***Socio-Economic Planning Sciences***, Vol. 63, (2018), 18-32. DOI: *10.1016/j.seps.2017.06.003*.
16. Alinaghian, M., M. Aghaie, and M.S. Sabbagh," A mathematical model for location of temporary relief centers and dynamic routing of aerial rescue vehicles", ***Computers & Industrial Engineering***, Vol. 131, (2019), 227-241. DOI: 10.1016/j.cie.2019.03.002.
17. Javadian, N., S. Modares, and A. Bozorgi-Amiri, "A bi-objective stochastic optimization model for humanitarian relief chain by using evolutionary algorithms", ***International Journal of Engineering, Transactions A: Basics***, Vol. 30, No. 10, (2017). 1526-1537. doi: 10.5829/ije.2017.30.10a.14
18. Abazari, S.R., A. Aghsami, and M. Rabbani, "Prepositioning and distributing relief items in humanitarian logistics with uncertain parameters", ***Socio-Economic Planning Sciences***, (2020). DOI: 10.1016/j.seps.2020.100933. In Press.
19. Nikkhoo, F. and A. Bozorgi-Amiri, "A Procurement-distribution Coordination Model in Humanitarian Supply Chain Using the Information-sharing Mechanism", ***International Journal of Engineering, Transactions A: Basics***,, Vol. 31, No. 7, (2018), 1057-1065. doi: 10.5829/ije.2018.31.07a.08
20. Isaloo, F. and M.M. Paydar," Optimizing a robust bi-objective supply chain network considering environmental aspects: a case study in plastic injection industry", ***International Journal of Management Science and Engineering Management***, Vol. 15, No.1, (2020),26-38. DOI: 10.1080/17509653.2019.1592720.
21. Saremi, S., S. Mirjalili, and A. Lewis, "Grasshopper optimisation algorithm: theory and application*",* ***Advances in Engineering Software***, Vol. 105, (2017), 30-47. DOI: 10.1016/j.advengsoft.2017.01.004.
22. Perry, C. and I. Greig, "Estimating the mean and variance of subjective distributions in PERT and decision analysis", ***Management Science***, Vol. 21, No. 12, (1975), 1477-1480. DOI: 10.1287/mnsc.21.12.1477.

Persian Abstract

چکیده

با توجه به اینکه حوادث غیرقابل اجتناب است و هر ساله افراد زیادی از آنها رنج می برند ، باید حوادث را مدیریت کنیم و به خوبی برای آنها برنامه ریزی کنیم تا تلفات و خسارات مالی را کاهش دهیم. یکی از اقداماتی که سازمانها پس از فاجعه باید انجام دهند ، ارزیابی شرایط و نیازهای مردم است. ارزیابی باید در اسرع وقت انجام شود و اطلاعات باید سریع جمع آوری شود. ما چند ویژگی برای سایت ها و جاده ها و دو تیم متفاوت برای ارزیابی و همچنین زمان ارزیابی غیر قطعی برای مدل سازی در نظر می گیریم. یک مدل برنامه ریزی عدد صحیح ترکیبی چند هدفه در این مقاله ارائه شده است. اولین تابع هدف حداکثر بهره حاصل از ارزیابی مناطق و جاده ها را به حداکثر می کند. تابع هدف های دوم و سوم پوشش را در مناطق و جاده های آسیب دیده به حداکثر می رسانند. ما از روش LP-متریک برای حل مسائل کوچک در نرم افزارگمز(GAMS) و الگوریتم بهینه سازی ملخ به عنوان یک الگوریتم فرا ابتکاری برای حل مسایل در اندازه های بزرگ استفاده می کنیم. نتایج عددی برای اثبات اعتبار و کارایی مدل ارائه شده است.

International Journal of Engineering

Journal Homepage: www.ije.ir

A New Method for Computation the Success Probability of Coverage for Switch Unit in the Switching Systems

A. Yaghoubi*[a], P. Gholami[b]

[a] *Department of Industrial Engineering, Sharif University of Technology, Tehran, Iran*
[b] *Department of Aerospace Engineering, Sharif University of Technology, Tehran, Iran*

PAPER INFO

Paper history:
Received 09 April 2020
Received in revised form 06 August 2020
Accepted 05 September 2020

Keywords:
Redundancy
Switching Systems
Switch Mechanism
Stress-Strength Method

ABSTRACT

Redundancy technique is used to improve performance and achieving to increase the lifetime of a system. Nowadays, the redundancy method is applied in many industries. One of the common methods of redundancy is its utilization in the switching systems. In switching systems, one or more components are considered active mode and the others in the standby state to be used by switch if necessary. In order to be fully utilized all the components in the redundant device, the switch unit must perform its function, such as switching, perfectly. Successful coverage by switch unit is expressed with a probability. In this paper, a new approach to the likelihood of switch success is proposed, and showing that as increases switching in the system, the efficiency and performance of the switch gradually decreases. The analysis of this method was based on the stress-strength method. Finally, a few numerical examples for the validation of results were applied.

***doi**: 10.5829/ije.2020.33.12c.11*

1. INTRODUCTION

In recent years, the word "redundancy" has been considered one of the idioms that researchers widely used frequently in the reliability field. Redundancy in a system means that there is an alternative path to successful system performance and to enhance machine reliability, it used. The redundancy method is widely used in the switch component in the construction of the complex system and other mechanical systems. The switch unit in the switching systems are usually exposed to various loadings in different situations. Therefore, in order to prevent unknown failures, it is necessary to investigate and analyze the failure probability of switch before their implementation.

Generally, redundancy divided into active (static) redundancy and standby (dynamic) redundancy categories. In active redundancy, all components operate simultaneously at time zero. In other words, all components of the system are exposed to tension and failure. For the active redundancy, *k*-out-of-*n* systems are an example of these types of systems. Whereas in standby redundancy, redundant components are sequentially put into operation when the active one fails, *k*-out-of-*n* standby systems are well-known examples of these types of systems [1, 2].

Standby redundancy is classified into three types: cold, warm, and hot standby. In the cold standby state, the redundant components are completely dormant and do not fail in this mode, in fact, the failure rate in cold standby is zero. The other state is the hot standby mode. The pressure that the components tolerate in the hot state, is exactly the same as that in the fully active state. Finally, the standby mode which is far more complex in terms of mathematical modeling than the two previous ones is warm standby. In this situation, the components are in the semi-active state, hence less pressure than in the fully-active state. So, their failure rate in warm mode is lower than their failure rate in active mode [1-5].

The redundancy allocation problem (RAP) is one of the most important problems in applying the redundancy technique. RAP history goes back to the introduction of a system by Fyffe [6]. He considered a system with 14 subsystems and in each subsystem, there were three or

*Corresponding Author Email: *yafshin50@yahoo.com* (A. Yaghoubi)

Please cite this article as: A. Yaghoubi, P. Gholami, A New Method for Computation the Success Probability of Coverage for Switch Unit in the Switching Systems, International Journal of Engineering, Transactions C: Aspects Vol. 33, No. 12, (2020), 2509-2513.

four different components connected in parallel. Numerous researchers have analyzed Fyffe system reliability using various methods and assumptions. For example, it could be referred to as the works of Ardakan et al. [3], Guilani et al. [7], Sajjadi et al. [8], and Aziz Mohammadi et al. [9].

The main emphasis of this article has been to develop a method based on the stress-strength approach that can be used to find the failure probability of detector/switch unit in complex systems in the second scenario (i.e., detection and switching only at time of failure). This proposed method can be used in the optimization redundancy allocation problem to the selection of components with appropriate levels of redundancy or reliability to maximize the system reliability under some predefined constraints.

2. SWITCH UNIT PERFORMANCE

In switching systems, the switch unit is of particular importance; because it has a duty too, if necessary, inter the redundant components into the circuit for operation. In research related to switching systems, there are two mechanisms for coverage. The first mechanism is the perfect switch. That is, the switch unit, it is 100% reliable and failure-free during its mission. But in reality, the switch device will be damaged due to the stresses that are applied to it during the mission, i.e., the switch is incomplete, this means that the switch, will fail like other components of the system.

Yaghoubi et al. [1], Wu and Wu [10], Huang et al. [11], have used in their models, assuming of the perfect switch, whereas, Coit [5], Pan [12], Kececioglu and Jiang [13], Jia et al. [4], Amari [14] and Sadeghi and Roghanian [15] have used imperfect switching in their work.

2. 1. Problem Statement Generally, there are two scenarios called the first scenario (i.e., continual monitoring and detection) and the second scenario (i.e., detection and switching only at time of failure) for switching component mechanisms in switching systems [5]. Usually, the first scenario is given more concern by the authors, whilst in the second scenario, probably nothing has been done because of its simple mathematical model, and for it, a constant probability is considered. So, in this study, we are concerned with the second scenario.

In recent decades, extensive researches have been conducted on investigating the first scenario and its application in complex systems [16-18]. But based on the second scenario, there are not a method to calculate the failure probability of switch device in switching systems. Hence, probability analysis of the switching system requires further investigations in the field of the second scenario.

The first scenario in terms of computation, is more complex than the second scenario, especially when the number of system components increases and as well as, the time-to-failure of component follows the non-exponential distributions. But in the second scenario, typically, a constant probability of success for the changeover element (denoted P_S) is considered. The P_S , is obtained ratio the number of successful switches to the total number of trials possible [19].

In practice, the switch unit is subjected to various stresses due to its dynamics during its mission. So, the probability of failure of the switch unit increase over time. Therefore, it is expected that the success probability of the switch unit will decrease at each switching, and it will not be constant during the mission. Hence, in our study, we are most concerned about the second scenario in which, the probability of the switch unit has been considered constant according to previously conducted studies, while in this study the probability of switch at each step is calculated according to the proposed method. For this purpose, in this study, the stress-strength probabilistic method is used to analyze the performance of the switch unit. In the stress-strength approach, stress or load refers to the set of environment activities which tends to increase of failure a component, whereas, strength is the ability of that component versus to the environmental loads [20]. For the applications of redundancy strategies, unlike other approaches in the second scenario, this method because of the use of non-constant probability for switch unit, to make it more realistic.

The switch performance is decreased for a variety of physical reasons, such as consecutive coverages. In other words, if the number of switching will be increased, the performance of the switch unit decreased. If the components of the system (active and standby components) represented stresses applied to the switch, and the switch component stands for strength, then, in order for the switch would not fail, strength must be dominated on stress, i.e., it must be Pr (Strength> Stress). In fact, the lifetime of the switch should be more than the sum of the lifetime of the system all components.

Let us consider a system with an active component and (n - 1) standby components. By assuming that all spare components do not fail in the standby state. In this case, the number of successful changeovers for the switch unit is (n - 1). So, if T_s and T_j , be lifetimes of the switch and jth active component, respectively that follows any possible distribution, then the probability that the switch can control all components of the switching system should have a longer lifetime than the total lifetime of the system components.

If ρ_i , be the probability of successful switching of the i^{th} order, then calculating this probability is as follows:

$$\rho_i = Pr\left(T_s \geq \sum_{j=0}^{i} T_j\right) = \int_0^{\infty}\int_s^{\infty} f_{S_j}(s) f_{T_s}(t)\,dtds$$
$$= \int_0^{\infty}\int_0^{t} f_{T_s}(t) f_{S_j}(s)\,dsdt; \quad i = 1,\ldots,n-1 \tag{1}$$

where *j* denotes the time of failure of system components. The probability density function (PDF), of the summation of these variables, i.e., $S_n = T_1 + T_2 + \ldots + T_n$ is obtained as follows [21]:

$$f_{S_n}(s) = \left[\prod_{i=1}^{n}\lambda_i\right]\sum_{j=1}^{n}\frac{e^{-\lambda_j s}}{\prod_{\substack{k=1\\k\neq j}}^{n}\left(\lambda_k - \lambda_j\right)}; \; s > 0 \tag{2}$$

In special case, where all exponential parameters are identical with a constant failure rate $\lambda_i = \lambda$, for each of *i*'s, Equation (2) simplifies to the following form:

$$f_{S_n}(s) = \frac{\lambda^n}{\Gamma(n)} s^{n-1} e^{-\lambda s}; \; s > 0 \tag{3}$$

where $\Gamma(.)$, is the gamma function. Equation (3) shows the PDF of the gamma distribution with shape parameter *n* and scale parameter λ.

Now, let's consider a system with *n* component. By assuming that all spare components do not fail in the standby state. As mentioned, to use all the standby components in the system, (*n*-1) successful switching is required for the switch unit.

If T_j follows the exponential distribution with the parameter λ_j $\left(f_{T_j}(t) = \lambda_j e^{-\lambda_j t}, t > 0\right)$, then ρ_i can be expressed as:

$$\rho_i = \left[\prod_{j=0}^{i}\lambda_j\right]\sum_{j=0}^{i}\frac{1}{\left(\lambda_j + \lambda_s\right)\left(\prod_{\substack{k=0\\k\neq j}}^{i}\left(\lambda_k - \lambda_j\right)\right)} \tag{4}$$
$$i = 1,\ldots,n-1$$

If all system components are identical, $\lambda_j = \lambda$, then ρ_i is computation from the following equation:

$$\rho_i = \left(\frac{\lambda}{\lambda + \lambda_s}\right)^i; i = 1,\ldots,n-1 \tag{5}$$

3. NUMERICAL EXAMPLE

Regarding the results obtained in sections 2, some numerical example is solved.

Example 1. Consider a redundant system with 6 dissimilar components that are operating with one component at the first, and 5 components are available in the standby state to replace the failed component. Failure rate of components are given in Table 1.

For different values of the failure rate of the switch unit, the switch reliability in each of switching has been evaluated by using Equation (4). These results are presented in Table 2. According to Table 2, as expected, the performance of the switch unit decreases due to the increase in switching. When $\lambda_s = 0$, it means $\rho_i = 1$, for each *i*. In other words, the switch is the completely reliable, or so-called perfect switch. If all the components of the system are identical and their failure rate in the active mode is equal to 0.01, and the failure rate of the switch unit is equal to 0.0001 failure per hour, then result of the success probability for the switch unit in each of changeover (or ρ_i 's) according to Equation (5), are apparent in the Table 3.

Example 2. One of the continuous statistical distributions in statistics and probability theory is Gamma distribution. The probability density function (pdf) of the Gamma distribution with shape parameter k and scale parameter λ is given by $f(t) = \frac{\lambda^k}{\Gamma(k)} t^{k-1} e^{-\lambda t}$ [22]. This distribution is widely used in various fields. If $k = 1$, the exponential distribution is obtained. When *k* is a positive integer, then the distribution represents an Erlang distribution and for large k the gamma distribution converges to a normal distribution.

TABLE 1. Failure rate for components system

λ_0	λ_1	λ_2	λ_3	λ_4	λ_5
0.01	0.02	0.03	0.04	0.05	0.06

TABLE 2. Switch reliability with identical units

λ_s	0	10^{-6}	10^{-4}	10^{-2}
ρ_1	1.000	0.9999	0.9852	0.3333
ρ_2	1.000	0.9998	0.9819	0.2500
ρ_3	1.000	0.9998	0.9795	0.2000
ρ_4	1.000	0.9998	0.9775	0.1667
ρ_5	1.000	0.9998	0.9759	0.1429

TABLE 3. Reliability of switch with identical units

ρ_1	ρ_2	ρ_3	ρ_4	ρ_5
0.9091	0.8264	0.7513	0.6830	0.6209

TABLE 4. Reliability of switch for Example 2

k_s	ρ_1	ρ_2	ρ_3
0.5	0.6152	0.5705	0.5410
1	0.8658	0.8379	0.8174
2.5	0.9955	0.9938	0.9923
3	0.9986	0.9980	0.9975

Consider a system of 1-out-of-4 with non-identical components. In this case, three switchings are required to use all the components in the system. If the failure time of the switch unit follows the Gamma distribution with different parameters of k_s that listed in Table 4 and the parameter scale $\lambda_s = 0.01$, and time to failure of all system components in active state follows the exponential distribution with the failure rate $\lambda_i = 0.i$; $i = 1, 2, 3, 4$, then, according to Equation (1), the success probability of the switch at each stage of the switching is calculated. These results are presented in Table 4. It can be observed that the increase in value of k_s leads to higher probability. Moreover, calculating the probability values of ρ_i in the above table, when $k_s = 1$, can be also obtained from Equation (4). The reliability function of mentioned system is equal to:

$$R_S(t) = r_1(t) + \rho_1 I_1 + (\rho_1\rho_2) I_2 + (\rho_1\rho_2\rho_3) I_3 \qquad (6)$$

Where, I_1, I_2, and I_3 are the convolution integrals, and determined as follows:

$$I_1 = \int_0^t f_0(t_0) r_1(t - t_0) dt_0$$

$$I_2 = \int_0^t \int_0^{t-t_0} f_0(t_0) f_1(t_1) r_2(t - t_0 - t_1) dt_1 dt_0 \qquad (7)$$

$$I_3 = \int_0^t \int_0^{t-t_0} \int_0^{t-t_0-t_1} \prod_{j=0}^{2} f_j(t_j) r_3(t - \sum_{i=0}^{2} t_i) dt_2 dt_1 dt_0$$

Now, as for Example 2 and Table 4, we want to evaluate the reliability function of the system up to the 100-hour mission. Figure 1, shows the computing of system reliability, i.e., Equation (6), up to time t=100, hours.

In the above figure, the reliability function of the system is plotted with different values of shape parameters in Table 4. It is clear that as the value of k_s increases, the reliability functions are equal.

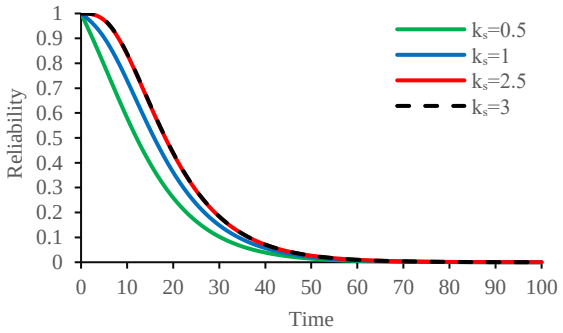

Figure 1. Reliability functions diagram

It is obvious that these values are obtained for validation of the implemented model with the system only five components subjected to a specific situation and are expected to be different for other types of systems or under different situations. As a result, it is suggested that the very complex switching systems with lots of sub-systems and the choice of multiple components be identified by the approach developed in the present study. For this purpose, due to the limited available experimental data, Taguchi method [23], which could be employed as a virtual laboratory to extract required data for a theoretical model, is proposed for future studies to determine probability analysis of switch in complex switching system with various stochastic uncertainty, in addition, to optimization redundancy allocation problem.

4. CONCLUSION

This study aimed to propose a new method for calculating the probability of the switch unit in the changeover condition (second scenario for the switch mechanism in reference [5]). It should be noted that in this method, it has been assumed that unlike the previous studies in the second scenario, the probability of the switch is not constant and the probability of switch unit at each step is calculated according to the proposed method. So, having the time-to-failure of switch unit and components, this probability assessment can be performed on the system. The evaluation of this probability was based on the stress-strength method. In this method, the switch unit represents strength, while other system components demonstrate stress, then in order for the switch to be able to overcome all system components, it must be able to properly connect all subsystem components into the system if required. The developed method was then applied to some numerical example and observed that the performance of the switch decreases as expected by increasing the switching in the system, or in other words by increasing the spare parts in the system. Thus, using developed approach, probability of any switching system under other failure mechanisms and optimization redundancy allocation problem can be investigated which is an ongoing research by the authors.

6. REFERENCES

1. Yaghoubi, A., Niaki, S.T.A. and Rostamzadeh, H., "A closed-form equation for steady-state availability of cold standby repairable k-out-of-n", ***International Journal of Quality & Reliability Management***, Vol. 37, No. 1, (2019), 145-155, doi: 10.1108/IJQRM-08-2018-0212.

2. Levitin, G., Xing, L. and Dai, Y., "Optimal design of hybrid redundant systems with delayed failure-driven standby mode transfer", ***IEEE Transactions on Systems, Man, and***

Cybernetics: Systems, Vol. 45, No. 10, (2015), 1336-1344, doi: 10.1109/TSMC.2015.2399472.

3. Ardakan, M.A. and Rezvan, M.T., "Multi-objective optimization of reliability–redundancy allocation problem with cold-standby strategy using NSGA-II", ***Reliability Engineering & System Safety***, Vol. 172, No., (2018), 225-238, doi: 10.1016/j.ress.2017.12.019.
4. Jia, X., Chen, H., Cheng, Z. and Guo, B., "A comparison between two switching policies for two-unit standby system", ***Reliability Engineering & System Safety***, Vol. 148, (2016), 109-118, doi: 10.1016/j.ress.2015.12.006.
5. Coit, D.W., "Cold-standby redundancy optimization for nonrepairable systems", ***Iie Transactions***, Vol. 33, No. 6, (2001), 471-478, doi: 10.1023/A:1007689912305.
6. Fyffe, D.E., Hines, W.W. and Lee, N.K., "System reliability allocation and a computational algorithm", ***IEEE Transactions on Reliability***, Vol. 17, No. 2, (1968), 64-69, doi: 10.1109/TR.1968.5217517.
7. Guilani, P.P., Sharifi, M., Niaki, S. and Zaretalab, A., "Redundancy allocation problem of a system with three-state components: A genetic algorithm", ***International Journal of Engineering, Transactions B: Applications***, Vol. 27, No. 11, (2014), 35-43, doi: 10.5829/idosi.ije.2014.27.11b.03.
8. Zangeneh, E., Makui, A., Sadjadi, S. and Mohammadi, S.E., "Reliability optimization for complicated systems with a choice of redundancy strategies", ***International Journal of Engineering, Transactions A: Basics***, Vol. 28, No. 10, (2015), 1476-1485, doi: 10.5829/idosi.ije.2015.28.10a.11.
9. Tavakkoli-Moghaddam, R., Amiri, M. and Azizmohammadi, R., "Solving a redundancy allocation problem by a hybrid multi-objective imperialist competitive algorithm", ***International Journal of Engineering, Transactions C: Aspects***, Vol. 26, No. 9, (2013), 1031-1042, doi: 10.5829/idosi.ije.2013.26.09c.10.
10. Wu, Q. and Wu, S., "Reliability analysis of two-unit cold standby repairable systems under poisson shocks", ***Applied Mathematics and computation***, Vol. 218, No. 1, (2011), 171-182, doi: 10.1016/j.amc.2011.05.089.
11. Huang, W., Loman, J. and Song, T., "A reliability model of a warm standby configuration with two identical sets of units", ***Reliability Engineering & System Safety***, Vol. 133, (2015), 237-245, doi: 10.1016/j.ress.2014.09.008.
12. Pan, J.-N., "Reliability prediction of imperfect switching systems subject to multiple stresses", ***Microelectronics Reliability***, Vol. 37, No. 3, (1997), 439-445, doi: 10.1016/S0026-2714(96)00046-7.
13. Kececioglu, D. and Jiang, S., "Reliability of a repairable standby system with imperfect sensing and switching", in Annual Proceedings on Reliability and Maintainability Symposium, IEEE., (1990), 260-267, doi: 10.1109/ARMS.1990.67967.
14. Amari, S.V., "Reliability of k-out-of-n standby systems with gamma distributions", in 2012 Proceedings Annual Reliability and Maintainability Symposium, IEEE., (2012), 1-6, doi: 10.1109/RAMS.2012.6175471.
15. Sadeghi, M. and Roghanian, E., "Reliability analysis of a warm standby repairable system with two cases of imperfect switching mechanism", ***Scientia Iranica***, Vol. 24, No. 2, (2017), 808-822, doi: 10.24200/SCI.2017.4063.
16. Kim, H. and Kim, P., "Reliability–redundancy allocation problem considering optimal redundancy strategy using parallel genetic algorithm", ***Reliability Engineering & System Safety***, Vol. 159, (2017), 153-160, doi: 10.1016/j.ress.2016.10.033.
17. Sadeghi, M. and Roghanian, E., "Reliability optimization for non-repairable series-parallel systems with a choice of redundancy strategies: Erlang time-to-failure distribution", ***Proceedings of the Institution of Mechanical Engineers, Part O: Journal of Risk and Reliability***, Vol. 231, No. 5, (2017), 587-604, doi: 10.1177/1748006X17717615.
18. Feizollahi, M.J., Ahmed, S. and Modarres, M., "The robust redundancy allocation problem in series-parallel systems with budgeted uncertainty", ***IEEE Transactions on Reliability***, Vol. 63, No. 1, (2014), 239-250. doi: 10.1109/TR.2014.2299191
19. Billinton, R. and Allan, R.N., Reliability evaluation of engineering systems, Springer, (1992).
20. Dhillon, B.S., "Stress—strength reliability models", ***Microelectronics Reliability***, Vol. 20, No. 4, (1980), 513-516, doi: 10.1016/0026-2714(80)90599-5.
21. Radmard, M., Chitgarha, M.M., Majd, M.N. and Nayebi, M.M., "Antenna placement and power allocation optimization in mimo detection", ***IEEE Transactions on Aerospace and Electronic Systems***, Vol. 50, No. 2, (2014), 1468-1478, doi: 10.1109/TAES.2014.120776.
22. Ghahramani, S., Fundamentals of probability with stochastic process, Pearson Education India, (2005).
23. Roy, R.K., Design of experiments using the taguchi approach: 16 steps to product and process improvement, John Wiley & Sons, (2001).

Persion Abstract

چکیده

به منظور کارکرد بهتر و افزایش طول عمر سیستم‌ها از تکنیک افزونگی استفاده می‌شود. امروزه از روش افزونگی در بسیاری از صنایع استفاده می‌شود. بهترین استفاده از این روش، استفاده آن در سیستم‌های سویچینگ است. در سیستم‌های سویچینگ، یک یا چند جز در حالت فعال و بقیه در حالت ذخیره هستند تا در صورت لزوم توسط سوییچ از آن‌ها استفاده شود. برای آن‌که دستگاه افزونه بتواند به طور کامل از تمامی اجزای موجود خود استفاده کند، جز سوییچ باید وظیفه خود مثل کلیدزنی را بدون نقص انجام دهد. کلیدزنی موفق در جز سوییچ با یک احتمال صورت می‌گیرد. در این مقاله، یک روش جدید برای احتمال موفقیت سوییچ پیشنهاد شده است و نشان می‌دهد که با افزایش کلیدزنی‌ها در سیستم، کارایی و عملکرد سوییچ به تدریج کاهش می‌یابد. تحلیل این روش بر اساس رویکرد احتمالی قدرت – فشار بوده است. در نهایت، به منظور صحت و اعتبار نتایج به‌دست آمده، چند مثال عددی زده شده است.

International Journal of Engineering

Journal Homepage: www.ije.ir

Experimental Investigation of Friction Pressure Influence on the Characterizations of Friction Welding Joint for AISI 316

A. Jabbar Hassan*[a], T. Boukharouba[a], D. Miroud[b], N. Titouche[c], S. Ramtani[d]

[a] *LMA, USTHB, BP. 32, El-Alia, 16111 Bab-Ezzoaur, Algiers, Algeria*
[b] *LSGM, USTHB, BP. 32; El-Alia, 16111 Bab-Ezzouar, Algiers, Algeria*
[c] *DEMEM, DTN, Centre de Recherche Nucléaire de Birine, BP. 180, Ain Oussera, Djelfa, Algeria*
[d] *CSPBAT – LBPS, UMR 7244 CNRS, Paris University 13, Galilée Institute, 99, J.B. Clément Street, Villetaneuse, France*

PAPER INFO

Paper history:
Received 02 April 2020
Received in revised form 23 April 2020
Accepted 12 June 2020

Keywords:
Austenitic Stainless Steel
Friction Pressure
Hardness
Micro-hardness
Ultimate Tensile Strength

ABSTRACT

This study focuses on the effect of friction pressure on the welding joint strength of AISI 316. Single factor method was used to evaluate the influence of friction pressure, whilst the other conditions kept constant. The experimental data were achieved by temperature measurement using infrared thermometer and thermometer by touch, where hardness Hv_{10} and micro-hardness $Hv_{0.1}$ realized along the axial direction, tensile test specimen with 8 mm effective diameter, scanning electronic microscopy (SEM) to observe tensile fracture surface and x-ray diffraction (XRD) to analyze the concentration of gamma iron. The results by high friction pressure provide increased temperature during friction and forging phase, elevated hardness and micro-hardness values at the welding center, improved ductility and ultimate tensile strength (UTS). Whilst the central region of tensile fracture seemed most ductile mode and presence of micro-porosities with different forms and dimensions, hence concentration of face centered cubic (FCC) structure of gamma iron clearly revealed at level of 111.

***doi**: 10.5829/ije.2020.33.12c.12*

1. INTRODUCTION

Austenitic stainless steel AISI 316 is used for various applications in chemical, manufacture of textile equipment, marine, and electrical appliance industries, etc. This type of steel is similar to AISI 304, but with addition of molybdenum to improve its resistance to pitting corrosion and resistance at high temperatures. Moreover, AISI 316 is easy to weld by fusion welding techniques, but it is prefered to avoid fusion welding due to phase transformations occuring in the welding and heat affected zones [1], also creating intermetallic compounds due to high amount of heat input [2], hence leading to loss of some useful original mechanical properties of the metal [3].

Considering all aspects, conditions and disadvantages, several studies have suggested replacing fusion welding by modern techniques such as friction welding [4]. This technique is one of the solid state welding processes which provides welding below the melting temperature of the metal being joined. It is also subdivided mainly into two most prominent processes: direct drive [5-6] and friction stir [7-11]. The direct drive friction welding is a technique which creates joining by heat developed between contact surfaces under the effect of rotation speed and applied pressure, one of the parts is stationary whereas the other is rotating and the two still in contact with each other until rotation stops abruptly, where the pressure increases to complete welding joint. This technique is preferred because of sub-melting temperature, high reproducibility, and low input energy, easy and fast procedure with reduced formation of the inter-metallic compounds [6, 12].

Several researches have been reported the influence of the friction pressure on the properties of welding joint [13-14]. In general and according to earlier studies, friction pressure should be always kept high to obtain elevated strength of welding joint, because of low

*Corresponding Author Email: *jabbarhassan1973@yahoo.fr* (A. Jabbar Hassan)

Please cite this article as: A. Jabbar Hassan, T. Boukharouba, D. Miroud, N. Titouche, S. Ramtani, Experimental Investigation of Friction Pressure Influence on the Characterizations of Friction Welding Joint for AISI 316, International Journal of Engineering, Transactions C: Aspects Vol. 33, No. 12, (2020), 2514-2520.

friction pressure rendering lack of bonding [15]. Friction pressure is a significant parameter in changing tensile strength and hardness followed by forging pressure and speed of rotation. Note that high friction pressure increases hardness and tensile strength due to higher friction pressure lead to more heat generation [16].

It is worthwhile to mention that some works explained the effect of temperature and thermal curve during friction welding process [14, 17-18]. Since the temperature in the welding center is low relative to the peripheral [19], H. Ma et al. [14] and E. P. Alves et al. [20] support the idea of measuring the temperature at the center. Therefore, the present study explains the relation between friction pressure and temperature measured in the welding center cause of this relation had a low importance in the previous articles. The welding temperature created from high friction pressure and rotation speed will determine the nature of forging, and that will affect the welding joint strength.

2. MATERIALS AND METHOD

The steel used in the current study is commercial austenitic AISI 316 stainless steel with Ref. No. 4401. The metal received as a long shaft of 6 m length and cut to small pieces, 45 mm length and 12 mm diameter. The general properties are shown in the tables below. Table 1 illustrates the chemical composition showing the amount of alloying elements added to the base metal. Tables 2 and 3show the mechanical and physical properties of the parent metal, respectively.

TABLE 1. Alloying elements of base metal (spectrum, wt. %)

C	Mn	Si	P	S	Mo	Cr	Ni
0.070	1.500	0.670	0.030	0.021	2.93-3.00	17.93-18.00	9.95-10.00

TABLE 2. Mechanical properties of base metal (as received, Ref. No. 4401)

UTS (MPa)	Young's modulus (MPa)	Elongation (%)	Average micro-hardness ($Hv_{0.1}$)	Average hardness (Hv_{10})
670 - 680	≈ 1.93 10^5	≈ 45	260 - 265	203 - 206

TABLE 3. Physical properties of the test metal (as received, Ref. No. 4401)

Density (g/cm^3)	Specific heat (j/kg. °k) 0-100°C	Thermal conductivity (w/mk)	T. melting (°C)
8	5	16.00-16.20	1371-1400

Figure 1 explains the flow chart of procedure of friction welding steps, after initializing of the welding machine end effector and selects welding conditions, provide tests of temperature, mechanical and metallography to obtain the results and understand the behaviour of friction pressure influence on the joint strength. Figure 2 exposes the variation of friction welding conditions,that is friction and forging pressure during time of welding. It also shows evolution of flash during heating cycle under the effect friction and forging pressure.

The machine used in this study was designed and fabricated as a direct drive friction welding machine; it is controlled numerically by computer to examine the welding conditions. The machine is shown in Figure 3; its operating speed can be varied from 0 to 3000 rpm, and a maximum pressure of 300 MPa can be applied. Selection of the welding conditions were depending on the single factor method (Table 4) by changing one condition and keeping the others constant. This procedure was time consuming and required hard work, but achieved better vision on the performance of welding joint. Thus, there were other factors considered for the selected friction welding conditions, such as work-piece dimensions, nature of metal and refer to the previous researches [1, 6, 14-15, 19].

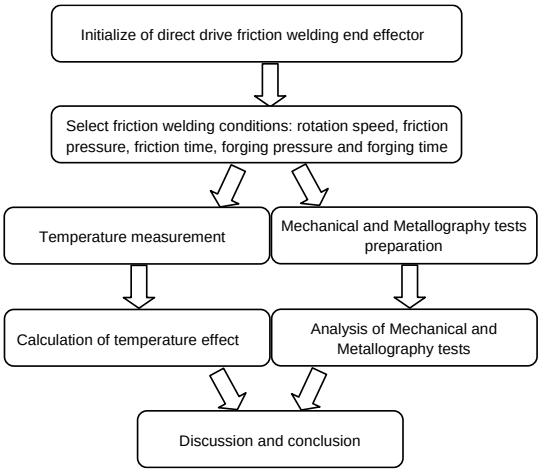

Figure 1. Flow chart of friction welding procedure

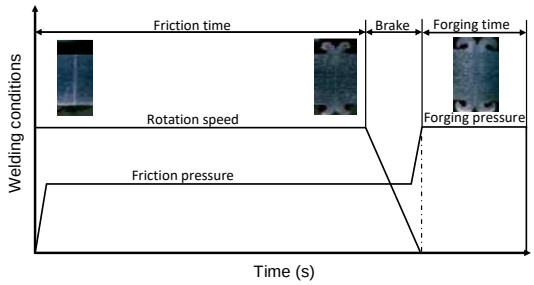

Figure 2. Diagram of direct drive friction welding conditions

Welding temperature recorded near the center of the interface of the stationary part (Figure 4). The temperature was recorded and verified by two methods as revealed in Figure 3, first one is thermometer by touch from type K with wire diameter of 0.5 mm and maximum temperature is 1400 °C (± 50°C), while second one is infrared thermometer (remote) from type K with maximum temperature is 1350 °C (± 50°C).

Scaning electronic microscopy (SEM) performed by JEOL JSM-6360 with magnifications of X 27 and X 150. X-ray diffraction (XRD), on the other hand, achieved by X'Pert PRO PANalytical. Whereas macroscopic observations were carried out by optical macroscopic from type NIKON SMZ 745T to measure the form of flash. SHIMADZU HMV testing machine were used in ambient temperature conditions for micro-hardness measurements in axial direction. While, The test pieces were polished with abrasive paper up to 1200 grit follow by 1 µm diamond paste on light disc cloth and oiled by ethanol and cleaned via deionized water.

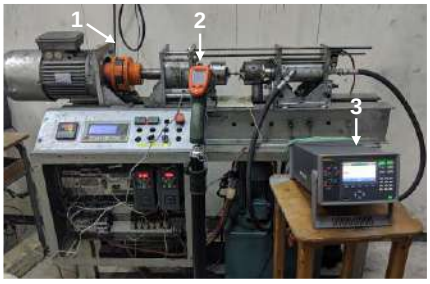

Figure 3. Friction welding machine and the two thermometers, 1. welding machine; 2. Infrared thermometer (remote); 3. Thermometer by touch

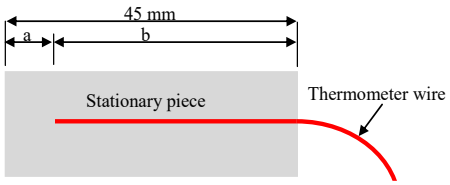

Figure 4. Thermometer by touch, position of the wire into the center of stationary piece, a: axial shortening + 0.5 mm; b: penetration distance of thermometer wire into center of stationary piece

TABLE 4. Friction welding conditions

Rotation speed (rpm)	Friction time (s)	Friction presssure (MPa)	Forging time (s)	Forging pressure (MPa)
3000	12	110 130 150 170	5	260

Vickers micro-hardness conditions were 100 gf load for 10 s. Whilst Vickers hardness test measurements achieved by INSTRON WOLPERT HARDNESS tester analyzed along the axial direction also, with 10 kg load applied for 10 s. The tensile tests were performed by using INSTRAN 5500 with 8 mm diameter under the standard of ISO 6892-1: 2009 (F).

3. RESULTS AND DISCUSSION

The thermal curves as shown in Figure 5 introduced the average values of temperature versus time. The rubbing between two pieces increased the temperature at the interface until reaches the maximum value (T_{max}), while the metal at that point still in the solid state. The created heat converted the solid metal to soft state, which is led to decreased the friction and that gradually reducing temperature. Under high rotation speed and pressure, the metal extruded from central to the peripheral to form flash metal. At the end of friction phase the rotation stops suddenly and the pressure increased at level of temperature which is called forging temperature (T_f) during forging phase period, this temperature has an important influence on the obtained welding joint.

The relation between T_{max} and T_f as shown in Figure 6 exposed that T_{max} regularly increased with higher friction pressure, the variation of maximum temperature between 793 °C - 1057 °C, that make clear of friction pressure elevation influences on the maximum temperature (T_{max}), hence forging temperature (T_f) roughly increased between 299 °C - 445 °C. In general, friction pressure has a direct proportional with T_{max} and T_f. Remarkable, with low friction pressure, the forging performed in low temperature and that consequently effected on the final properties of the joint.

The macroscopic observation as shown in Figure 7 represented the amount of flash formation of four friction pressures. Notes that with increasing friction

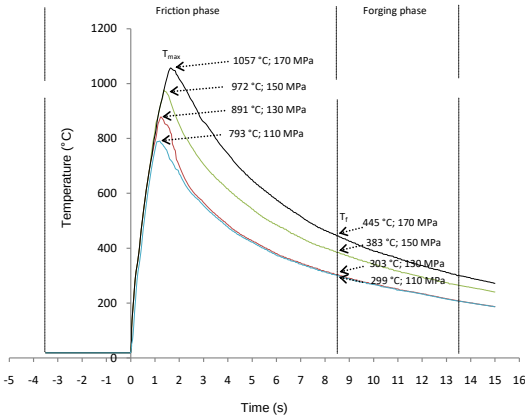

Figure 5. The thermal curves for the average values of temperatures versus time for different friction pressure

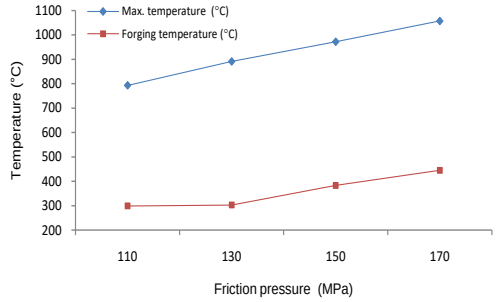

Figure 6. The relation between maximum temperature (T_{max}) and forging temperature (T_f) for different friction pressure

pressure; high amount of flash formation can be obtained [13, 15]. Obviously, Figure 8 reveals that inceasing friction pressure elevated axial shortening, that because of increasing in friction pressure leads to rising T_{max} and T_f, which provide enough superheating and amplified the displaced metal from central to the peripheral under effect of friction pressure and rotation. The amount of flash formation depends on the mechanical properties of the metal being welded [21] such as hardness [22] also relies on the quantity of alloying elements and capability of thermo-plastic deformation [6], furthermore, presence of Cr, Ni and Mo provide stainless steel to be refractory, which requires more presssure and temperature during friction welding phases to obtain considerable amount of flash formation.

The hardness obtained along the axial direction (Figure 9) recorded the highest values at the welding interface, this increasing of hardness due to high friction pressure application [19]. While, shows falling of hardness when moving from central toward the base

Figure 7. Flash formation for different friction pressure

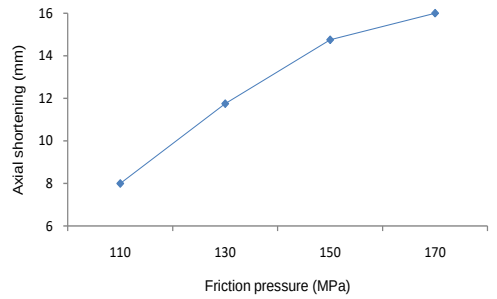

Figure 8. Axial shortening vs. friction pressure

metal, the increasing of hardness perhaps explained by the thermo-plasic deformation which exist in the interface resulting from dynamic recrystallisation, particularly at high friction presssure and temperature. P. M. AJITH et al. [16] agreed that with increasing friction pressure leads to high level of hardness at the interface due to dynamic recrystallization which results fine grains, there are also another source which is the high temperature at tangential area.

Micro-hardness profiles for axial direction as demonstrated in Figure 10, explain the effect of friction pressure has responsibility on the micro-hardness increasing of welding interface [13]. Moreover, due to high friction pressure with high rotation speed increased the superheated which produces dynamic recrystallisation. F.C. Liu, and T. W. Nelson [23] revealed that when the metal subjected to high plastic deformation under high temperature the dynamic recrystallisation occurs. On the other hand, the micro-hardness decreasing in the adjacent zone, due to amount of Mo. According to the alloying elements as shown in Table 1, AISI 316 has 2.93 % of Mo, that made the steel more refractory and led to reduce cooling rate speed and slow of heat diffusion causing decreasing micro-hardness at neighboring zone of welding joint [6].

Tensile test curves shown in Figure 11 illustrates the effect of friction pressure on the ultimate tensile

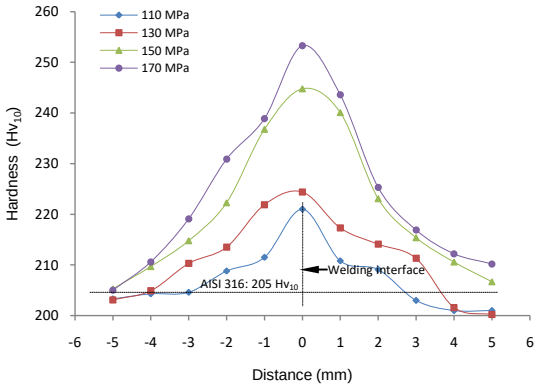

Figure 9. Hardness profile for axial direction

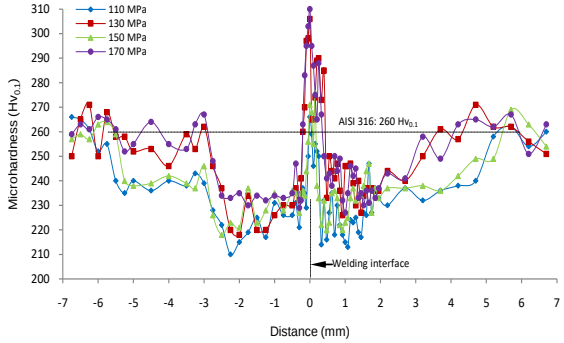

Figure 10. Micro-hardness profile for axial direction

strength (UTS) and ductility, the curves reveal also the values of UTS varied from 649 MPa to 667 MPa for friction pressure of 110 MPa to 170 MPa respactively, whilst ductility increased from 24 % to 29 % for friction pressure of 130 MPa to 170 MPa respactively. Explain this increasing of UTS and ductility by elevation of friction presssure because of thermo-plastic deformation in the bond line increases, which lead to more mass displaced at the interface [13]. I. Kirik and N. Ozdemir [21] exposed that high tensile strength was refer to more heat input and large plastic deformation at the interface under effect of high rotation speed. Moreover, rotation speed has important influence on the UTS, with high rotation speed UTS increases, while with low rotation exhibited a reverse trend, that because of heat generation elevates with high rotation speed. This phenomenon also observed in friction stir welding as mentioned in the references [10, 24]. Thus, the elevation of temperature at the two phases (friction and forging) has large consequence on the value of UTS and ductility. Finally, high friction pressure (170 MPa) and high rotation speed (3000 rpm) cause elevated temperature (1057 °C), that lead to high level of hardness and micro-hardness at the interface, and also elevation in UTS and ductility.

Figure 12 illustrated, on the other hand, the tensile specimens after tests, the figure exposed the position of fracture in the region close to the welding interface, elongation in the gauge length and the necking in the fracture position explained the amount of heat input at this region. In addition, the reduction in across sectional area (necking) provided more explanation about ductility than elongation of gauge length. Therefore, the necking proved of ductility nature of fracture for 170 MPa more than in 110 MPa, this is also agreed with the tensile curves.

SEM observation for tensile fracture surface as shown in Figure 13 appears the spirals shape on the fracture surface for the friction pressure of 110 MPa and 170 MPa. The thermo-plastic deformation demonstrates by existing of that spirals shape on the fracture surface. Furthermore, the degree of thermo-plastic deformation seems according to the amount of spiral forms, while the phenomenon of spiral occurs due to metal flow neighboring of weld [6]. In addition, the result of aggressive friction pressure at elevated temperature and high rotation occurs that type of spiral forms. Whilst, magnification of central region of fracture seems most ductile mode with micro-porocities of different forms and dimensions. This mode of ductile fracture looks more clear at 170 MPa, which have the same opinion with the results of tensile curves as discussed earlier.

XRD analysis for friction pressure of 110 MPa and 170 MPa with compared to the base metal as shown in Figure 14. The concentration of FCC structure of gamma iron at level of 111 was evidently. This concentration gives explanation of thermo-plastic deformation due to thermomechanical strain because of high rotation speed under application of aggressive friction pressure. On the other side, the elevated temperature during process and nature of metal play major roles on the properties of welding joint. Additionally, amount of alloying elements, particularly

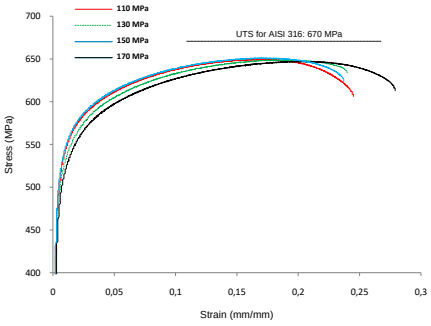

Figure. 11. Curves of tensile tests for all welded joint relative to UTS of AISI 316

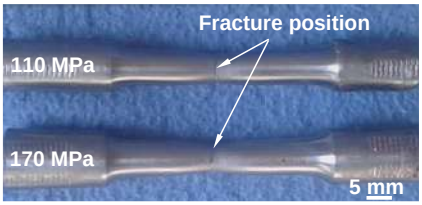

Figure 12. Macro-graphic of tensile test pieces

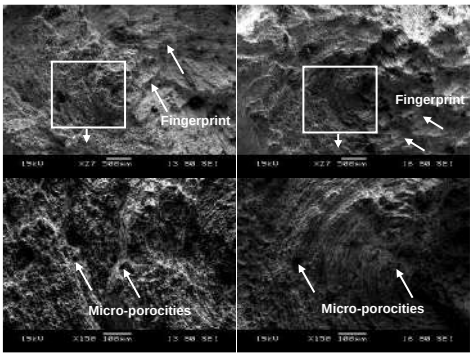

110 MPa 170 MPa

Figure 13. SEM observation for 110 MPa and 170 MPa

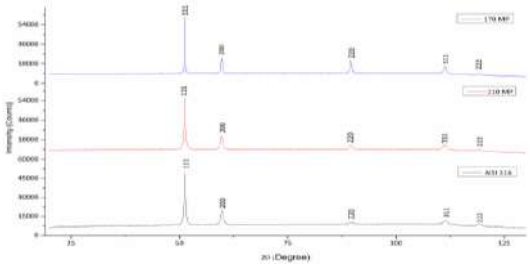

Figure 14. XRD analysis for 110 MPa, 170 MPa and AIS 316

Mo element effects on the quantity of heat diffusion or absorptions because of cooling rate that give Mo ability to effect on the phase attentiveness in the welding joint.

4. CONCLUSION

The effect of friction pressure on the evolution of the welding joint properties for AISI 316 summarized as following:

- Friction pressure has a direct proportional with maximum temperature (T_{max}) and forging temperature (T_f), that gives enough superheat which responsible on high amount of flash formation. On the other hand, with low friction pressure, the forging performed in low temperature and that consequently effected on the final propertie of welding joint,
- The hardness and micro-hardness variations recorded that the highest values at joint center, this elevation due to high friction pressure application. Whereas, shows falling of hardness and micro-hardness when moving from central toward the base metal,
- Tensile test curves shown increasing of UTS and ductility by elevation of friction presssure and due to used of high rotation speed led to increases of UTS,
- SEM observation seemed the degree of thermo-plastic deformation according to the amount of spiral forms, that result of aggressive friction pressure at elevated temperature and high rotation. Whilst, magnification of central region of fracture seems most ductile mode with micro-porocities of different forms and dimensions. This mode of ductile fracture seems more clear at 170 MPa,
- XRD analysis exposed the concentration of FCC structure of gamma iron at level of 111 due to thermomechanical strain at high rotation speed and aggressive friction pressure application. Thus, Mo element effects on the cooling rate which give it ability to effect on the phase attentiveness in the welding joint,
- Concerning the grade AISI 316, increasing of friction pressure (170 MPa) with high rotation speed (3000 rpm) cause elevated temperature (1057 °C), which lead to high level of hardness and micro-hardness at the interface, and also elevation in UTS and ductility. On the other hand, low friction pressure provides poor properties of welding joint.

5. REFERENCES

1. Titouche, N., Boukharoubab, T., Amzert, S., Hassan, A. J., Lechelah, and R., Ramtani, S., Direct Drive Friction Welding Effect on Mechanical and Electrochemical Characteristics of Titanium Stabilized Austenitic Stainless Steel (AISI 321) Research Reactor Thick Tube**, *Journal of Manufacturing Processes***, Vol. 41 (2019), 273-283, https://doi.org/10.1016/j.jmapro.2019.03.016.
2. Hincapié, O. D., Salazar, J. A., Restrepo, J. J., Torres, E. A., and Graciano-Uribe, J., Control of Formation of Intermetallic Compound in Dissimilar Joints Aluminum-steel, ***International Journal of Engineering , Transactions B: Applications***, Vol. 32, No. 1, (2019), 127-136, doi: 10.5829/ije.2019.32.01a.17.
3. Hamdan, A. I., Stress Concentration Factors (SCFs) in Circular Hollow Section CHS-to-H-shaped Section Welded T-Joints under Axial Compression, ***Civil Engineering Journal***, Vol. 5, No. 1 (2019), 33-47, http://dx.doi.org/10.28991/cej-2019-03091223.
4. André, S. J., Douglas, M., Vieira Braga, L. G., Afonso, R., and Dornelles, R. F., Replacement of Gas metal arc welding by friction welding for joining tubes in the hydraulic cylinders industry. ***Materials Research***, 21, No. 4. (2018), https://doi.org/10.1590/1980-5373-MR-2018-0015.
5. Peng, L., Jinglong, L., Muhammad, S., Li, L., Jiangtao, X., and Fusheng, Z., Effect of Friction Time on Mechanical and Metallurgical Properties of Continuous Drive Friction Welded Ti6Al4V/SUS321 Joints, ***Materials and Design***, Vol. 56, (2014), 649-656, http://dx.doi.org/10.1016/j.matdes.2013.11.065.
6. Hassan, A.J., Boukharouba, T., Miroud, D, and Ramtani, S., Metallurgical and Mechanical Behavior of AISI 316- AISI 304 during Friction Welding Process, ***International Journal of Engineering , Transactions B: Applications***, Vol. 32, No. 2, (2019), 284-291, doi:10.5829/ije.2019.32.02b.16.
7. Ethiraj, N., Sivabalan, T., Sivakumar, B., Vignesh Amar, S., N. Vengadeswaran, and Vetrivel K., Effect of Tool Rotational Speed on the Tensile and Microstructural Properties of Friction Stir Welded Different Grades of Stainless Steel Joints, ***International Journal of Engineering , Transactions A: Basics***, Vol. 33, No. 1, (2020), 141-147, doi: 10.5829/ije.2020.33.01a.16.
8. Villegas, J.F., Guarín, A.M., and Unfried-Silgado, J., A Coupled Rigid-viscoplastic Numerical Modeling for Evaluating Effects of Shoulder Geometry on Friction Stir-welded Aluminum Alloys, ***International Journal of Engineering, Transactions B: Applications***, Vol. 32, No. 2, (2019), 184-191, doi: 10.5829/ije.2019.32.02b.17.
9. Hasanzadeh, R., Azdast, T., Doniavi, A., Babazadeh, S., Lee, R. E., Daryadel, M., and Shishavan, S. M., Welding Properties of Polymeric Nanocomposite Parts Containing Alumina Nanoparticles in Friction Stir Welding Proces, ***International Journal of Engineering Transactions A: Basics***, Vol. 30, No. 1, (2017), 143-151, doi: 10.5829/idosi.ije.2017.30.01a.18.
10. Singh, R., Rizvi, S. A., and Tewari, S. P., Effect of Friction Stir Welding on the Tensile Properties of AA6063 Under Different Conditions, ***International Journal of Engineering. Transactions A: Basics***, Vol. 30, No. 4, (2017), 597-603, doi: 10.5829/idosi.ije.2017.30.04a.19.
11. Shishavan, S. M., Azdast, T., Aghdam, K. M., Hasanzadeh, R., Moradian, M., and Daryadel, M., Effect of Different Nanoparticles and Friction Stir Process Parameters on Surface Hardness and Morphology of Acrylonitrile Butadiene Styrene, ***International Journal of Engineering Transactions A: Basics***, Vol. 31, No. 7 , (2018), 1117-1122, doi: 10.5829/ije.2018.31.07a.16.
12. Muralimohan, C.H., Muthupandi, V., and Sivaprasad, K., Properties of Friction Welding Titanium-Stainless Steel Joints with a Nickel interlayer, ***Procedia Material Science***, Vol. 5, (2014), 1120-1129, https://doi.org/10.1016/j.mspro.2014.07.406.
13. Handa, A., and Chawla, V., Mechanical Characterization of Friction Welded Dissimilar Steels at 1000 rpm, ***Materials Engineering***, Vol. 20, (2013), 102-111, http://fstroj.uniza.sk/journal-mi/PDF/2013/14-2013.pdf.

14. Ma, H., Qin, G., Geng P., Li, F., Fu, B., and Meng, X., Microstructure Characterization and Properties of Carbon Steel to Stainless Steel Dissimilar Metal Joint Made by Friction Welding. ***Materials and Design***, Vol. 86, (2015), 587–597, https://doi.org/10.1016/j.matdes.2015.07.068.
15. Hassan, A.J., Boukharouba, T., and Miroud, D., Characterizations of Friction Welding Joint Interface for AISI 316, ***China Welding***, Vol. 28, No. 1, (2019), 42-48, doi: 10.12073/j.cw.20180811001.
16. Ajith, P. M., Afsal Husain, T. M., Sathiya, P., and Aravindan, S., Multi-objective Optimization of Continuous Drive Friction Welding Process Parameters Using Response Surface Methodology with Intelligent Optimization Algorithm, ***Journal of Iron and Steel Research, International***, Vol. 22, No. 10, (2015), 954-960, https://doi.org/10.1016/S1006-706X(15)30096-0.
17. Hassan, A.J., Lechelah, R., Boukharouba, T., Miroud, D., Titouche N., and Ouali N., History of Microstructure Evolution and its Effect on the Mechanical Behavior During Friction Welding for AISI 316, Edts. T. Boukharouba; et al., ***Springer International Publishing Switzerland***, (2017), 51-65, http://doi: 10.1007/978-3-319-41468-3_5.
18. Kimura, M., Kusaka, M., Kaizu, K., Nakata K., and Nagatsuka K., Friction Welding Technique and Joint Properties of Thin-Walled Pipe Friction Welded Joint Between Type 6063 Aluminum Alloy and AISI 304 Austenitic Stainless Steel, ***International Journal of Advanced Manufacturing Technology***, Vol. 82, (2016), 489-499, https://doi.org/10.1007/s00170-015-7384-8
19. Ajith, P.M., Barik, B. K., Sathiya, P., and Aravinda S., Multiobjective Optimization of Friction Welding of UNS S32205 Duplex Stainless Steel, ***Defence Technology***, Vol. 11, (2015), 157-165, https://doi.org/10.1016/j.dt.2015.03.001.
20. Alves, E. P., Neto, F. P., An, C. Y., and Castorino da Silva E., Experimental Determination of temperature During Rotary Friction Welding of AA1050 Aluminum with AISI 304 Stainless Steel. ***Journal of Aerospace Technology and Managment***, Vol. 4, No.1, (2012), 61-67, doi 10.5028/jatm.2012.04013211.
21. Kirik, I., and Ozdemir, N., Weldability and Joining Characteristics of AISI 420/AISI 1020 Steels using friction welding, ***International Journal of Materials Research***, Vol. 104, No. 8, (2013), 769-775, https://doi.org/10.3139/146.110917.
22. Khidhir, G. I., and S. A. Baban, Efficiency of Dissimilar Friction Welded 1045 Medium Carbon Steel and 316L Austenitic Stainless Steel Joints, ***Journal of Materials Research and Technology***, Vol. 8, No. 2, (2019), 1926–1932, https://doi.org/10.1016/j.jmrt.2019.01.010.
23. Liu, F.C., and Nelson, T.W., Twining and Dynamic Recrystallization in Austenitic Alloy 718 During Friction Welding, ***Material Characterization***, Vol. 140, (2018), 39-44, https://doi.org/10.1016/j.matchar.2018.03.035.
24. Kaushik, N., and Singhal, S., Experimental Investigations on Microstructural and Mechanical Behavior of Friction Stir Welded Aluminum Matrix Composite, ***International Journal of Engineering, Transactions A: Basics***, Vol. 32, No. 1, (2019), 162-170, doi: 10.5829/ije.2019.32.01a.21.

Persian Abstract

چکیده

این مطالعه بر روی تأثیر فشار اصطکاک بر مقاومت اتصال جوشکاری AISI 316 متمرکز است. برای ارزیابی تأثیر فشار اصطکاک از روش تک عاملی استفاده شد ، در حالیکه سایر شرایط ثابت نگه داشته می شوند. داده های تجربی با اندازه گیری دما با استفاده از دماسنج مادون قرمز و دماسنج با لمس ، جایی که سختی Hv10 و میکروسختی Hv0.1 در امتداد جهت محوری ، نمونه آزمایش کششی با قطر موثر ۸ میلی متر ، میکروسکوپ الکترونی روبشی (SEM) برای مشاهده کشش به دست آمد ، به دست آمد. سطح شکستگی و پراش اشعه ایکس (XRD) برای تجزیه و تحلیل غلظت آهن گاما. نتایج حاصل از فشار اصطکاک بالا ، افزایش دما در مرحله اصطکاک و جعل ، مقادیر سختی و ریز سختی بالا در مرکز جوشکاری ، شکل پذیری بهبود یافته و مقاومت کششی نهایی (UTS) را فراهم می کند. در حالی که ناحیه مرکزی شکستگی کششی به نظر می رسد بیشتر حالت شکل پذیری و وجود ریز تخلخل ها با اشکال و ابعاد مختلف باشد ، از این رو غلظت ساختار مکعب صورت محور (FCC) آهن گاما به وضوح در سطح ۱۱۱ نشان داده شده است.

International Journal of Engineering

Journal Homepage: www.ije.ir

Experimental Investigation and Statistical Modeling of the Effective Parameters in Charpy Impact Test on AZ31 Magnesium Alloy with V-shape Groove Using Taguchi Method

M. R. Maraki[a], H. Tagimalek*[b], M. Azargoman[b], H. Khatami[c], M. Mahmoodi[b]

[a] *Department of Materials and metallurgy, Birjand University of Technology, Birjand, Iran*
[b] *Faculty of Mechanical Engineering, Semnan University, Semnan, Iran*
[c] *Department of Mechanics, Urmia University, Urmia, Iran*

PAPER INFO

Paper history:
Received 02 December 2019
Received in revised form 03 July 2019
Accepted 21 October 2020

Keywords:
Charpy Impact Test
AZ31 Magnesium Alloy
V-shape Groove
Taguchi
Optimization

ABSTRACT

Today, the charpy impact test is required as a general quality control test in various industries. Several industrial standards have been formulated to perform the test accurately. It is important to determine the dynamic fracture energy in the charpy impact test and its relation to the fracture toughness through semi-empirical equations. In the present study, the charpy impact test on AZ31 magnesium alloy with standard ASTM E23 sample size is measured by the effect of groove depth, temperature and angle of groove on fracture energy. Taguchi and L18 arrays have been used to design the experiments and obtain the optimal state according to the number of factors studied. The effect of each input variable on the target parameter was analyzed by using ANOVA and the values of input parameters were extracted to maximize the amount of fracture energy by signal to noise method. The results showed that the groove depth has the greatest effect on the fracture energy and decreased with increasing groove depth. Also the best combination to maximize fracture energy was obtained in the non-grooved sample at -10 °C with a groove angle of 60 °.

***doi**: 10.5829/ije.2020.33.12c.13*

1. INTRODUCTION

Today, one of the strongest alloys in the industrial is AZ31 magnesium alloy [1]. Its high strength to weight ratio, coupled with the old natural features, make it attractive for aircraft construction applications [2].

Impact testing is one of the standard methods for determining the fracture energy of materials caused by dynamic stress [3]. The basis of the impact testing is the determination of the amount of energy needed to break the component [4, 5]. The information obtained from this test is very useful in understanding how the strength of materials in real applications [6]. The purpose of the impact testing is to simulate actual conditions in an attempt to prevent failure and to predict the failure of the sample [7]. Two of the most important and common methods of impact testing are the two methods of Izod and Charpy [8, 9]. The two methods differ only in how the samples are placed in the impact tester [10]. The behavior of the material against the instantaneous load (impact) is very different from the similar static load (tension) [11]. Impact testing is a good criterion for determining and classifying different plastics tendency for crisp behavior [12]. Given that several factors are involved in empirically determining the energy of sharp fracture (primary groove angle, groove depth, groove root radius, Exit the center of groove relative to the center of mass of the hammer, sample cross-section dimensions, radius and spacing of supports, geometry and velocity Hammer blow and primary groove making method). It is important to study the changes in these parameters and quantify the effect of these changes on the measured final energy [13, 14]. The charpy impact test as a general quality control test in various industries is required and

*Corresponding Author Institutional Email: *h_tagimalek@semnan.ac.ir* (H. Tagimalek)

Please cite this article as: M. R. Maraki, H. Tagimalek, M. Azargoman, H. Khatami, M. Mahmoodi, Experimental Investigation and Statistical Modeling of the Effective Parameters in Charpy Impact Test on AZ31 Magnesium Alloy with V-shape Groove Using Taguchi Method, International Journal of Engineering, Transactions C: Aspects Vol. 33, No. 12, (2020), 2521-2529.

several industrial standards have been accurately formulated to perform this test [15].

Druce et al. [16] investigated the effect of groove geometry and its behavior at different temperatures on the charpy impact experiment in stainless steel. They used a cast stainless steel sample containing 25% delta ferrite for testing, which resulted in the optimal determination of the sample for fracture toughness and energy. Sidener et al. [17] investigated the numerical study of fracture energy of charpy impacted samples for groove depth, groove angle, and groove radius on three point bending test samples in two types of U and V grooves. They used a pressure fracture tensile method to start the modeling, which stated that the results of the fitting width were 2.5 mm, which is consistent with the experimental results of other researchers. Barati et al. [18] have experimentally and numerically investigated the influence of the depth and radius of the U-shaped groove on the value of J-integrals in a three-point bending experiment. They used Elastic-Plastic to study the fracture behavior of cracked parts in specimens with high radius of plastic around the crack, which are the results of two J-integral parameters and the crack tip displacement as the fracture parameter. Salavati-Pour et al. [19] experimentally and numerically investigated the effect of groove depth and radius on the force applied in a three point bending experiment on graded steels that perform austenitic stainless steel and carbon steel. The root radius parameters of the gap are from 0.2 to 2 mm and the gap depth from 5 to 7 mm. They presented simulation results with empirical process experiments in high compatibility complex loading mode. Hossein-Zadeh et al. [20] experimentally investigated the effect of groove depth in charpy impact testing on API X65 steel, the results of which were used in the pipeline industry and provided a equation for groove depth and fracture energy, which is linear.

The presence of geometrical discontinuities, such as grooves or holes in an object, cause an uneven distribution of stress around it or the same concentration of stress, which is the main reason for the less stress of the applied failure than the theoretical failure stress; therefore, the harmful effect of cracks, the increase in local stress, and the emergence of a three-dimensional stress state in front of the crack root, which is loaded under plane strain conditions. It is important to determine the dynamic fracture energy in the Charpy impact test and its relation to the dynamic fracture toughness through semi-empirical equation. In recent years, the U and V grooves have received much attention due to large radius of plastic zone around the groove.

Due to extensive research done on the charpy impact test, no research was conducted on the design of experiments to investigate the failure energy. For this purpose, in the present study, at first, different variables of Charpy test including groove depth, temperature and angle of groove were investigated. Experimental design based on Taguchi method with L18 array was designed by Minitab software and the effect of groove depth, temperature and angle on AZ31 magnesium alloy fracture energy was analyzed and the optimum case is presented.

2. MATERIALS, EQUIPMENT AND TESTS

2. 1. Materials and Equipment AZ31 magnesium alloy is a thermal alloy and is commonly used in the manufacturing of components such as body panels and aircraft wings in the aerospace industry. The materials selected in this study were AZ31 magnesium alloy with dimensions of 55 mm×10 mm×10 mm. Using the quantmetric test, the chemical composition and mechanical properties of the AZ31 magnesium alloy from are shown in Tables 1 and 2, respectively.

To prepare samples from the raw material, the parts are subjected to a machining process. The size, tolerance, and groove characteristics are notable features in the fabrication of the samples as shown in Figure 1, American society for testing and materials (ASTM E23) charpy impact test. Sample machining after the final heat treatment, all machining and sealing steps are performed. Unless the impact characteristics of the samples before heat treatment and after are proved to be exactly the same. The groove should be perfectly flat, and since the change in the test results is highly influential; it is necessary to observe the transitions given in Figure 1.

TABLE 1. Chemical Composition of AZ31 Magnesium Alloy

Element	W_t (%)
Mg	Bal
Al	2.45
Zn	0.92
Mn	0.31
Cu	0.006
Ni	0.002
Si	0.07
Fe	0.023

TABLE 2. Mechanical Properties of AZ31 Magnesium Alloy

Mechanical Properties	Value
Yield Strength (Pa)	172×10^6
Ultimate Tensile Strength (Pa)	244×10^6
Elasticity Modulus (Pa)	34×10^6
Total Elongation (%)	16.7

It has been proven that high surface smoothness is not necessary, but a 2 µm surface finish is required for the grooved and opposite surface and 4 µm for the other surfaces. The groove can be struck in any way, but it must be careful not to damage the surface of the whole (the starting point of the sample failure).

Sample grooves can be pressed or machined (Chevron groove V-shape) according to API 5L3 standard, which is created by a wire cut machine and electric discharge machine. The pressing groove created in the laboratory by pressing the sample is sharp enough and there are no residual stresses in the groove tip and also the type of groove can affect the fracture start energy. In this research, the grooves were created by wire cut machine on the samples. Samples were with standard dimensions of 55×10×10 mm and grooves with angles of 45 to 60 degrees (18 samples with a difference of 15 degrees), groove depths of 0 to 10 mm (18 samples with 2 mm differences) and temperatures of (-10 to +10 °C) using liquid nitrogen and boiling water bath (18 samples with difference of 10 °C).

In order to achieve the objectives of the study, 90 charpy samples were selected in 18 groups of 5. The impact test was performed using the charpy Gant impact machine shown in Figure 2 with a capacity of (25 J and 40 J) with a C-shaped impactor, an 8 mm radius hammer at 23 °C.

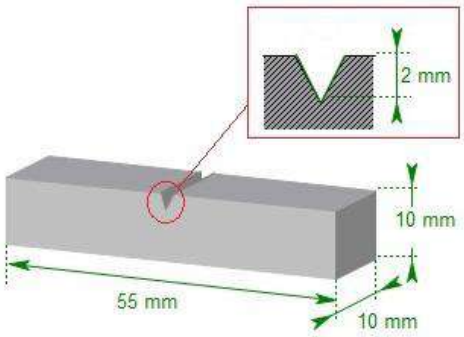

Figure 1. Standard Sample Dimensions of Charpy Impact Test

Figure 2. Charpy Gant Impact Machine

2. 2. Experimental Design Method The Taguchi method was used to design the experiments. In the present work, the factors that are important and controllable in the process of charpy impact testing and are considered as input factors in the experiments are groove depth (mm), temperature (°C) and angle respectively (degree). The range of values used in the design of the experiments is shown in Table 3.

In Table 4, considering the different levels of the three factors of groove depth, temperature and angle of the groove, the experiments were designed by Taguchi method and empirical process experiments were performed in 18 experiments. Then, a total mean failure energy response was calculated. In the following, the results of the experiments for each response are analyzed and the effect of each factor on the responses is analyzed. Table 5 illustrates the experiments designed by the Taguchi method. With respect to the L18 array used, no duplication experiments were performed in Table 5, which is one of the reasons for the reduction in the cost of experimental work in the design of the experiment.

3. RESULTS AND DISCUSSION

By designing the experiments according to the L18 array and performing the empirical experiments, the fracture energy values were extracted in Table 6 and by using ANOVA, Taguchi signal to noise and response surface diagrams, the effect of groove depth parameters, temperature and angle of groove on fracture energy, were investigated.

3. 1. Charpy Impact Test Results After preparing the specimens for use with the charpy impact testing machine, the samples were first used with wire cut to create groove depth and groove angle. Temperature changes were based on the parameters to reduce the temperature using liquid nitrogen and boiling water bath

TABLE 3. Range of Sharp Process Input Factor Values

Factor	Symbol	Low	High
Groove depth (mm)	H	0	10
Temperature (°C)	T	-10	10
Angle of groove (degree)	A	30	60

TABLE 4. Levels for the Factors in the Experiments

Factor \ level	1	2	3	4	5	6
Groove depth (mm)	0	2	4	6	8	10
Temperature (°C)	-10	0	10	-	-	-
Angle of groove (degree)	30	45	60	-	-	-

TABLE 5. Experiments the Taguchi L18 array

Ex	Groove depth (mm)	Temperature (°C)	Angle of groove (degree)
1	0	-10	30
2	0	0	45
3	0	10	60
4	2	-10	30
5	2	0	45
6	2	10	60
7	4	-10	30
8	4	0	45
9	4	10	60
10	6	-10	30
11	6	0	45
12	6	10	60
13	8	-10	30
14	8	0	45
15	8	10	60
16	10	-10	30
17	10	0	45
18	10	10	60

was used to increase the temperature. Empirical experiments were performed at room temperature and completely identical conditions. Samples were prepared for each parameter five samples in 18 groups. The reported fracture energy is an average of five samples based on Joules. The experimental results are shown in Table 6.

According to Table 6, the Sharpe impact test was repeated 5 times for each sample and the average failure energy was obtained. It should be noted that the testing of the specimens was initially performed with a capacity of 25 Joules sharp impact machine, but the non-grooved sample exhibited a fracture energy greater than 80% capacity, so the experiment was repeated with a capacity of 40 Joules machine and the results were reported. This device has a power display system and can digitally read the sample failure energy from its monitor screen. All samples of charpy impact test have been broken, indicating the correctness of the test.

3. 2. Analysis of Variance An analysis of variance is an important method for analyzing the effect of determinants on a response [21]. Statistical analysis of variance was performed to investigate whether process parameters had a significant and statistically significant effect on fracture energy. The F-value and percentage share for each parameter indicates which input

TABLE 6. Experimental Results of the Charpy Impact Test

Ex	Sample 1	Sample 2	Sample 3	Sample 4	Sample 5	Average fracture energy (J)
1	21.85	20.68	21.54	21.37	21.90	20.90
2	21.12	20.98	21.10	21.04	21.30	20.70
3	20.78	20.95	20.90	20.8	20.57	20.80
4	11.10	10.78	10.68	10.85	10.93	10.87
5	10.42	10.12	10.35	10.45	10.65	10.74
6	9.98	10.10	9.92	9.97	9.90	9.95
7	6.03	6.10	5.89	6.03	6.17	5.98
8	5.69	5.72	5.61	5.67	5.70	5.63
9	5.51	5.49	5.38	5.43	5.41	5.36
10	3.53	3.21	3.45	3.39	3.42	3.37
11	3.12	3.07	3.21	3.13	3.10	3.18
12	3.09	2.89	2.98	3.02	3.01	3.08
13	1.69	1.63	1.78	1.69	1.71	1.66
14	1.53	1.49	1.43	1.48	1.48	1.51
15	1.32	1.25	1.29	1.27	1.21	1.30
16	0.78	0.87	0.76	0.82	0.80	0.89
17	0.64	0.63	0.59	0.62	0.61	0.64
18	0.53	0.61	0.59	0.58	0.63	0.57

parameters and how much they contribute to the response. To investigate the effect of parameters on the mean fracture energy of the mean, ANOVA using P-value was used. The P-value indicates the occurrence of the first type of error [22]. A P-value less than 0.05 indicates a significant effect of the parameter on the response [23]. For the accuracy of analysis of variance, the distribution of data must be normal. Figure 3 is a probability distribution graph for the response values where the distribution of points around the diagonal line represents the normality of the data distribution. The obtained results clearly show the effect of each factor separately and interoperable on the mean failure energy function model presented in Table 7. Among the two factors, the groove angle factor had the smallest effect on the response variations, while the groove depth factor had a significant effect on the mean failure energy response function.

The adequacy of the R^2 model was 99.99%, which is acceptable. The R^2 parameter indicates the adequacy of the model, which indicates the correct estimation of the data with the model. Equation (1) is used to calculate R^2:

$$R^2 = 1 - \frac{SS_{Error}}{SS_{Total}} = \frac{SS_{Regression}}{SS_{Total}} \quad (1)$$

In this respect, SS_{Error} is the sum of squares caused by error, regression is the sum of squares caused by treatments, and SS_{Total} is the sum of squares corrected. In Equation (2) the failure energy regression model was presented:

$$E = 21.3611 + 0.0\,H_1 - 10.6467\,H_2 - 15.36\,H_3 - 17.89\,H_4 - 19.59\,H_5 - 20.3967\,H_6 + 0.0\,T_1 - 0.2933\,T_2 - 0.5133\,T_3 + 0.0\,A_1 + 0.0233\,A_2 - 0.09\,A_3 \quad (2)$$

Influence of input factors and their values are presented in Tables 7 and 8 which had the greatest effect on groove depth with 96% contribution and then temperature with 4% and finally groove angle had zero degree percent fracture energy on sample.

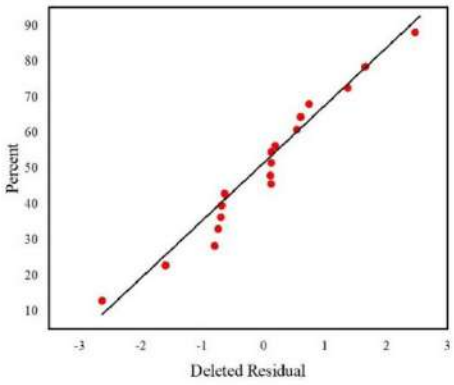

Figure 3. Normal Distribution Probability Diagram for Fracture Energy

TABLE 7. Analysis of Variance for Charpy Impact Test

Source	DF	SS	MS	F	P
Regression	9	890.008	98.890	8884.53	0.000
H	5	889.169	177.834	15977.09	0.000
T	2	0.796	0.398	35.75	0.000
A	2	0.043	0.021	1.93	0.207
Error	8	0.089	0.011		
Total	17	890.097			
R-Sq (adj)= 99.98%		R-Sq= 99.99%		R-Sq(pred)= 99.95%	

TABLE 8. Signal to Noise Analysis Results of Charpy Impact Test

Level	H	T	A
1	**26.4728**	**12.7248**	11.6392
2	20.3549	11.8465	11.9793
3	15.1247	11.3293	**12.2821**
4	10.0383		
5	3.34635		
6	-3.53578		
Optimum level	H_1	T_1	A_3

3. 3. Signal to Noise Analysis and Main Effects of Parameters For Charpy Impact Testing Sharp impact tests were performed on laboratory samples by measuring the depth of groove failure. The average failure energy of 5 samples was then obtained from each groove depth as shown in Table 6.

By incorporating charpy impact test results into Minitab software and signal to noise analysis data into the larger is better method (since it aims to increase the failure energy of the samples). The results of the main effects of the parameters and the signal to noise are shown in Figure 4 and Table 7. Table 8 also shows the order of parameters by degree of impact.

Figure 5 illustrates the interaction effects on fracture energy. According to the values obtained from the analysis of variance and the diagrams of Figure 5, only two factors of groove depth and temperature were observed. According to the signal to noise results, the groove depth is the most effective parameter on the charpy impact test of the AZ31 samples, which decreased with increasing depth of groove energy of the samples fracture and signal to noise ratio. As the groove depth increases, the fracture energy of the sample is significantly reduced. This can be attributed to the

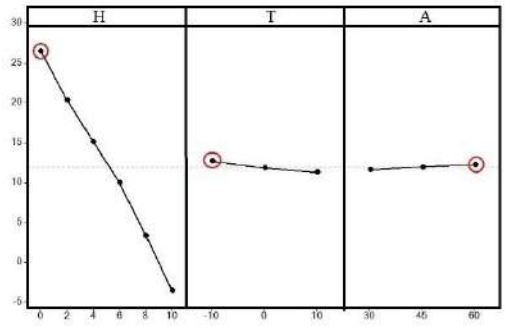

Figure 4. Main Effects Of Parameters For Fracture Energy

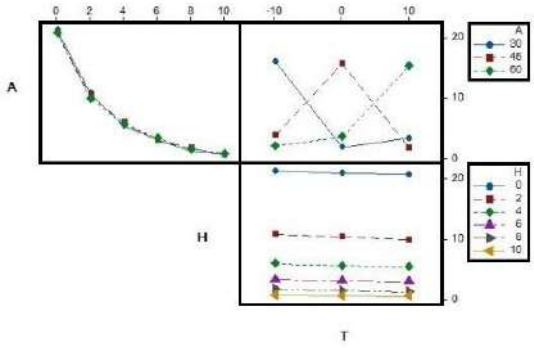

Figure 5. Diagram of Interaction of Factors on Fracture Energy

approach of the groove on the sample with neutral filament in the sample, which in experiment 1 (without groove) had the highest fracture energy, which caused the groove on the sample to weaken the sample and reduce its strength. The results of Table 7 showed that temperature is the second most effective parameter on the fracture energy of the specimens which decreases with increasing temperature, charpy impact test and signal to noise ratio. The reason for this can be stated that with decreasing temperature, contraction is created within the material and the grains approach each other and are pressurized to each other. For this reason, the failure energy for negative temperature samples is higher than for high temperature samples. According to the results presented in Table 7, the parameter that had the least impact on the fracture energy is the groove angle. As the groove angle increases, the fracture energy and signal to noise ratio increase. In other words, the best level for the groove angle is 60 °C. The reason for this can be claimed to be the departure of the groove tip from the neutral thread.

4. RESPONSE LEVELS

Another evaluation that can be made of the influence of process parameters on output parameters is the use of three dimensional response surface graphs. In the plots, two parameters are changed and the other parameter is kept constant. Three dimensional surfaces for groove depth, temperature, and angle are shown in Figures 6-8. Figure 5 shows that with decreasing depth of fracture energy increases and with decreasing temperature in the test specimen it is higher than the temperatures.

4. 1. Optimization With Taguchi Method Taguchi method uses the signal to noise ratio to optimize. The term "signal" represents the desired effect for the output characteristics and the term "noise" stands for the undesirable effect for the output characteristics. Since the

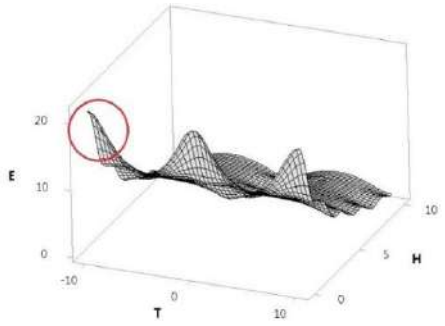

Figure 6. Three dimensional Diagram of the Effects of Groove Depth and Temperature on Fracture Energy

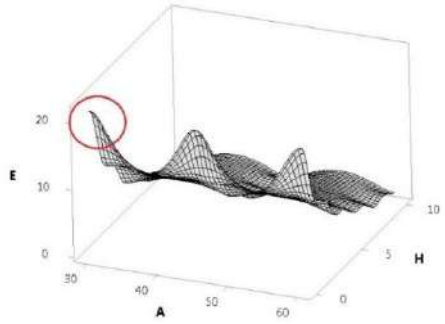

Figure 7. Three dimensional Diagram of the Effects of Groove Depth and Groove Angle on Fracture Energy

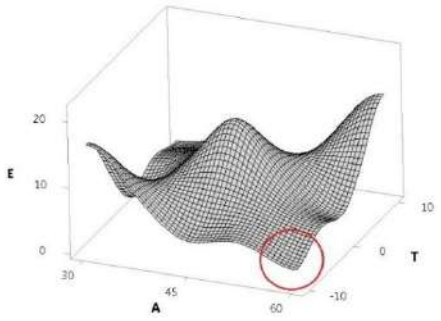

Figure 8. Three Dimensional Surface Diagram for the Effects of Groove Angle and Temperature on Fracture Energy

goal in this paper is to achieve more fracture energy, the larger is better of the signal to noise ratio was used. The larger is better equation is shown in Equation (3):

$$S/N = -10\, log_{10}\left[\frac{1}{n}(\sum_{i=1}^{n} y_i{}^2)\right] \quad (3)$$

Y_i is the response value measured in the i-th experiment and in the number of iterations per experiment. The signal to noise ratio values calculated from Equation (3) are presented using the results given in Table 7.

According to the signal to noise results in Table 9, the level of parameters having the highest signal to noise ratio is the optimal level. In the main graph, the deviation from the horizontal line indicates the greater impact of the process parameter on the response variable.

TABLE 9. Signals to Noise Results

Ex	S/N
1	26.5961
2	26.4609
3	26.3613
4	20.7086
5	20.3823
6	19.9739
7	15.6063
8	15.0717
9	14.6960
10	10.6040
11	9.9109
12	9.6001
13	4.5577
14	3.4052
15	2.0761
16	-1.7237
17	-4.1522
18	-4.7314

5. CONCLUSION

In this study, the effect of three groove depth, temperature, and groove angles on the fracture energy of the charpy impact test in AZ31 magnesium alloy was investigated. For this purpose, first, using Taguchi method, experiment design was performed. For this purpose, 90 samples were prepared in 18 groups of 5 and then the experimental results were extracted. The fracture energy of the samples was then obtained by performing a charpy impact test on the fabricated samples. The average failure energy of the five samples was then calculated for each groove depth and the equation between the Charpy failure energy; the changes of the three factors were determined. Using the normal probability distribution graph, the normality of the data distribution was confirmed. Then, the effect of factors on each of the responses was investigated by drawing diagrams of main and interaction effects. The summary of results are:

1. According to the S/N ratio, the best combination values for maximizing fracture energy in a non-grooved sample are -10 °C and a groove angle of 60°. Also the groove depth factor has the greatest impact on fracture energy.
2. ANOVA analysis showed that the greatest impact was the groove depth with 96% and then the temperature with 4% and finally the groove angle on the sample with 0° percent fracture energy.
3. Depth of groove and temperature have a significant impact on the fracture energy of the charpy impact test. By increasing the groove depth or increasing temperature, the fracture energy decreased. But regarding the effects of the groove angle due to the very small amount of fracture energy changes due to the groove angle it can be said that the effect of this factor is not significant compared to the other two factors. Concerning the interaction, it can be said that the interaction of parameters is not significant in affecting the failure energy response function.
4. Regarding the effect of parameters on the fracture energy uniformity, it can be said that the results of analysis of variance showed that the groove depth had the greatest effect on the uniformity of the transverse strain distribution after which the temperature had the greatest effect but the groove angle distance was almost ineffective. But the main effect diagrams showed that the variations of the fracture energy value were very small in the range of parameter changes and the effect of the parameters cannot be judged on the basis of the main effect diagrams. As for the interaction of parameters, the effect of groove depth, temperature, partly the interaction of groove depth and groove angle, on the transverse strain uniformity.

6. REFERENCES

1. Ghavidel, N., Allahkaram, S. R., Naderi, R., Barzegar, M., and Bakhshandeh, H., "Corrosion and wear behavior of an electroless Ni-P / nano-SiC coating on AZ31 Mg alloy obtained through environmentally-friendly conversion coating", ***Surface and Coatings Technology***, Vol. 382, (2020), 125-156, https://doi.org/10.1016/j. surfcoat.2019.125156.
2. Fata, A., Faraji, G., Mashhadi, M. M., and Tavakkoli, V., "Hot tensile deformation and fracture behavior of ultrafine-grained AZ31 magnesium alloy processed by severe plastic deformation", ***Materials Science and Engineering: A,*** Vol. 674, (2016), 9-17, https://doi. org/ 10.1016/j.msea.2016.07.117.

3. Liu, F., Lin, X., Shi, J., Zhang, Y., Bian, P., Li, X., and Hu, Y., "Effect of microstructure on the Charpy impact properties of directed energy deposition 300M steel", ***Additive Manufacturing***, Vol. 29, (2019), 100795, https: //doi.org/10.1016/j.addma.2019.100795.
4. Dziubinska, A., Gontarz, A., Horzelska, K., and Pieskoa, P., "The microstructure and mechanical properties of AZ31 magnesium alloy aircraft brackets produced by a new forging technology", 2nd International Materials, Industrial, and Manufacturing Engineering Conference, (2015), 337-341, Doi: 10.1016/j.promfg .2015. 07.059.
5. Trojanova, Z., Gartnerova, V., Jager, A., and Namesny, A., "Mechanical and fracture properties of an AZ91 Magnesium alloy reinforced by Si and SiC particles", ***Composites Science and Technology***, Vol. 69, No. 13, (2009), 2256-2264, https://doi.org/10.1016/j. compscitech.2009.06.016.
6. Daud, M. A. M., Nasir, N. Z., Rivai, A., and Selamat, M. Z., "Dynamic Fracture Toughness of Magnesium Alloy under Impact Loading Conditions", ***Procedia Engineering***, Vol. 53, (2013), 639-644, https://doi. org/ 10.1016/j.proeng.2013.02.082.
7. Rajakumar, S., Muralidharan, C., and Balasubramanian, V., "Influence of friction stir welding process and tool parameters on strength properties of AA7075-T6 aluminium alloy joints", ***Materials & Design***, Vol. 32, No. 2, (2011), 535-549. DOI:10.1016/j.matdes .2010. 08.025.
8. Hashemi, S.H., "Apportion of Charpy energy in API 5L grade X70 pipeline steel", ***International Journal of Pressure Vessels and Piping***, Vol. 85, No. 12, (2008), 879-884, https://doi.org/10.1016/j.ijpvp.2008.04.011.
9. Hashemi, H., and Hashemi, S.H., "Investigation of Macroscopic Fracture Surface Characteristics of API X65 Steel Using Three-point Bending Test", ***Modares Mechanical Engineering***, Vol. 19, No. 7, (2019), 219-228. http://journals.modares.ac.ir/article-15-21024-fa. html.
10. Cao,Y.,Zhen, Y., Song, M., Yi, H., Li, F., and Li, X., "Determination of Johnson–Cook parameters and evaluation of Charpy impact test performance for X80 pipeline steel", ***International Journal of Mechanical Sciences***, Vol. 179, (2020), 105627, https://doi.org/ 10.1016/j.ijmecsci.2020.105627
11. Tavares, S. S. M., Silva, M. B., Macedo, M. C. S. D., Strohaecker, T. R., and Costa, V. M., "Characterization of fracture behavior of a Ti alloyed supermartensitic 12%Cr stainless steel using Charpy instrumented impact tests", ***Engineering Failure Analysis***, Vol. 82, (2017), 695-702, doi.org/10.1016/j.engfailanal .2017 .06.002.
12. Tanks, J., Sharp, S., and Harris, D., "Charpy impact testing to assess the quality and durability of unidirectional CFRP rods", ***Polymer Testing***, Vol. 51, (2016), 63-68, doi.org/10.1016/ j.polymer testing.2016. 02.009.
13. Khiratkar, V. N., Mishra, K., Srinivasulu, P., and Singh, A., "Effect of inter-lamellar spacing and test temperature on the Charpy impact energy of extremely fine pearlite", ***Materials Science and Engineering: A***, Vol. 754, (2019), 622-627, https://doi.org/10.1016 /j.msea.2019. 03.121.
14. Demirci, M. T., Tarakcioglu, N., Avci, A., and Erkendirci, O, F., "Fracture toughness of filament wound BFR and GFR arc shaped specimens with Charpy impact test method", ***Composites Part B: Engineering***, Vol. 66, (2014), 7-14, doi.org /10.1016/j.compositesb .2014.04. 015.
15. Ghash, A., Sahoo, S., Ghosh, M., Ghosh, R. N., and Chakrabarti, D., "Effect of microstructural parameters, microtexture and matrix strain on the Charpy impact properties of low carbon HSLA steel containing MnS inclusions", ***Materials Science and Engineering: A***, Vol. 613, (2014), 37-47, doi.org/10.1016/j.msea .2014.06.091.
16. Druce, S.G., Gage, G., and Popkiss, E., "Effects of notch geometry on the impact fracture behavior of a cast duplex stainless steel", ***International Journal of Pressure Vessels and Piping***, Vol. 33, No. 1, (1988), 59-81, doi.org/10.1016/0308-0161(88)90117-2.
17. Sidener, S. E., Kumar, A. S., Oglesby, D. B., Schubert, L. E., Hamilton, M.L., and Rosinski, S. T., "Dynamic finite element modeling of the effects of size on the upper shelf energy of pressure vessel steels", ***Journal of Nuclear Materials***, Vol. 239, No. 1, (1996), 210-218, doi.org/10.1016/S0022-3115(96)00483-7.
18. Barati, E., Aghazadeh Mohandesi, J., and Alizadeh, Y., "The effect of notch depth on J-integral and critical fracture load in plates made of functionally graded aluminum–silicone carbide composite with U-notches under bending", ***Materials & Design***, Vol. 31, No. 10, (2010), 4686-4692, doi.org/10.1016 /j.matdes. 2010.05. 025.
19. Salavati Pour, H. S., Alizadeh, Y., and Berto, F., "Effect of notch depth and radius on the critical fracture load of bainitic functionally graded steels under mixed mode I + II loading", ***Physical Mesomechanics***, Vol. 17, No. 3, (2014), 178-189, Doi: 10.1134/S1029959914030023.
20. Hosseinzadeh, A., and Hashemi, S. H., "Experimental Investigation of the effect of groove depth on sharp fracture energy in XIP X65 steel", 26th Annual Conference of the Iranian Society of Mechanical Engineers, (2018), Tehran, Iran.
21. Tewari, S. P., and Rizvi, S., "Effect of Different Welding Parameters on the Mechanical and Microstructural Properties of Stainless Steel 304H Welded Joints", ***International Journal of Engineering, Transactions A: Basics,*** Vol. 30, No. 10, (2017), 1592-1598, doi: 10.5829/ije.2017.30.10a.21.
22. Hoten, H., Mainil, A. K., and Mulyadi, I., "Parameters Optimization in Manufacturing Nanopowder Bioceramics of Eggshell with Pulverisette 6 Machine using Taguchi and ANOVA Method (TECHNICAL NOTE) ", ***International Journal of Engineering, Transactions A: Basics***, Vol. 31, No. 1, (2018), 45-49, doi: 10.5829/ije. 2018. 31.01a. 07.
23. Afrasiabi, H. A., Khayati, G. R., and Ehteshamzadeh, M., "Studying of Heat Treatment Influence on Corrosion Behavior of AA6061-T6 by Taguchi Method", ***International Journal of Engineering, Transactions C: Aspects***, Vol. 27, No. 9, (2014), 1423-1430, doi:10.5829 /idosi.ije. 2014.27. 09c .12.

Persian Abstract

چکیده

امروزه تست ضربه شارپی به عنوان یک تست کنترل کیفیت عمومی در صنایع مختلف مورد نیاز است و چندین استاندارد صنعتی برای انجام دقیق این آزمون تدوین شده است. تعیین انرژی شکستگی پویا در آزمایش ضربه شارپی و ارتباط آن با چقرمگی شکستگی از طریق روابط نیمه تجربی بسیار مهم است. در مطالعه حاضر، تست ضربه شارپی بر روی آلیاژ منیزیم AZ31 با اندازه استاندارد ASTM E23 با استفاده از عمق شیار، دما و زاویه شیار بر انرژی شکستگی اندازه گیری شده است. از روش تاگوچی و آرایه‌های L18برای طراحی آزمایش ها و بدست آوردن حالت مطلوب با توجه به تعداد فاکتورهای مورد مطالعه استفاده شده است. تأثیر هر متغیر ورودی در پارامتر هدف توسط ANOVAمورد تجزیه و تحلیل قرار گرفت و مقادیر پارامترهای ورودی برای به حداکثر رساندن مقدار انرژی شکست با استفاده از روش سیگنال به نویز استخراج شد. نتایج نشان می‌دهد که عمق شیار بیشترین تأثیر را در انرژی شکستگی دارد و با افزایش عمق شیار کاهش می‌یابد. همچنین بهترین ترکیب برای به حداکثر رساندن انرژی شکست در نمونه غیر شیار در ۱۰- درجه سانتیگراد با زاویه شیار ٦۰ درجه به دست آمد.

IJE TRANSACTIONS C: Aspetcs Vol. 33, No. 12, (December 2020) 2530-2537

International Journal of Engineering

Journal Homepage: www.ije.ir

A New Mechanical Design for Legged Robots to Reduce Energy Consumption

M. J. Mahmoodabadi[a], D. Dresscher[b], S. Stramigioli[b]

[a] *Department of Mechanical Engineering, Sirjan University of Technology, Sirjan, Iran*
[b] *Robotics and Mechatronics, University Twente, Postbus 217, 7500AE Enschede, The Netherlands*

PAPER INFO

Paper history:
Received 17 April 2019
Received in revised form 22 August 2020
Accepted 03 September 2020

Keywords:
Robotics
Legged Locomotion
Energy Consumption
Four-bar Linkage
Passive Dynamics

ABSTRACT

Many legged robots have been designed and built by universities, research institutes and industry; however, few investigations regard energy consumption as a crucial design criterion. This paper presents a novel configuration for legged robots to reduce the energy consumption. The proposed leg can be either used as a single leg or easily attached to bodies with four, six and eight legs. This mechanism is a parallel four-bar linkage equipped with one active and four passive joints. In fact, the usage of the passive elements leads to simple feed-forward control paradigms. Moreover, another distinctive feature of this design is the arrangement of one-way clutches and flat springs to store the potential energy for utilizing it in the next step. A locomotion prototype of the proposed mechanical structure is built and its simulation is also presented in this paper. Comparing the results with other structures demonstrates the superiority and efficiency of this work regarding energy consumption problem.

***doi**: 10.5829/ije.2020.33.12c.14*

1. INTRODUCTION

Multi-legged robots exhibit many advantages over wheeled and tracked counterparts on natural terrains. However, current implementations have the disadvantage of achieving poor energy efficiency along with the fact that walking robots are relatively complex compared to the wheeled and tracked robots [1-5]. In other words, the energy consumption plays a key role in the design and development of walking robots in regard to not only electronics systems and control algorithms but mechanisms as well [6]. Different approaches have been employed by a number of researchers to enhance the energy efficiency for the multi-legged robots [7-11]. One of these techniques is the employment of energy storage devices to recover the energy. Alexander [12] and Shin and Streit [13] are among the first investigators who used the springs to decrease the power demand in the legged robots. A 2D monopod, which uses leg and hip compliances has been designed [14] and implemented in [15]. This plan saves the energy in the leg and hip actuators and presents more efficient locomotion. Linear rotational springs have been implemented to store and release the kinetic and potential energy of the body and legs during each gait cycle for multi-legged walking vehicles [16]. Furthermore, series of elastic actuators have been implemented for biped robots in order to store a part of the impact energy, preserving the gait efficiency and stability [17,18]. Hyon and Mita [19] have proposed a one-legged running robot that contains an articulated leg, two hydraulic actuators as muscles and a tensile spring as a tendon. Iida and Pfeifer [20] have described a four-legged robot model and successfully applied the elastic materials for making efficient the rapid locomotion. In an under actuated one-legged hopping robot model has been proposed for researching the utilization of the elastic energy of flexible mechanical systems, repeatedly [21]. Scarfogliero et al. [22] have implemented compliant joints and elastic elements to store the energy in bio-inspired legged robots. A completely passive model has been introduced in literature [22] to reuse a part of the impact energy. He and Geng have studied the design and the applications of elastic underactuated mechanisms for improving the energy efficiency of a one-legged hopping robot [23]. In [24], spring clutches have been utilized in all active leg

*Corresponding Author Institutional Email: *mahmoodabadi@sirjantech.ac.ir* (M. J. Mahmoodabadi)

Please cite this article as: M. J. Mahmoodabadi, D. Dresscher, S. Stramigioli, A New Mechanical Design for Legged Robots to Reduce Energy Consumption, International Journal of Engineering, Transactions C: Aspects Vol. 33, No. 12, (2020), 2530-2537.

joints to absorb unused kinetic energy (maximum torque) and transmit it to the joints. Gürel et al. [25] have studied the trade-off between the cycle time and the energy consumption of a robot that produces identical parts in a robotic cell for loading and unloading of machines. A task energy characteristic model has been suggested by Cao et al. [26] as a polynomial function of the feedrate override to forecast the energy consumption of the polishing process. Sun et al. [27] have addressed an energy efficient robotic assembly line balancing problem with some criteria to minimize both the cycle time and total energy consumption. A mathematical model of the total energy consumption of cycle pick-and-place tasks, which considers operating motion and homing motion of a given trajectory with different joint configurations has been investigated by Feng et al. [28].

From this literature survey, it is obvious that improvement of the energy efficiency is an important factor, especially for the legged robots. Here, in an attempt to reduce the energy consumption via applying elastic springs and decreasing the number of actuators, a parallel four-bar linkage is proposed for the leg of the walking robots. In this model, there are four passive joints and only one active joint. A motor is installed on the location of the active joint and used to move the leg vertically. Further, the kinetic energy of the leg is stored as the elastic potential energy in the flat springs and applied to move it to forward. To the best of authors' knowledge, this is the most successful work to consider the energy-efficient problem for multi-legged robots, and conduct and implement experiments in a real-life environment.

The rest of the paper is organized as follows. Section 2 deals with mechanical design of the proposed one-leg model. The dynamical motion equations are explained in Section 3. Experiments and simulation results in the 20-sim software environment are compared in Section 4. Some concluding remarks are made in Section 5.

2. MECHANICAL DESIGN

The proposed leg is an ultra-lightweight mechanism and can be either used as a single leg (as a test-bed for general robotic research) or combined in quadruped, hexapod or octopod constructions (Figure 1). This model is a parallel four-bar linkage that has one active and four passive joints, i.e. the first, second, third and fourth joints' axes are parallel to each other and perpendicular to the fifth joint's axis (Figure 2). The first, second, third and fourth links are about 150 mm, 100 mm, 100 mm and 150 mm long, respectively. This skeleton is made of the Delrin rod with an easy snap-in system construction. The overall weight of the leg is about 500g. Furthermore, a motor is installed on the location of joint 3 and used to move the leg vertically. This motor is rated at 20 W (MAXON DC motor), coupled through a one stage 4.8:1 planetary gear head and has a three-channel encoder (MAXON HED_5540 encoder). When link 2 moves, then link 3 will rotate parallel to it around joint 4. A series of mechanisms is prepared on the location of joint 4 to store and transfer energy via the created torque on this joint.

At first, when the leg is going up by the motor, the first one-way clutch between the shaft and helical gear 1 does not transmit any torque (Figure 3). However, when the leg is going down, then the power is transmitted to the helical gears (ratio 2:1) through this clutch. In this situation, the second one-way clutch between the support and the shaft allows the shaft to rotate (similar to Figure 3), and the impact and kinetic energies of the leg will be stored as elastic potential energy in the flat spring set (Figure 2). During this locomotion, the gear lock mechanism is locked, and only when the leg is near the maximum height, this mechanism is opened by a cable,

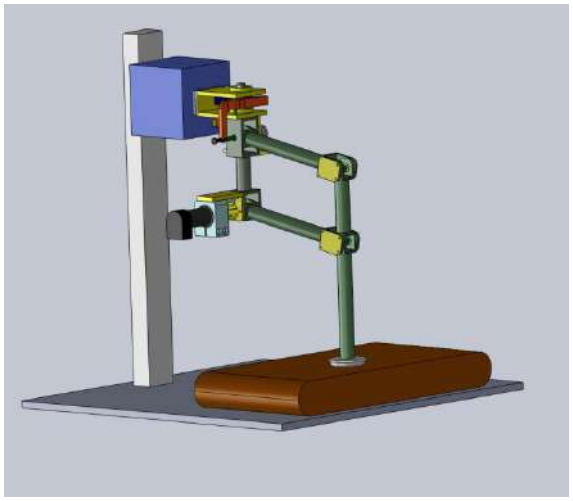

(a) Used as a test-bed for general robotic researches

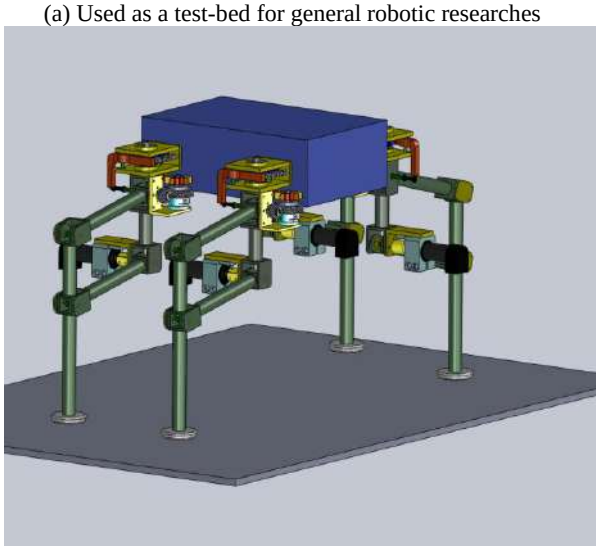

(b) Attached to a multi-legged body

Figure 1. Different applications of the proposed leg

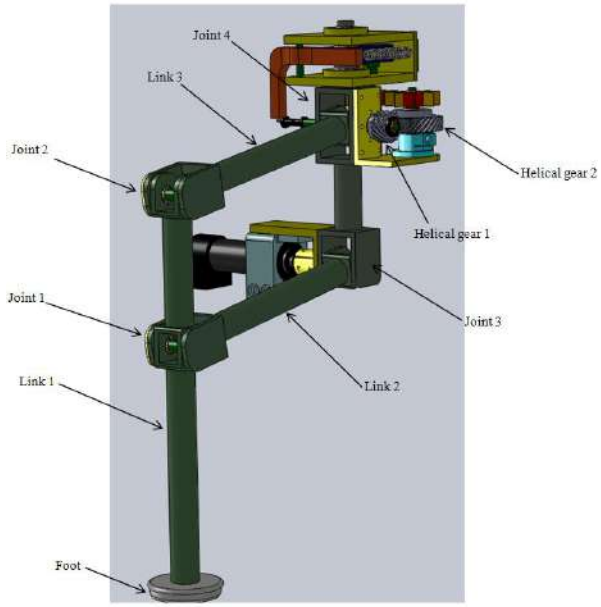

(a) Front view

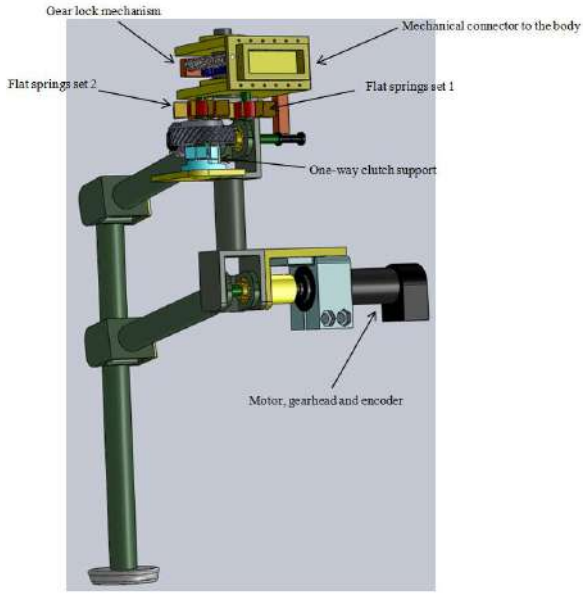

(b) Back view

Figure 2. An overview of the proposed leg

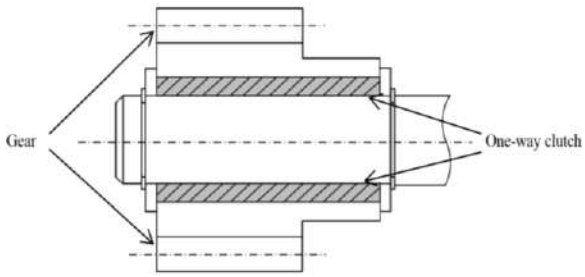

Figure 3. Structure of a one-way clutch with a gear and a shaft

and the elastic potential energy is released. Via two spur gears (ratio 1:1); this power will be transferred to rotate the leg to forward.

3. MATHEMATICAL MODELLING AND DYNAMICAL MOTION EQUATIONS

Figure 4 shows a simple configuration of the robot model (four links and five joints) that we use to represent a single leg of our walking robot. In this figure, θ and γ represent the angles of link 2 with respect to x and z axis, respectively.

In order to derive the mathematical dynamic equations of the model, Lagrange's formulation [29] is used:

$$\frac{d}{dt}\frac{\partial L}{\partial \dot{q}_i} - \frac{\partial L}{\partial q_i} = Q_i \quad (1)$$

where, $L = K - P$ is the Lagrangian function. K and P are the kinetic and potential energy functions, respectively. q_i denotes the generalized coordinate of the system, and Q_i represents the corresponding external force/torque .

Initially, it is supposed that the proposed leg is gone up by the motor; therefore, the generalized coordinate is $q_1 = \theta$, and the corresponding external torque is $Q_1 = \tau_m$ (τ_m is the motor torque). Thus, the kinetic energy could be achieved by the following formulation:

$$K = \sum_{i=1}^{3}[\frac{1}{2}m_i v_i^2 + \frac{1}{2}J_i^z \dot{\theta}^2] \quad (2)$$

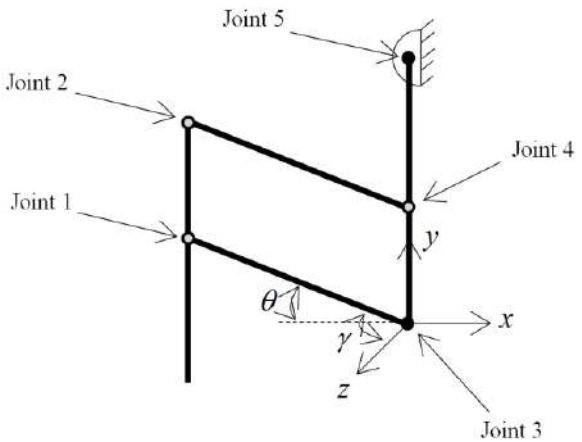

Figure 4. Frame assignment of the leg model. Black circles denote the actuated joints (joint 3 is actuated by a motor and joint 5 actuated by flat springs) and white circles show the passive joints

where, i indicates the link number, v_i is the velocity of the mass centre of link i th. m_i is the mass of link i th. Moreover, J_i^z is the inertia moment of link i th with respect to rotation around z axes. It is obvious that link 1 has a pure transfer motion, and $J_1^z = 0, v_1 = l_2\dot{\theta}$. Links 2 and 3 have pure rotation motion and $v_2 = \frac{1}{2}l_2\dot{\theta}, v_3 = \frac{1}{2}l_3\dot{\theta}$. That l_i $(i = 1,2,3,4)$ indicates the length of link i th. Therefore:

$$K = \frac{1}{2}m_1v_1^2 + \frac{1}{2}m_2v_2^2 + \frac{1}{2}J_2^z\dot{\theta}^2 + \frac{1}{2}m_3v_3^2 + \frac{1}{2}J_3^z\dot{\theta}^2 \quad (3)$$

Or

$$K = \frac{1}{2}m_1(l_2\dot{\theta})^2 + \frac{1}{2}m_2(\frac{1}{2}l_2\dot{\theta})^{2^2} + \frac{1}{2}J_2^z\dot{\theta}^2 + \frac{1}{2}m_3(\frac{1}{2}l_3\dot{\theta})^2 + \frac{1}{2}J_3^z\dot{\theta} \quad (4)$$

Furthermore, the potential energy function can be computed as follows.

$$P = m_1gl_2\sin(\theta) + m_2g(\frac{1}{2}l_2\sin(\theta)) + m_3g(\frac{1}{2}l_3\sin(\theta)) \quad (5)$$

Thus,

$$\frac{\partial L}{\partial\dot{\theta}} = [J_2^z + J_3^z + \frac{1}{4}(4m_1l_2^2 + m_2l_2^2 + m_3l_3^2)]\dot{\theta} \quad (6)$$

And

$$\frac{\partial L}{\partial\theta} = -\frac{1}{2}[2m_1l_2 + m_2l_2 + m_3l_3]g\cos(\theta) \quad (7)$$

Finally, the equation of motion for the leg with respect to generalized coordinate $q_1 = \theta$ results in:

$$[J_2^z + J_3^z + \frac{1}{4}(4m_1l_2^2 + m_2l_2^2 + m_3l_3^2)]\ddot{\theta} + \frac{1}{2}[2m_1l_2 + m_2l_2 + m_3l_3]g\cos(\theta) = \tau_m \quad (8)$$

Secondly, it is supposed that the proposed leg is moved forward by the flat springs; therefore, the generalized coordinate is regarded as $q_2 = \gamma$, and the corresponding external torque is defined as $Q_2 = \tau_s$ (τ_s is the flat spring torque). Via a procedure similar to the first generalized coordinate, the motion equation of the leg for second generalized coordinate $q_2 = \gamma$ results to:

$$(J_1^y + J_2^y + J_3^y + J_4^y)\ddot{\gamma} + C\dot{\gamma} = \tau_s \quad (9)$$

where, J_i^y $(i = 1,2,3,4)$ is the inertia moment of link i with respect to axes y. C is the coulomb friction coefficient of the spur gears.

4. EXPERIMENTAL AND SIMULATION RESULTS

Figure 5 shows the one-legged robot designed and built based on the leg model proposed in the previous sections at the Robotics and Mechatronics (RAM) group, University of Twente. Its main specifications are given in Table 1. Moreover, the simulation of this model is conducted in 20-sim-4.2 to reflect the essential characteristics of the real robot in the 3D environment. It consists of four links and five joints in which the third joint is actuated by a motor and the fifth joint is actuated by a spring (compare Figure 2 with Figure 6). In Figure 6, a dynamical model of the one-legged robot is provided in the 20-sim 3D mechanics toolbox. Furthermore, Figure 7 shows a complete model of the proposed mechanism in the graphical editor environment of the software. Here, a spring and motor torque are used to actuate joints 3 and 5, respectively. Non-ideal gearbox mechanisms are applied to simulate planetary, spur and helical gears. Furthermore, to control the motor torque, a simple Proportional Derivative (PD) controller with coefficients and is implemented. The observations show

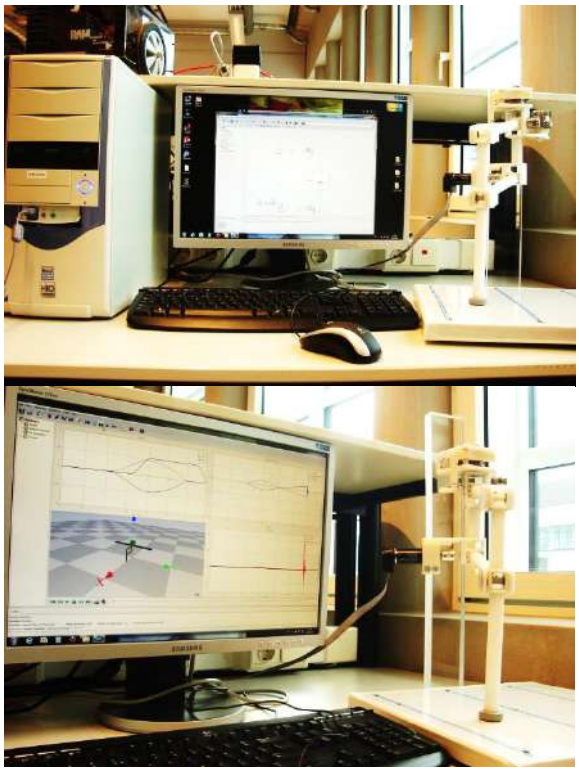

Figure 5. One-legged robot prototype developed at RAM group, University of Twente, the Netherlands

TABLE 1. Specifications of the leg model

Parameter	Description	Value
m_1	Mass of link 1	91.16 g
m_2	Mass of link 2	68.45 g
m_3	Mass of link 3	68.45 g
m_4	Mass of link 4	60.05 g
l_1	Length of link 1	293 mm
l_2	Length of link 2	220 mm
l_3	Length of link 3	220 mm
l_4	Length of link 4	193 mm
C	Coulomb friction coefficient	0.07
r	Radius of the rod for the skeleton	18 mm
k	Flat spring constant	36.6 N/mm
η_1	Spur gears efficiency	0.9
η_2	Helical gears efficiency	0.8
η_3	Planetary gear head efficiency	0.8
g	Gravity acceleration	9.81 m/s^2

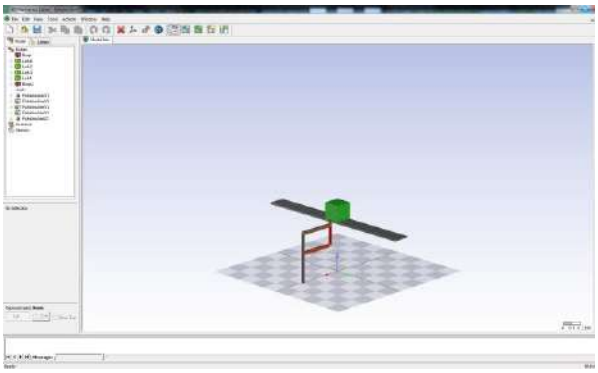

Figure 6. Proposed leg model in the three-dimensional mechanics toolbox of 20-sim software

that the simulated dynamical locomotion is fairly comparable to the real one.Figure 8 illustrates the typical time responses of the joint angles which characterize the movement of the robot body. As shown in this figure, the motor brings leg up during 1s to about 25 degrees. Then, the leg will go down in about 1s. Furthermore, when the leg is near the maximum height, the elastic potential energy is realized, and the leg rotates forward at about 37 degrees. Moreover, all angles go back to the beginning state of the of the leg step cycle, which ensures a periodic gain pattern.

The observations in Figure 9 further validatee the previous simulation results. In this figure, the electrical energy transforms to the gravity potential and kinetic energies of the leg between 1s and 2s. During this

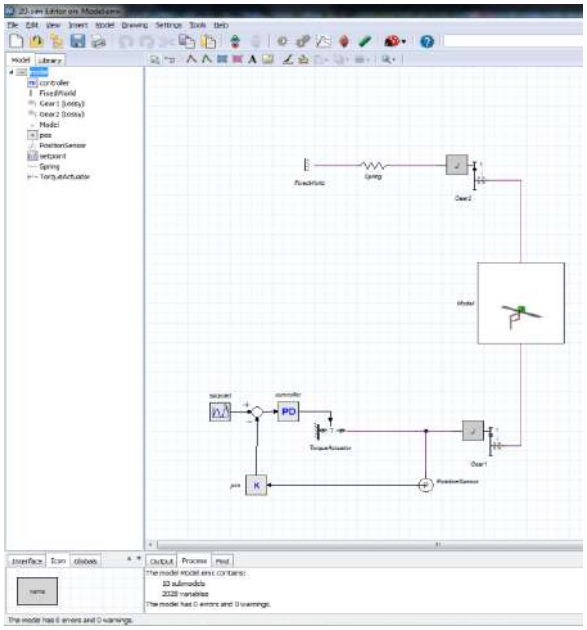

Figure 7. A model of the proposed mechanism in the graphical editor environment of 20-sim

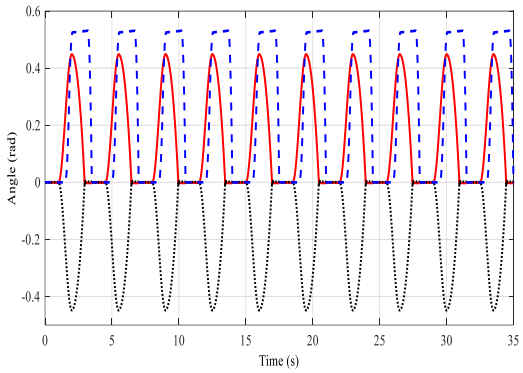

(a) ten leg step cycles

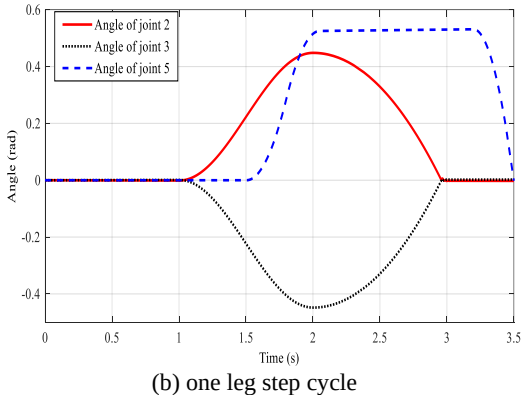

(b) one leg step cycle

Figure 8. Time responses of the joint angles during different step cycles

locomotion, the gravity potential energy changes from a minimum value ($P=0$) to a maximum value ($P=0.15j$), and the kinetic energy oscillate between a minimum value ($K=0$) and a maximum value ($K=0.0021j$). The elastic potential energy of the flat springs modelled as linear springs is realized between 1.75s and 2s. After 2s, the gravity potential, kinetic and impact energies of the leg transform to the elastic potential energy of the spring.

In the following, in order to complete our comprehensive behavior analysis, we compare our proposed structure with two other models in the term of the energy consumption. The first model shown in Figure 10(a) has been used in References [30-32] (first structure). This model has two active joints and three passive joints. Besides, the second model illustrated in Figure 10(b) has been applied in References [33, 34] and has three active joints (second structure). In this two models, all actuated joints are activated by the electrical motors, whereas the proposed structure has two stimulated joints that one of them implements the potential energy saved in the flat springs, and only the other one has a motor. The main specifications of these models are determined similar to our model such that their torque demands are comparable. Figure 11 shows a complete 20-sim model of these mechanisms in the graphical editor environment. Table 2 illustrates the simulation results in terms of the energy consumption for three different models in the one leg step cycle. From this table, we can see that our model can achieve an average of 2.5371 and 4.2897 times reduction for the energy consumption compared to the first and second structures, respectively.

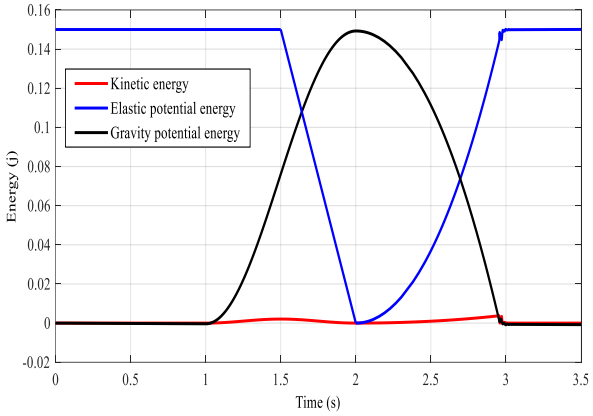

Figure 9. Time responses of the energy of the leg during one leg step cycle with respect to the first generalized coordinate

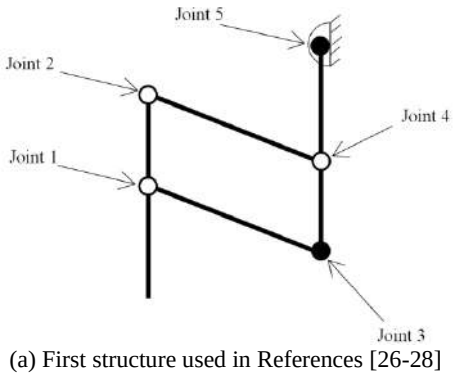

(a) First structure used in References [26-28]

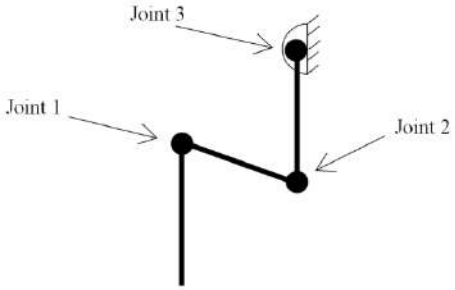

(b) Second structure utilized in References [29,30]

Figure 10. Structures applied to compare with the proposed model. Black circles denote actuated joints and white circles represent passive joints

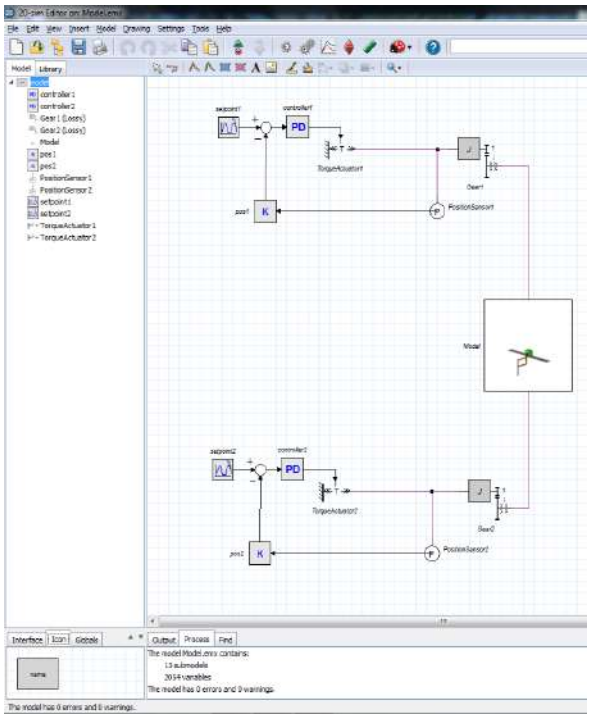

(a) First structure implemented in References [26-28]

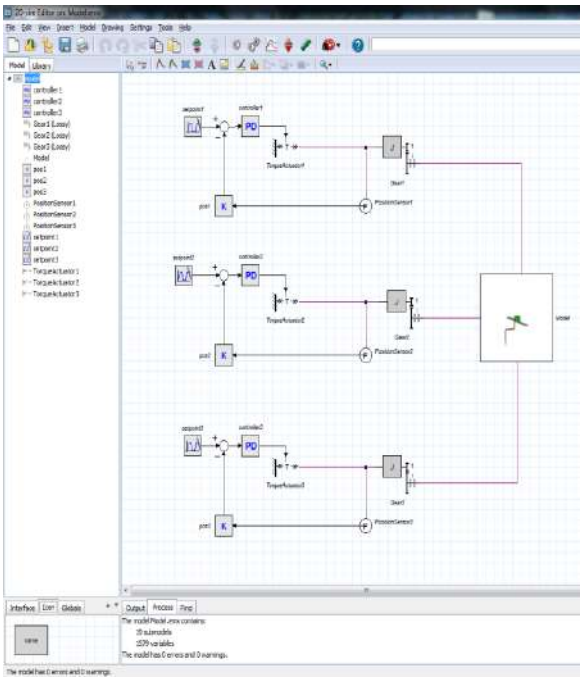

(b) Second structure employed in References [29,30]

Figure 11. 20-sim models of the compared mechanisms

TABLE 2. Comparison of the energy consumption for the different models

Model	Energy consumption (J)
First structure (Figure 10(a)) used in References [26-28]	0.8924
Second structure (Figure 10(b)) used in References [29,30]	1.3346

5. CONCLUSIONS

The legged robots are preferred to the wheeled robots to move through environments which generally contain some irregularities. In such an environment, the legged robots offer better mobility than their wheeled counterparts. In the legged robot design, one of the most challenging problems is minimization of the energy consumption. A reduction in energy consumption results in robots thatcan not only travel more, but also require smaller actuators that typically yield a reduction in the robot's weight and cost. The main objective of the present study is to minimize the energy consumption of the multi-legged robots through the storing and releasing of the kinetic and potential energy of the leg during each cycle. The passive and elastic elements have been adapted to strongly increase the robots performances and keep it simple and cheap. The dynamical modelling of the proposed one-legged robot has been provided in the 20-sim 3D mechanics toolbox. Moreover, a real world sample of it has been successfully built at the Robotics and Mechatronics (RAM) group, University of Twente. The analyses of the results have demonstrated that this structure operates considerably better in terms of power demand in comparison with those introduced in the literature.

6. ACKNOWLEDGMENTS

This work was sponsored by the Dutch Technology Foundation STW through the ROSE project under grant 10550.

7. REFERENCES

1. Shahzad, K. and Bilal Khan, M., "Control of a robotic wheel-chair prototype for people with walking disabilities", ***International Journal of Engineering, Transactions B: Applications***, Vol. 31, No. 5, (2018), 693-698, doi: 10.5829/ije.2018.31.05b.02.
2. Ni, W., Zhang, J., Tao, W, and Liu, T., "The design and realization of a gait rehabilitation training robot with body supporting mechanism", ***International Journal of Engineering, Transactions C: Aspects,*** Vol. 29, No. 9, (2016), 1314-1318, doi: 10.5829/idosi.ije.2016.29.09c.18.
3. Korayem, M. H., Peydaie, P. and Azimirad, V., "Investigation on the effect of different parameters in wheeled mobile robot error", ***International Journal of Engineering, Transactions A: Basics***, Vol. 20, No. 2, (2007), 195-210, doi: 10.5829/ ije.2007.20.02a.18.
4. Pishkenari, H. N., Mahboobi, S. H. and Alasty, A., "Trajectory tracking of a mobile robot using fuzzy logic tuned by genetic algorithm", ***International Journal of Engineering, Transactions A: Basics***, Vol. 19. No. 1, (2006), 95-104, doi: 10.5829/ije.2006.19.01a.02.
5. Korayem, M. H. and Bani Rostam, T., "Experimental analysis for measuring errors in wheeled mobile robots"**,** ***International Journal of Engineering, Transactions A: Basics***, Vol. 18, No. 2, (2005), 115-133, doi: 10.5829/ije.2005.18.02a.02.
6. Song, S.M. and Waldron, K.J., "Machines that walk: The adaptive suspension vehicle, Cambridge", ***Massachusetts: The MIT Press***, (1989), doi: 10.1002/acs.4480040308.
7. Roy, S. S. and Pratihar, D. K., "Dynamic modeling, stability and energy consumption analysis of a realistic six-legged walking robot", ***Robotics and Computer-Integrated Manufacturing***, Vol. 29 , No. 2, (2013), 400-416, doi: 10.1016/j.rcim.2012.09.010.
8. Chen, D., Li, N., Wang, H. and Chen, L., "Effect of Flexible Spine Motion on Energy Efficiency in Quadruped Running", ***Journal of Bionic Engineering***, Vol. 14, No. 4, (2017), 716-725, doi: 10.1016/S1672-6529(16)60436-5.
9. Hoffmann, M. and Simanek, J., "The Merits of Passive Compliant Joints in Legged Locomotion: Fast Learning, Superior Energy Efficiency and Versatile Sensing in a Quadruped Robot", ***Journal of Bionic Engineering***, Vol. 14, No. 1, (2017), 1-14, doi: 10.1016/S1672-6529(16)60374-8.
10. Mahapatra, A., Roy, S. S. and Pratihar, D. K., "Study on feet forces' distributions, energy consumption and dynamic stability measure of hexapod robot during crab walking", ***Applied Mathematical Modelling***, Vol. 65, (2019), 717-744, doi: 10.1016/j.apm.2018.09.015.
11. Koivumäki, J., Zhu, W.H. and Mattila, J., "Energy-efficient and high-precision control of hydraulic robots", ***Control Engineering Practice***, Vol. 85, (2019), 176-193, doi: 10.1016/j.conengprac.2018.12.013.

12. Alexander, R.M., "Three uses of springs in legged locomotion", ***The International Journal of Robotics Research***, Vol. 9, (1990), 53–61, doi: 10.1177/027836499000900205.
13. Shin, E.and Streit, D.A., "An energy of spring efficient quadruped with two stage equilibrator", ***Journal of Mechanical Design***, Vol.115, (1993), 156-163, doi: 10.1115/1.2919313.
14. Ahmadi, M. and Buehler, M., "Stable Control of a Simulated One-Legged Running Robot with Hip and Leg Compliance", ***IEEE Transactions on Robotics and Automation***, Vol. 13. No.1, (1997), 96-104, doi: 10.1109/70.554350.
15. Gregorio, P., Ahmadi, M. and Buehler, M., "Design, Control and Energetics of an Electrically Actuated Legged Robot", ***IEEE Transactions on Systems, Man, and Cybernetics***, Vol. 27, No.4, (1997), 626-634, doi: 10.1109/3477.604106.
16. Raby, E.Y. and Orin, D.E., "Passive Walking with Leg Compliance for Energy Efficient", ***Proceedings of the 1999 IEEE International Conference on Robotics & Automation***, (1999), 1702-1707, doi: 10.1109/ROBOT.1999.770354.
17. Pratt, J., Chew, C.M. Torres., Dilworth, A. P. and Pratt, G., "Virtual model control: an intuitive approach for bipedal locomotion", ***The International Journal of Robotics Research,*** Vol. 20, (2001), 129-143, doi: 10.1177/02783640122067309.
18. Scarfogliero, U., Folgheraiter, M. and Gini LARP, G., "biped robotics conceived as human modelling"***, in: S. Wermter et al. (Eds.)***, ***Biomimetic Neural Learning***, (2005), 298-313, doi: 10.1007/11521082_18.
19. Hyon, S.H., and Mita, T., "Development of a Biologically Inspired Hopping Robot - "Kenken", in: Proceedings of the 2002 IEEE International Conference on Robotics 8 Automation Washington DC, (2002), 3904-3991, doi: 10.1109/ROBOT.2002.1014356.
20. Iida, F.and Pfeifer, R., "Sensing through body dynamics", ***Robotics and Autonomous Systems,*** Vol. 54, (2006), 631-640, doi: 10.1016/j.robot.2006.03.005.
21. He, G.P., Tan, X.L., Zhang, X.H. and Lu, Z., "Modeling, motion planning, and control of one-legged hopping robot actuated by two arms", ***Mechanism and Machine Theory***, Vol. 43, (2008), 33-49, doi: 10.1016/j.mechmachtheory.2007.01.001
22. Scarfogliero, U., Stefanini, C. and Dario, P., "The use of compliant joints and elastic energy storage in bio-inspired legged robots", ***Mechanism and Machine Theory***, Vol. 44, (2009), 580-590, doi: 10.1016/j.mechmachtheory.2008.08.010.
23. He, G.and Geng, Z., "Dynamics synthesis and control for a hopping robot with articulated leg", ***Mechanism and Machine Theory***, Vol. 46, (2011), 1669-1688, doi: 10.1016/j.mechmachtheory.2011.06.013.
24. Von Twickel, A., Hild, M., Siedel, T., Patel, V. and Pasemann, F., "Neural control of a modular multi-legged walking machine: Simulation and hardware", ***Robotics and Autonomous Systems***, Vol. 60, (2012), 227-241, doi: 10.1016/j.robot.2011.10.006.
25. Gürel, S., Gultekin, H., and Eghbal Akhlagh, V., "Energy conscious scheduling of a material handling robot in a manufacturing cell", ***Robotics and Computer-Integrated Manufacturing***, Vol. 58, (2019), 97-108, doi: 10.1016/J.RCIM.2019.02.002.
26. Cao, H., Zhou, J., Jiang, P., Hon, K. and Dong, C., "An integrated processing energy modelling and optimization of automated robotic polishing system", ***Robotics and Computer-Integrated Manufacturing***, Vol. 65, (2020), 101973, doi: 10.1016/j.rcim.2020.101973.
27. Sun, B., Wang, L. and Peng, Z., "Bound-guided hybrid estimation of distribution algorithm for energy-efficient robotic assembly line balancing", ***Computers & Industrial Engineering***, Vol. 146, (2020), 106604, doi: 10.1016/j.cie.2020.106604.
28. Feng, Y., Ji, Z., Gao, Y., Zheng, H. and Tan, J., "An energy-saving optimization method for cyclic pick-and- place tasks based on flexible joint configurations", ***Robotics and Computer-Integrated Manufacturing***, Vol. 67, (2021), 102045, doi: 10.1016/j.rcim.2020.102037.
29. De Jalon, J.G. and Bayo, E., "Kinematic and Dynamic Simulation of Multibody Systems – The Real-Time Challenge", ***Springer***, (1994).
30. Kurazume, R., Yoneda, K. and Hirose, S., "Feedforward and feedback dynamic trot gait control for quadruped walking vehicle", ***Autonomous Robots***, Vol. 12, (2002), 157-172, doi: 10.1023/A:1014045326702.
31. Galvez, J.A., Estremera, J. and de Santos, P.G., "A new legged-robot configuration for research in force distribution", ***Mechatronics***, Vol. 13, (2003), 907-932, doi: 10.1016/S0957-4158(03)00008-4.
32. Roy, S.S. and Pratihar, D.K., "Soft computing-based expert systems to predict energy consumption and stability margin in turning gaits of six-legged robots", ***Expert Systems with Applications,*** Vol. 39, (2012), 5460-5469, doi: 10.1016/j.eswa.2011.11.039 .
33. Hirose, S., Masui, T. and Kikuchi, H., "TITAN III: A quadruped walking vehicle-its structure and basic characteristics", ***Second International Symposium on Robotic Research***, (1985), 325-331.
34. Bares, J. and Wettergreen, D., "Dante II: technical description, results and lessons learned", ***International Journal of Robotics Research,*** Vol. 18, 7, (1999), 621-649, doi: 10.1177/02783649922066475.

Persian Abstract

چکیده

روبات‌های دارای پا پادار بسیاری توسط دانشگاه‌ها، موسسات تحقیقاتی و صنایع طراحی و ساخته شده‌اند. با این حال، تحقیقات نسبتاً کمی بر روی مصرف انرژی این‌گونه ربات‌ها به عنوان یک معیار اساسی انجام شده است. در این مقاله، پیکربندی جدیدی برای ربات‌های دارای پا پادار به منظور کاهش مصرف انرژی در آن‌ها ارائه شده است. ساختار مکانیکی پیشنهادی را می‌توان به عنوان یک پا استفاده کرد یا به‌راحتی به ربات‌های دارای چهار، شش و هشت پا متصل نمود. این مکانیزم، یک اتصال چهار میله‌ای موازی مجهز به یک مفصل فعال و چهار مفصل غیرفعال است. در واقع، به‌کارگیری عناصر غیرفعال منجر به پارادایم‌های کنترل پس‌خور ساده می‌شود. علاوه‌براین، یکی دیگر از ویژگی‌های بارز این طرح، چیدمان کلاچ‌های یک‌طرفه و فنرهای تخت برای ذخیره انرژی پتانسیل به منظور استفاده از آن در مرحله بعد است. یک نمونه اولیه از مکانیزم مکانیکی پیشنهادی ساخته شده و شبیه‌سازی آن نیز در این مقاله ارائه شده است. مقایسه نتایج با سایر ساختارها، برتری و کارایی کار حاضر را از نقطه نظر کاهش مصرف انرژی نشان می‌دهد.

IJE TRANSACTIONS C: Aspetcs Vol. 33, No. 12, (December 2020) 2538-2548

International Journal of Engineering

Journal Homepage: www.ije.ir

Study on Equal Channel Angular Pressing Process of AA7075 with Copper Casing by Finite Element-response Surface Couple Method

M. Daryadel*

Mechanical Engineering Department, Urmia University, Urmia, Iran

P A P E R I N F O

Paper history:
Received 04 May 2020
Received in revised form 15 July 2020
Accepted 02 August 2020

Keywords:
Equal Channel Angular Pressing
Finite Element Method
Response Surface Methodology
Copper Casing
Forming Force
Strain

A B S T R A C T

Equal channel angular pressing (ECAP) process of AA7075 billet with the copper casing is comprehensively investigated. Firstly, ECAP process is simulated based on finite element method (FEM) in ABAQUS software and then is verified in comparison to the experimental data. The design of experiments using response surface methodology (RSM) is performed in order to investigate the processing parameters. The main effect of four considered parameters (channel angle, corner angle, friction coefficient and thickness of casing) on the maximum required force and strain was studied. Also, the regression models for estimating the maximum forming force and strain are represented in high reliability using analysis of variance (ANOVA). The results indicated that channel angle by 93.5% of contribution is the most effective parameter on the required forming force. It is concluded that the thickness of copper casing does not affect the forming force. Also, all terms of the presented regression model are effective on the strain value, according to the obtained results. Based on ANOVA results, channel and corner angel are the most effective parameters on the strain by 80 and 16% of the contribution, respectively. Also, the friction coefficient and the thickness of copper casing have almost no significant effects on the strain.

***doi**: 10.5829/ije.2020.33.12c.15*

1. INTRODUCTION

Nowadays, the attention of researchers has been particularly attracted to the production of ultra-fine grained (UFG) structure, because of the physical and mechanical properties of these materials are significantly higher than ordinary materials [1]. In addition to high strength, the UFG materials have good deformation properties so that, even at the lower temperature and higher strain rates, they exhibit excellent superplastic properties [2]. In general, nanostructure materials are made by two main approaches of top-down and bottom-up. In the first approach, the nanostructure is created by connecting atoms and molecules. In the second approach, the nanostructure is produced by applying severe plastic deformation (SPD) processes on the materials with large macroscopic dimensions and coarse grains [3]. In this method, due to applying strain to the material, its structure changes and it is possible to modify the microstructure, reduce the grain size to the nanometer scale and improve the mechanical properties, especially the strength, without changing its apparent dimensions [4]. There are no limits on the applying of strain in these processes because the dimensions of the samples are remained constant and following that the achieving to high strain is easy in the material [5].

One of the SPD methods is the equal channel angular pressing (ECAP) for bulk materials. The die of this method consists of two channels with equal cross sections which have an intersection in the channel and corner angles. The schematic of the ECAP process is shown in Figure 1. The billet is inserted from one side of the channel, and then it is guided into the channel by the punch and passes through it. The billet is bent when it passes through the intersection of two channels; hence the created strain in the sample is purely shear strain at this stage. Since the dimensions of the cross-section of the billet remain unchanged, the pressing may be

*Corresponding Author Institutional Email: *m.daryadel@urmia.ac.ir* (M. Daryadel)

Please cite this article as: M. Daryadel, Study on Equal Channel Angular Pressing Process of AA7075 with Copper Casing by Finite Element-response Surface Couple Method, International Journal of Engineering, Transactions C: Aspects Vol. 33, No. 12, (2020), 2538-2548.

repeated several times to attain very high strains. Also, there is no possibility of cracking and fracturing of billet, because it is bound to the channel and a high hydrostatic stress is applied to the billet. One of the important parameters in the ECAP process is the amount of applied strain at each stage of deformation, which can be obtained as Equation (1) [6].

$$\varepsilon_{eq} = \frac{N}{\sqrt{3}}\left[2\cot\left(\frac{\phi+\psi}{2}\right)+\psi\csc\left(\frac{\phi+\psi}{2}\right)\right] \quad (1)$$

where Φ is the angle between the two channels, Ψ is the corner angle of intersection of two channels, and *N* is the number of passes.

Yu et al. [7] studied the effect of fine-grained Al-Mg-Si alloy on the mechanical and electrical properties in the ECAP process. They found that after the ECAP process, the mechanical properties and the electrical conductivity of samples were improved. Extruded ZK60 Mg alloy samples were processed in ECAP for four passes at 250 °C by Dumitru et al. [8] The results showed a reduction in the grain size and forming of high angle grain boundaries. Also, there was a slight increase in the recrystallization temperature. The tensile test revealed that after four passes of ECAP, the elongation to failure had increased about twice as much as extruded specimens. The pure titanium samples were processed for four passes using the ECAP by Zhao et al. [9]. They found that the grain size has decreased from 25 μm to 150 nm. Also, the results showed that hardness, tensile strength, and elongation to failure were significantly increased after the ECAP process. Goodarzy et al. [10] investigated the mechanical properties of 2024 Al alloy after the ECAP process. The hardness and yield stress of the samples were significantly increased. The ductility and work hardening exponent of the deformed specimens were decreased due to the formation of shear bands within the microstructure. Mostaed et al. [11] used the ECAP process in four passes for ZM21 Mg alloy. After the first stage of ECAP, they observed the UFG structure in the specimens. Also, the tensile test results revealed that the yield stress and the elongation to failure of samples were increased by the ECAP process. Tang et al. [12] investigated the effect of the ECAP process on the yield strength and elongation to failure of AZ80 Mg alloys. They concluded that the yield strength and the elongation to failure improved by 135% and 17% by ECAP process, respectively. Safari and Joudaki [13] studied the effect of performing the ECAP process at elevated temperature on the tensile strength of pure aluminum and aluminum alloy samples. Their results showed that high temperature reduces the tensile strength of AA6063 and pure Al samples by 5% and 12%, respectively. Djavanroodi et al. [14] investigated of the effect of channel angle and corner angle on the strain distribution behavior in the ECAP process. They introduced Φ=60° and Ψ=15° as optimal conditions for

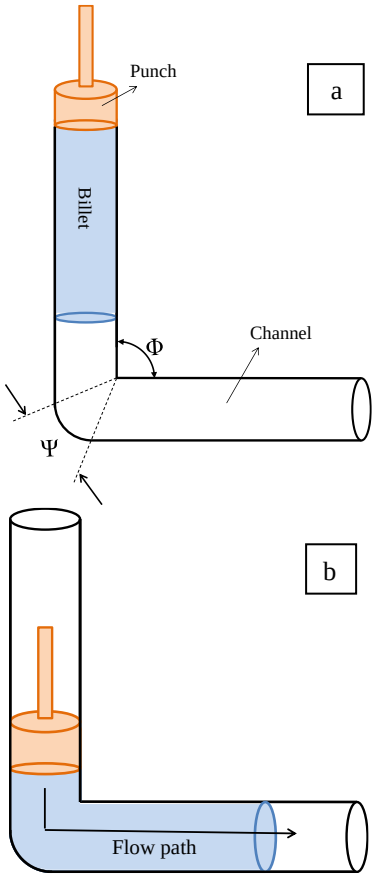

Figure 1. Schematic of a) before and b) after the ECAP process

achieving uniform strain distribution. A proper die for the ECAP process was designed and constructed by Reihanian et al. [15]. The mechanical properties and deformation behavior of pure Al have been investigated. Also, the effect of the pass numbers on the microstructure of the material is discussed. The significant increase in hardness and yield stress has been observed after the ECAP process.

Design of experiments (DOE) is one of the important issues in scientific researches to reduce the number of experiments, cost and time. Also, its purpose is simultaneous investigation effects of changing several parameters on an output variable and finding the optimal conditions. One the most important methods of DOE that are used in scientific studies especially in engineering investigations is response surface methodology (RSM). Lqbal et al. [16] studied the twist extrusion forming on the AA6082-T6 Al alloy. For this purpose, they used the RSM to investigate the effects of forming load, temperature, and number of passes on the tensile strength and hardness of samples. Balta et al. [17] obtained the relationship between the welding parameters of steel tube and their mechanical properties using the RSM. They studied the effects of friction pressure, friction time,

forging pressure and forging time on the tensile strength, elongation and petal crack length. The results showed that there is a little difference between the prediction results of RSM and the experimental results. Hasan-nejad et al. [18] used the RSM to examine the effects of blank holder force, die nose radius, punch nose radius, blank radius, and friction coefficients parameters on the forming load and thickness reductions of the produced brass-steel laminated sheets in the deep drawing process. They simulated the designed experiments by using the finite element (FE) model, which the obtained results showed a good correlation with the experimental results. Teimouri and Ashrafi [19] investigated the effects of die geometry and fluid pressure on the thinning ratio and punch force in the hydrodynamic deep drawing process of Al 7075. Also, they used the desirability approach to determine the desired parameters to achieve the minimum thinning and forming force simultaneously. The results indicated that the punch and die corner radiuses and fluid pressure have significant effects on the response parameters. Guo and Tang [20] used the RSM to determine the limiting sheet diameter in the deep drawing process to predict the early quality before production of samples. Also, it should be noted that the obtained results had a good correlation with the simulation results.

Naseri et al. [21] experimentally investigated the ECAP process of 7075 aluminum alloys. They stated that some age-hardenable aluminum alloys are difficulty to process by ECAP at room temperature. In this case, to use a casing is a new idea in ECAP. They used a copper casing that has good frictional properties due to the possibility of cracking aluminum because of its undesirable frictional properties. They reported that by using of copper casing the required force forming is decreaced and the hardness is increased.

The comprehensive investigation of a process especially when numerous parameters affect that process is experimentally difficult, costly and time-consuming. According to the literature, DOE methods can be effective in these situations. The comprehensive study of ECAP processes as one the most important UFG approaches seems to be necessary. For this purpose, the ECAP process of 7075 Al alloy with copper casing is simulated using a FEM model. The simulation process is verified in comparison to experimental results reported in literature [21]. The most important parameters are selected as input and their effects on the required force and strain were investigated using RSM. In fact, the aim and innovation of the present paper are a comprehensive study of the effect of important processing parameters of the ECAP process and the effect of using the casing for samples by the FEM-RSM couple method. It also provides optimal conditions for simultaneously achieving the minimum forming required force and the maximum strain. So that such a comprehensive study was not seen in the literature. Therefore a comprehensive study is performed and helpful results are demonstrated using the combination of the FEM-RSM model.

2. FINITE ELEMENT (FE) SIMULATION

In order to investigate the effects of processing parameters and casing thickness on the maximum required force and the strain in ECAP process, the finite element software of Abaqus/CAE 6.12-3 was used. The die and punch were modeled as analytical rigid according to the presented dimensions in Figure 2. Deformable form is used to model samples that including billet and casing as shown in Figure 3. The AA7075 and copper have been utilized as the billet and casing in this process, respectively. The used Holloman equations for AA7075 and copper are $\sigma=642\varepsilon^{0.35}$ and $\sigma=297\varepsilon^{0.443}$, respectively according to the experiments results reported in literature [22, 23]. Figure 4 shows the stress-strain diagram for AA7075 and copper. Also the properties of the AA7075 and copper are given in Table 1. The friction coefficient is considered between aluminum billet and copper casing, because they should not have relative movement on each other during the ECAP process [21]. The billet and casing have been meshed using tetrahedral elements. The number of elements was selected based on the mesh sensitivity test and by considering the lower modeling time. The final sample after ECAP process respect to strain is shown in Figure 5.

3. FEM VALIDATION

In order to verify the simulation results of present study, the maximum force is compared to the experimental results of Naseri et al. [21]. The simulation conditions

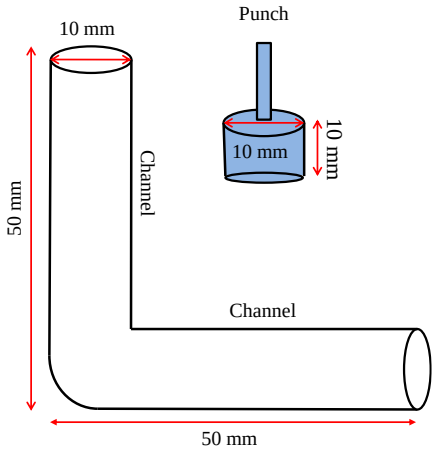

Figure 2. Schematic geometry and dimensions of die and punch

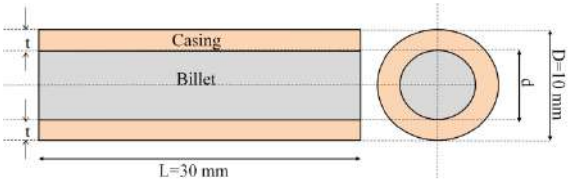

Figure 3. Schematic geometry and dimensions of samples

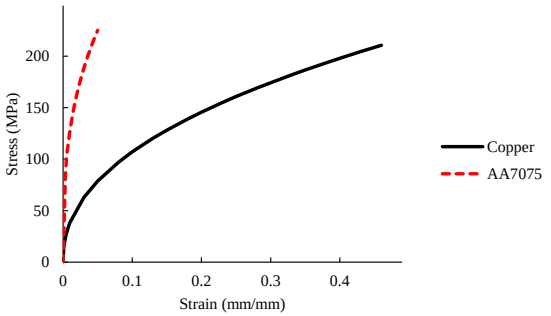

Figure 4. The stress-strain diagram of AA7075 and copper [22,23]

TABLE 1. Mechanical and physical properties of materials [22,23]

Materials	Properties				
	Yield stress (MPa)	Ultimate stress (MPa)	Young's modulus (GPa)	Density (kg/m^3)	Poisson' s ratio
AA7075	103	228	71.7	2810	0.33
Cu	33.3	210	110	8930	0.343

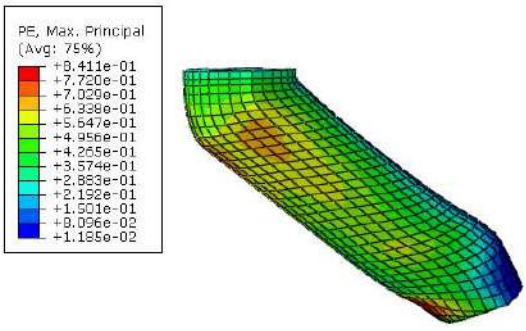

Figure 5. The FEM simulation of final sample after ECAP process respect to strain

from literature [21] are given in Table 2. The comparison results are presented in Table 3. According to Table 3, the simulation results of present study have a good correlation with experimental results of Naseri et al. [21] and maximum difference between the experimental and simulation maximum force is almost 4.5%; therefore, the simulation of this study is highly authenticated.

TABLE 2. Conditions of validation runs [21]

Run	t (mm)	d (mm)	D (mm)	L (mm)
R1	0	20	20	140
R2	1	18		
R3	2	16		
R4	3	14		
R5	4	12		
R6	5	10		

TABLE 3. Maximum force validation

Run	Maximum force (kN)		
	Experimental [23]	Simulation (present study)	Difference (%)
R1	196	194	1.02
R2	180	182	1.11
R3	152	152	0.00
R4	135	141	4.44
R5	125	128	2.40
R6	112	109	2.68

4. RESPONSE SURFACE METHODOLOGY (RSM)

RSM is one of the mathematical and statistical techniques that is used to optimize response variables in the presence of various factors. This method saves time and cost by reducing the number of experiments. Furthermore, the RSM accurately predicts the interactions of different independent variables that change at the same time on the response variable. Another advantage of the RSM is its non-linearity model, which improves the modeling accuracy. Therefore, in addition to evaluating the best level, this model finds the exact value that optimizes the design. The most recommended types of RSM designs are Box-Behnken and central composite designs (CCD). CCD is used for the design of experiments in this study [24-26]. Equation (2) shows the second-order polynomial for the RSM [27, 28].

$$y = \beta_0 + \sum_{i=1}^{k} \beta_i x_i + \sum_{i=1}^{k} \beta_{ii} x_i^2 + \sum \sum_{i<j} \beta_{ij} x_i x_j + \varepsilon \quad (2)$$

In Equation (2), y is the response variable, β_0, β_i, β_{ii} and β_{ij} are constants, linear, quadratic and interaction coefficients, respectively. x_i and x_j are the independent variables and ε is the statistical error. The correctness of regression model is determined using the R^2 that obtained by analysis of variance (ANOVA). So that R^2 to be closer to one, the model will be more efficient.

In the present study, the angle between the two channels (Φ), the corner angle (Ψ), and friction

coefficient (μ) as ECAP process parameters and the thickness of casing (t) were considered as variable parameters. Their effects were investigated on the maximum force and strain distribution as the criteria in DOE approach by using FEM-RSM couple method. For this purpose, according to the processing and applicable conditions in the validated simulation, by applying lower and higher levels of variable parameters, according to Table 4 the experiments were designed in accordance with the CCD procuring 31 experiments using Minitab software as shown in Table 5.

TABLE 4. The considered levels of variable parameters

Parameters	Levels	
	Low	High
Φ (deg)	82.5	127.5
Ψ (deg)	7.5	22.5
μ	0.038	0.112
t (mm)	1	3

5. RESULT AND DISCUSSION

The simulation process of ECAP samples was performed according to the design of experiments and the conditions set as Table 5. The obtained results for the maximum force and the strain are reported in Table 6.

5. 1. Maximum Force

5. 1. 1. Contribution The contribution of each parameter on the maximum force is expressed based on the results of analysis of variance (ANOVA) tool of RSM method as Table 7. The results indicate that Φ is the most effective parameter on the maximum force and has a significant contribution of 93.5%. After Φ, μ and Ψ are the second and third effective parameters on the maximum force by contribution of 3.8 and 2.5%, respectively. Also, the results illuminate that *t* has not influence on the maximum force.

TABLE 5. Design of experiments according to RSM

	Parameters			
Run	Φ (deg)	Ψ (deg)	μ	t (mm)
1	127.5	7.5	0.112	3
2	82.5	7.5	0.038	1
3	105.0	15.0	0.075	2
4	82.5	7.5	0.038	3
5	105.0	15.0	0.075	2
6	127.5	7.5	0.112	1
7	105.0	15.0	0.075	2
8	105.0	15.0	0.075	2
9	82.5	22.5	0.112	3
10	105.0	15.0	0.149	2
11	127.5	7.5	0.038	3
12	82.5	22.5	0.038	1
13	82.5	22.5	0.112	1
14	127.5	22.5	0.038	1
15	105.0	15.0	0.075	0
16	105.0	15.0	0.075	4
17	127.5	7.5	0.038	1
18	82.5	7.5	0.112	1
19	105.0	15.0	0.075	2
20	60.0	15.0	0.075	2
21	82.5	22.5	0.038	3
22	105.0	15.0	0.075	2
23	82.5	7.5	0.112	3
24	105.0	0.0	0.075	2
25	105.0	30.0	0.075	2
26	127.5	22.5	0.038	3
27	105.0	15.0	0.001	2
28	127.5	22.5	0.112	1
29	150.0	15.0	0.075	2
30	127.5	22.5	0.112	3
31	105.0	15.0	0.075	2

TABLE 6. The results of the obtained maximum force and strain from FEM simulation

Run	Maximum force (kN)	Strain (mm/mm)
1	15.3	0.95
2	49.6	1.82
3	22.2	1.11
4	50.3	1.82
5	22.2	1.11
6	15.7	0.82
7	22.2	1.11
8	22.2	1.11
9	41.0	1.46
10	29.5	1.33
11	10.7	0.72
12	47.9	1.12
13	49.7	1.23
14	11.0	0.75
15	21.6	0.89

16	22.2	1.04
17	13.0	0.72
18	74.9	2.12
19	22.2	1.11
20	75.5	2.24
21	39.2	1.28
22	22.2	1.11
23	72.9	2.25
24	22.3	1.60
25	20.6	0.88
26	10.5	0.76
27	18.3	1.02
28	16.2	0.74
29	7.4	0.63
30	15.2	0.84
31	22.2	1.11

TABLE 7. Contribution of parameters on the maximum force

Parameters	Contribution (%)	Rank
Φ	93.5	1
Ψ	2.5	3
μ	3.8	2
t	0.2	4

5. 1. 2. Main Effect of Parameters Main effect of considered parameters on the maximum force is shown in Figure 6. According to Figures 6(a) and 6(b), by increasing Φ and Ψ, the required force for the ECAP process is reduced. By increasing Φ from 75 to 100° and Ψ from 5 to 15° the maximum force decreases 48 and 18%, respectively. By increasing Φ and Ψ, the sample flows through a less bending path; therefore, the lower forming force is needed. But as can be seen, with a further increase in Φ (from 125 to 150°) and Ψ (from 25 to 30°), the maximum force remains almost constant. In fact, increasing Φ and Ψ to a certain amount reduces the maximum force, due to the increase in ease of movement, and the further increase will not have much effect on the force. Also, Figure 6(c) illustrates that increasing μ increases the required force. By increasing μ, the maximum force is increased 48%. The contact between the sample and the channel justifies this occurrence. Increasing friction coefficient between the casing and the inner surface of the channel increases the forming force to confront with the friction force in the opposite direction. As shown in Figure 6(d), the t does not have significant effect on the forming force as the ANOVA results illuminated.

5. 1. 3. Regression Model Using the ANOVA results, the regression model to calculate the maximum force was obtained using Equation (3).

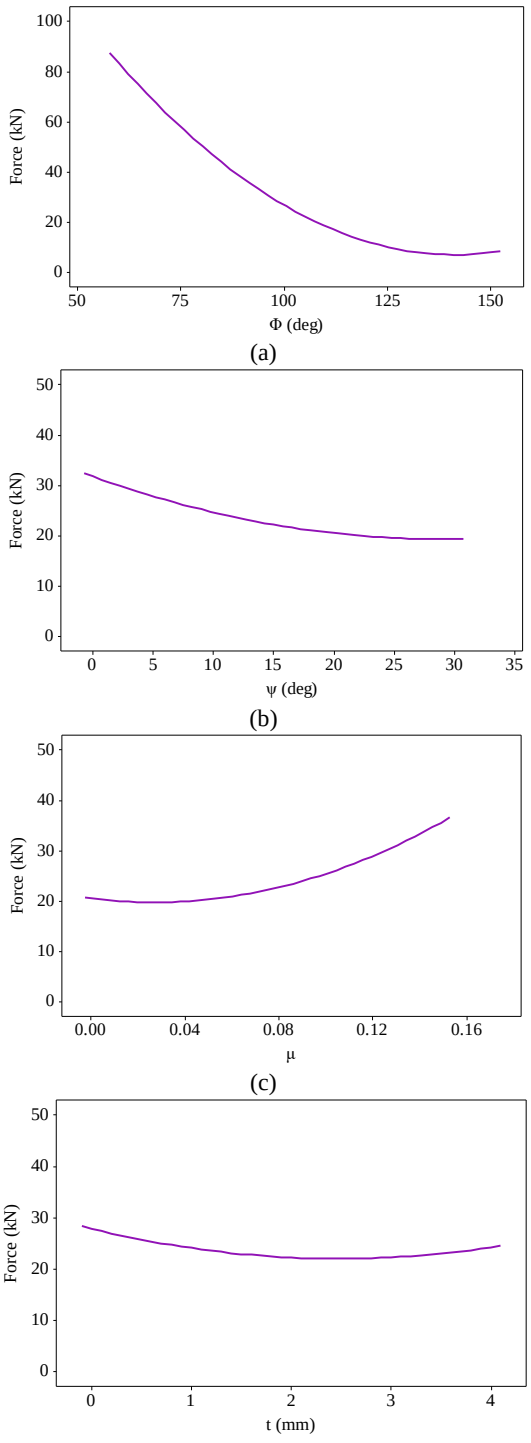

Figure 6. Main effect of a) Φ, b) Ψ, c) μ, and d) *t* on the maximum force

$$Maximumforce = 264.7 - 3.530\phi - 2.57\psi + 357\mu - 6.97t + 0.01153\phi^2 + 0.0150\psi^2 + 1060\mu^2 + 0.96t^2 + 0.02529\phi\times\psi - 2.57\phi\times\mu + 0.0404\phi\times t - 9.34\psi\times\mu - 0.124\psi\times t - 1.8\mu\times t \quad (3)$$

According to the ANOVA results, R^2 value is 95.4%, that shows the obtained model is efficient and can be used to estimate the maximum force with high reliability. The P-value results for each term of regression model of maximum force are presented in Table 8. According to the default error which is considered by Minitab software (i.e. 5%), a P-value smaller than 0.05 shows that the corresponding parameter has a significant contribution in the maximum force. In other words, a P-value larger than 0.05 indicate that the corresponding parameter can be eliminated from the model due to its ineffectiveness.

According to the results given in Table 8, t can be deleted among the linear terms and among the square and interaction terms, Φ^2 and $\Phi^{\times}\Psi$ have significant contribution, respectively and the other terms can be ignored. Finally, the regression model is presented using Equation (4).

$$Maximumforce = 264.7 - 3.530\phi - 2.57\psi + 357\mu + 0.01153\phi^2 + 0.02529\phi\times\psi \quad (4)$$

5. 1. 4. Interaction Effects of Parameters Since $\Phi^{\times}\Psi$ had a significant contribution, the interaction effect of Φ and Ψ on the maximum force is investigated in Figure 7 by surface and contour plots. The results indicate that in all values of Ψ, the force decreases by increasing Φ, but the effect of Φ is more significant in the lower Ψ. Also, the changes of Ψ have a noteworthy effect in the lower Φ and by increasing Ψ, the force reduces, while changes of Ψ are almost effectless in large Φ. Finally, according to Figure 7(b), it is revealed that high values of Φ and low values of Ψ are suitable for reducing the forming force.

TABLE 8. Obtained P-value for terms of regression model of maximum force using the ANOVA

Terms of regression model	P-value
Φ	0.000
Ψ	0.016
μ	0.005
t	0.442
Φ^2	0.000
Ψ^2	0.438
μ^2	0.190
t^2	0.381
$\Phi^{\times}\Psi$	0.008
$\Phi^{\times}\mu$	0.152
$\Phi^{\times}t$	0.531
$\Psi^{\times}\mu$	0.087
$\Psi^{\times}t$	0.520
$\mu^{\times}t$	0.963

5. 2. Strain

5. 2. 1. Contribution The ANOVA results show the contribution of parameters on the strain as presented in Table 9. According to the results, Φ with contribution of 79.8% affect the strain as the most effective parameter. Ψ and μ are the next effective parameters on the strain. The contribution of Ψ and μ on the strain is 15.9 and 3.4%, respectively. Also, t has a contribution lesser than 1% on the strain.

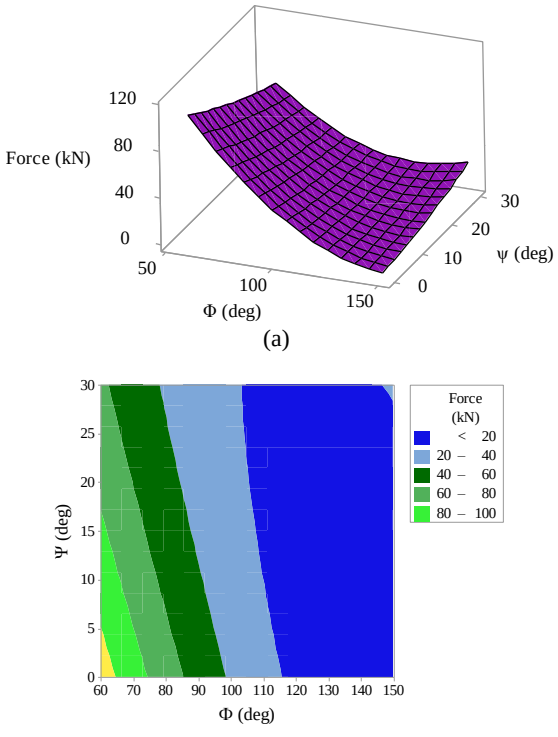

Figure 7. Interaction effect of Φ and Ψ on the maximum force a) surface plot b) contour plot

TABLE 9. Contribution of parameters on the strain

Parameters	Contribution (%)	Rank
Φ	79.8	1
Ψ	15.9	2
μ	3.4	3
t	0.9	4

5. 2. 2. Main Effect of Parameters Main effect of considered parameters on the strain is shown in Figure 8. Figure 8 shows that by increasing Φ and Ψ the strain decreases. By increasing Φ from 75 to 125° and Ψ from 5 to 20° the strain reduces 55 and 21%, respectively. It can be explicated that by increasing Φ and Ψ, the sample flows easily from the intersection of two channels, it bends a little and subjected to less shear forces, therefore lower strain is generated. Also, Figure 8 reveals that the effects of μ and t have almost no significant effects on the strain as shown by ANOVA results in previous section.

5. 2. 3. Regression Model The obtained regression model based on the ANOVA results for the strain is expressed as Equation (5). The results illuminate that R^2 parameter for regression model of strain is 99.81%. Therefore, the regression model has a high reliability to estimate the strain of ECAP samples.

$$\begin{aligned} Strain = {} & 6.141 - 0.06360\phi - 0.14386\psi + 6.28\mu + 0.1780t + 0.000165\phi^2 \\ & 0.000606\psi^2 + 13.39\mu^2 - 0.03413t^2 + 0.001035\phi\times\psi - 0.04745\phi\times\mu \\ & -0.000783\phi\times t - 0.1600\psi\times\mu + 0.002103\psi\times t + 0.708\mu\times t \end{aligned} \quad (5)$$

According to the P-value results that are given in Table 10, it is clear that all terms of regression model have a significant contribution on the strain since all P-values are lesser than 0.05.

5. 2. 4. Interaction Effects of Parameters Since t has little effect on the output and for brevity, the interaction effect of the other three parameters (i.e. Φ, Ψ and μ) will be examined on the strain. The interaction effect of Φ and Ψ on the strain is shown in Figure 9 by surface and contour plots. It can be seen that increasing Φ in the lower values of Ψ has led to significant reduction

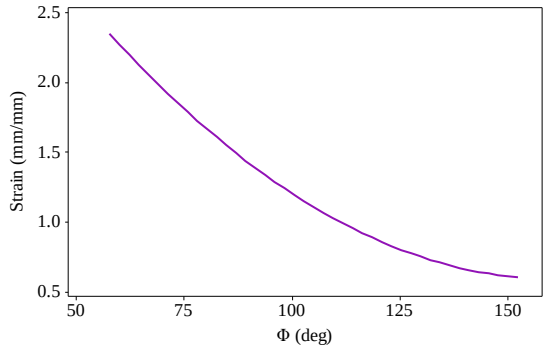

(a)

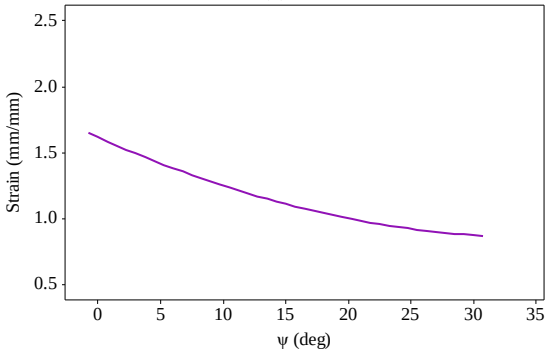

(b)

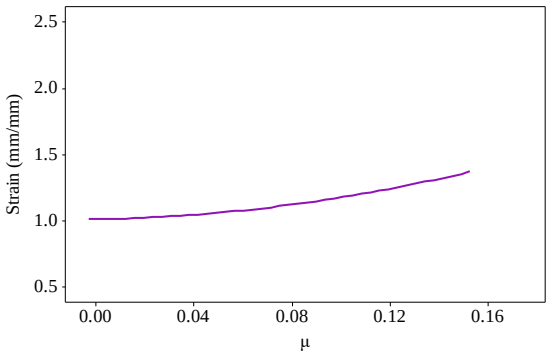

(c)

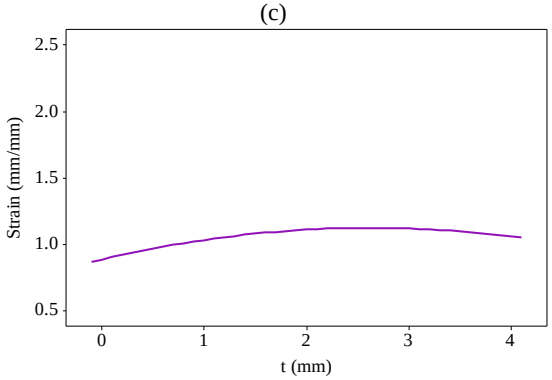

(d)

Figure 8. Main effect of a) Φ, b) Ψ, c) μ, and d) *t* on the strain

TABLE 10. Obtained P-value for terms of regression model of strain using the ANOVA

Terms of regression model	P-value
Φ	0.000
Ψ	0.000
μ	0.000
t	0.000
Φ^2	0.000
Ψ^2	0.000
μ^2	0.002
t^2	0.000
Φ×Ψ	0.000
Φ×μ	0.000
Φ×t	0.019
Ψ×μ	0.000
Ψ×t	0.034
μ×t	0.001

in the strain, whereas in the larger values of Ψ, have not significant effect on the strain. Also, by increasing Ψ in all values of Φ, the strain decreases but the effect of Ψ is more significant in the lower values of Φ. As shown in Figure 9(b), lower Φ and Ψ values are required to achieve high strain.

Figure 10 shows the interaction effect of Φ and μ on the strain. By increasing Φ, the strain reduces in all values of μ. Also, contrary to larger values of Φ, the strain enhances sharply by increasing of μ in the lower values of Φ. The contour plot also shows that the highest strain is obtained at low values of Φ and high values of μ.

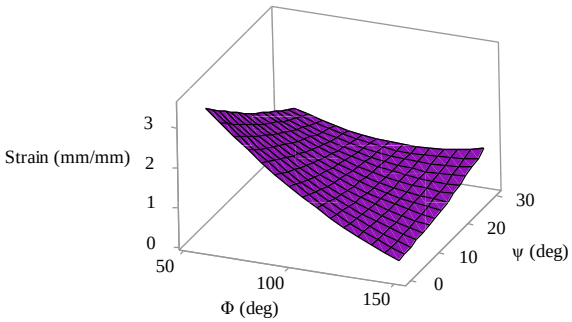

(a)

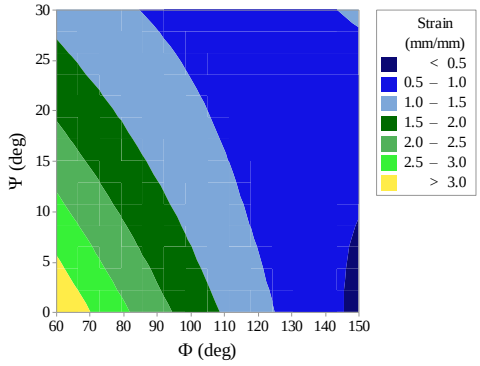

(b)

Figure 9. Interaction effect of Φ and Ψ on the strain a) surface plot b) contour plot

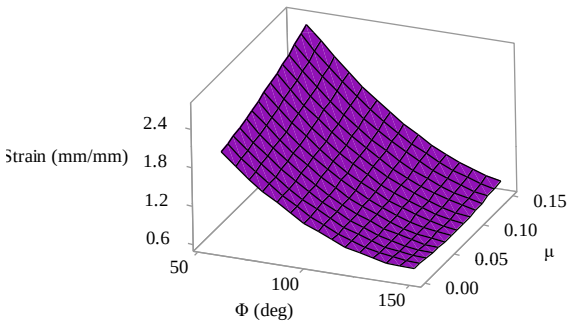

(a)

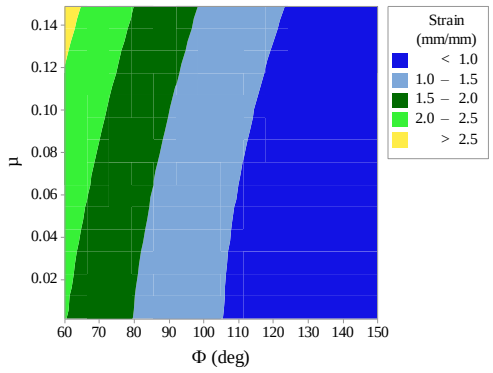

(b)

Figure 10. Interaction effect of Φ and μ on the strain a) surface plot b) contour plot

Also, the interaction effect of Ψ and μ on the strain is presented in Figure 11 by surface and contour polts. According to Figure 11, increasing Ψ decreases the strain, while its effect is more significant in the larger values of μ. The increasing μ in the lower values of Ψ causes increasing the strain. But in the larger values of Ψ, there is no significant effect of μ on the strain. The strain increases by decreasing Ψ and increasing μ.

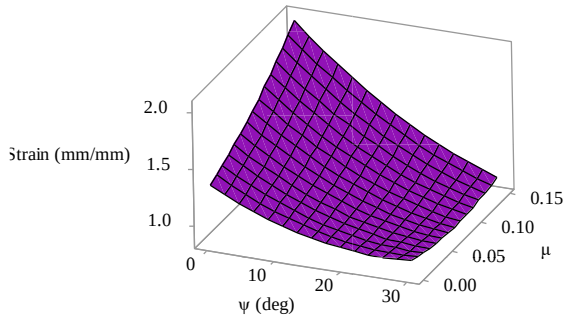

(a)

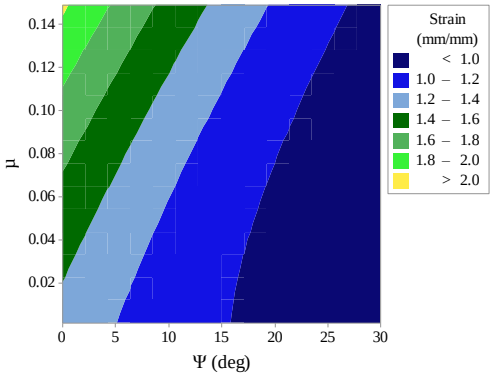

(b)

Figure 11. Interaction effect of Ψ and μ on the strain a) surface plot b) contour plot

6. OPTIMIZATION

Based on the prediction of Minitab software using the RSM method, the optimal conditions for minimizing the maximum required force and maximizing the strain are Φ=93.64°, Ψ=0°, μ=0.001, and t=1.62 mm. Under these conditions, the maximum force and strain are obtained 32.65 N and 1.72, respectively, by presented regression models.

7. CONCLUSION

In this study, a verified finite element simulation of the ECAP process of billet with the casing was studied. RSM was implemented in order to the investigation of the process in proposed 31 tests. The channel angle, corner angle, friction coefficient, and the casing thickness of the samples were introduced as variable parameters and the maximum force and strain were considered as the output parameters. The most important results are listed below:

- The most effective parameters in the order of significance on the maximum force are: channel angle, friction coefficient and corner angle.
- The most effective parameters in the order of significance on the strain are: channel angle, corner angle and friction coefficient.
- The thickness of copper casing has almost no significant effects on the maximum force and strain.
- The required forming force was reduced by increasing channel and corner angles and decreasing the friction coefficient.
- The strain was increased by decreasing channel and corner angles and increasing friction coefficient.
- The high accuracy regression models for estimating the required force and strain were obtained using ANOVA results.
- The interaction effects of parameters were investigated and it was revealed that the minimum required force is obtained at high values of Φ and low values of Ψ.
- The interaction effects of parameters showed that the maximum strain is obtained at low values of Φ and Ψ.
- The optimal conditions for reducing the maximum required force and increasing the strain in the ECAP process were predicted as Φ=93.64°, Ψ=0°, μ=0.001, and t=1.62 mm.

8. REFERENCES

1. Stráská, J., Janeček, M., Čížek, J., Stráský, J. and Hadzima, B., "Microstructure stability of ultra-fine grained magnesium alloy AZ31 processed by extrusion and equal-channel angular pressing (EX–ECAP)", ***Materials Characterization***, Vol. 94, (2014), 69-79. DOI: 10.1016/j.matchar.2014.05.013
2. Rao, M.P., Sarma, V.S. and Sankaran, S., "Development of high strength and ductile ultra-fine grained dual phase steel with nano sized carbide precipitates in a V–Nb microalloyed steel" , ***Materials Science and Engineering: A***, Vol. 568, (2013), 171-175. DOI: 10.1016/j.msea.2012.12.084
3. Shaarbaf, M. and Toroghinejad, M.R., "Nano-grained copper strip produced by accumulative roll bonding process", ***Materials Science and Engineering: A***, Vol. 473, (2008), 28-33. DOI: 10.1016/j.msea.2007.03.065
4. Faraji, G., Yavari, P., Aghdamifar, S. and Mashhadi, M.M., "Mechanical and microstructural properties of ultra-fine grained AZ91 magnesium alloy tubes processed via multi pass tubular channel angular pressing (TCAP)", ***Journal of Materials Science & Technology***, Vol. 30, (2014), 134-138. DOI: 10.1016/j.jmst.2013.08.010
5. Ravisankar, B., "Equal-Channel Angular Pressing (ECAP)", ***Handbook of Mechanical Nanostructuring***, (2015), 277-297. DOI: 10.1002/9783527674947.ch13
6. Osman, M., Zhang, D.T., Tong, Y.X., Zheng, Y.F. and Li, L., "3D FEM Simulation of multipass ECAP Ti-50.8% Ni at various temperatures", ***In Advanced Materials Research,*** Vol. 1004, (2014), 1204-1210. DOI: 10.4028/www.scientific.net/AMR.1004-1005.1204
7. Murashkin, M.Y., Sabirov, I., Kazykhanov, V.U., Bobruk, E.V., Dubravina, A.A. and Valiev, R.Z., "Enhanced mechanical properties and electrical conductivity in ultrafine-grained Al alloy processed via ECAP-PC", ***Journal of Materials Science***, Vol. 48, (2013), 4501-4509. DOI: 10.1007/s10853-013-7279-8
8. Dumitru, F.D., Higuera-Cobos, O.F. and Cabrera, J.M., "ZK60 alloy processed by ECAP: Microstructural, physical mechanical characterization", ***Materials Science and Engineering: A***, Vol. 594, (2014), 32-39. DOI: 10.1016/j.msea.2013.11.050
9. Zhao, X., Yang, X., Liu, X., Wang, C.T., Huang, Y. and Langdon, T.G., "Processing of commercial purity titanium by ECAP using a 90 degrees die at room temperature", ***Materials Science and Engineering: A***, Vol. 607, (2014), 482-489. DOI: 10.1016/j.msea.2014.04.014
10. Goodarzy, M.H., Arabi, H., Boutorabi, M.A., Seyedein, S.H. and Najafabadi, S.H., "The effects of room temperature ECAP and subsequent aging on mechanical properties of 2024 Al alloy", ***Journal of Alloys and Compounds***, Vol. 585, (2014), 753-759. DOI: 10.1016/j.jallcom.2013.09.202
11. Mostaed, E., Fabrizi, A., Dellasega, D., Bonollo, F. and Vedani, M., "Microstructure, mechanical behavior and low temperature superplasticity of ECAP processed ZM21 Mg alloy" ***Journal of Alloys and Compounds***, Vol. 638, (2015), 267-276. DOI: 10.1016/j.jallcom.2015.03.029
12. Tang, L., Zhao, Y., Islamgaliev, R.K., Tsao, C.Y., Valiev, R.Z., Lavernia, E.J. and Zhu, Y.T., "Enhanced strength and ductility of AZ80 Mg alloys by spray forming and ECAP", ***Materials Science and Engineering: A***, Vol. 670, (2016), 280-291. DOI: 10.1016/j.msea.2016.06.031
13. Safari, M. and Joudaki, J., "Effect of Temperature on Strength and Hardness in Multi-pass Equal Channel Angular Pressing (ECAP) of Aluminum Alloys", ***Transactions of the Indian Institute of Metals***, (2020), 1-9. DOI: 10.1007/s12666-020-01877-0
14. Djavanroodi, F., Omranpour, B., Ebrahimi, M. and Sedighi, M., "Designing of ECAP parameters based on strain distribution uniformity", ***Progress in Natural Science: Materials International***, Vol. 22, (2012), 452-460. DOI: 10.1016/j.pnsc.2012.08.001
15. Reihanian, M., Ebrahimi, R., Tsuji, N. and Moshksar, M.M., "Analysis of the mechanical properties and deformation behavior of nanostructured commercially pure Al processed by equal channel angular pressing (ECAP)", ***Materials Science and Engineering: A***, Vol. 473, (2008), 189-194. DOI: 10.1016/j.msea.2007.04.075

16. Mohammed Iqbal, U. and Senthil Kumar, V.S., "Modeling of twist extrusion process parameters of AA6082-T6 alloy by response surface approach", ***Proceedings of the Institution of Mechanical Engineers, Part B: Journal of Engineering Manufacture***, Vol. 228, (2014), 1458-1468. DOI: 10.1177/0954405413519606

17. Balta, B., Arici, A.A. and Yilmaz, M., "Optimization of process parameters for friction weld steel tube to forging joints", ***Materials & Design***, Vol. 103, (2016), 209-222. DOI: 10.1016/j.matdes.2016.04.072

18. Hasannejad, S.J., Hasanzadeh, R., Doniavi, A. and Modanloo, V., "Finite element simulation analysis of laminated sheets in deep drawing process using response surface method", ***The International Journal of Advanced Manufacturing Technology***, Vol. 93, (2017), 3245-3259. DOI: 10.1007/s00170-017-0780-5

19. Teimouri, R. and Ashrafi, H., "Optimization of Hydroforming Process for Deep Drawing of AA7075 Using Finite Element Simulation and Response Surface Methodology", ***Transactions of the Indian Institute of Metals***, Vol. 70, (2017), 2265-2275. DOI: 10.1007/s12666-017-1083-0

20. Guo, Z. and Tang, W., "The limiting sheet diameter prediction model for cup-shaped part drawing process with diverse mould assemblage based on RSM", In IOP Conference Series: Materials Science and Engineering, Vol. 191, No. 1, (April, 2017), IOP Publishing. DOI: 10.1088/1757-899X/191/1/012030

21. Naseri, R., Kadkhodayan, M. and Shariati, M., "An experimental investigation of casing effect on mechanical properties of billet in ECAP process", ***The International Journal of Advanced Manufacturing Technology***, Vol. 90, (2017), 3203-3216. DOI: 10.1007/s00170-016-9658-1

22. Shaeri, M.H., Djavanroodi, F., Sedighi, M., Ahmadi, S., Salehi, M.T. and Seyyedein, S.H., "Effect of copper tube casing on strain distribution and mechanical properties of Al-7075 alloy processed by equal channel angular pressing", ***The Journal of Strain Analysis for Engineering Design***, Vol. 48, (2013) 512-521. DOI: 10.1177/0309324713498234

23. Manafi, B. and Saeidi, M., "Development of a novel severe plastic deformation method: friction stir equal channel angular pressing", ***The International Journal of Advanced Manufacturing Technology***, Vol. 86, (2016), 1367-1374. DOI: 10.1007/s00170-015-8305-6

24. Teimouri, R. and Ashrafi, H., "Optimization of hydroforming process for deep drawing of AA7075 using finite element simulation and response surface methodology", ***Transactions of the Indian Institute of Metals***, Vol. 70, (2017), 2265-2275. DOI: 10.1007/s12666-017-1083-0

25. Kazemian, M.E. and Gandjalikhan Nassab, S.A., "Thermodynamic Analysis and Statistical Investigation of Effective Parameters for Gas Turbine Cycle using the Response Surface Methodology", ***International Journal of Engineering, Transactions B: Applications***, Vol. 33, No. 5, (2020), 894-905. DOI: 10.5829/ije.2020.33.05b.22

26 Davarnejad, R., Pishdad, R. and Sepahvand, S., "Dye adsorption ON the blends of saffron petals powder with activated carbon: Response surface methodology", ***International Journal of Engineering, Transactions C: Aspects***, Vol. 31, No. 12, (2018), 2001-2008. DOI: 10.5829/ije.2018.31.12c.02

27. Abbas, A.T., Taha, M.A., Ragab, A.E., El-Danaf, E.A. and Abd El Aal, M.I., "Effect of equal channel angular pressing on the surface roughness of solid state recycled aluminum alloy 6061 chips", ***Advances in Materials Science and Engineering***, (2017). DOI: 10.1155/2017/5131403

28. Rashahmadi, S., Karimi, Y. and Hasanzadeh, R., "The Effects of Newmark Method Parameters on Errors in Dynamic Extended Finite Element Method Using Response Surface Method", ***International Journal of Engineering, Transactions A: Basics***, Vol. 31, No. 1, (2018) 50-57. DOI: 10.5829/ije.2018.31.01a.08

Persian Abstract

چکیده

در این کار، فرآیند اکستروژن در کانال‌های هم مقطع زاویه‌دار برای میله آلومینیوم ۷۰۷۵ با پوشش مس بطور کامل بررسی شده است. ابتدا این فرآیند با استفاده از مدل اجزای محدود توسط نرم افزار آباکوس شبیه‌سازی شده و سپس صحت‌سنجی مدل در مقایسه با نتایج تجربی تایید شده است. به منظور بررسی تاثیر پارامترهای فرآیندی، طراحی آزمایش‌ها به وسیله روش رویه پاسخ صورت گرفت و تاثیر چهار پارامتر در نظر گرفته شده(زاویه کانال، زاویه گوشه، ضریب اصطکاک و ضخامت پوشش) بر روی حداکثر نیروی مورد نیاز و کرنش مورد مطالعه قرار گرفت. همچنین با استفاده از تحلیل واریانس، مدل رگرسیونی با قابلیت اطمینان بالا برای برآورد حداکثر نیرو و کرنش ارائه شده است. نتایج نشان داد که زاویه کانال تاثیرگذارترین پارامتر بر روی حداکثر نیروی مورد نیاز می‌باشد که به میزان ۹۳/۵٪ مشارکت دارد. آشکار گردید که ضخامت پوشش مسی تاثیر قابل ملاحظه‌ای بر روی نیروی شکل‌دهی نداشته است. همچنین مطابق نتایج بدست آمده مشخص شد که تمامی متغیرهای ارائه شده در مدل رگرسیون بر میزان کرنش تاثیر می‌گذارند. نتایج آنالیز واریانس نیز حاکی از این است که زاویه کانال و خم گوشه به ترتیب با ۸۰ و ۱۶ درصد مشارکت، موثرترین پارامترها بر روی کرنش می‌باشند و تقریبا تاثیر پارامترهای ضریب اصطکاک و ضخامت پوشش مسی قابل چشم‌پوشی هستند.

IJE TRANSACTIONS C: Aspects Vol. 33, No. 12, (December 2020) 2549-2555

International Journal of Engineering

Journal Homepage: www.ije.ir

A Non-destructive Ultrasonic Testing Approach for Measurement and Modelling of Tensile Strength in Rubbers

A. Foorginejad[a], M. Taheri*[b], N. Mollayi[c]

[a] *Department of Mechanical Engineering, Birjand University of Technology, Birjand, Iran*
[b] *Department of Mechanical Engineering, Tarbiat Modares University, Tehran, Iran*
[c] *Department of Computer Engineering, Birjand University of Technology, Birjand, Iran*

PAPER INFO

Paper history:
Received 25 April 2020
Received in revised form 27 June 2020
Accepted 03 September 2020

Keywords:
Longitudinal Ultrasonic Waves' Velocity
Relevance Vector Machine
Rubber
Tensile Strength

ABSTRACT

Currently, non-destructive testing is widely used to investigate various mechanical and structural properties of materials. In the present study, non-destructive ultrasonic testing was applied to study the relationship between the tensile strength value and the velocity of longitudinal ultrasonic waves. For this purpose, fourteen specimens of composites with different formulations were prepared. The tensile strength of the composites and the velocity of longitudinal ultrasonic waves inside them was measured. The relevance vector machine regression analysis, as a new methodology in supervised machine learning, was used to define a mathematical expression for the functional relationship between the tensile strength and the velocity of longitudinal ultrasonic waves. The accuracy of the mathematical expression was tested based on standard statistical indices, which proved the expression to be an efficient model. Based on these results, the developed model has the capability of being used for the online measurement of the tensile strength of rubber with the proposed formulation in the rubber industry.

***doi**: 10.5829/ije.2020.33.12c.16*

NOMENCLATURE

$K(.,.)$	Kernel function	**Greek Symbols**	
$N(.\|\mu,\sigma^2)$	Normal distribution with mean μ and variance σ^2	α	Vector of hyper-parameters
$p(.\|.)$	Conditional probability distribution function	μ	Mean Value
t	Vector of targets	σ^2	Variance of Gaussian distribution
W	Vector of weight coefficients		

1. INTRODUCTION

The microstructure of the material shows its macrostructure properties. It is typically believed that the macrostructural properties of a material, such as its physical and mechanical properties, cannot be determined by merely investigating its structural data. One of the conventional approaches to investigate the relationship between the microstructure of materials and some of their macrostructural properties is via the ultrasonic wave velocity through these materials [1]. The characteristics of a pulse traversing among the medium are changed and take information on the medium's microstructure and macrostructure. The application of the ultrasonic wave velocity measurement technique is not confined only to the measurement of physical and mechanical properties but is also used in non-destructive tests.

There are various experimental methods for evaluating the physical and mechanical properties of materials. The samples were taken from the considered sample port which caused destruction. Non-destructive testing is used as one of the analytical techniques to evaluate the properties of many materials without causing damage. The specimen remains usable for the detection of defects and the determination of material

*Corresponding Author Institutional Email: *morteza.taheri@modares.ac.ir* (M. Taheri)

Please cite this article as: A. Foorginejad, M. Taheri, N. Mollayi, A Non-destructive Ultrasonic Testing Approach for Measurement and Modelling of Tensile Strength in Rubbers, International Journal of Engineering, Transactions C: Aspects, Vol. 33, No. 12, (2020), 2549-2555.

properties. With the use of an ultrasonic test, it is possible to determine several properties of a material by measuring the time duration between the emission and reflection of ultrasonic waves [2]. The investigation of quality and the determination of the physical and mechanical properties of materials have been practiced by calculating the changes in the ultrasonic wave velocity for a wide variety of materials and applications. The investigations have ranged from the investigation of fruit quality [3] and the determination of limestone properties in historical monuments [4], to the evaluation of weld quality in friction stir welding of aluminum [5]. In this method, the ultrasonic waves and their reflection are displayed on the monitor, and the required data is obtained by interpretation of these signals, i.e., the initial and the reflected pulses, as shown in Figure 1.

As the ultrasonic test parameters are greatly affected by the material's microstructure and mechanical properties, this method has been proven as one of the best and most cost-effective non-destructive testing approaches for investigating mechanical material properties. Due to the recent advances in the electronic components used in the testing equipment, the precise measurement of the ultrasonic wave properties has provided the possibility of evaluating various mechanical properties at a reasonable and satisfactory level. Thanks to high test speeds, lack of part damage during the test, and the ability to perform the test on the parts while being manufactured, non-destructive tests provide a suitable substitute for traditional inspection methods.

Remarkable studies have been conducted on the determination of properties by ultrasonic waves for metals. Grain size, the presence of impurities, elasticity modulus, hardness, toughness, and yield strength in metals are among the items that have been measured by ultrasonic testing [6]. Also, the wave-mode-converted principle was used to calculate the shear wave and longitudinal wave velocities of magnesium-based composite samples; to evaluate the relationship among the reinforcement content and the dual-mode ultrasonic velocities. The elastic modulus is also calculated [7]. Based on the relationship between surface roughness and ultrasonic attenuation, an inverse model for the attenuation, using Weaver's diffuse scattering theory, is fixed to measure grain size in polycrystals [8]. However, only a few surveys have been performed on the application of ultrasonic testing for the determination of the properties of rubbers.

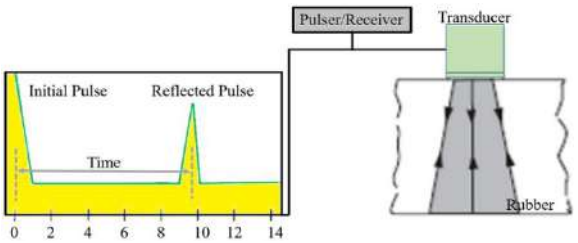

Figure 1. Schematic of Ultrasonic Test

One of the fundamental properties of rubber is its ultimate tensile strength, which is a measure of its ability to withstand a pulling force. The ultimate tensile strength, often shortened to tensile strength, is measured by the maximum stress that a material can withstand while being stretched or pulled before breaking. Although rubber does not reach its ultimate tensile strength, this property is regarded as an index of the quality of the produced rubber. However, online measurement of this property in the production cycle is not possible, and therefore non-destructive testing approaches provide an efficient alternative for this purpose.

In line with previous research by the authors on the use of ultrasonic waves in the rubber industry [9, 10], in this study, an ultrasonic test has been presented as a novel approach for the measurement of the tensile strength of rubber. The proposed method is capable of online measurement of the rubbers' tensile strength while being manufactured. To this end, the tensile strength values in several specimens with different formulations were measured together with the longitudinal ultrasonic wave velocity through them. In addition, the relationship between the tensile strength value and the longitudinal ultrasonic wave velocity was investigated using a novel supervised machine learning algorithm, namely the relevance vector machine (RVM).

Machine learning is a subfield of computer science, in which the study and construction of algorithms that are capable of learning from and making predictions based on a limited set of observed data are explored. Supervised learning is the machine learning task of inferring a function from a set of labeled training data. For this purpose, a model is generated from the dependency of the targets on the inputs based on a set of N observed input vectors $\{x_n\}_{n=1}^{N}$ and the corresponding targets $\{t_n\}_{n=1}^{N}$, in order to predict the targets for inputs that have not been observed [11].

Supervised learning algorithms can be used to establish a global model from the functional relationship between the outputs and the inputs based on a limited number of measurements [12].

Support vector machines (SVMs) are supervised learning models with associated learning algorithms used for the classification and regression analysis [13], which have proven to be efficient in many practical applications [14]. For SVM-based regression, the input space is mapped into a high dimensional feature space, based on a set of kernel functions and then an optimal linear regression is performed in this space, which can be expressed as follows:

$$f(x) = y(x_i, w) = \sum_{i=1}^{N} w_i K(x, x_i) + w_0 \quad (1)$$

where {wi} is the model weights, K (.,.)a kernel function, and N the number of training samples. The most common formulation of the kernel function is the radial basis function (Gaussian) defined in Equation (2) in which σ is the kernel function parameter. Substituting this kernel function in Equation (1) results in function f(x) estimated in the form of Equation (3).

$$K(x, x_i) = exp\left(-\frac{x-x_i^2}{\sigma^2}\right) \quad (2)$$

$$f(x) = y(x_i, w) = \sum_{i=1}^{N} w_i exp\left(-\frac{x-x_i^2}{\sigma^2}\right) + w_0 \quad (3)$$

Despite its widespread success, the SVM suffers from some disadvantages, which have been overcome in a newer probabilistic approach named the Relevance Vector Machine (RVM) as proposed by Tipping [15]. RVM is a nonlinear pattern recognition model with a simple structure based on the Bayesian Theory and Marginal Likelihood [15]. The main advantage of the RVM over SVM in our application is the fact that in addition to precision and sparseness, it utilizes a fewer number of kernel functions. Therefore, it is suitable for the development of a formula for an input-output relationship.

In this study, the relevance vector machine regression analysis was used to obtain a mathematical expression for the tensile strength based on the longitudinal ultrasonic wave velocity. The accuracy and generalization capability of the obtained expression are verified based on standard statistical indices, which prove it to a suitable model for the rubber tensile strength based on the ultrasonic wave velocity.

2. EMPIRICAL EXPERIMENTS

2. 1. Materials For the fabrication of composites, the following materials have been used: solution caoutchouc styrene-butadiene 1500, butadiene cis caoutchouc, soot, high dispersible silica (HDS), silane, sulphur, sulfonamide accelerator, zinc oxide, stearic acid, zinc stearate.

2. 2. Preparation of Composites In the present research, in order to investigate the relationship between the tensile strength of rubber and longitudinal ultrasonic wave velocity, 14 rubber specimens with different formulations (Table 1) were produced.

The composites were prepared in a 2-lit experimental Banbury made by Pomini under similar conditions. The R-E Mccin 305x152 double-roll grind made by Italian Bergamo for material mixing, the experimental 100 tones vulcanizing press made in Japan for the vulcanization of rubber composites, and the Rheometer made by English Alpha co. have been utilized for determination of vulcanization properties. The rotor's revolution in the stages of adding caoutchouc, chemical materials, and filler was a constant value of 20 rev/min. To ensure complete silanization, the rotor's revolution was a set variable during the final stages of mixing to maintain the mixing temperature for a long time within a range of 130–150 °C. The overall mixing duration for the composites was set to be six minutes.

2. 3. Tensile Strength Test To evaluate the tensile strength of the rubber specimens, 14 dumbbell-shaped samples were prepared, as shown in Figure 2,

TABLE 1. The weight of the materials used in final formulations of the sample rubbers used

No	Sulphor (gr)	CBS (gr)	High Dispersible Silica (gr)	Silane (gr)	Soot N330 (gr)	BR CIS (gr)	SBR1500 (gr)	Other Chemicals (gr)
1	5.7	4.95	0	0	386.86	0	773.71	39.43
2	5.7	4.95	0	0	386.86	232.11	541.6	39.43
3	5.56	4.82	377.13	30.17	0	0	754.26	38.44
4	5.56	4.82	377.13	30.17	0	226.28	527.98	38.44
5	6.39	5.54	260.69	26.07	0	260.69	608.27	44.28
6	4.87	4.22	461.29	46.13	0	197.7	461.29	33.58
7	6.53	5.66	0	0	266.48	266.48	621.78	45.26
8	5.06	4.39	0	0	479.74	205.6	479.74	34.92
9	6.29	5.36	377.13	30.17	0	226.28	527.98	38.44
10	7.22	6.16	260.69	26.07	0	260.69	608.27	44.28
11	5.51	4.7	461.29	46.13	0	197.7	461.29	33.58
12	7.02	5.36	377.13	30.17	0	226.28	527.98	38.44
13	8.06	6.15	260.69	26.07	0	260.69	608.27	44.28
14	6.15	4.69	461.29	46.13	0	197.7	461.29	33.58

based on the ASTM D624 standard [16] employed a dynamometer made by Hounsfield.

2. 4. Ultrasonic Test To investigate the relationship between the tensile strength of rubber and ultrasonic wave velocity, the longitudinal wave velocity for each specimen was measured. To this end, a Tru-Sonic ultrasonic test machine was employed. The specifications of the machine, specimens, and the probe are shown in Table 2. The ultrasonic waves, which are transmitted through the material, always lose a portion of their energy due to the dispersion at microscopic interfaces, as well as the effect of internal frictions in the material. The attenuation effect is actually the drop of the sonic wave energy during the emission of waves through the environment. In this empirical study, regarding the more intense attenuation effect in rubbers [17], a probe with a frequency of 4 MHz was utilized for the determination of the ultrasonic wave' velocity.

The longitudinal ultrasonic wave emission velocity for different specimens was measured by recording the elapsed time between the emission of waves and their reflex, which is displayed on the monitor by the standard electronic circuit. The ultrasonic wave measurement system is shown in Figure 3. The measurement precision of the ultrasonic wave velocity is 1 m/s. Because the calculated duration between the transmission and reception of the wave incorporates the time of the wave's traverse across the probe and coupler during each stage of the wave's travel, the time carries some errors. Consequently, it causes an error in the calculation of the wave emission velocity. First, the travel duration of the

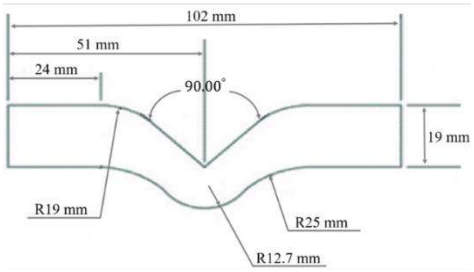

Figure 2. Tensile strength test sample based on the ASTM D624 standard [16]

TABLE 2. Specification of Instrument, Probe, and Samples

Specification	Value
Manufacturer	tru-sonic
Probe diameter (mm)	12
Probe frequency (MHz)	4
Sample diameter (mm)	41
Sample thickness (mm)	6

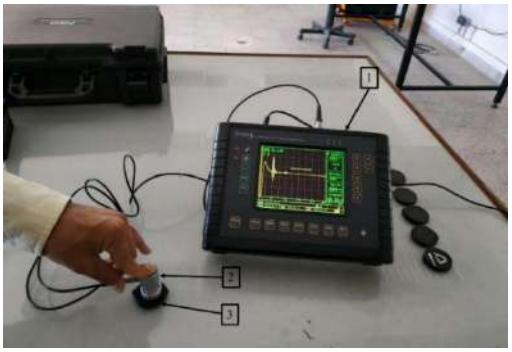

Figure 3. A System for Measuring Ultrasonic Waves Velocity: (1) Ultrasonic Instrument, (2) Probe, (3) Rubber Compound Sample

longitudinal ultrasonic wave across the probe and coupler was measured using the standard block. It was eliminated from the calculations for the approximation of the longitudinal wave emission velocity, and then the longitudinal wave velocity in specimens was calculated. The measurements were accomplished at a frequency of 4 MHz at the room temperature.

3. THEORY of RELEVANCE VECTOR MACHINE

In RVM-based regression, to predict a function based on a set of N input-target pairs$\{x_n, t_n\}_{n=1}^{N}$, each target is modeled as a function of the corresponding inputs with additive white Gaussian noise to accommodate measurement error on the target:

$$t_i = y(x_i, w) + \varepsilon_i \quad (4)$$

ε_i is assumed to be mean-zero Gaussian with variance σ^2 and similar to the SVM, $y(x, w)$, is considered as a linear combination of N kernel functions centered at the training samples inputs, in the form of Equation (3). Therefore, with the assumption that we know $y(x_n)$, each target is of normal independent distribution with the mean $y(x_n)$ and variance σ^2, expressed as [17]:

$$p(t_n|x) = N(t_n|y(x_n), \sigma^2) \quad (5)$$

Due to the assumption of independence of the targets, the likelihood function of whole samples can be obtained by the multiplication of the probability distributions as

$$p(t|w,\sigma^2) = \frac{e^{\left\{\frac{-t-\varphi w^2}{2\pi\sigma^2}\right\}}}{(2\pi\sigma^2)^{\frac{N}{2}}} \quad (6)$$

where

$$t = (t_1 \dots t_N)^T \quad (7)$$

$$w = (w_0 \dots w_N)^T \quad (8)$$

and $\boldsymbol{\varphi}$ is an N*(N+1) matrix, calculated as follows:

$$\varphi_{N*(N+1)} = \begin{bmatrix} 1 & k(x_1, x_1) & k(x_1, x_2) & \dots & k(x_1, x_N) \\ 1 & k(x_2, x_1) & k(x_2, x_2) & \dots & k(x_2, x_N) \\ \vdots & \vdots & \vdots & \ddots & \vdots \\ 1 & k(x_N, x_1) & k(x_N, x_2) & \dots & k(x_N, x_N) \end{bmatrix} \quad (9)$$

To avoid over-fitting, a 'prior' zero-mean Gaussian probability distribution is assumed for the weights as:

$$p(w|\alpha) = \prod_{i=0}^{N} N(w_i|0, \alpha_i^{-1}) \quad (10)$$

where $\boldsymbol{\alpha}$ is a vector of N+1 hyper-parameters [17]. The variance of this Gaussian probability distribution, α_i^{-1} controls how far from zero each weight can deviate.

The posterior over w can be obtained based on the Bayesian posterior inference as:

$$p(w|t, \alpha, \sigma^2) = \frac{p(t|w,\sigma^2)\ p(w|\alpha)}{p(t|\alpha,\sigma^2)} = (2\pi)^{-\frac{N}{2}}\ |\sum|^{-\frac{1}{2}}\ e^{\left\{-\frac{(w-\mu)^T \sum^{-1} (w-\mu)}{2}\right\}} \quad (11)$$

In this formulation, $\sum$ is the variance and is calculated as

$$\sum = (\sigma^{-2}\varphi^T\varphi + A)^{-1} \quad (12)$$

wherein A is a diagonal matrix formulated as

$$A = diag(\alpha_0, \alpha_1, \dots, \alpha_N) \quad (13)$$

The mean value μ can be obtained as

$$\mu = \sigma^{-2}\sum\varphi^T t \quad (14)$$

It can also be concluded based on this formulation that when $\alpha_i \to \infty$, $\mu_i \to 0$.

Integrating $p(\boldsymbol{w}|\boldsymbol{t}, \boldsymbol{\alpha}, \sigma^2)$ over the weights w, the marginal likelihood [13] for the hyper-parameters is calculated as

$$p(t|\alpha, \sigma^2) = \int p(t|w, \sigma^2)\ p(w|\alpha)\ dw \quad (15)$$

The above integral is a convolution of Gaussians, which can be calculated as

$$p(t|\alpha, \sigma^2) = (2\pi)^{-\frac{N}{2}}\ |\Omega|^{-\frac{1}{2}}\ e^{\left\{-\frac{t^T \Omega^{-1} t}{2}\right\}} \quad (16)$$

The matrix Ω in the marginal likelihood can be obtained as

$$\Omega = \sigma^2 I + \varphi\ A^{-1}\varphi^T \quad (17)$$

The optimal parameters $\boldsymbol{\alpha}$ and $\boldsymbol{\sigma^2}$ can be obtained by maximizing the marginal likelihood $p(\boldsymbol{t}|\boldsymbol{\alpha}, \sigma^2)$ over the training dataset. They are estimated in an iterative re-estimation procedure in the learning process of RVM. Following the approach of MacKay [18], the following iterative relationships were proposed for this purpose:

$$\alpha_i^{new} = \frac{1 - \alpha_i \sum_{ii}}{\mu_i^2} \quad (18)$$

$$\left(\sigma^2\right)^{new} = \frac{\boldsymbol{t} - \boldsymbol{\varphi\mu}^2}{N - \sum_{i=0}^{N}(1 - \alpha_i \Sigma_{ii})} \quad (19)$$

The iterative calculation of the parameters α_i and σ^2 from Equations (18) and (19) concurrent with updating of the following statistics $\sum$ and μ from Equations (12) and (14) is repeated until some suitable convergence criteria have been satisfied.

At the end of this procedure, the maximizing values $\boldsymbol{\alpha}_{MP}$ and σ_{MP}^2 are obtained, and the predictions for the new samples are made based on the posterior distribution over the weights conditioned on them. For a new sample x^*, a Gaussian predictive distribution is assumed for the output, expressed as [19]:

$$p(t^*|t) = N(t^*|y^*, \sigma_*^2) \quad (20)$$

where

$$y^* = \mu^T\ \varphi(x^*) \quad (21)$$

$$\sigma_*^2 = \sigma_{MP}^2 + \varphi(x^*)^T \sum \varphi(x^*) \quad (22)$$

$$\varphi(x^*) = [1, K(x^*, x_1), \dots, K(x^*, \boldsymbol{x}_N)]^T, \quad N = 1, \dots, N \quad (23)$$

The mean value of the distribution y^* is considered as the predicted output value and the variance, σ_*^2, provides an index of uncertainty in prediction.

In the iterative calculation of hyper-parameters α_i, many of them tend to infinity. This means that the probability distribution of the corresponding weights w_i is peaked at zero and they are estimated to be zero; thus, pruning many of the kernel functions used in Equation (1), which results in the sparseness of the model. The training set, which associates with the remaining nonzero weights, is called the relevance vector.

4. RESULTS AND DISCUSSION

In this survey, non-destructive tests using ultrasonic waves were used to examine the tensile strength of rubber composites, and a database of fourteen values of tensile strength and the corresponding longitudinal ultrasonic wave speed was obtained, as shown in Table 3. The RVM model was trained by eleven values of the measurements listed in Table 3, and it was tested by three of them, marked in bold. The Sparse Bayes package for Matlab [20] was used for the implementation of the model. Using the Gaussian kernel function formulated as Equation (25), with the parameter of $\sigma = 45$, the relevance vector contains only two of the training samples. Therefore, based on the calculated weights, the functional relationship between the tensile strength and the longitudinal wave speed can be defined as

$$\hat{y} = 1.483 * exp\left(-\frac{(x-1749.5)^2}{2025}\right) - 8.796 * exp\left(-\frac{(x-1483.2)^2}{2025}\right) + 16.153 \quad (24)$$

TABLE 3. The resilience and longitudinal ultrasonic waves' velocity of the samples used

No	Longitudinal ultrasonic waves' velocity (m/s)	Tensile Strength (MPa)
1	1717	17.04
2	1537.5	15.25
3	1749.5	18.46
4	**1494**	**7.53**
5	1469.6667	7.47
6	1536.75	14.9045
7	1501.16667	7.63
8	**1573.75**	**15.34**
9	1559.833	13.65
10	1500.8	10
11	1483.2	7.67
12	**1599**	**16.94**
13	1467	10.03
14	1467.125	6.06

The accuracy of the proposed expression was evaluated based on root-mean-square error (RMSE) and the coefficient of determination (R^2) of statistical indices, defined as follows:

$$RMSE = \sqrt{\frac{\sum_{i=1}^{N}\left(y_i - y_i\right)^2}{N}} \tag{25}$$

$$R^2 = 1 - \frac{\sum_{i=1}^{N}\left(y_i - y_i\right)^2}{\sum_{i=1}^{N}\left(y_i - \bar{y}\right)^2} \tag{26}$$

In these equations, y_i and $\hat{y}_i$ are the measured and the predicted outputs, respectively. N is the number of training samples, y_{max} and y_{min} are the maximum and minimum values of the measured outputs, and $\bar{y}$ is the mean value of the measured output, calculated as follows:

$$\bar{y} = \frac{\sum_{i=1}^{N} y_i}{N} \tag{27}$$

The calculated values of the indices are listed in Table 4. As it can be observed, the RVM method provides the possibility of defining an explicit mathematical expression along with reasonable accuracy and a generalization capability. The measured outputs, together with the outputs predicted by the RVM method, are depicted in Figure 4, showing a good agreement between them.

TABLE 4. Statistical indices for evaluation of the RVM model

Database	RMSE	R^2
Training	1.2957	0.9023
Testing	0.6259	0.9768

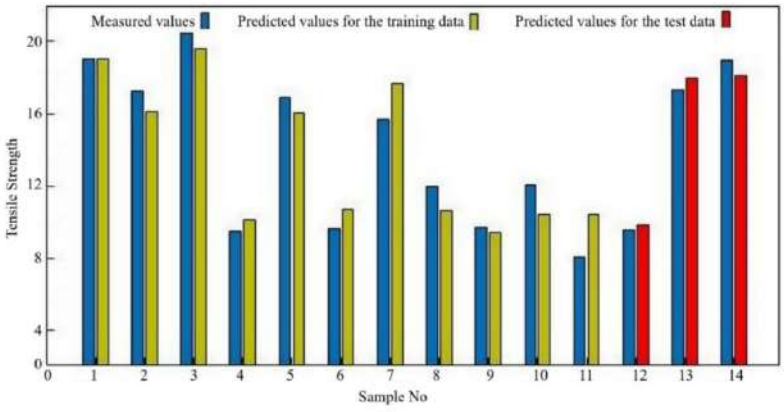

Figure 4. The measured outputs and the outputs predicted by RVM

5. CONCLUSION

In this paper, the application of ultrasonic testing for the measurement and modeling of the tensile strength of rubber has been proposed. For this purpose, the tensile strength of a set of rubber samples together with longitudinal ultrasonic wave velocity is measured. Based on these measurements, the relevance vector machine regression analysis is used to define an explicit mathematical expression to model the relationship between the tensile strength and the wave velocity, which is proven to provide reasonable accuracy and generalization capability. Based on these results, the developed model has the capability of being used for the online measurement of the tensile strength of rubber with the proposed formulation in the rubber industry.

6. REFERENCES

1. Stegemann, D., Raj, B., and Bhaduri, A. "NDT for Analysis of Microstructures and Mechanical Properties of Metallic Materials." In Reference Module in Materials Science and Materials Engineering, Elsevier, 2016. https://doi.org/10.1016/B978-0-12-803581-8.03429-9
2. Yilmaz, T., Ercikdi, B., Karaman, K., and Külekçi, G. "Assessment of strength properties of cemented paste backfill by ultrasonic pulse velocity test." ***Ultrasonics***, Vol. 54, No. 5, (2014), 1386–1394. https://doi.org/10.1016/j.ultras.2014.02.012
3. Morrison, D. S., and Abeyratne, U. R. "Ultrasonic technique for non-destructive quality evaluation of oranges." ***Journal of Food Engineering***, Vol. 141, (2014), 107–112. https://doi.org/10.1016/j.jfoodeng.2014.05.018
4. Vasanelli, E., Colangiuli, D., Calia, A., Sileo, M., and Aiello, M. A. "Ultrasonic pulse velocity for the evaluation of physical and mechanical properties of a highly porous building limestone." ***Ultrasonics***, Vol. 60, (2015), 33–40. https://doi.org/10.1016/j.ultras.2015.02.010
5. Hynes, N. R. J., Nagaraj, P., and Sujana, J. A. J. "Ultrasonic evaluation of friction stud welded AA 6063/AISI 1030 steel joints." ***Materials and Design***, Vol. 62, (2014), 118–123. https://doi.org/10.1016/j.matdes.2014.05.017
6. Agrawal, M., Prasad, A., Bellare, J. R., and Seshia, A. A. "Characterization of mechanical properties of materials using ultrasound broadband spectroscopy." ***Ultrasonics***, Vol. 64, (2016), 186–195. https://doi.org/10.1016/j.ultras.2015.09.001
7. Liu, Y., Song, Y., Li, X., Chen, C., and Zhou, K. "Evaluating the reinforcement content and elastic properties of Mg-based composites using dual-mode ultrasonic velocities." ***Ultrasonics***, Vol. 81, (2017), 167–173. https://doi.org/10.1016/j.ultras.2017.07.001
8. Li, X., Han, X., Arguelles, A. P., Song, Y., and Hu, H. "Evaluating grain size in polycrystals with rough surfaces by corrected ultrasonic attenuation." ***Ultrasonics***, Vol. 78, (2017), 23–29. https://doi.org/10.1016/j.ultras.2017.02.018
9. Foorginejad, A., Taheri, M., and Mollayi, N. "Measurement and Modelling of the Rubber Resilience based on Ultrasonic Non-destructive Testing in Tires." ***AUT Journal of Modeling and Simulation***, Vol. 50, No. 2, (2018), 165–170. https://doi.org/10.22060/miscj.2018.14543.5109
10. Foorginejad, A., Taheri, M., Mollayi, N., and Shiva, M. "Tire Hardness Modeling Based on Longitudinal Ultrasonic Velocity Using the Gaussian Process Regression." ***Amirkabir Journal of Mechanical Engineering***, Vol. 51, No. 5, (2019), 317–318. https://doi.org/10.22060/mej.2018.13494.5649
11. Provost, F. "Glossary of Terms." ***Journal of Machine Learning***, Vol. 30, No. 2–3, (1998), 271–274. Retrieved from http://robotics.stanford.edu/~ronnyk/glossary.html
12. Bishop, C. M. Pattern Recognition and Machine Learning. Springer, 2006. Retrieved from https://cds.cern.ch/record/998831
13. Cortes, C., and Vapnik, V. "Support-vector networks." ***Machine Learning***, Vol. 20, No. 3, (1995), 273–297. https://doi.org/10.1007/bf00994018
14. Meyer, D., Leisch, F., and Hornik, K. "The support vector machine under test." ***Neurocomputing***, Vol. 55, No. 1–2, (2003), 169–186. https://doi.org/10.1016/S0925-2312(03)00431-4
15. Tipping, M. E. "The relevance vector machine." In NIPS'99: Proceedings of the 12th International Conference on Neural Information Processing Systems, (1999), 652–658. Retrieved from https://dl.acm.org/doi/abs/10.5555/3009657.3009750
16. ASTM 624-00: Standard test method for tear strength of conventional vulcanized rubber and thermoplastic elastomers. (2007).
17. Tipping, M. E. "Sparse Bayesian Learning and the Relevance Vector Machine." ***Journal of Machine Learning Research***, Vol. 1, No. Jun, (2001), 211–244. Retrieved from https://www.jmlr.org/papers/v1/tipping01a.html
18. Mackay, D. J. C. "Introduction to Gaussian processes." ***NATO ASI Series F Computer and Systems Sciences***, Vol. 168, (1998), 133–166. Retrieved from http://www.cs.toronto.edu/~radford/.
19. Tipping, M. E. "Bayesian inference: An introduction to principles and practice in machine learning." ***Lecture Notes in Computer Science (including subseries Lecture Notes in Artificial Intelligence and Lecture Notes in Bioinformatics)***, Vol. 3176, (2004), 41–62. https://doi.org/10.1007/978-3-540-28650-9_3
20. Tipping, M. E. "SPARSEBAYES V1.1: A Baseline Matlab Implementation of 'Sparse Bayesian' Model Estimation", (pp. 1–5). Retrieved from https://usermanual.wiki/Pdf/sb1manual.1468011241/view

Persian Abstract

چکیده

امروزه، استفاده از بازرسی غیرمخرب برای بررسی ویژگی‌های مختلف مکانیکی و ساختاری مواد گسترش فراوانی یافته است. در پژوهش حاضر، از آزمون غیرمخرب فراصوتی برای بررسی رابطه بین مقدار استحکام کششی و سرعت امواج فراصوتی طولی استفاده شده است. برای این منظور چهارده نمونه کامپوزیت با فرمول‌های مختلف تهیه شده و استحکام کششی کامپوزیت‌ها با سرعت امواج فراصوتی طولی در داخل آن‌ها اندازه‌گیری شده است. تحلیل رگرسیون ماشین بردار رابط، به عنوان یک روش جدید در یادگیری ماشین تحت نظارت، برای پیدا کردن رابطه ریاضی بین مقاومت کششی و سرعت امواج فراصوتی طولی مورد استفاده قرار گرفته است. ارزیابی دقت بیان ریاضی براساس شاخص‌های آماری استاندارد ثابت کرد که مدل پیشنهادی یک مدل کارآمد است. براساس نتایج به دست آمده، مدل ارائه شده قابلیت استفاده در اندازه‌گیری برخط استحکام کششی لاستیک را در صنعت لاستیک دارد.

International Journal of Engineering

Journal Homepage: www.ije.ir

Numerical Simulation of Frost Formation in Interrupted Micro Channel Heat Sinks Considering Microfluidic Effects in Slip Regime

H. Safikhani*, H. Shaabani

Department of Mechanical Engineering, Faculty of Engineering, Arak University, Arak, Iran

P A P E R I N F O

Paper history:
Received 18 August 2020
Received in revised form 06 September 2020
Accepted 09 September 2020

Keywords:
Micro Channels Heat sinks
Microchannel
Frost Formation
Computational Fluid Dynamics
Slip Regime
Microfluidic

A B S T R A C T

Frost formation is a renowned phenomenon in HVAC, aeronautical and refrigeration industries. In this paper, numerical modeling and parametric study of the frost formation in the interrupted Micro Channels Heat sinks (MCHS) is investigated considering microfluidic effects in slip flow regime. For numerical modeling, basic equations of humid air and frost including continuum, momentum, energy and phase change mechanism are numerically solved and results are compared with reported data. Knudsen number (Kn) is changed so that slip flow regime requirement is accomplished. This requirement is also considered for setting boundary conditions. The effect of different parameters like cold surface temperature, time and Kn are studied on the frost formation and details of the flow field. Results revealed that with an increase in time and a decrease in Kn and cold surface temperature, weight and thickness of the frost increase. Moreover, with thicker frost maximum flow velocity rises in the microchannel. The details of frost formation and flow field, revealed by the numerical results can remarkably assist designing interrupted microchannel.

***doi**: 10.5829/ije.2020.33.12c.17*

1. INTRODUCTION

Frost formation is a renowned phenomenon in HVAC, aeronautical and refrigeration industries. Frost mounting on the heat exchanger surfaces, causing higher thermal resistance and also it blocks the air path. Both phenomena decrease energy efficiency of the system. Frost naturally is a porous media with packs of the air trapped in the ice matrix. Therefore, it possesses a marked thermal resistance. The presence of frost in the heat exchanger's channels causes pressure drop with narrowing down the path of the air. In the process of the frost formation, humid flows pass coolant surface and mass transfer of steam present in the wet flow to the ice crystals when the air is saturated. This causes thicker frost and higher freezing density. Many researchers already have studied frost formation by numerical and experimental approaches. Hayashi et al. [1] was one of the pioneers who studied the growth of frost in three different time periods. The first period includes the primary initiation of the ice crystals which is quite short in comparison of the total time period. In this period frost does not grow markedly thick. Moreover, for this phase, it is not a porous media as it can be assumed as ice idols where convection heat and mass transfer are main growth mechanisms and diffusion to the frost sounds trivial. For the second period known as frost growth phase, frost is a porous media where molecular diffusion of the water vapor is dominant. Mass flow of the water vapor contributed in both increasing the density of the frost as well as growing it. Finally, in the complete growth period of the frost, the temperature of the freezing surface reaches to water triple-point temperature. Therefore, a cyclic process starts where compressed water vapor diffuses through the frost and gradually freezes due to internal temperature gradient. Aoki et al. [2] thoroughly investigated this phase. Modeling frost formation can be classified in analytical models and computational fluid dynamics (CFD) based models. Analytical models generally assume the growth of the frost in only one

*Corresponding Author Institutional Email: *h-safikhani@araku.ac.ir* (H. Safikhani)

Please cite this article as: H. Safikhani, H. Shaabani, Numerical Simulation of Frost Formation in Interrupted Micro Channel Heat Sinks Considering Microfluidic Effects in Slip Regime, International Journal of Engineering, Transactions C: Aspects Vol. 33, No. 12, (2020), 2556-2562.

direction. Tao et al. [3, 4] proposed a model for mass transfer in frost layer. Lee et al. [5, 6] presented a uni-dimensional model for simulating growth in frost density and thickness and also they developed a model for analyzing frost layer and air flow. Using averaging local volume method Le Gall et al. [7] introduced the relative equilibrium to anticipate frost growth. Na and Webb [8-10] suggested a model based on density of supersaturated water vapor in the frost layer. Yang et al. [11] found an effective model to prognosticate the performance of the fin-tube heat exchanger. Recently, Hermes et al. [12] developed a mathematical model which could accurately predict the frost thickness with a 10% discrepancy with experimental results. Kandula [13, 14] proposed novel equations for frost over the straight surface and investigated the effect of different ambient parameters on frost characteristics.

Micro-channel heat exchangers are very efficient compact exchangers. Their benefit in comparison with fin-tube exchangers includes lower volume and weight and higher efficiency. They also possess lower internal space which decreases refrigeration load of the exchanger and potentially decreases the contribution in global warming with lower possible leakage of the refrigerant [15]. Lately, micro-channel exchangers are prevalent in HVAC systems. These exchangers are increasingly applied in chillers especially thermal pumps where they should work in wet and freezing condition. Shao et al. [16] studied a model with distributed micro-channel exchangers used in commercial thermal pumps to analyze the frost over the fin-tube evaporators. Moallem et al. [17, 18] investigated the effect of surface temperature, surface coating and water blockage on the freezing performance of the micro-channel heat exchangers. Surface temperature was more important than surface coating and water blockage over frost growth speed and freezing time. Some other studies focused on the frost-defrost cycle of the heat exchangers which is very vital in designing thermal pump systems. Xia et al. [19] studied five different louvered-fin micro-channel heat exchangers and found that condensed droplets dramatically influence the pressure drop and heat transfer in recurring freezing cycles. Zhang and Hrnjak [20] studied the freezing performance of the micro-channel heat exchangers with parallel-flow parallel-fin (PF2) horizontal flat tubes. In comparison with conventional serpentine fins, the freezing performance was improved which is attributed to the superior permeability of the PF2 exchangers. Tso et al. [21] developed a distribution model taking into account the non-uniform distribution of the wall and air temperature in the coil to anticipate dynamic behavior of the finned-tube heat exchanger for both frost and non-frost conditions. Wu et al. [22] studied the frost properties of a micro-channel exchanger with louvered-fin and derived the equation for the thickness of the frost. In recent years, Zhu et al. [23, 24] concentrated on increasing thermal transfer through the concept of reconstruction of developed thermal layers. This study included some parallel longitudinal micro-channels with some transverse channels. The transverse channels were used to divide the length of the flow into some independent streams. They found that computed hydraulic and thermal boundary layers were readily improved due to the shorter total length of the divided streams within the micro-channel. In addition, it was that the pressure drop and also heat transfer improved in divided micro-channels in comparison with conventional micro-channels. In another similar study Cheng [25] analyzed the flow and heat transfer of a double accumulated micro-channel using some micro-processor. The effect of height of the fin's wall to the height of the micro-channel was examined. They found their superior performance compared to the conventional micro-channels. The evaluation of the 3D micro-channels divided with the transverse micro-pores was followed by Chai et al. [26] using experimental and numerical methods. They found the pressure drop and heat transfer for different conditions and geometries of rectangular walls in transverse micro-pores. Wang and Li [27] numerically simulated flow field in micro-channels with triangular walls in transverse micro-pores. Their parametric studies eventuated in an optimized micro-channel with promising performance. Hajmohammadi et al. [28] investigated the slip regime in microchannel heat sinks with one phase flow. They finally compared the results with the related results without slip regime. To the best of author's knowledge, there has been no study focusing on the numerical modeling of the frost in micro channels considering the micro-fluidic effects in slip regime. Therefore, such an issue is the aim of this paper.

2. MATHEMATICAL MODELING

The details of numerical modeling is described in this section.

2. 1. Geometry The geometry investigated in this paper has been schematically illustrated in Figure 1. As is shown in this figure, a number of parallel domains

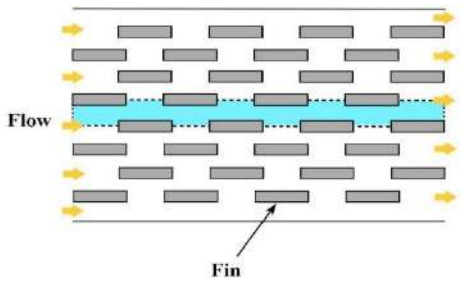

Figure 1. The schematic of geometry

have been placed next to each other and formed a MCHS. Since, in this MCHS, the flow field in each computational domain is the same, the governing equations have been numerically solved for one domain and finally, the amount of heat transfer from total MCHS have been multiplied by the number of domains to get the total values. The total pressure drop and heat transfer for the set of MCHS are computed as follows:

$$Q_{tot} = nQ_1 \quad (1)$$

$$\Delta P_{tot} = \Delta P_1 \quad (2)$$

$$n = \frac{W}{2(c+2a)} \quad (3)$$

In this paper, the basic dimensions of the MCHS (W and L) are constant and equal to 5 mm, while channel width (D) is 160 μm. In this way, the examined channels are classified as microchannels ($10\,\mu m < D \leq 200\,\mu m$). Other geometrical and non-geometrical parameters are shown in Table 1 and Figure 2.

2. 2. Governing Equations In the present CFD modeling it is assumed that humid air is treated as an incompressible Newtonian fluid in laminar flow and density (ρ_a), mass diffusivity coefficient (D_a) and specific heat capacity (c_{pa}) of air are constant. Natural convection is negligible in both humid air and frost. Moreover, the humid air within the frost layer is considered saturated [13, 29]. The continuity, 2D momentum, energy and mass transport equations are as follows:

$$\frac{\partial \rho_a}{\partial t} + \frac{\partial (\rho_a u)}{\partial x} + \frac{\partial (\rho_a v)}{\partial y} = 0 \quad (4)$$

TABLE 1. Geometrical and non-geometrical parameters

Parameter	Value
Half of fin thickness (a)	20 μm
Fin length (b)	225 μm
Half of channel width (c)	80 μm
Chip length (L)	5 mm
Chip width (W)	5 mm
Inlet velocity	0.1 $^m/_S$
Kn	0, 0.05, 0.1
Time	5, 10, 15 Min
Cold wall temperature	-15, -10, -5 ℃

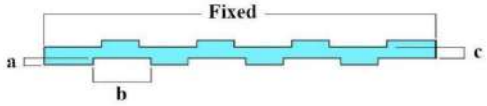

Figure 2. Geometrical parameters

$$\frac{\partial (\rho_a u)}{\partial t} + \frac{\partial (\rho_a u.u)}{\partial x} + \frac{\partial (\rho_a v.u)}{\partial y} = -\frac{\partial P}{\partial x} + \frac{\partial}{\partial x}\left(\mu \frac{\partial u}{\partial x}\right) + \frac{\partial}{\partial y}\left(\mu \frac{\partial u}{\partial y}\right) \quad (5)$$

$$\frac{\partial (\rho_a v)}{\partial t} + \frac{\partial (\rho_a u.v)}{\partial x} + \frac{\partial (\rho_a v.v)}{\partial y} = -\frac{\partial P}{\partial y} + \frac{\partial}{\partial x}\left(\mu \frac{\partial v}{\partial x}\right) + \frac{\partial}{\partial y}\left(\mu \frac{\partial v}{\partial y}\right) \quad (6)$$

$$\frac{\partial (\rho_a T)}{\partial t} + \frac{\partial (\rho_a u.T)}{\partial x} + \frac{\partial (\rho_a v.T)}{\partial y} = \frac{\partial}{\partial x}\left(\frac{\lambda_a}{C_{p,a}} \frac{\partial T}{\partial x}\right) + \frac{\partial}{\partial y}\left(\frac{\lambda_a}{C_{p,a}} \frac{\partial T}{\partial y}\right) \quad (7)$$

$$\frac{\partial (\rho_a w)}{\partial t} + \frac{\partial (\rho_a u.w)}{\partial x} + \frac{\partial (\rho_a v.w)}{\partial y} = \frac{\partial}{\partial x}\left(\rho_a D_a \frac{\partial w}{\partial x}\right) + \frac{\partial}{\partial y}\left(\rho_a D_a \frac{\partial w}{\partial y}\right) \quad (8)$$

Using an energy balance for a differential frost volume in the interior of the frost layer, energy equation can be expressed as:

$$\frac{\partial (\rho_f T)}{\partial_t} = \frac{\partial}{\partial x}\left(\frac{\lambda_f}{c_{p,f}} \frac{\partial T}{\partial x}\right) + \frac{\partial}{\partial y}\left(\frac{\lambda_f}{c_{p,f}} \frac{\partial T}{\partial y}\right) + \frac{q_{sub}}{c_{pf}} \frac{\partial \rho_f}{\partial t} \quad (9)$$

For the densification rate of frost layer, the equation proposed by Na and Webb [9] has been used:

$$\frac{\partial \rho_f}{\partial t} = \frac{\partial}{\partial x}\left(\rho_a D_{ef} \frac{\partial w}{\partial x}\right) + \frac{\partial}{\partial y}\left(\rho_a D_{ef} \frac{\partial w}{\partial y}\right) \quad (10)$$

The viscosity and thermal conductivity are considered to be temperature dependent. The thermal conductivity of frost is commonly expressed as a function of frost density. In this study, it is used a correlation reported by Lee et al. [6]:

$$\lambda_f \left[{}^{W}/_{(m.K)^{-1}}\right] = A_1 + A_2 \rho_f + A_3 \rho_f^2 \left[\rho \text{ in } {}^{kg}/_{m^3}\right] \quad (11)$$

where $A_1 = 0.132$ $A_2 = 3.13 \times 10^{-4}$ and $A_3 = 1.6 \times 10^{-7}$. The specific heat is defined as a function of frost density and porosity, as follows:

$$c_{p,f} = \frac{(c_{p,f}\rho_g(1-\varepsilon) + c_{p,a}\rho_a \varepsilon)}{\rho_f}. \quad (12)$$

The diffusive mass coefficient in the frost layer is determined as Na and Webb [8]:

$$D_{ef} = D_a \varepsilon \frac{1+\varepsilon}{2}. \quad (13)$$

2. 3. Boundary and Initial Conditions For numerical simulation, the equations of previous sections should be solved subject to the related boundary and initial conditions. The schematic subjected boundary conditions are shown in Figure 3. The fluid entered to the channel with known velocity and temperature (inlet) and exited with the known pressure (outlet). The fins are walls with known temperature lower than freezing temperature. The slip 1st order boundary conditions (0.001<Kn<0.1) are investigated for walls. This study

models the frost layer growth period while the effects of crystal growth period are treated as initial conditions. Initial frost layer temperature is assumed to be constant and equal to the plate temperature, since the initial thickness is sufficiently thin.

2. 4. Numerical Methods Numerical simulation is performed using finite volume method. A second order upwind method is used for the convective and diffusive terms and the SIMPLE algorithm is employed to solve the coupling between the velocity and pressure fields. To make sure that the results are independent of the size and the number of generated grids, several grids with different sizes along different directions has been tested for each MCHS; and it has been attempted to consider for each one the best grid, with the highest accuracy and the lowest computation cost. A sample of generated grid is shown in Figure 4.

2. 5. Validation To validate the numerical model, its finding is compared with reliable results reported in related references. Since, there is neither experimental nor numerical study available on the frost formation in micro channels considering microfluidic effect in slip regime each frost formation and microfluidic effect should be evaluated separately. Figure 5 compares the results of frost formation in a conventional macro channel with that of Wu et al. [22]. As can be seen from Figure 5, present modeling is able to accurately simulate the frost formation. Similarly, Figure 6 shows the effect of slip effects in a micro-channel developed in this study with that of Hajmohammadi et al. [28] with one phase which reveals great correlation. Therefore, it can be said that presented model is accurate and reliable for simulation of frost formation in micro-channels considering microfluidic effects.

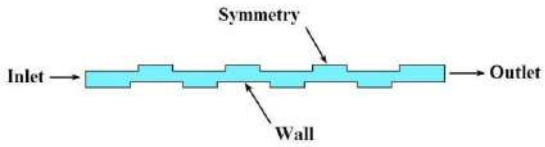

Figure 3. The schematic subjected boundary conditions

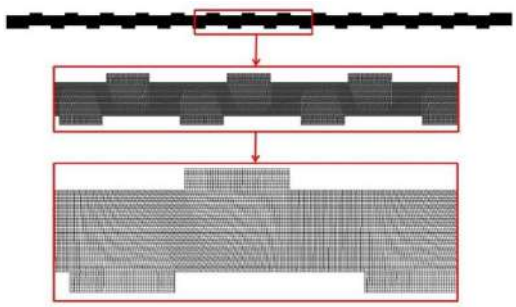

Figure 4. Sample of grid generation

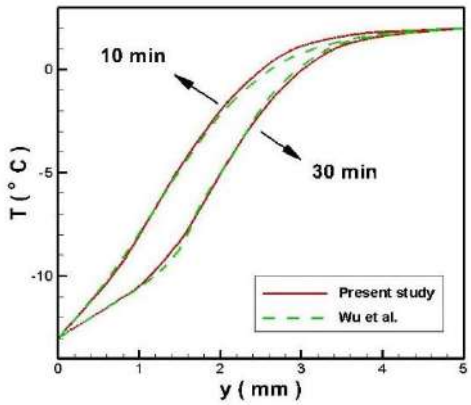

Figure 5. Validation of the model predictions of the frost formation

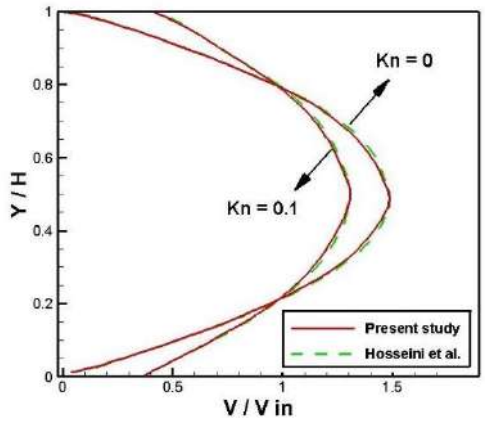

Figure 6. The effect of slip conditions in a micro-channel

3. RESULTS AND DISCUSSION

The effect of different parameters like time, cold wall temperature and Kn number on the growth of the frost and flow field are discussed in this section.

Frost formation is studied in three different time periods of 5, 10 and 15 minutes. Figure 7 illustrates the volume fraction contour of humid air with the time passing by. As can be observed from Figure 7, with increasing time from 5 to 15 minutes the growth of the frost speeded up and minimum volume fraction of humid air decreases from 0.7 to 0.3 which shows the frost growth with time increasing. Figure 8 depicts the velocity contour of the humid air with time corresponding to the higher frost growth. It can be inferred that until 15 minutes of time there is no discernable change in air velocity and it is probable that with a longer time period the air path becomes blind.

Similarly, frost formation is studied in three different cold wall temperatures of -15, -10 and -5 ^{o}C. Figure 9 illustrates the volume fraction contour of humid air with the cold wall temperature changing. As can be observed

from Figure 9, with decreasing cold wall temperature from -5 to -15 ºC, the growth of the frost speeds up and minimum volume fraction of humid air decreases from 0.9 to 0.2 which shows the frost growth with decreasing of cold wall temperature. Figure 10 depicts the velocity contour of the humid air with cold wall temperature. It can be inferred that as the cold wall temperature decreases, maximum humid air velocity increases due to growth in frost formation and narrowing of the air passage.

Three different Kn numbers 0, 0.05 and 0.1 is examined to analyze frost formation. Figure 11 shows the humid air volume fraction contour with different Kn numbers which reveals that with higher Kn number, lower growth of the frost occurs. Figure 12 shows the

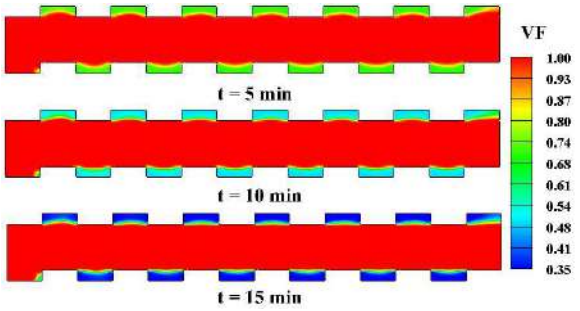

Figure 7. The volume fraction contour of humid air with the time passing

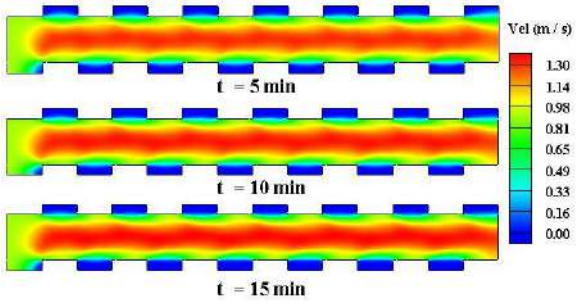

Figure 8. The velocity contour of humid air with the time passing

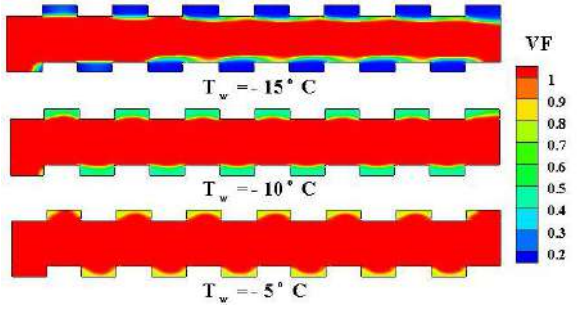

Figure 9. The volume fraction contour of humid air with the cold wall temperature changing

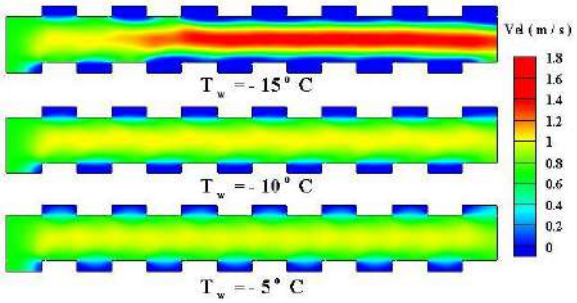

Figure 10. The velocity contour of humid air with the cold wall temperature changing

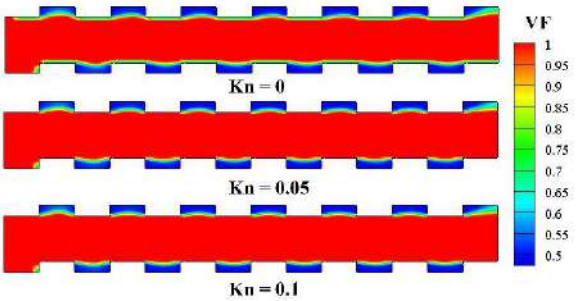

Figure 11. The humid air volume fraction contour with different Kn number

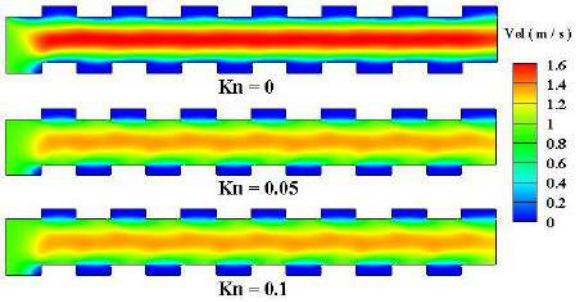

Figure 12. The humid air velocitycontour with different Kn number

humid air velocity contour with increasing Kn number corresponding to the frost reduction. As can be observed with Kn number equal to 0, which corresponds to non-slipping condition, air flow velocity is maximized.

4. CONCLUSION

In this paper, numerical modeling and parametric study of the frost formation in the interrupted MCHS was investigated considering microfluidic effects in slip flow regime. For numerical modeling, basic equations of humid air and frost including: continuum, momentum, energy and phase change mechanism were numerically solved. Kn number was changed so that slip flow regime

requirement was accomplished. This requirement was also considered for setting boundary conditions. The effect of different parameters like cold surface temperature, time and Kn were studied on the frost formation and details of the flow field. Results revealed that with an increase in time and a decrease in Kn and cold surface temperature, weight and thickness of the frost increase. The details of frost formation and flow field, revealed by the numerical results can remarkably assist designing interrupted microchannels.

5. REFRENCES

1. Hayashi, Y., Aoki, A., Adachi, S. and Hori, K., "Study of frost properties correlating with frost formation types", ***Journal of Heat Transfer***, Vol. 99, (1977), 239-245. doi:10.1115/1.3450675.
2. Aoki, K., Katayama, K. And Hayashi, Y., "A study on frost formation: The process of frost formation involving the phenomena of water permeation and freezing", ***Bulletin of JSME***, Vol. 26, No. 211, (1983), 87-93. https://doi.org/10.1299/jsme1958.26.87.
3. Tao, Y.-X., Besant, R. and Rezkallah, K., "Modeling of frost formation in a fibrous insulation slab and on an adjacent cold plate", ***International Communications in Heat and Mass Transfer***, Vol. 18, No. 5, (1991), 609-618. https://doi.org/10.1016/0735-1933(91)90074-E.
4. Tao, Y.-X., Besant, R. and Rezkallah, K., "A mathematical model for predicting the densification and growth of frost on a flat plate", ***International Journal of Heat and Mass Transfer***, Vol. 36, No. 2, (1993), 353-363. https://doi.org/10.1016/0017-9310(93)80011-I.
5. Lee, K.-S., Kim, W.-S. and Lee, T.-H., "A one-dimensional model for frost formation on a cold flat surface", ***International Journal of Heat and Mass Transfer***, Vol. 40, No. 18, (1997), 4359-4365. https://doi.org/10.1016/S0017-9310(97)00074-4.
6. Lee, K.-S., Jhee, S. and Yang, D.-K., "Prediction of the frost formation on a cold flat surface", ***International Journal of Heat and Mass Transfer***, Vol. 46, No. 20, (2003), 3789-3796. https://doi.org/10.1016/S0017-9310(03)00195-9.
7. Le Gall, R., Grillot, J. and Jallut, C., "Modelling of frost growth and densification", ***International Journal of Heat and Mass Transfer***, Vol. 40, No. 13, (1997), 3177-3187 . https://doi.org/10.1016/S0017-9310(96)00359-6.
8. Na, B. and Webb, R.L., "Mass transfer on and within a frost layer", ***International Journal of Heat and Mass Transfer***, Vol. 47, No. 5, (2004), 899-911. https://doi.org/10.1016/j.ijheatmasstransfer.2003.08.023.
9. Na, B. and Webb, R.L., "New model for frost growth rate", ***International Journal of Heat and Mass Transfer***, Vol. 47, No. 5, (2004), 925-936. https://doi.org/10.1016/j.ijheatmasstransfer.2003.09.001.
10. Na, B. and Webb, R.L., "A fundamental understanding of factors affecting frost nucleation", ***International Journal of Heat and Mass Transfer***, Vol. 46, No. 20, (2003), 3797-3808. https://doi.org/10.1016/S0017-9310(03)00194-7.
11. Yang, D.-K., Lee, K.-S. and Song, S., "Modeling for predicting frosting behavior of a fin–tube heat exchanger", ***International Journal of Heat and Mass Transfer***, Vol. 49, No. 7-8, (2006), 1472-1479. https://doi.org/10.1016/j.ijheatmasstransfer.2005.09.022.
12. Hermes, C.J., Piucco, R.O., Barbosa Jr, J.R. and Melo, C., "A study of frost growth and densification on flat surfaces", ***Experimental Thermal and Fluid Science***, Vol. 33, No. 2, (2009), 371-379. https://doi.org/10.1016/j.expthermflusci.2008.10.006.
13. Kandula, M., "Frost growth and densification in laminar flow over flat surfaces", ***International Journal of Heat and Mass Transfer***, Vol. 54, No. 15-16, (2011), 3719-3731.https://doi.org/10.1016/j.ijheatmasstransfer.2011.02.056.
14. Kandula, M., "Correlation of water frost porosity in laminar flow over flat surfaces", ***Special Topics & Reviews in Porous Media: An International Journal***, Vol. 3, No. 1, (2012), 79-87. DOI: 10.1615/SpecialTopicsRevPorousMedia.v3.i1.70
15. Garimella, S., "Innovations in energy efficient and environmentally friendly space-conditioning systems", ***Energy***, Vol. 28, No. 15, (2003), 1593-1614. https://doi.org/10.1016/S0360-5442(03)00120-8.
16. Shao, L.-L., Yang, L. and Zhang, C.-L., "Comparison of heat pump performance using fin-and-tube and microchannel heat exchangers under frost conditions", ***Applied Energy***, Vol. 87, No. 4, (2010), 1187-1197. https://doi.org/10.1016/j.apenergy.2009.08.021.
17. Moallem, E., Padhmanabhan, S., Cremaschi, L. and Fisher, D.E., "Experimental investigation of the surface temperature and water retention effects on the frosting performance of a compact microchannel heat exchanger for heat pump systems", ***International Journal of Refrigeration***, Vol. 35, No. 1, (2012), 171-186. https://doi.org/10.1016/j.ijrefrig.2011.08.010.
18. Moallem, E., Cremaschi, L., Fisher, D.E. and Padhmanabhan, S., "Experimental measurements of the surface coating and water retention effects on frosting performance of microchannel heat exchangers for heat pump systems", ***Experimental Thermal and Fluid Science***, Vol. 39, No., (2012), 176-188. https://doi.org/10.1016/j.expthermflusci.2012.01.022.
19. Xia, Y., Zhong, Y., Hrnjak, P.S. and Jacobi, A.M., "Frost, defrost, and refrost and its impact on the air-side thermal-hydraulic performance of louvered-fin, flat-tube heat exchangers", ***International Journal of Refrigeration***, Vol. 29, No. 7, (2006), 1066-1079. https://doi.org/10.1016/j.ijrefrig.2006.03.005.
20. Zhang, P. and Hrnjak, P.S., "Air-side performance of a parallel-flow parallel-fin (pf2) heat exchanger in sequential frosting", ***International Journal of Refrigeration***, Vol. 33, No. 6, (2010), 1118-1128. https://doi.org/10.1016/j.ijrefrig.2010.04.011.
21. Tso, C., Cheng, Y. and Lai, A., "An improved model for predicting performance of finned tube heat exchanger under frosting condition, with frost thickness variation along fin", ***Applied Thermal Engineering***, Vol. 26, No. 1, (2006), 111-120. https://doi.org/10.1016/j.applthermaleng.2005.04.009.
22. Wu, J., Ouyang, G., Hou, P. and Xiao, H., "Experimental investigation of frost formation on a parallel flow evaporator", ***Applied Energy***, Vol. 88, No. 5, (2011), 1549-1556. https://doi.org/10.1016/j.apenergy.2010.11.006.
23. Xu, J., Gan, Y., Zhang, D. and Li, X., "Microscale heat transfer enhancement using thermal boundary layer redeveloping concept", ***International Journal of Heat and Mass Transfer***, Vol. 48, No. 9, (2005), 1662-1674. https://doi.org/10.1016/j.ijheatmasstransfer.2004.12.008.
24. Xu, J., Song, Y., Zhang, W., Zhang, H. and Gan, Y., "Numerical simulations of interrupted and conventional microchannel heat sinks", ***International Journal of Heat and Mass Transfer***, Vol. 51, No. 25-26, (2008), 5906-5917. https://doi.org/10.1016/j.ijheatmasstransfer.2008.05.003.
25. Cheng, Y., "Numerical simulation of stacked microchannel heat sink with mixing-enhanced passive structure", ***International Communications in Heat and Mass Transfer***, Vol. 34, No. 3,

(2007), 295-303. https://doi.org/10.1016/j.icheatmasstransfer.2006.12.007.

26. Chai, L., Xia, G., Zhou, M., Li, J. and Qi, J., "Optimum thermal design of interrupted microchannel heat sink with rectangular ribs in the transverse microchambers", ***Applied Thermal Engineering***, Vol. 51, No. 1-2, (2013), 880-889. https://doi.org/10.1016/j.applthermaleng.2012.10.037.
27. Wong, K.-C. and Lee, J.-H., "Investigation of thermal performance of microchannel heat sink with triangular ribs in the transverse microchambers", ***International Communications in Heat and Mass Transfer***, Vol. 65, No., (2015), 103-110. https://doi.org/10.1016/j.icheatmasstransfer.2015.04.011.
28. Hajmohammadi, M., Alipour, P. and Parsa, H., "Microfluidic effects on the heat transfer enhancement and optimal design of microchannels heat sinks", ***International Journal of Heat and Mass Transfer***, Vol. 126, No., (2018), 808-815. https://doi.org/10.1016/j.ijheatmasstransfer.2018.06.037.
29. Topçuoğlu, K., "Trombe wall application with heat storage tank", ***Civil Engineering Journal***, Vol. 5, No. 7, (2019), 1477-1489. DOI: 10.28991/cej-2019-03091346.

Persian Abstract

چکیده

در این مقاله مدل‌سازی عددی تشکیل برفک در میکروکانال‌های با زائده‌های مستطیلی انجام شده است. میکروکانال در نادسن‌های ۰، ۰.۰۰۵ و ۰.۱ که دارای محدوده‌ی ضریب لغزشی هستند مدل‌سازی شده است. با ترکیب مدل برفک و روش جریان چند فازی اولرین، تشکیل برفک محلی و مشخصات جریان بخار آب شبیه‌سازی می‌شوند. این مقاله با مقایسه‌ی VF و همچنین تغییر دمای محلی با داده‌های تجربی صحه‌گذاری شده است. این مدل برفک، پخش چگالی برفک، پخش دما و پخش سرعت بخارآب را پیش‌بینی می‌کند. نتایج نشان می‌دهد که با گذر زمان وزن و ضخامت برفک افزایش می‌یابد. مشخصات متفاوت انتقال حرارت در منطقه‌ی لایه‌ی برفک و منطقه‌ی بخارآب توسط پخش دمایی شبیه‌سازی شده نشان داده می‌شوند. پخش سرعت شبیه‌سازی شده نشان می‌دهد که سرعت هوا در منطقه‌ی لایه‌ی برفک نزدیک به صفر است و در منطقه‌ی بخارآب هر چقدر برفک رشد می‌کند سرعت هوا افزایش می‌یابد. دمای محلی شبیه‌سازی شده، ضخامت برفک محلی، پروفایل برفک، ضخامت برفک میانگین و وزن برفک با نتایج آزمایشگاهی تطابق دارند.

International Journal of Engineering

Journal Homepage: www.ije.ir

Studying the Effective Parameters on Teeth Height in Internal Gear Flowforming Process

M. Khodadadi, K. Khalili*, A. Ashrafi

Department of Mechanical Engineering, University of Birjand, Birjand, Iran

PAPER INFO

Paper history:
Received 17 July 2020
Received in revised form 30 August 2020
Accepted 03 September 2020

Keywords:
Design of Experiments
Finite Element Analysis
Flowforming
Internal Gear
Optimization

ABSTRACT

The flowforming process is a chipless metal forming process that is used to produce precise thin walled tubes. Manufacturing of internal gears using flowforming process is a difficult-to-achieve, but very interesting process in which the gear may be produced without the need for high forming forces and r high tooling cost. In this study, manufacturing of internal gears using flowforming process is studied. The process has been numerically analyzed and simulated. The plastic behavior of the material, and friction conditions were determined using tensile and friction tests, respectively. Several controlled test were performed to evaluate the validity of simulation results. A comparison of simulation and experimental results indicates very good agreement. Once the simulation is verified, the effects of roller diameter, thickness reduction percentage, feed rate and attack angle on tooth height were obtained using design of experiments (DOE) procedure. According to DOE results, attack angle (α), thickness reduction percentage (T), interaction between roller diameter and attack angle (D×α), and interaction between roller diameter and feed rate (D×f) are the most significant parameters affecting the tooth height. The tooth height increases with increasing the roller diameter and thickness reduction, but decreases with increasing the feed rate and attack angle.

***doi**: 10.5829/ije.2020.33.12c.18*

NOMENCLATURE

D	Roller diameter (mm)	f	Feed rate (mm/rev)
T	Thickness reduction (%)	α	Attack angle (degree)

1. INTRODUCTION

Flowforming, also known as tube spinning, is a novel metal forming method that is used to produce thin-walled high precision tubular products. A tubular workpiece (preform) is held onto a mandrel, and the material can be displaced axially by one or more rollers moving axially along the mandrel. The advantages of flowforming are flexibility, simple tooling, low production cost and low forming loads, which makes it suitable for automotive production [1]. Forming a tube along with internal teeth (such as internal gears) is another application of this process. Internal gears are widely used in defense and aerospace industries as external sun gears of planetary mechanisms due to their compact structure, large torque-to-weight ratio, high gear ratio, reduced noise and vibration, etc. [2]. Gears are generally manufactured via metal cutting processes, which require more time and can lead to material waste. Moreover, gears are subjected to various stress conditions and should be strong enough to withstand these conditions. A gear that is manufactured through metal cutting procedure has poor strength [3]. To overcome this drawback, flowforming can be used for manufacturing of internal gears.

Because of the importance of flowforming in manufacturing the tubular parts including internal teeth, a number of studies have been carried out using theoretical analyses and experimental methods. Groche and Fritsche [4] investigated gear manufacturing using flowforming. They studied the influence of the number of rollers on the force applied to the mandrel teeth. To achieve a uniform distribution of the force on the mandrel teeth, they suggested using a ring instead of a roller. Jiang et al. [5] studied manufacturing of thin-walled tubes

*Corresponding Author Institutional Email: *kkhalili@birjand.ac.ir* (K. Khalili)

Please cite this article as: M. Khodadadi, K. Khalili, A. Ashrafi, Studying the Effective Parameters on Teeth Height in Internal Gear Flowforming Process, International Journal of Engineering, Transactions C: Aspects, Vol. 33, No. 12, (2020), 2563-2571.

including internal teeth using ball spinning process. They calculated the influence of thickness reduction on teeth height using the finite element method, and compared the results with experiments. Jiang et al. [6] studied the influences of roller diameter, feed rate and the initial thickness of the tube on the height of teeth using neural networks. Jiang et al. [7] simulated manufacturing of thin-walled tubes with internal teeth using finite element method (FEM). They investigated the influence of the roller diameter on teeth height and surface roughness. Jiang et al. [8] investigated the influence of the number of passes during thickness reduction on teeth height, surface roughness and microstructure of the tube. Haghshenas et al. [9–11] investigated the influences of microstructure, hardness, thickness reduction and strain hardening rate on the plastic strain in metals with FCC structure. Xia et al. [12] analyzed Trapezoidal internal gear production defects, experimentally and numerically. They examined the effect of thickness reduction and direction of rotation of the mandrel on the shape of the gear. Xu et al. [13] studied both experimentally and numerically the multi-stage internal gear production using a plate. They investigated the effect of process parameters on the tooth height and filling rate of the mandrel cavity. The process was applied to ASTM 1035 mild steel using three rollers in two stages. Although the process has received attention from the research community, the application of flowforming to manufacture of internal gears has been a new attempt so far. Achieving the desired teeth is one of the most critical tasks in flowforming of internal gears and the deformation mechanism of teeth in this process is more complex compared with the counterparts with no inner ribs. Moreover, the influence of parameters has not been studied so far.

In the present study, the emphasis is on investigating the influence of process parameters on tooth height in backward flowforming of internal gears using the results of experiment and FEM. In this study, the flowforming process is simulated using FEM, and then the results are validated by experimental tests. This FEM model is used in DOE and determination of parameters affecting teeth height. Finally, the optimum value is predicted. Research methodology is shown in Figure 1.

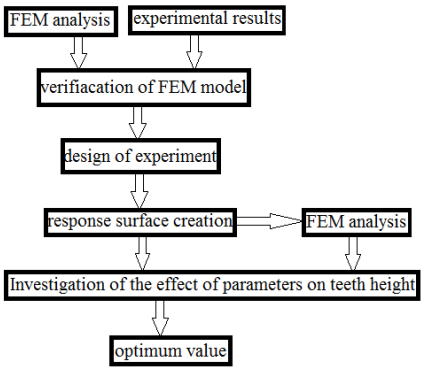

Figure 1. Research methodology in this study

Figure 2. Setup of tensile test equipment

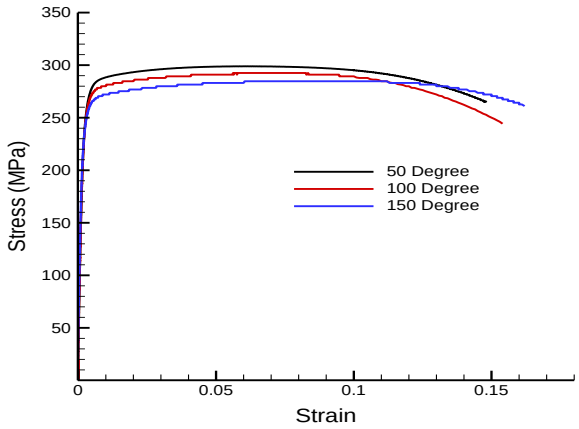

Figure 3. Stress-strain curves of copper workpiece at different temperatures in degrees Celsius

2. Material and method

2. 1. Tensile Test To determine the plastic behavior of the material, tensile testing was carried out using the Zwick/Roell tensile test machine with a maximum load of 600 kN and a servo motor control. The setup is shown in Figure 2. Test samples were prepared according to the ASTM. The tests were carried out with a rate of 20 mm/min at temperatures of 25, 100 and 150ºC. The obtained stress-strain diagrams are presented in Figure 3.

2. 2. Friction Test To determine the friction coefficient, the ring pressure test was carried out at temperatures of 25, 60, 100, and 150ºC. The test samples were rings with a standard geometric ratio of 2:3:6 (thickness, internal diameter and external diameter of 8, 12 and 24 mm, respectively). A Zwick/Roell pressure test machine with a maximum load of 600 kN was used to carry out the tests (Figure 4).

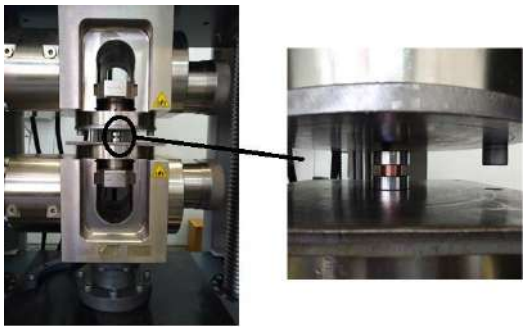

Figure 4. Setup of ring pressure test

2. 3. Flowforming Process In this study, a backward flowforming was performed using a universal lathe. The preform was a C12200 copper alloy tube with an internal diameter of 13.2 mm and a wall thickness of 2.5 mm (Figure 5). A ball-bearing (deep groove ball-bearing SKF 6203/VA201 with a diameter of 40 mm and a width of 12 mm) was used as the roller. A gear with 20 teeth and an outer diameter of 13.2 mm, which was heat-treated to get the surface hardness of 58 RC, was used as the mandrel (Figure 6). The experimental setup is shown in Figure 7. The gear was complete in four passes of forming. The minimum thickness reduction should be determined so that the plastic metal flow not to be limited to the external surface, which is usually 15% [14]. The primary preform was removed from the mandrel when 25% thickness reduction was achieved. This was repeated in the second step, i.e., another 25% thickness reduction was carried out in the second step. In the third step, the thickness reduction was 20%, and in the fourth step 15%. To evaluate the quality of the gear teeth, it was necessary to section the specimens; this was done using a wire-cutting machine. A video measuring machine (VMM) was used to measure the profile and teeth height of gear in the sectioned specimens. Then, the gear microstructure was investigated.

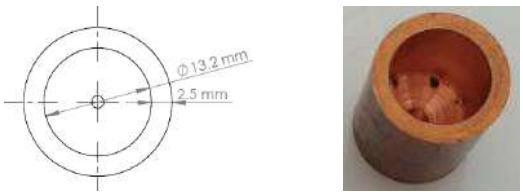

Figure 5. Dimensions of preform

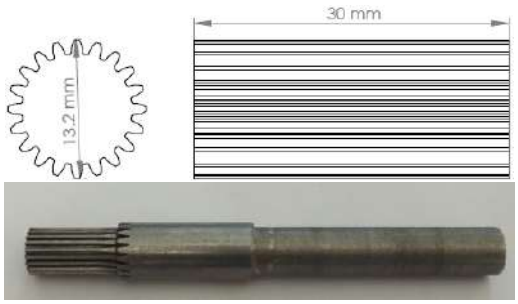

Figure 6. Mandrel used to form internal gear

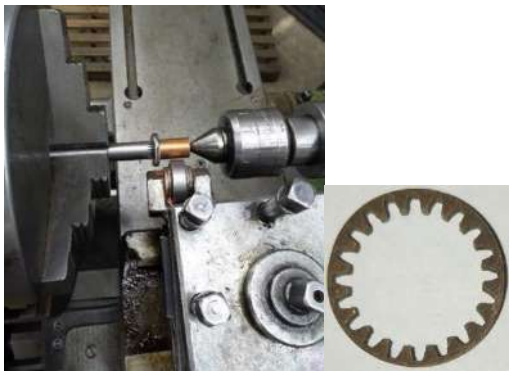

Figure 7. Setup of the experiment and the produced final gear

3. MODELING OF FLOWFORMING PROCESS

The model is shown in Figure 8. In this study, the workpiece material was C12200 copper alloy that is considered an elastic-plastic material (the stress-strain curve is shown in Figure 3). The mechanical properties of C12200 are shown in Table 1. The geometrical dimensions of pre-form, rollers and mandrel are described in Section 2.3. To investigate the effects of friction and temperature on the process a thermo-mechanical analysis was carried out, and 41470 C3D8RT type elements with the ALE formulation were used for

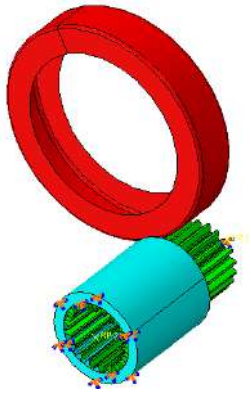

Figure 8. Schematic of backward flowforming in FEM model

TABLE 1. Mechanical properties of copper workpiece

Material	σy(MPa)	σu(MPa)	E(GPa)	υ	ρ(kg/m3)
C12200	227	295	115	0.3	8930

meshing [15, 16]. For simplicity, the mandrel and roller were considered to be rigid. The Coulomb friction model was used to define the contact surfaces, and the friction coefficient was determined according to the friction test (as it is described in Section 2.2). Due to high deformation and complicated contact conditions in the flowforming process, the dynamic explicit solving procedure used because of the numerical robustness and computational efficiency in the case of highly non-linear and large-scale applications [1]. In this analysis, the mass scaling factor was used to reduce the solution time. The process was simulated using FEM software along with some codings. Finally, to validate the simulation model, the tooth height was compared in two experimental and simulation in four steps, which is shown in Table 2.

4. RESULTS

4. 1. Experimental and Simulation Results In this section, the results of simulation and experiments are discussed. The manufacturing of the gear was carried out in four steps and the gear teeth were formed gradually. Figures 9 and 10 present the form and height of a gear tooth in four steps, which was obtained from the simulation and experimental results.

4. 2. Microstructure of Gear Analysis of the microstructure of the gear produced by flowforming helps to understand the deformation mechanism. In this research, samples from the preform and gear (in four passes) were prepared. Microstructures of the samples were obtained using a light microscope, and the results are shown in Figures 11 and 12. As can be seen in Figure 11, the microstructure of the preform consists of equiaxed grains. However, as shown in Figure 12, severe deformation and misaligned orientation of the grains in the gear are quite evident; hence, an inhomogeneous plastic deformation can be inferred. As shown in Figure 12, the grains are oriented in the tangential and radial directions so that the mandrel grooves are snugly filled. In each pass, the amounts of elongation and deformation of the grains are increased until the fourth pass in which the maximum elongation of the grains is achieved.

TABLE 2. Comparison between Tooth heights in four steps

	Step 1	Step 2	Step 3	Step 4
Simulation	0.44	0.84	1.19	1.35
Experimental	0.5	0.89	1.21	1.35
Error	12%	5%	2%	0

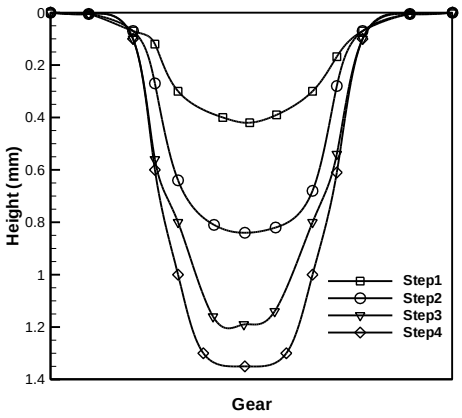

Figure 9. Tooth height at different steps of simulation

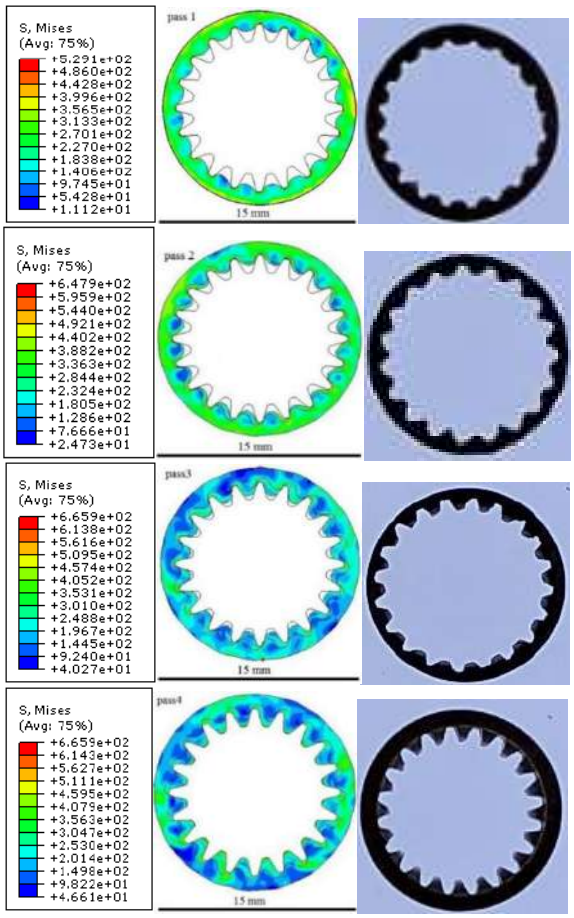

Figure 10. Tooth formation in four steps

Figure 11. Microstructure of preform

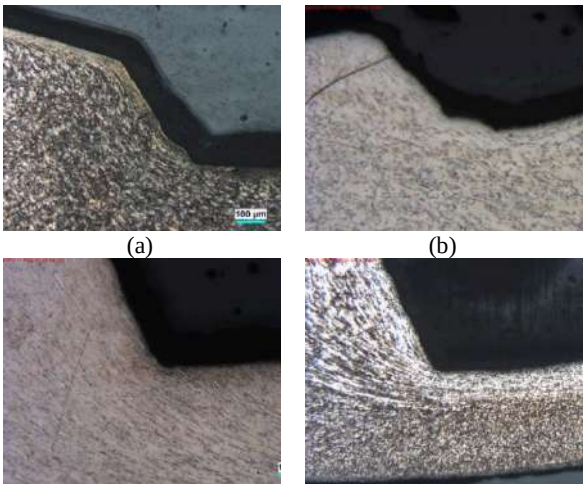

Figure 12. Microstructure of gear, a) Pass 1, b) Pass 2, c) Pass 3, and d) Pass 4

4. 3. Effective Parameters and Statistical Optimization Achieving a specific geometry is important in manufacturing industrial components; thus, the investigation of the influence of each parameter on tooth height is necessary. However, there is no concrete objective function to be used by statistical methods for optimizing the process parameters. Response surface method (RSM) was used to investigate the effect of each parameter on tooth height. Response surface method is a statistical method that is used to model and analyze processes that are affected by several parameters. The goal of this method is to model and optimize the response [17]. In this study, a central composite design (CCD) was applied. In this process, four parameters including roller diameter, thickness reduction percentage, feed rate and attack angle (as shown in Figure 13) are more important than others [1]. The levels of these parameters are given in Table 3. According to the applied method, 31 experiments were considered with α=2.

After doing the tests, the teeth height was obtained for each test, and the ANOVA results were obtained (Table 4). Figure 14 presents the residual distribution of the present study, and the normality of the distribution can be

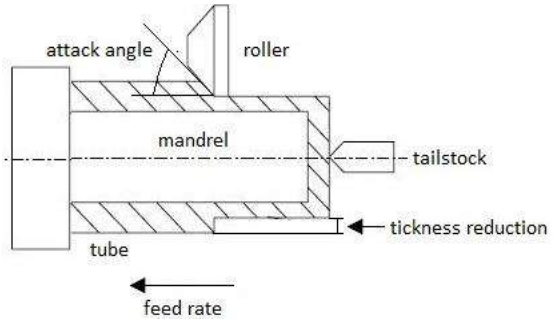

Figure 13. Effective parameters in flowforming process

TABLE 3. Effective parameters and their levels

Parameter	Roller diameter (d)	Thickness reduction (t%)	Feed rate (f)	Attack angle (α)
Low level	20 mm	15%	0.05 mm/rev	20°
High level	60 mm	35%	0.25 mm/rev	60°

TABLE 4. ANOVA table for teeth height

Source	DF	Adj SS	Adj MS	F-Value	P-Value
Model	14	0.34517	0.02465	24023.3	0.000
Linear	4	0.27014	0.06753	65804.2	0.000
D	1	0.00003	0.00003	31.62	0.000
T	1	0.05008	0.05008	48794.7	0.000
f	1	0.00265	0.00265	2577.73	0.000
α	1	0.22187	0.22187	216185.5	0.000
Square	4	0.02220	0.00555	5408.29	0.000
D*D	1	0.00040	0.00040	391.79	0.000
T*T	1	0.00818	0.00818	7967.74	0.000
f*f	1	0.00000	0.00000	8.52	0.011
α*α	1	0.01111	0.01111	10821.1	0.000
2-Way Interaction	6	0.04441	0.00741	7211.73	0.000
D*T	1	0.00859	0.00859	8367.28	0.000
D*f	1	0.01111	0.01111	10827.4	0.000
D*α	1	0.01256	0.01256	12238.9	0.000
T*f	1	0.00069	0.00069	668.81	0.000
T*α	1	0.00553	0.00553	5385.69	0.000
f*α	1	0.00039	0.00039	386.19	0.000
Error	15	0.00001	0.00000		
Lack-of-Fit	9	0.00001	0.00000	1.81	0.242
Pure Error	6	0.00000	0.00001		
Total	29	0.34518			

confirmed. A significance level of 95% was selected; that is the results are correct with a confidence level of 95%. Therefore, a parameter is significant if the P-value is less than 0.05.

According to Table 4, all parameters and interactions are significant and affect the teeth height. Pareto chart is shown in Figure 15, which expresses the magnitude of the effect of each parameter on tooth height. According to Figure 15, attack angle (α), thickness reduction (T), interaction between roller diameter and attack angle

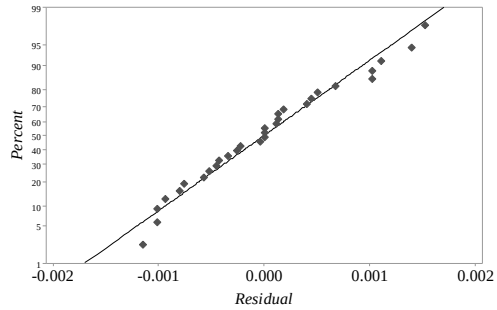

Figure 14. Normal probability of residuals for tooth height

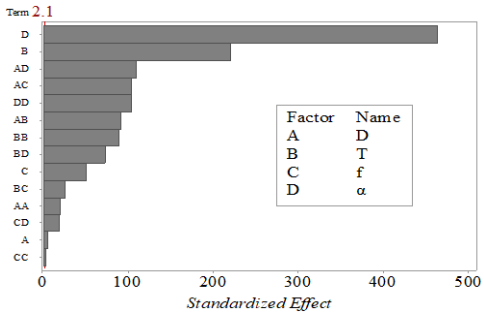

Figure 15. Pareto chart for teeth height

(D×α), and interaction between roller diameter and feed rate (D×f) are, respectively, the most significant parameters affecting the tooth height. In this analysis, R-Sq = 99.99 and R-Sq (adj) = 99.98 that confirm ultra-high accuracy of the model developed using RSM. To investigate the influences of the parameters effective on the teeth height, the main effects and interactions should be investigated precisely. In this section, the influence of each parameter will be discussed. In the analysis of interactions, other parameters were considered in a balanced mode (central point) of tests.

4. 3. 1. Influence of Roller Diameter The influence of the roller diameter on tooth height is shown in Figure 16, which indicates that the tooth height increases with increasing the roller diameter up to 40 mm and decreases with further increase. Additionally, according to the D×T interaction, which is shown in Figure 17, the height increases with increasing the roller diameter at low thickness reductions, but at values above 25%, the height decreases. As the roller diameter increases, the plastic deformation zone increases, and this leads to an increase in material flow beneath the roller and tooth height. However, as the roller diameter increases (more than 40 mm in Figure 16 and at thickness reductions above 25% in Figure 17), the S/L ratio (circumferential contact length (S) to axial contact length (L)) increases, and due to friction, the material flow increases in axial direction. However, to increase the gear height, the axial flow must be reduced. According to the D×f interaction in Figure 18, the increase in feed rate decreases the tooth height because at high feed rates, the material does not remain beneath the roller and tends to escape from underneath it and flow in the opposite direction of the roller axial movement. However, this effect is reversed by increasing the roller diameter. As the roller diameter increases, the contact area becomes larger and the engagement of roller and the workpiece increases, so the material escape from the roller less frequently. Consequently, increasing the diameter of the roller results in a better flow of material in the radial direction and an increased tooth height. According to Figure 19, which shows the D×α interaction, the tooth height increases with increasing the roller diameter.

4. 3. 2. Influence of Thickness Reduction Percentage According to the main effect of thickness reduction percentage (Figure 20) as well as the interactions of T×F (Figure 21), T×α (Figure 22) and D×T (Figure 17), the tooth height increases with increasing the thickness reduction percentage. As the thickness reduction percentage increases, the plastic deformation zone increases, and this causes an increase in material flow and tooth height. In addition, at high thickness reduction, the S/L ratio decreases and the axial flow is restricted. According to the F- value in the Table 4, the interaction of T×f has little effect on the tooth height which is shown in Figure 21.

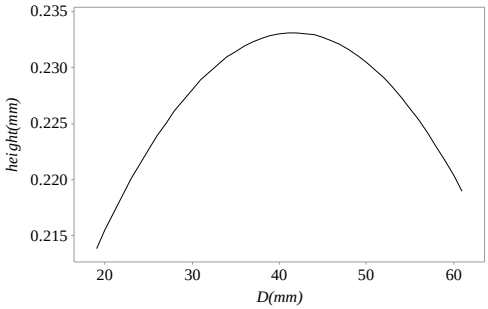

Figure 16. Effect of roller diameter on tooth height

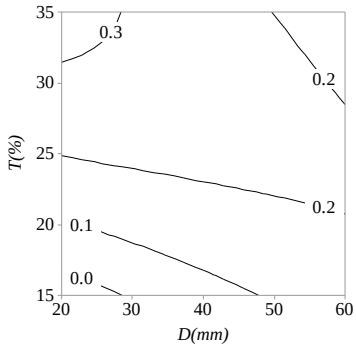

Figure 17. Interaction effects of roller diameter and thickness reduction on tooth height

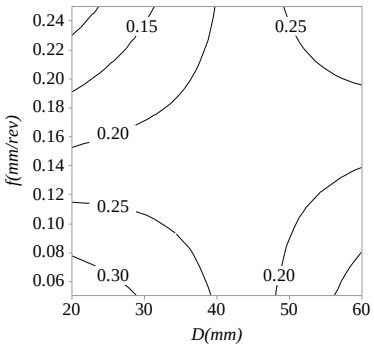

Figure 18. Interaction effects of roller diameter and feed rate on tooth height

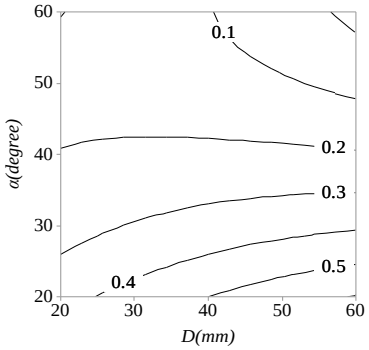

Figure 19. Interaction effects of roller diameter and attack angle on tooth height

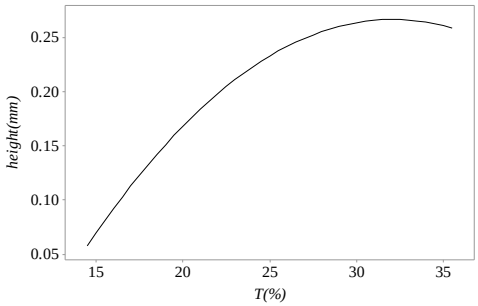

Figure 20. Effect of thickness reduction on tooth height

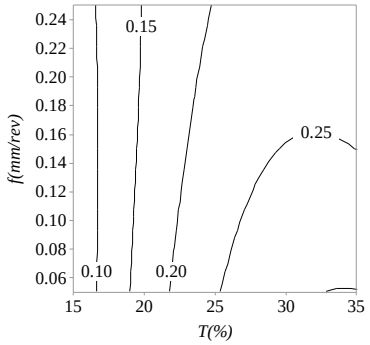

Figure 21. Interaction effect of thickness reduction on tooth height

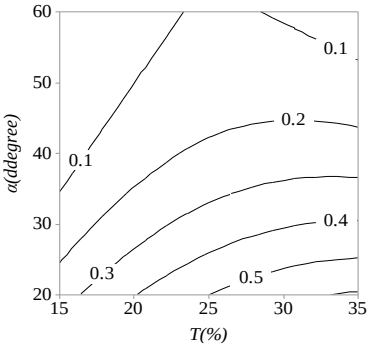

Figure 22. Interaction effects of thickness reduction and attack angle on tooth height

4. 3. 3. Influence of Feed Rate According to Figure 23, increasing the feed rate, reduces the tooth height, as described in Subsection 4.3.1. Increasing feed rate increases the S/L ratio, and due to the friction, the material flow increases in the axial direction and the tooth height decreases. The interaction of D×f and T×f was explained in Subsection 4.3.1 and 4.3.2 respectively. The interaction of f×α Almost no effect on the tooth height as shown in Figure 24.

4. 3. 4. Influence of Attack Angle The influence of attack angle is shown in Figure 25, which indicates that the tooth height decreases with increasing the attack

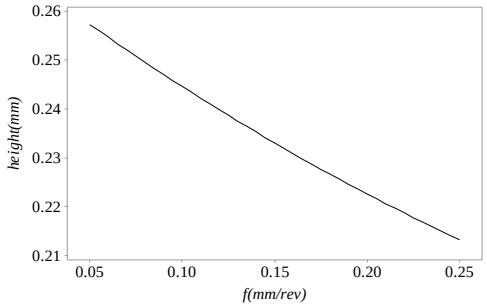

Figure 23. Effect of feed rate on tooth height

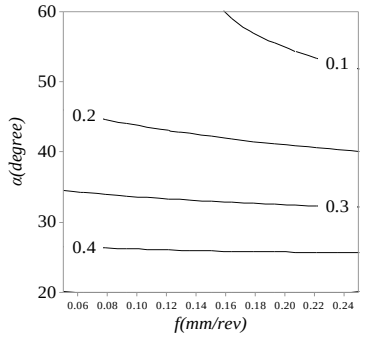

Figure 24. Interaction effects of feed rate and attack angle on tooth height

angle. This effect can also be seen in Figure 19 (interaction of D×α), Figure 22 (interaction of T×α) and Figure 24 (interaction of f×α). If the attack angle is zero, the flow of materials is in the radial direction and increases the gear height. As the attack angle increases, the axial flow of the material also increases, and the gear height decreases.

4. 3. 5. Response Optimization In the previous sections, the parameters affecting tooth height were found. In this section, we can find the situation for optimizing the response by using response optimization. In fact, in this method, from the selected levels, the best settings are set to achieve the desired goal, which is to achieve maximum teeth height. As shown in Figure 26, a maximum tooth height of 0.7272 is obtained for D=20 mm, T=35%, f=0.05 mm/rev and α=20°.

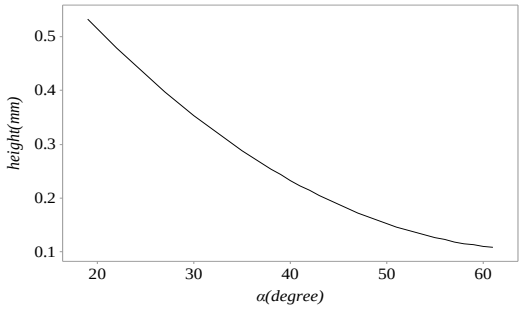

Figure 25. Effect of attack angle on tooth height

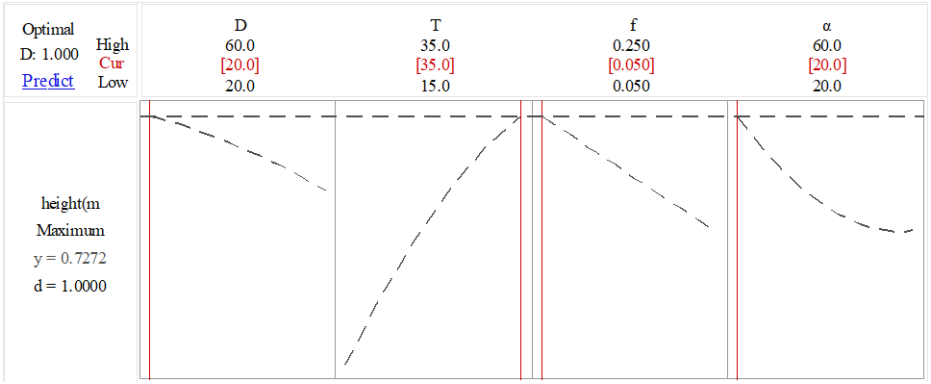

Figure 26. Response optimization plot for tooth height

5. CONCLUSION

The flowforming process is a relatively new method for producing internal gears that is suitable for batch production. In the present study, flowforming process was used to produce an internal gear on a lathe. Then, the process was modelled and the model was verified by comparing the simulation and experimental results. Achieving the desired teeth is one of the most critical tasks in flowforming of internal gears and formability of the tooth depends mainly on roller diameter, thickness reduction, feed rate, and attack angle of the roller. Due to the complexity of the process, the effect of input parameters on tooth height can not be calculated analytically, and therefore the design of experiment method (DOE) was used. By analyzing the process and obtaining the tooth height for each test, the results of the ANOVA analysis were obtained as follows:

- All parameters and interactions affect tooth height. attack angle (α), thickness reduction (T), interaction between roller diameter and attack angle (D×α), and interaction between roller diameter and feed rate (D×f) are, respectively, the most significant parameters affecting the tooth height.
- The tooth height initially increases with increasing the roller diameter up to 40 mm, and then, decreases with a further increase in the diameter.
- The tooth height increases with increasing the thickness reduction.
- The tooth height decreases with increasing feed rate.
- The tooth height decreases with increasing the attack angle.
- A maximum tooth height of 0.7272 is obtained for D=20 mm, T=35%, f=0.05 mm/rev and α=20°.

Predicting the formation and tooth height with statistical and optimization methods (such as ANN), as well as investigating the effect of process parameters on the defects of this process is one of the tasks that can be done in the future.

6. REFERENCES

1. Wong, C. C., Dean, T. A., and Lin, J. "Incremental forming of solid cylindrical components using flow forming principles." ***Journal of Materials Processing Technology***, Vol. 153–154, No. 1–3, (2004), 60–66. https://doi.org/10.1016/j.jmatprotec.2004.04.102
2. Safak Tunalioglu, M., Tuc, B., and Emin Erdin, M. "Effect of

Coating Material on Wear in Internal Gears." ***International Journal of Engineering, Transactions B: Applications***, Vol. 30, No. 11, (2017), 1792–1799. https://doi.org/10.5829/ije.2017.30.11b.22
3. Nägele, H., Wörner, H., and Hirschvogel, M. "Automotive parts produced by optimizing the process flow forming- Machining." ***Journal of Materials Processing Technology***, Vol. 98, No. 2, (2000), 171–175. https://doi.org/10.1016/S0924-0136(99)00195-8
4. Groche, P., and Fritsche, D. "Application and modelling of flow forming manufacturing processes for internally geared wheels." ***International Journal of Machine Tools and Manufacture***, Vol. 46, No. 11 SPEC. ISS., (2006), 1261–1265. https://doi.org/10.1016/j.ijmachtools.2006.01.016
5. Jiang. S, Ren. Z, Bin. W, and Wu. G., "General issues of FEM in backward ball spinning of thin-walled tubular part with longitudinal inner ribs." ***Transactions of Nonferrous Metals Society of China (English Edition)***, Vol. 17, No. 4, (2007), 793–798. https://doi.org/10.1016/S1003-6326(07)60176-9
6. Jiang, S., Ren, Z., Xue, K., and Li, C. "Application of BPANN for prediction of backward ball spinning of thin-walled tubular part with longitudinal inner ribs." ***Journal of Materials Processing Technology***, Vol. 196, No. 1–3, (2008), 190–196. https://doi.org/10.1016/j.jmatprotec.2007.05.034
7. Jiang. S, Zheng. Y, Ren. Z, and Li. C., "Multi-pass spinning of thin-walled tubular part with longitudinal inner ribs." ***Transactions of Nonferrous Metals Society of China (English Edition)***, Vol. 19, No. 1, (2009), 215–221. https://doi.org/10.1016/S1003-6326(08)60255-1
8. Jiang, S., Ren, Z., Li, C., and Xue, K. "Role of ball size in backward ball spinning of thin-walled tubular part with longitudinal inner ribs." ***Journal of Materials Processing Technology***, Vol. 209, No. 4, (2009), 2167–2174. https://doi.org/10.1016/j.jmatprotec.2008.05.006
9. Haghshenas, M., Jhaver, M., Klassen, R. J., and Wood, J. T. "Plastic strain distribution during splined-mandrel flow forming." ***Materials and Design***, Vol. 32, No. 6, (2011), 3629–3636. https://doi.org/10.1016/j.matdes.2011.02.014
10. Haghshenas, M., Wood, J. T., and Klassen, R. J. "Investigation of strain-hardening rate on splined mandrel flow forming of 5052 and 6061 aluminum alloys." ***Materials Science and Engineering A***, Vol. 532, (2012), 287–294. https://doi.org/10.1016/j.msea.2011.10.094
11. Haghshenas, M., Wood, J. T., and Klassen, R. J. "Effect of strain-hardening rate on the grain-to-grain variability of local plastic strain in spin-formed fcc metals." ***Materials Science and Engineering A***, Vol. 552, (2012), 376–383. https://doi.org/10.1016/j.msea.2012.05.054
12. Xia, Q.X., Sun, L.Y., Cheng, X.Q. and Ye, B.Y., "Analysis of the forming defects of the trapezoidal inner-gear spinning." In IEEM 2009 - IEEE International Conference on Industrial Engineering and Engineering Management, (2009), 2333–2337. https://doi.org/10.1109/IEEM.2009.5373016
13. Xu, W., Zhao, X., Shan, D., Li, J., Deng, Q., Cui, X., and Li, Z. "Numerical simulation and experimental study on multi-pass stagger spinning of internally toothed gear using plate blank." ***Journal of Materials Processing Technology***, Vol. 229, (2015), 450–466. https://doi.org/10.1016/j.jmatprotec.2015.10.001
14. Rasoli, M. A., Abdullah, A., Farzin, M., Tehrani, A. F., and Taherizadeh, A. "Influence of ultrasonic vibrations on tube spinning process." ***Journal of Materials Processing Technology***, Vol. 212, No. 6, (2012), 1443–1452. https://doi.org/10.1016/j.jmatprotec.2012.02.006
15. El Amri, A., El Yakhloufi Haddou, M., and Khamlichi, A. "Thermal-Mechanical Coupled Manufacturing Simulation in Heterogeneous Materials." ***Civil Engineering Journal***, Vol. 2, No. 11, (2016), 600–606. https://doi.org/10.28991/cej-2016-00000062
16. Suryo, S. H., Bayuseno, A. P., Jamari, J., and Wahyudi, A. I. "Analysis of Rake Angle Effect to Stress Distribution on Excavator Bucket Teeth Using Finite Element Method." ***Civil Engineering Journal***, Vol. 3, No. 12, (2018), 1222. https://doi.org/10.28991/cej-030952
17. Montgomery, D. Design and analysis of experiments. John wiley & sons, 2017.

Persian Abstract

چکیده

ساخت چرخ‌دنده‌ی داخلی با استفاده از فرآیند فلوفرمینگ، فرایندی جدید است که در آن دندانه‌ها با نیروی کم و بدون نیاز به ابزارآلات پُرهزینه تولید می‌شوند .در این تحقیق، ساخت چرخ‌دنده‌ی داخلی با استفاده از فرایند فلوفرمینگ مورد بررسی قرار گرفته است. این فرآیند به صورت عددی مورد تحلیل و شبیه‌سازی قرار گرفت .چندین آزمایش تجربی برای ارزیابی صحت نتایج شبیه‌سازی انجام شد. مقایسه‌ی نتایج شبیه‌سازی و تجربی نشان‌دهنده‌ی تطابق بسیار خوب بین این نتایج است. پس از تایید نتایج شبیه‌سازی، با کمک روش طراحی آزمایش‌های (DOE) اثرات قطر غلتک، درصد کاهش ضخامت، پیشروی و زاویه‌ی حمله بر روی ارتفاع دندانه بررسی گردید. طبق نتایج تحلیل واریانس(ANOVA)، زاویه‌ی حمله، درصد کاهش ضخامت، اثر متقابل (D×α) و (D×f) به ترتیب بیشترین تاثیر را بر روی ارتفاع دندانه دارند. با افزایش قطر غلتک و درصد کاهش ضخامت ارتفاع دندانه افزایش می‌یابد، اما پیشروی و زاویه‌ی حمله اثر معکوس بر روی ارتفاع دندانه دارند.

International Journal of Engineering

Journal Homepage: www.ije.ir

Simulation Study on Efficiency of Woven Matrix Wire and Tube Heat Exchanger

I. M. Arsana*, M. A. H. Rahardjo

Department of Mechanical Engineering, Faculty of Engineering, Universitas Negeri Surabaya, East Java, Indonesia

P A P E R I N F O

Paper history:
Received 31 July 2020
Received in revised form 02 October 2020
Accepted 30 October 2020

Keywords:
Woven Matrix Wire and Tube Heat Exchanger
Wire Pitch
Massflow Rate
Wire Efficiency
Heat Transfer
Temperature and Velocity Contour

A B S T R A C T

Wire and tube heat exchanger has been utilized in refrigerators whose cooling performance depends on how much the wire are releasing heat. Wire efficiency is an important factor of the performance. The woven matrix is a new design of wire configuration on wire and tube heat exchanger. This research focused on optimization design of woven matix by varying wire pitch (p_w 5,7,9 mm) and three inlet massflows with controlling the hot fluid temperature at 353K. Computational Fluid Dynamic Simulation is used to determine heat transfer distribution of fluid in tube. The validation was conducted experimentally by measuring 9 temperature points at heat exchanger. This research revealed that p_w 7 mm with massflow rate 0.000571kg/s can decrease fluid temperature until it reaches 30^{o}C with all wires working to release the heat and it results 74% wire efficiency. Then, p_w 9 mm with massflow 0.0011kg/s has 64% wire efficiency, it was because the heat exchanger cannot decrease the fluid temperature to 303K. At high massflow, heat exchanger need more wire to decrease the temperature down to 303K. This research is recommended for cooling system widely applied in food industry, an optimal cooling system will reduce the cost of electricity consumption for cooler.

doi: *10.5829/ije.2020.33.12c.19*

NOMENCLATURE

h	Convection heat transfer coefficient	**Greek Symbols**	
A_w	Wire area	η_w	Wire efficiency
A_t	Tube area	**Subscripts**	
T	Temperature	t	Tube
p_w	Wire picth	w	Wire
		∞	Surrounding

1. INTRODUCTION

Heat exchanger has been widely used in power generation industry, food industry, manufacturing industry and even in our home appliances. Design of heat exchanger is very important for the application and performance. The optimal design can increase heat transfer performance [1].

The performance is a heat exchanger having high heat transfer. One of types of heat exchanger is wire and tube that is usually used in refrigeration system as a condenser which decrease temperature without changing a phase of a fluid [2]. Following the times, the wire and tube has many development design to increase its performance.

In the Wire and tube condenser, to decrease temperature optimally, some studies have investigated on design to optimize a performance, such an experiment who studied about energy saving and cost reduction of wire and tube designs [3]. Wei etal. [4] used the numerical approach to investigate the thermal performance of a new design of wire and tube condenser and another case predicted the performance of wire and tube using mathematical approach in matlab [5].

A design variation of wire and tube has been investgated by Arsana et al. [6] using numerical approach. The researchers have reviewed about the effect of design to wire and tube efficiency in single staggered design. This research obtained pitch wire and wire

*Corresponding Author Institutional Email: *madearsana@unesa.ac.id* (I. M. Arsana)

Please cite this article as: I. M. Arsana, M. A. H. Rahardjo, Simulation Study on Efficiency of Woven Matrix Wire and Tube Heat Exchanger, International Journal of Engineering, Transactions C: Aspects Vol. 33, No. 12, (2020), 2572-2577.

diameter p_w/d_w has a variations value of efficiency to temperature of inlet fluid. Then Arsana et al. [7] have studied to find out optimization p_w/l_w. Based on optimization studies using the Hooke-Jevees method, the maximum optimization factor (fre_f) is in the wire diameter (d_w) of 0.9 mm and the distance between wires (pw) of 11 mm. But, in another research a new design of wire and tube namely woven matrix design experimentally studied which use wire pitch variation and inlet temperature variation. According to this research, the woven matrix needs to be optimum design with massflow variations to reach optimal performance of the woven matrix design.

Lately, many studies have been conducted with computational fluid dynamic (CFD) to visualize fluid distribution with minimum cost and research performance of heat transfer. The research using CFD about heat transfer is very intersting to use. The research by Kostikov and Romanenkov [8] studied about approximation of convergence solution of CFD modelling. Sengupta et al. [9] used CFD for improved design of stove system. The reseach by Yamini et al. [10] provided numerical modelling of wind turbine. Rahate and Sarode [11] about design of air distribution system visualized the airflow. The research by Rani and Thermal [12] analyzed heat transfer and visualized airflow with fin variation effect. Gonul et al. [13] investigated airflow surrounding at wire and tube which had error arround 10% in modelling by CFD.

Based on previous work, the researchers have done a lot to study for wire and tube optimization. So, this research provide innovation using CFD simulation to figure out the optimization values of a single woven matrix with variations in pitch wires and massflow rates. The efficient heat exchanger will help to increase production and reduce an operational cost in industries or home activities. This research uses three models of wire and tube which is three wire pitch (5, 7 and 9 mm) with three variation of massflow. This research uses simulation approach with validation experimentally of one of wire and tube model. Analysis was conducted by heat transfer visualization, diagram of heat transfer efficient, and wire efficiency

2. MATERIALS AND METHODS

2. 1. Materials This research was conducted by developing the models using simulation with validation experimentally. In the first process, an experiment was performed as a reference and validation. Then simulate the other models with ANSYS Fluent software to obtain the parameters accurately. The detail of object is shown in Table 1.

2. 2. Simulation Setup There are 3 steps in simulation processes which are pre-processing, solving, and post-processing [7]. At the pre-processing conducted by designing wire and tube heat exchanger with a type of woven matrix wire. Detailed of simulation flow is shown in Figure 1.

TABLE 1. Specification detail of single woven matrix wire and tube heat exchanger

Properties	Value or Information
Wire and tube material	Steel
Heat exchanger height	445 mm
Heat exchanger width	436 mm
Tube out diameter	4.8 mm
Tube in diameter	3.2 mm
Wire diameter	1.2 mm
Wire pitch	5, 7, 9 mm
Total concentric tube	12
Tube pitch	40 mm
Fluid	Thermo oil-32
Specific heat (cp)	2000 J/kgK
Density (ρ)	856 kg/m^3

There are 3 methods that used in this study which are simulation set up, validation models and some equations to find out heat transfer coefficient and wire efficiency heat exchanger.

2. 2. 1. Pre-processing This step was designed for the simulation model. The simulation was conducted with a 3D geometry model.

2. 2. 2. Solving The next step of the simulation was solving, this step determined the boundary conditions of models. Detail of boundary condition is summarized in Table 2.

2. 2. 3. Post-processing First step visualize model which was the wire and tube model. The result of this

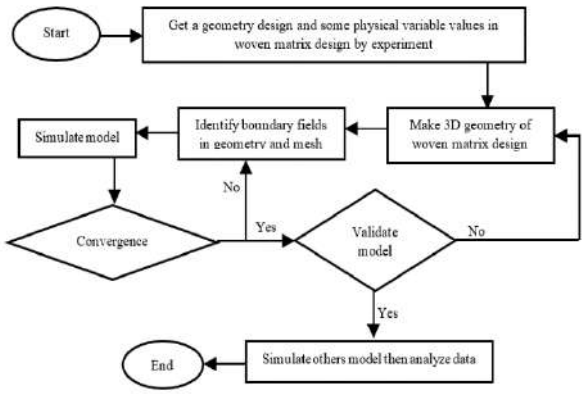

Figure 1. Simulation Flowchart

TABLE 2. Boundary condition of wire and tube simulation

No.	Parts of wire and tube	Boundary Condition
1	Inlet	Inlet Massflow
2	Outlet	Outflow
3	Wall Tube	Wall
4	Wall Wire	Wall

model showed the distribution of heat transfer of fluid in the tube. The second step was air simulation model, this result model showed how the movement of the air around the wire and tube heat exchanger.

2. 3. Validation Model The experiment was carried out at p_w 7 mm to obtain the data for validation. It was compared to simulation results with a maximum error 5% of 9 points on wire and tube heat exchanger that were measured with a thermocouple [7]. If the simulation have been valid, and then the simulation was processed on the next variable which was p_w 5 mm and 9 mm. The single woven matrix wire and tube and 9 points of thermocouple on the Heat Exchanger are shown in Figures 2 and 3.

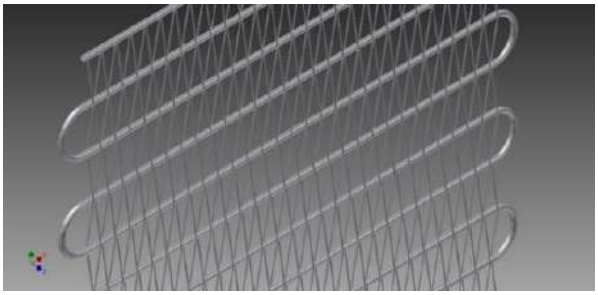

Figure 2. Single Woven Matrix Wire and Tube Heat Exchanger

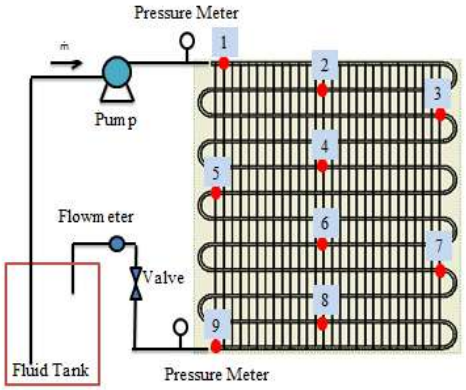

Figure 3. Experimental Setup

2. 4. Wire Efficiency Wire efficiency is the ratio between the rate of heat transfer by the wire with the maximum heat transfer rate that occurs when the entire surface of the wire is at the base temperature of the wire [7].

$$\eta_f = \frac{q\ fin}{q\ maks} = \frac{h,A_w(T_w - T_\infty)}{h,A_w(T_t - T_\infty)} \quad (1)$$

3. RESULT AND DISCUSSION

3. 1. Contour of Single Woven Matrix Wire and Tube Temperature The results of the simulation are displayed in the form of a contour visualization of the wire and tube temperature and air velocity. It is shown in Figure 4.

According to Figure 4 (a) the massflow 0.0011 kg/s has a contour color that dominated by red, yellow and green. This indicates that the fluid in the wire and tube is still hot or above the ambient temperature. At this condition, wire and tube is able to decrease the fluid temperature to 320 K (47 ^{o}C). The massflow 0.000571 kg/s Figure 4 (b) and 0.000549 kg/s Figure 4 (c) began to appear blue temperature contours which shows the heat exchanger has decreased the fluid temperature to reach an ambient temperature of 30 ^{o}C.

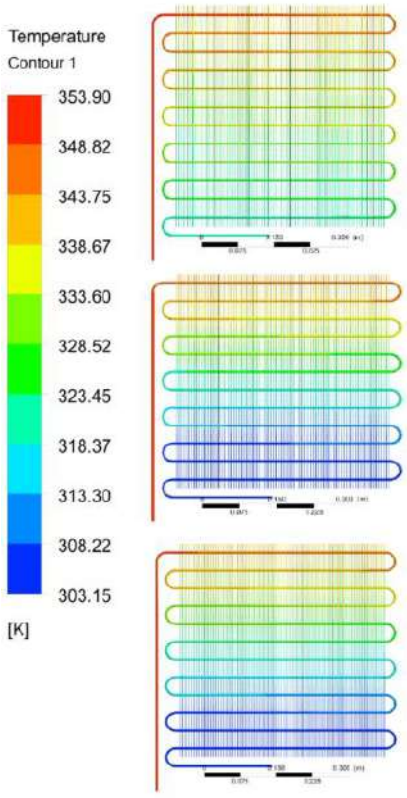

Figure 4. Contour of Temperature Single Woven Matrix Wire and Tube 5 mm

The results above showed at p_w 5 mm, the slower massflow can decrease temperature to optimal performance. However, overall heat transfer at p_w 5 mm does not maximal as wire and tube has reached optimal temperature to 30 ºC at 3/4 of the entire surface of the wire and tube. This occurs because more narrow wire picth requires the higher inlet temperature [6, 7].

According to Figure 5 (d), the massflow 0.0011 kg/s decreases the fluid temperature to 325 K (52 ºC). Figure 5 (e) the massflow 0.000571 kg/s and Figure 5 (f) 0.000549 kg/s began to appear blue temperature contours where it shows that the heat exchanger has cooled the fluid temperature to reach an ambient temperature of 30 ºC. At a distance of 7 mm wire and tube work with the whole of wire discharged the heat, so the heat transfer occurs at the entire surface of the wire and tube.
This indicates that wire and tube at p_w 7 mm has good performance at three mass flow rates and good performance at inlet temperature of 353 K.

According to Figure 6 (g), the massflow 0.0011 kg/s indicates that the fluid in the wire and tube is still hot. At this condition, wire and tube decrease the fluid temperature to 328 K (55 ºC).

Unlike the p_w 5 and 7 mm, at the massflow 0.000571 kg/s and 0.000549 kg/s, according to Figure 6 shows that the heat exchanger at p_w 9 mm with massflow 0.000571 kg/s (h) was able to decrease the fluid temperature down to 309 K (36 ºC). Whereas for the massflow 0.000549 kg/s (i) it was able to decrease the fluid temperature to 310 K (37 ºC).

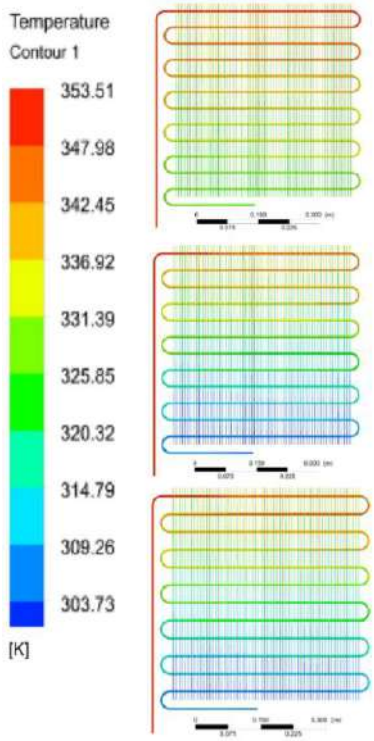

Figure 5. Contour of Temperature Single Woven Matrix Wire and Tube 7 mm

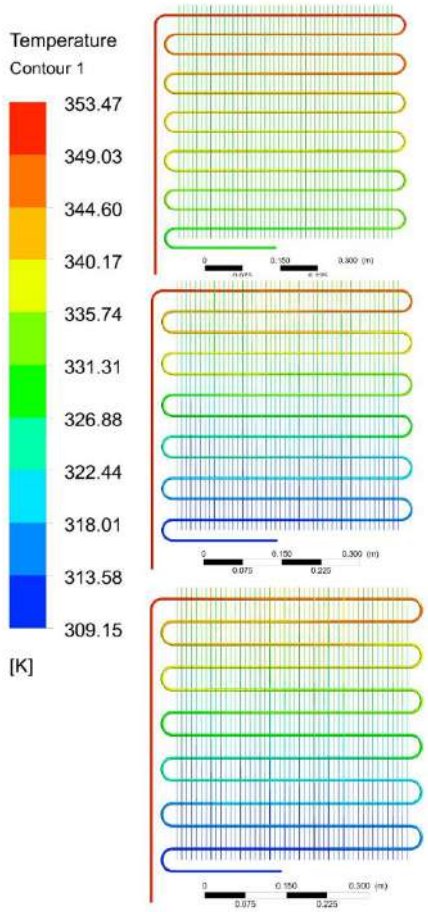

Figure 6. Contour of Temperature Single Woven Matrix Wire and Tube 9 mm

The p_w 9 mm does not reach the ambient temperature in outlet. This indicates for this design has less performance than p_w 7 because the heat transfer area is not as high as the other designs [7].

3. 2. Wire Efficiency (η_w) Wire efficiency is the ratio between the rate of heat transfer by the wire with the maximum heat transfer rate that occurs when the entire surface of the wire is at the base temperature of wire. The wire efficiency of single woven matrix wire and tube is shown in Figure 7.

Figure 7 shows the effect of the wires pitch (p_w) on wire efficiency of single woven matrix wire and tube. Heat exchanger p_w 5 mm with massflow 0.0011 kg/s influences the value of wire efficiency. At this condition the heat exchanger decreased the fluid temperature to 47 ºC, the efficiency value in this condition is 73%. At the same wires pitch but with 0.000571 kg/s massflow rate, the heat exchanger can decreased the fluid temperature to 30 ºC in 2/3 of the overall surface area of the heat

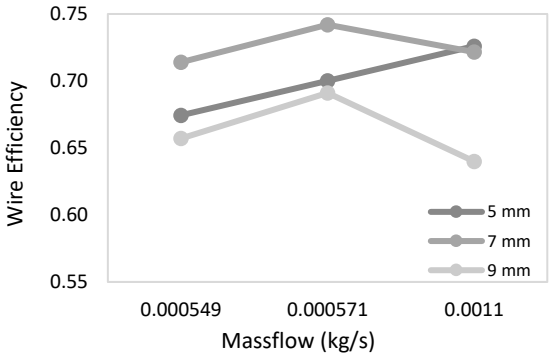

Figure 7. Wire Efficiency

exchanger. This shows that the heat transfer process doesn't occur equally, it means that in the last 1/3 of the heat exchanger area there was a wire that doesn't work release the heat because the design is not optimal for this condition [7]. The wire efficiency has a value of 70%. For the same reason as the 0.0011 kg/s mass flow, at a wires pitch 5 mm with 0.000549 kg/s has a wire efficiency value of 67%**.**

Heat exchanger p_w 7 mm with 0.0011 kg/s massflow decreased the fluid reaches temperature 52^o C, this causes the wire efficiency at Pw 7 mm was smaller than 5 mm which is equal to 72%. This shows that at the high massflow, more wire was needed to increase the efficiency value. Heat exchanger p_w 7 mm with 0.000571 kg/s massflow, heat transfer occurs equally. In this condition the heat exchanger could decreased the fluid temperature until it reaches 30^o C with all wires working to dissipate the heat, so the wire efficiency value was 74%. For the same reasons p_w 7 mm at 0.000549 kg/s could cool the fluid to ambient temperature, but the wire efficiency at this condition was only 71% this was because the T_w value of 47.85 ^{o}C, smaller than p_w 7 mm with a 0.000571 kg/s massflow which had a T_w value of 48.55 ^{o}C.

At p_w 9 mm on 0.0011 kg/s massflow, the wire efficiency has the smallest value between p_w 5 and 7 mm. This was because at the fast massflow more wire was needed to increase wire efficiency. Wire efficiency at p_w 9 mm with 0.0011 kg/s massflow has a value of 64%. Heat exchanger p_w 9 mm at 0.000571 kg/s and 0.000549 kg/s also has a small wire efficiency, in both conditions the heat exchanger couldn't decreased the fluid to reach an ambient temperature. The high temperature of the out fluid causes the value of the divider (T_t - T_∞) to be high. So the wire efficiency values for p_w 9 mm at the 0.000571 kg/s and 0.000549 kg/s were 69 and 66%, respectively.

Referring to research was conducted by Arsana et al. [6] that the wire pitch affects value of wire and tube efficiency. That research showed a small wire pitch p_w/d_w = 0.015 had the highest wire efficiency value at a fluid inlet temperature of 80 ^{o}C, the wire efficiency was 82%. This was in line with this research that at the high temperatures heat exchanger requires more wires to achieve an optimal values. In addition, at the high mass flow rate, the heat exchanger with p_w 5 mm just has an efficiency 67% because high massflow made the wire didn't have time contact to absorb the heat from fluid flow. Beside this, the visualization using CFD as research describes clearly and more imagines the mind in analysing heat transfer [8-10].

4. CONCLUSION

According to this result, the simulation study of wire and tube heat exchanger has obtained the optimal design is p_w 7 mm with massflow rate of 0.000571 kg/s which indicates the highest efficiency wire is 74%. It occurs as in this condition the heat exchanger has been able to decrease the fluid to an ambient temperature with all the wires working to transfer the heat.

Based on this research the optimal design depends on the characteristic of every condition. This design can help to improve the optimal design for wire and tube which is be able to use for refrigeration system in home appliance or industry. This work is also useful for other researches of refrigeration system and CFD applications.

5. REFERENCES

1. Wu, F., Lu, Y., Wang, M., Zhang, X., Yang, C., "Catalytic Removal of Ozone by Pd/ACFs and Optimal Design of Ozone Converter for Air Purification in Aircraft Cabin", ***Civil Engineering Journal,*** Vol. 5, No. 8, (2019), 1656-1671. Doi: 10.28991/cej-2019-03091361.
2. Akbar, F.R., Arsana, I M., "Effect of Wire Pitch on Capacity of Single Staggered Wire and Tube Heat Exchanger Using Computational Fluid Dynamics", ***International Journal of Engineering, Transactions B: Applications",*** Vol. 33, No. 8, (2020), 1637-1642. Doi:10.5829/IJE.2020.33.08B.
3. Badwar, S.R., Joshi, M., Mandale, S., Kujur, A., "Experimentation and Performance Analysis of Natural Draft Wire and Tube Condenser", ***International Journal of Recent Technology and Engineering,*** Vol. 8, No. 3, (2019), 4303-4308. Doi: 10.35940/ijrte.c5174.098319.
4. Wei, J., Liu, J., Xu, X., Ruan, J., Li, G., "Experimental and Computational Investigation of the Thermal Performance of a Vertical Tube Evaporative Condenser", ***Applied Thermal Engineering,*** Vol. 160, (2019), 114100. Doi: 10.1016/j.applthermaleng.2019.114100.
5. Kumra, A., Rawal, N., Samui, P., "Prediction of Heat Transfer Rate of a Wire-on-Tube Type Heat Exchanger: An Artificial Intelligence Approach", ***Procedia Engineering,*** Vol. 64, (2013), 74-83. Doi: 10.1016/j.proeng.2013.09.078.
6. Arsana, I M., Budhikardjono, K., Susianto., Altway, A., "Modelling of The Single Staggered Wire and Tube Heat Exchanger", ***International Journal of Applied Engineering Research***, Vol. 11, No. 8, (2016), 5591-5599.
7. Arsana, I M., Budhikardjono, K., Susianto., Altway, A., "Optimization of the Single Staggered Wire and Tube Heat Exchanger", MATEC Web of Conference**,** No. 58, (2016), 01017. Doi: 10.1051/matecconf/20165801017.

8. Kostikov, Y.A., Romanenkov, A.M., "Approximation of Multidimensional Optimal Control Problem for the Heat Equation (Applicable to Computational Fluid Dynamic (CFD))", ***Civil Engineering Journal,*** Vol. 6, No.4, (2020), 743-768. Doi: 10.28991/cej-2020-03091506.
9. Sengupta, A. R., Gupta, R., Biswas, A., "Computational Fluid Dynamic Analysis of Stove Systems for Cooking and Drying of Muga Silk", ***Emerging Science Journal,*** Vol. 3, No. 5, (2019), 285-292. Doi: 10.28991/esj-2019-01191.
10. Yamini, O.A., Mousavi, S.H., Kavianpour, M.R., Movahedi, A., "Numerical Modelling of Sediment Scouring Phenomenon Around the Offshore Wind Turbine Pile in Marine Environment", ***Enviromental Earth Sciences***, Vol. 77, No. 23, (2018), 776. Doi: 10.1007/s12665-018-7967-4.
11. Rahate, S.D., Sarode, A.D., "Design of Distribution System for Operation Theatre Using Flow Visualization Techniques to Improve Flow Characteristics", ***International Journal of Engineering: Transaction A: Basics,*** Vol. 33, No. 01, (2020), 164-169. Doi: 10.5829/ije.2020.33.01a.19.
12. Rani, B.U., Thermal, M.E., "Analysis of Heat Transfer Through External Fins Using CFD Tool" ***International Journal of Modern Trends in Engineering and Research,*** Vol. 4, No. 12, (2017), 81-87. Doi: 10.21884/ijmter.2017.4385.67dgg.
13. Gonul, A., Agra, O., Atayilmaz, O., Demir, H., Sevendir, Kemal, M., Teke, "Experimental and Numerical Investigation of Air Side Forced Convection on Wire-on-Tube Condensers", ***International Journal of Thermal Science,*** Vol. 151, (2020), 106241. Doi: 10.1016/j.ijthermalsci.2019.106241.

Persian Abstract

چکیده

مبدل حرارتی سیم و لوله در یخچال ها بسیار مورد استفاده قرار گرفته است ، عملکرد خنک کننده خوب به این بستگی دارد که سیم بتواند گرما آزاد کند. کارایی سیم عامل مهمی در عملکرد است. پیکربندی سیم ماتریس بافته شده طراحی جدیدی از سیم و لوله است. این تحقیق بر روی طراحی بهینه سازی ماتیکس بافته شده با گام سیم متغیر (Pw 5،7،9 میلی متر) و سه جریان انبوه ورودی با کنترل دمای مایع گرم در ۸۰ درجه سانتی گراد متمرکز شده است. شبیه سازی محاسباتی دینامیک سیالات (CFD) برای تعیین توزیع انتقال حرارت مایع در لوله استفاده می شود. اعتبار سنجی به طور آزمایشی با اندازه گیری ۹ نقطه دما در مبدل حرارتی انجام می شود. این تحقیق نشان داد که Pw 7 میلی متر با سرعت جرم ۰.۰۰۰۵۷۱ kg / s می تواند دمای مایع را کاهش دهد تا زمانی که به ۳۰ درجه سانتیگراد برسد در حالی که تمام سیم ها برای آزاد کردن گرما کار می کنند ، در نتیجه کارایی سیم ۷٤٪ است. پس از آن ، Pw 9 میلی متر با جریان توده ۰.۰۰۱۱ kg / s 64 درصد بهره وری سیم دارد ، به این دلیل است که مبدل حرارتی نمی تواند دمای سیال را به ۳۰oC کاهش دهد. در جریان جرم زیاد ، مبدل حرارتی به سیم بیشتری نیاز دارد تا دما را به ۳۰ درجه سانتیگراد کاهش دهد. این تحقیق برای سیستم خنک کننده توصیه می شود که به طور گسترده ای در صنایع غذایی استفاده می شود ، یک سیستم خنک کننده بهینه هزینه برق مصرفی کولر را کاهش می دهد

AIMS AND SCOPE

The objective of the International Journal of Engineering is to provide a forum for communication of information among the world's scientific and technological community and Iranian scientists and engineers. This journal intends to be of interest and utility to researchers and practitioners in the academic, industrial and governmental sectors. All original research contributions of significant value focused on basics, applications and aspects areas of engineering discipline are welcome.

This journal is published in three quarterly transactions: Transactions A (Basics) deal with the engineering fundamentals, Transactions B (Applications) are concerned with the application of the engineering knowledge in the daily life of the human being and Transactions C (Aspects) - starting from January 2012 - emphasize on the main engineering aspects whose elaboration can yield knowledge and expertise that can equally serve all branches of engineering discipline.

This journal will publish authoritative papers on theoretical and experimental researches and advanced applications embodying the results of extensive field, plant, laboratory or theoretical investigation or new interpretations of existing problems. It may also feature - when appropriate - research notes, technical notes, state-of-the-art survey type papers, short communications, letters to the editor, meeting schedules and conference announcements. The language of publication is English. Each paper should contain an abstract both in English and in Persian. However, for the authors who are not familiar with Persian, the publisher will prepare the latter. The abstracts should not exceed 250 words.

All manuscripts will be peer-reviewed by qualified reviewers. The material should be presented clearly and concisely:

- *Full papers* must be based on completed original works of significant novelty. The papers are not strictly limited in length. However, lengthy contributions may be delayed due to limited space. It is advised to keep papers limited to 7500 words.
- *Research* notes are considered as short items that include theoretical or experimental results of immediate current interest.
- *Technical notes* are also considered as short items of enough technical acceptability with more rapid publication appeal. The length of a research or technical note is recommended not to exceed 2500 words or 4 journal pages (including figures and tables).

Review papers are only considered from highly qualified well-known authors generally assigned by the editorial board or editor in chief. Short communications and letters to the editor should contain a text of about 1000 words and whatever figures and tables that may be required to support the text. They include discussion of full papers and short items and should contribute to the original article by providing confirmation or additional interpretation. Discussion of papers will be referred to author(s) for reply and will concurrently be published with reply of author(s).

INSTRUCTIONS FOR AUTHORS

Submission of a manuscript represents that it has neither been published nor submitted for publication elsewhere and is result of research carried out by author(s). Presentation in a conference and appearance in a symposium proceeding is not considered prior publication.

Authors are required to include a list describing all the symbols and abbreviations in the paper. Use of the international system of measurement units is mandatory.

- On-line submission of manuscripts results in faster publication process and is recommended. Instructions are given in the IJE web sites: www.ije.ir-www.ijeir.info
- Hardcopy submissions must include MS Word and jpg files.
- Manuscripts should be typewritten on one side of A4 paper, double-spaced, with adequate margins.
- References should be numbered in brackets and appear in sequence through the text. List of references should be given at the end of the paper.
- Figure captions are to be indicated under the illustrations. They should sufficiently explain the figures.
- Illustrations should appear in their appropriate places in the text.
- Tables and diagrams should be submitted in a form suitable for reproduction.
- Photographs should be of high quality saved as jpg files.
- Tables, Illustrations, Figures and Diagrams will be normally printed in single column width (8cm). Exceptionally large ones may be printed across two columns (17cm).

PAGE CHARGES AND REPRINTS

The papers are strictly limited in length, maximum 6 journal pages (including figures and tables). For the additional to 6 journal pages, there will be page charges. It is advised to keep papers limited to 3500 words.

Page Charges for Papers More Than 6 Pages (Including Abstract)	
For International Author ***	**$55 / per page**
For Local Author	**100,000 Toman / per page**

AUTHOR CHECKLIST

- Author(s), bio-data including affiliation(s) and mail and e-mail addresses).
- Manuscript including abstracts, key words, illustrations, tables, figures with figure captions and list of references.
- MS Word files of the paper.

International **J**ournal of **E**ngineering, P.O. Box 13145-1659, Tehran, I.R. Iran
Materials and Energy Research Center, 5 Ahuramazda St., Alvand Ave., Argentina Sq., Tehran, Islamic Republic of Iran
www.merc.ac.ir - www.emerc.ac.ir

THOMSON REUTERS

WEB OF SCIENCE

Scopus®

CAS®
A DIVISION OF THE
AMERICAN CHEMICAL SOCIETY

Google
Scholar